Analysis of nonlinear flow problems with heat transfer

By

Rai Sajjad Saif

Department of Mathematics and Statistics

Faculty of Basic and Applied Sciences

International Islamic University, Islamabad, Pakistan

2018

Reg. No # 23-FBAS/PhDMA/F12

Analysis of nonlinear flow problems with heat transfer

By

Rai Sajjad Saif

Supervised by

Dr. Rahmat Ellahi

Co-Supervised by

Prof. Dr. Tasawar Hayat

Department of Mathematics and Statistics

Faculty of Basic and Applied Sciences

International Islamic University, Islamabad, Pakistan

2018

Analysis of nonlinear flow problems with heat transfer

A THESIS
SUBMITTED IN THE PARTIAL FULFILLMENT OF THE REQUIREMENTS FOR THE DEGREE OF

DOCTOR OF PHILOSOPHY

IN

MATHEMATICS

By
Rai Sajjad Saif

Supervised by
Dr. Rahmat Ellahi

Co-Supervised by
Prof. Dr. Tasawar Hayat

Department of Mathematics and Statistics

Faculty of Basic and Applied Sciences

International Islamic University, Islamabad, Pakistan

2018

Reg. No # 23-FBAS/PhDMA/F12

Acknowledgement

All praise for **ALLAH SWT**, the creator, the glorious and the merciful Lord, who guides me in darkness, helps me in difficulties and enables me to view stumbling blocks as stepping stones to the stars to reach the ultimate stage with courage. All of my veneration and devotion goes to our beloved **Prophet Muhammad (P.B.U.H)** the source of humanity, kindness and guidance for the whole creatures and who declared it an obligatory duty of every Muslim to seek and acquire knowledge.

I owe a great debt of sincerest gramercy to my benevolent & devoted supervisor Dr. Rahmat Ellahi. His tremendous enthusiasm and insight will continue to influence me throughout my career as a Mathematician. I wish to express my profound appreciation and sincerest thanks to my worthy co-supervisor Prof. Dr. Tasawar Hayat, Chairman, Department of Mathematics, Quaid-I-Azam University, for his unsurpassed, inexhaustible inspiration, selfless guidance, dedication and greatest support all the way of my research work. Despite of his engaging and hectic schedule, he always welcomed me for guidance and assistance in my work.

Salute to my Parents and Siblings, who did a lot for my thesis, financially and miscellaneous matters. I owe my heartiest gratitude for their assistance and never ending prayers for my success. I have no words to express millions of thanks to my Wife for her part which may never ever be compared or replaced with any reward.

My sincere thanks to all my respected teachers in my career; whom teachings, instructions, knowledge and experiences made it possible. I enact my heartiest thanks to all my friends, colleagues and well-wishers for the constructive, productive, fruitful and moral support throughout this whole journey.

Rai Sajjad Saif

Reg. No # 23-FBAS/PhDMA/F12

Dedication

This thesis is dedicated to my Sons:

Muhammad Umar Rai

and

Muhammad Abdur Rahman Rai

Preface

Recently the researchers and scientists are interested to explore the characteristics of fluid flow in the presence of heat transfer. This is due to its rapid advancements and developments in the technological and industrial processes. In fact the investigators are interested to enhance the efficiency of various machnies by increasing the rate of heat transfer and quality of the final products with desired characcteristics through rate of cooling. The combined effects of heat and mass transfer are further significant in many natural, biological, geophysical and industrial processes. Such phenomena include designing of many chemical processing equipment, distribution of temperature and moisture over agricultural fields, formation and dispersion of fog, damaging of crops due to freezing, environmental pollution, grooves of fluid trees, drying of porous solids, geothermal reservoirs, packed bed catalytic reactors, enhanced oil recovery, underground energy transport and thermal insulation. Inspired by such practical applications, the present thesis is devoted to analyze the nonlinear flows problems with heat transfer. This thesis is structured as follows.

Chapter one just includes basic concepts and fundamental equations.

Chapter two addresses the magnetohydrodynamic (MHD) flow of Powell-Eyring nanomaterial bounded by a nonlinear stretching sheet. Novel features regarding thermophoresis and Brownian motion are taken into consideration. Powell-Eyring fluid is electrically conducted subject to non-uniform applied magnetic field. Assumptions of small magnetic Reynolds number and boundary layer approximation are employed in the

mathematical development. Zero nanoparticles mass flux condition at the sheet is selected. Adequate transformations yield nonlinear ordinary differential systems. The developed nonlinear systems have been computed through the homotopic approach. Effects of different pertinent parameters on velocity, temperature and concentration fields are studied and analyzed. Further numerical data of skin friction and heat transfer rate is also tabulated and interpreted. **The contents of this chapter have been published in "Results in Physics, 7 (2017) 535–543".**

Chapter three investigates the magnetohydrodynamic (MHD) stagnation point flow of Jeffrey material towards a nonlinear stretching surface with variable thickness. Heat transfer characteristics are examined through the melting process, viscous dissipation and internal heat generation. A nonuniform applied magnetic field is considered. Boundary-layer and low magnetic Reynolds number approximations are employed in the problem formulation. Both the momentum and energy equations are converted into the non-linear ordinary differential system using appropriate transformations. Convergent solutions for resulting problems are computed. Behaviors of various parameters on velocity and temperature distributions are examined. Heat transfer rate is also computed and analyzed. **These observations have been published in "International Journal of Thermal Sciences, 132 (2018) 344-354".**

Chapter four extends the analysis of previous chapter for second grade nanofluid flow with mixed convection and internal heat generation. Novel features regarding Brownian motion and thermophoresis are present. Boundary-layer approximation is employed in the problem formulation. Momentum, energy and concentration equations are converted into the non-linear ordinary differential system through the appropriate transformations.

Convergent solutions for resulting problem are computed. Temperature and concentration are investigated. The skin friction coefficient and heat and mass transfer rates are also analyzed. Our results indicate that the temperature and concentration distributions are enhanced for larger values of thermophoresis parameter. **The contents of this chapter have been published in "Results in Physics, 7 (2017) 2821-2830".**

Darcy-Forchheimer flow of viscous fluid caused by a curved stretching sheet have been discussed in chapter five. Flow for porous space is characterized by Darcy-Forchheimer relation. Concept of homogeneous and heterogeneous reactions is also utilized. Heat transfer for Cattaneo--Christov theory characterizing the feature of thermal relaxation is incorporated. Nonlinear differential systems are derived. Shooting algorithm is employed to construct the solutions for the resulting nonlinear system. The characteristics of various sundry parameters are discussed. Skin friction and local Nusselt number are numerically described. **The conclusions have been published in "Results in Physics, 7 (2017) 2886-2892".**

In chapter six, the work of chapter five is extended to viscous nanofluid flow due to a curved stretching surface. Convective heat and mass boundary conditions are discussed. Flow in porous medium is characterized by Darcy-Forchheimer relation. Attributes of Brownian diffusion and thermophoresis are incorporated. Boundary layer assumption is employed in the mathematical development. The system of ordinary differential equations is developed by mean of suitable variables. Shooting algorithm is employed to construct the numerical solutions of resulting nonlinear systems. The skin friction coefficient and local Nusselt and Sherwood numbers have been analyzed. **These contents**

are accepted for publication in "International Journal of Numerical Methods for Heat and Fluid Flow".

In chapter seven, the work of chapter six is extended for magnetohydrodynamic (MHD) flow of micropolar fluid due to a curved stretching surface. Homogeneous-heterogeneous reactions are taken into consideration. Heat transfer process is explored through heat generation/absorption effects. Micropolar liquid is electrically conducted subject to uniform applied magnetic field. Small magnetic Reynolds number assumption is employed in the mathematical treatment. The reduction of partial differential system to nonlinear ordinary differential system has been made by employing suitable variables. The obtained nonlinear systems have been computed. The surface drag and couple stress coefficients and local Nusselt number are described by numerical data. **The contents of this chapter have been published in "Journal of Molecular Liquids 240 (2017) 209–220".**

Chapter eight extended the idea of chapter seven by considering magnetohydrodynamic (MHD) flow of Jeffrey nanomaterial due to a curved stretchable surface. Novel features regarding thermophoresis and Brownian motion are considered. Heat transfer process is explored through heat generation/absorption effects. Jeffrey liquid is electrically conducted subject to uniform applied magnetic field. Boundary layer and low magnetic Reynolds number assumptions are employed. The obtained nonlinear systems are solved. The characteristics of various sundry parameters are studied through plots and numerical data. Moreover the physical quantities such as skin friction coefficient and local Nusselt number are described by numerical data. **These findings have been submitted for publication in "International Journal of Heat and Mass Transfer".**

The objective of chapter nine is to provide a treatment of viscous fluid flow induced by nonlinear curved stretching sheet. Concept of homogeneous and heterogeneous reactions has been utilized. Heat transfer process is explored through convective heating mechanism. The obtained nonlinear system of equations has been computed and solutions are examined graphically. Surface drag force and local Nusselt number are numerically discussed. **Such contents are submitted for publication in "Applied Mathematics and Mechanics".**

Chapter ten provides a numerical simulation for boundary-layer flow of viscous fluid bounded by nonlinear curved stretchable surface. Convective conditions of heat and mass transfer are employed at the curved nonlinear stretchable surface. Heat generation/absorption and chemical reaction effects are accounted. Nonlinear ordinary differential systems are computed by shooting algorithm. The characteristics of various sundry parameters are explored. Further the skin friction coefficient and local Nusselt and Sherwood numbers are tabulated numerically. **The contents of present chapter have been published in "Results in Physics, 7 (2017) 2601-2606".**

Contents

Nomenclature	
A	ratio parameter of free stream and stretching velocities
$\mathbf{A}_1^*$	first Rivlin-Ericksen tensor
$\mathbf{A}_2^*$	second Rivilin-Erickson tensor
A_1 and B_1	chemical species of homogeneous and heterogeneous reactions
a_0	dimensional constant
a_1	positive constant for stretching surface
a^*	constant for variable thickness
a and b	chemical species concentrations
B_0	magnetic field strength
$B_1^*(x)$	non-uniform magnetic field
$B_2^*(x)$	non-uniform magnetic field for variable thickness
$\mathbf{b}$	body force
b_x, b_y and b_z	components of body force
C	concentration
C_m, C_w	surface concentrations
C_f	concentration of convective mass stretching surface
C_b	drag coefficient
C_{m_1}	couple stress coefficient
C_∞	ambient fluid concentration
C^* and β^*	material constants for Powell-Eyring fluid
C_{fx_1}, C_{fx_2}	Skin friction coefficients for Cartesian coordinates
$C_{f_{s_1}}, C_{f_{s2}}, C_{f_{s_3}}$	Skin friction coefficients for Curvilinear coordinates
C_i^* $(i = 1 - 45)$	arbitrary constants
c_p	specific heat
c_s	solid surface's heat capacity
$(\rho c)_p$	effective heat capacity of nanoparticles

D_B	Brownian diffusion coefficient
D_m	mass diffusivity
D_T	thermophoretic diffusion coefficient
D_{A_1} and D_{B_1}	chemical species diffusion coefficients
Ec	Eckert number
$F\left(=\frac{C_b}{s\sqrt{K_1}}\right)$	porous medium variable inertia coefficient
F_r	inertia coefficient
$F_1, \theta_1, \hat{f}, \hat{\theta}, \hat{\phi}, u(y)$ and Φ	unknown functions
f'	dimensionless velocity
f_1 and g_1	continuous functions
$f^*_{\hat{m}}$, $\theta^*_{\hat{m}}$, $\phi^*_{\hat{m}}$ and $g^*_{\hat{m}}$	special solutions
$f_{\hat{m}}$, $\theta_{\hat{m}}$, $\phi_{\hat{m}}$ and $g_{\hat{m}}$	general solutions
$f_{0_i}, \theta_{0_i}\,(i=1-3), \phi_{0_i}\,(i=1-4), g_{0_1}$ and $u_0(y)$	initial approximations/guesses
$\mathbf{g}$	gravitational acceleration
H	homotopy mapping
h_f	heat transfer coefficient
$\hbar, \hbar_f, \hbar_g, \hbar_\theta$ and $\hbar_\phi$	auxiliary parameters
ϕ, h	dimensionless concentrations
$\mathbf{I}$	identity tensor
$\mathbf{j}$	mass flux
j	micro-inertia per unit mass.
j_{w_1}, j_{w_2}	wall mass flux for Curvilinear coordinates
K_p	permeability of porous medium
K^*	material parameter
K and Λ	parameters for Powell-Eyring fluid
k	dimensionless curvature parameter
k_1	homogeneous reaction parameter
k_2	heterogeneous reaction parameter

k_m	mass transfer coefficient
k_v	vortex viscosity
k_c and k_s	rate constants
$\mathbf{L}\,(=\boldsymbol{\nabla}\mathbf{V})$	velocity gradient
Le	Lewis number
M	magnetic parameter
Me	melting parameter
$\mathbf{M}$	couple stress tensor
m_0	constant (for concentration of microelements)
n	power-law index/shape parameter
N	micro-rotation
N_r	buoyancy ratio variable
N_b	Brownian motion variable
N_t	thermophoresis variable
$Nu_{x_1}, Nu_{x_2}, Nu_{x_3}$	local Nusselt numbers
Nu_s	local Nusselt number for Curvilinear coordinates
$P\,(\zeta)$	dimensionless pressure
p	nondimensionless pressure
$\breve{p}$	embedding parameter
Pr	Prandtl number
$Q_0\,(x)$	heat absorption/generation coefficient for variable thickness
Q_0	heat absorption/generation coefficient
$\mathbf{q}\,(=-k_f\boldsymbol{\nabla}T)$	heat flux
q_{w_1}, q_{w_2}	wall heat fluxes
q_{w_r}	wall heat flux for Curvilinear coordinates
R	radius of curved stretchable surface
R_c	rate of chemical reaction

$\mathrm{Re}_{x_1}, \mathrm{Re}_{x_2}, \mathrm{Re}_{s_1}, \mathrm{Re}_{s_2}$	local Reynolds numbers
r_h	radiative heating
r, s	Curvilinear coordinate axes
$\mathbf{S}$	extra stress tensor
$\mathbf{S}_J$	stress tensor for Jeffrey fluid
$\mathbf{S}_2$	stress tensor for second grade fluid
Sc	Schmidt number
Sh_{x_1}	Sherwood number
Sh_{s_1}, Sh_{s_2}	Sherwood numbers for Curvilinear coordinates
S_{xx}, S_{xy}, S_{xz}, S_{yx}, S_{yy}, S_{yz}, S_{zx}, S_{zy} and S_{zz}	components of extra stress tensor for Jeffrey fluid
T	temperature
T_f	temperature of convective heat stretching surface
T_w	temperature of the stretching surface
T_m	melting temperature
T_0	constant temperature
T_∞	ambient/free stream fluid temperature
t	time
t^*	unit interval
$\boldsymbol{\nabla} T$	temperature gradient
d/dt	material time derivative
$\frac{\partial}{\partial t}$	partial derivative with respect to time
U_w	surface stretching velocity
U_e	free stream velocity
u_w	stretching velocity
u, v and w	velocity components
$u_0(y)$	initial guess
$u(y)$ and Φ	unknown functions
$\mathbf{V}$	fluid vector velocity
X and Y	topological spaces

x, y and z	Cartesian coordinate axes
α	surface thickness parameter
α_1 and α_2^*	normal stress moduli for second grade fluid
$\alpha_1^* (= k_f/(\rho c)_f)$	thermal diffusivity
α_2	local second grade parameter
α_ν, β_ν and γ_ν	spin viscosities
β_c	coefficient of concentration expansion
β	Deborah number
β_t	coefficient of thermal expansion
γ	dimensionless thermal relaxation variable
γ_c	concentration Biot number
γ_s	spin gradient viscosity
γ_t	thermal Biot number
δ	heat generation/absorption parameter
δ_1	ratio of diffusion coefficients
λ	porosity parameter
λ_1	relaxation to retardation times' ratio parameter
λ_2	retardation time
λ^*	latent heat of fluid
λ_1^*	bulk viscosity
λ_G	Grashof number
λ_t	relaxation time of heat flux
$\boldsymbol{\tau}$	Cauchy stress tensor
$\boldsymbol{\tau}_1$	stress tensor for Micropolar fluid
$\boldsymbol{\tau}_{ij}$	stress tensor for Powell-Eyring fluid
τ_{w_1}, τ_{w_2}	wall shear stress

τ_{rs_1}, τ_{rs_2}	wall shear stress for Curvilinear coordinates
τ	heat ratio parameter
$\Delta^{f}_{\hat{m}}$	residual error of dimensionless velocity
$\Delta^{\theta}_{\hat{m}}$	residual error of dimensionless temperature
$\Delta^{\phi}_{\hat{m}}$	residual error of dimensionless concentration
$\mathcal{L}$, $\mathcal{L}_{f_1}$, $\mathcal{L}_{\theta_1}$, $\mathcal{L}_{\phi_1}$, $\mathcal{L}_{g_1}$ and $\mathcal{L}_{f_2}$	auxiliary linear operators
$\mathcal{N}_{f_i}$, $\mathcal{N}_{\theta_i}$ $(i = 1-6)$, $\mathcal{N}_{\phi_i}$ $(i = 1-5)$ and $\mathcal{N}_{g_1}$	non-linear operators
$\tilde{\mathcal{R}}^{\hat{m}}_{f_i}$, $\tilde{\mathcal{R}}^{\hat{m}}_{\theta_i}$ $(i = 1-6)$, $\tilde{\mathcal{R}}^{\hat{m}}_{\phi_i}$ $(i = 1-5)$ and $\tilde{\mathcal{R}}^{\hat{m}}_{g_1}$	mth order non-linear operators
σ_{xx}, σ_{yy} and σ_{zz}	normal stresses
τ_{xy}, τ_{xz}, τ_{yx}, τ_{yz}, τ_{zx} and τ_{zy}	shear stresses
θ	dimensionless temperature
ϕ	dimensionless concentration
μ	dynamic viscosity
ρ_f	density of fluid
ν	kinematic viscosity
σ	electrical conductivity
$\boldsymbol{\omega}$	vorticity vector
$(\rho c)_f$	fluid heat capacity
κ	vortex viscosity
$\boldsymbol{\Omega}$	angular velocity
$\boldsymbol{\epsilon}$	third rank tensor
ε	small constant
tr	trace of a matrix
$\boldsymbol{\nabla}$	Del operator
ζ, η	dimensionless variables

Chapter 1

Some related review and equations

1.1 Introduction

This chapter intends to include literature survey, fluid models and equations useful for the analyses of next chapters.

1.2 Review

The analysis of boundary-layer flow over a stretchable boundary has various applications in metallurgical, industrial, engineering and manufacturing processes. Such applications involve crystal growing, plastic sheets extrusion and fibers, glass blowing, annealing and tinning of copper wire, drawing and paper production. Sakiadis [1] initiated axisymmetric two-dimensional (2-D) boundary layer flow over continuous solid surfaces. Then Crane [2] considered flow past a linearly stretchable surface and developed a closed form solution. There is no doubt that much attention in the past has been devoted to the flow caused by linear stretching velocity. However this consideration is not realistic in plastic industry. Hence some researchers studied the flow problem of nonlinear stretching surface. Gupta and Gupta [3] was the first who proposed that the phenomena of stretching for a surface may not necessarily be linear. Later on, flow over a non-linear heated stretching sheet is studied by Vajravelu [4]. Cortell [5] extended the work of [4] by considering prescribed surface temperature and constant surface temperature conditions. Prasad et al. [6] studied mixed convective flow over a non-linear stretchable surface

with non-uniform fluid characteristics. Yazdi et al. [7] investigated the slip flow by a nonlinear permeable stretched surface with chemical reaction. Mustafa et. al [8] studied axisymmetric nanofluid flow. Hayat et al. [9] investigated MHD flow of second grade nanomaterial. Numerous struggles have been made in this vision through different theoretical and physical aspects but all these investigations are carried out by considering linear and non-linear stretching of surfaces whereas the fluid flow over curved stretching surface has been rarely investigated. Investigation for fluid flow regarding curved stretching surface was first introduced by Sajid et al. [10]. The applications of fluid flow over a curved stretchable surface are curving jaws present in stretching assembling machines. Rosca et al. [11] presented time-dependent flow past a permeable curved shrinking/stretching sheet. Micropolar fluid flow with radiation over a curved stretchable surface is examined by Naveed et al. [12]. Few recent attempts on flow by curved stretching surface can be seen in the studies $[13-15]$. All these investigations are related to curved linear stretching surface whereas Sanni et al. [16] recently considered viscous fluid flow past a nonlinearly stretching curved sheet.

Flow caused by stretching surface of variable thickness has many technological applications. However much attention has not been paid to this concept of variable thickness of surface. Few studies have been presented in this direction. Fang et al. [17] analyzed flow over a linearly stretchable surface of variable thickness. Viscous fluid flow due to nonlinear stretchable sheet of variable thickness and slip velocity is analyzed by Khader and Megahed [18]. Subhashini et al. [19] considered the stretching sheet with variable thickness and find the dual solutions for thermal diffusive flow. Abdel-Wahed et al. [20] examined the viscous nanofluid flow due to a moving sheet having variable thickness. Hayat et al. [21] examined the homogenous-hetrogenous nanofluid flow reactions by a stretched surface of variable thickness. Few latest struggles on variable thickness of surface can be viewed in the studies $[22-24]$.

Non-Newtonian fluids are regarded very prominent for applications in chemical and petroleum industries, biological sciences and geophysics. The flow of non-Newtonian fluids due to stretching surface occurs in several industrial processes, for example, drawing of plastic films, polymer extrusion, oil recovery, food processing, paper production and numerous others. The well-known Navier-Stokes expressions are not appropriate to describe the flow behavior of non-Newtonian materials. However various constitutive relations of non-Newtonian materials are

proposed in the literature due to their versatile nature. Such materials are categorized as differential, integral and rate types. The fluid's class having nonsymmetric stress tensor with polar fluids characteristics are named as micropolar fluids. These are the fluids with microstructure and deals with micro-rotation of suspended particles. Micropolar fluid theory was firstly suggested by Eringen [25 and 26]. He pointed out that one cannot elaborate the impacts of local rotational inertia and couple stresses by classical Navier-Stokes relations. Further mathematical modeling for theory of lubrication and theory of porous media about micropolar fluid equations is derived by Lukaszewiez [27] and Eringen [28]. Micropolar fluids may physically show fluids containing randomly oriented (or spherical) or rigid particles suspended in a viscous medium, where the deformity of fluid particles is negligible. It is affected and not much intricate for both physicists and engineers who apply it and mathematicians who study its theory. The applications of micropolar fluids include animal blood, suspension of particles, paints, liquid crystals, theory of lubrication, turbulent shear flows and theory of porous media. Nazar et al. [29] examined free convected micropolar boundary layer fluid flow with uniform surface heat flux. Srinivasacharya and Reddy [30] examined natural convection flow of doubly stratified non-Darcy micropolar fluid. Impact of thermal radiation in unsteady magnetohydrodynamic flow of micropolar fluid is explored by Hayat and Qasim [31]. Rashidi et al. [32] provided an analytic solution for micropolar fluid flow with porous medium and radiation effects. Cao et al. [33] performed a Lie group analysis to study the flow of micropolar fluid. Waqas et al. [34] investigated the magnetohydrodynamic (MHD) micropolar fluid flow induced by a nonlinear stretchable surface with mixed convection. Recently Turkyilmazoglu [35] studied magnetohydrodynamic flow of micropolar fluid due to a porous heated/cooled deformable plate. The Powell-Eyring fluid model $[36-41]$ is derived from kinetic theory of gases instead of empirical relation as in the case of the power-law model. Ketchup, human blood, toothpaste, etc. are the examples of Powell-Eyring fluid. The features of both relaxation and retardation times are elaborated by Jeffrey fluid model $[42-46]$ which is a category of rate type fluids. Second grade fluid model $[47-51]$ illustrates the effects of normal stress.

Alternative form of fluids that are composition of convectional base liquids and nanometer sized particles are termed as nanofluids. Nanoparticles utilized in the nanomaterials are basically made of metals (Ag, Cu, Al) or nonmetals (carbon nanotubes, graphite) and the base

liquids include ethylene glycol, water or oil. Suspension of nanoparticles in the base liquids greatly varies the heat transfer characteristics and transport property. To obtain prominent thermal conductivity enhancement in the nanofluids, the studies have been processed both theoretically and experimentally. Applications of nanofluids in technology and engineering are nuclear reactor, vehicle cooling, vehicle thermal management, heat exchanger, cooling of electronic devices and many others. Moreover magneto nanofluids (MNFs) are useful in removal of blockage in arteries, wound treatment, cancer therapy, hyperthermia and resonance visualization. Further the nanomaterials enhances the heat transfer rate of computers, microchips in microelectronics, fuel cells, biomedicine, transportation, food processing etc. The pioneer investigation regarding enhancement of thermal properties of base liquid through the suspension of nanoparticles was presented by Choi [52]. Later the development of mathematical relationship of nanofluid with Brownian diffusion and thermophoresis is presented by Buongiorno [53]. Turkyilmazoglu [54] derived the exact analytical solutions for MHD slip flow of nanofluids by considering heat and mass transfer characteristics. Further relevant attempts on nanofluid flows can be quoted through the analysis $[55-78]$ and various studies therein.

The convective heat and mass transfer analysis has drawn the attention of many recent researchers. Choi and Kim [79] studied natural convective condition for initial cooling in heat and mass transfer of cryogenic surface. Thermal diffusion and Soret effects in two-dimensional Hartmann viscous fluid flow is examined by Zueco et al. [80]. Shirvan et al. [81] considered porous solar cavity for combined heat transfer and derived the numerical solution. EHD forced convective nanofluid flow with electric field dependent viscosity is explored by Sheikholeslami et al. [82]. Hayat et al. [83] addressed three-dimensional nanofluid flow due to convectively heated nonlinear stretchable surface with magnetohydrodynamic effects. Ramanaiah et al. [84] analyzed Sisko nanofluid flow due to nonlinear stretchable sheet with thermal radiation and convectively heat and mass transfer conditions. Second grade fluid flow due to convectively heated stretchable sheet is investigated by Das et al. [85].

Heat transfer via Cattaneo-Christov heat flux phenomenon has numerous applications in biomedical, engineering and industry which was initially explored by Fourier [86]. According to his model, the medium under consideration is instantaneously observe the initial disturbance which was not be compatible with the reality hence termed as "paradox of heat conduction".

To overcome such limitation, Cattaneo [87] changed this law by adding thermal relaxation time. Christov [88] further changed the Cattaneo theory [87] by the replacement of time derivative with upper-convected Oldroyd derivative. Ciarletta and Straughan [89] provided stability and uniqueness for Cattaneo-Christov heat flux. Later, incompressible flow with Cattaneo-Christov model via heat conduction is analyzed by Tibullo and Zampoli [90]. Han et al. [91] studied Cattaneo-Christov heat flux for coupled viscoelastic fluid flow. Cattaneo-Christov heat flux and variable thermal conductivity in boundary layer flow past a variable thickness sheet is analyzed by Hayat et al. [92]. Liu et al. [93] investigated fractional Cattaneo-Christov heat flux theory for anomalous convection diffusion. Recently Hayat et al. [94] examined the three dimensional Jeffrey fluid flow having the effects of Cattaneo-Christov heat flux.

In operations heat generation or absorption effects are quite dominant which involve underground disposal of radioactive waste material, heat removal from nuclear fuel debris, storage of food stuffs, disassociating fluids in packed-bed reactors and many others. During manufacturing processes, it is obvious that for controlling the heat transfer rate heat absorption/generation play a prominent role. Analytical solutions for the effects of first order chemical reaction and heat absorption/generation in a micropolar fluid flow is examined by Magyari and Chamkha [95]. Saleem and El-Aziz [96] considered the phenomenons of Hall current and heat sink/source in viscous fluid flow past a moving surface with chemical reaction. Chen [97] analyzed two types of viscoelastic fluids flow past a stretchable surface having magnetohydrodynamics, internal heat generation and viscous dissipation by deriving analytical solution. Chen [98] in another investigation presented the MHD power law fluid flow past a stretchable surface with internal heat absorption/generation and mixed convection. Siddiqa et al. [99] examined natural convective flow with temperature dependent viscosity over an inclined flat surface with heat source. Van Gorder and Vajravelu [100] examined MHD convective flow past a stretchable sheet with heat sink/source and injection/suction. Numerical solutions for the flow of nanofluid was constructed by Rana and Bhargava [101]. Alsaedi et al. [102] derived the series solutions for the stagnation point nanofluid flow with heat sink/source. Noor et al. [103] considered numerical solutions for MHD flow of viscous fluid subject to Joule heating, thermophoresis and heat sink/source. Turkyilmazoglu and Pop [104] analyzed heat generation and soret effects for an electrically conducting fluid flow past a permeable sheet.

Heat transfer with melting effect has received much interest in the field of silicon wafer process, magma solidification and melting of permafrost [105]. Thus Tien and Yen [106] performed an analysis to analyze the behavior between the fluid and melting body through forced convection heat transfer. Later on non-time dependent laminar flow past a flat surface with melting heat transfer is studied by Epstein and Cho [107]. Melting effect in mixed convective flow saturating porous medium is studied by Cheng and Lin [108]. Yacob et al. [109] analyzed the micropolar fluid flow over shrinking/stretching surface with melting heat transfer. Few other studies in this direction can be seen through the attempts [110 – 114].

Homogeneous-heterogeneous reactions occur in abundant chemical reacting processes. These processes include biochemical systems which contain homogeneous-heterogeneous reactions. Complex relation occurs between homogeneous and heterogeneous reactions. In the presence of a catalyst, these reactions have tendency to proceed rapidly whereas in the absence of it they proceed even very slowly or not all together. Some common applications of chemical reactions are ceramics and polymer production, fog dispersion and formation, food processing, hydrometallurgical industry and numerous others. Homogeneous-heterogeneous reactions in viscous fluid flow is examined by Merkin [115]. Chaudhary and Merkin [116] analyzed boundary layer flow for different diffusivities of reactant and autocatalyst in an isothermal model for homogeneous–heterogeneous reactions. Bachok et al. [117] addressed homogeneous–heterogeneous reactions in stagnation-point flow towards a stretchable sheet. Homogeneous-heterogeneous reactions in nanofluid flow past a porous stretchable surface is investigated by Kameswaran et al. [118]. Melting heat transfer and heterogeneous-homogeneous reactions in nanofluid flow is considered by Hayat et al. [119]. Some recent investigations on homogeneous–heterogeneous reactions can be quoted through the analysis [120 – 124] and several studies therein.

Fluid flow saturating porous media has abundant applications in environmental and industrial systems such as heat exchanger design, catalytic reactors, geothermal energy systems and geophysics. The classical Darcy model is later extended to non-Darcian model which incorporates inertia and boundary features. Particularly the flows in porous media are much favorable in fermentation process, grain storage, ground water pollution, movement of water in reservoirs, crude oil production, ground water systems, beds of fossil fuels, recovery systems, nuclear waste disposal, energy storage units, petroleum resources, solar receivers and several

others. The classical Darcy's law is insufficient when inertia and boundary features are taken into account at high flow rate. Forchheimer [125] incorporated a square velocity factor in Darcian velocity to analyzed the inertia and boundary features. This factor is always valid for large Reynolds number. Then Muskat [126] called this factor as "Forchheimer term". Federico et al. [127] considered vertical graded porous media in radial gravity currents for both Newtonian and power-law fluids. Stream wise Darcy-Brinkman-Forchheimer model for MHD fluid flow and heat transfer is explored by Rashidi et al. [128]. Hayat et al. [129] considered Darcy-Forchheimer flow with Cattaneo-Christov heat flux and variable thermal conductivity. Darcy-Forchheimer flow of viscoelastic nanofluids due to nonlinear stretching boundary is also explored by Hayat et al. [130]. Recently Kang et al. [131] considered Neumann boundary conditions for generalized Darcy-Forchheimer model by employing block-centered finite difference method.

1.3 Basic laws

1.3.1 Mass conservation law

The continuity equation or mass conservation law states that the mass can neither be destroyed nor created. Mathematically

$$\frac{\partial \rho_f}{\partial t} + \boldsymbol{\nabla} \cdot \left(\rho_f \mathbf{V}\right) = 0, \tag{1.1}$$

For the case of incompressible fluid Eq. (1.1) can takes the form:

$$\boldsymbol{\nabla} \cdot \mathbf{V} = 0. \tag{1.2}$$

In Cartesian coordinates for two dimensional flow one has

$$\frac{\partial u}{\partial x} + \frac{\partial v}{\partial y} = 0, \tag{1.3}$$

whereas for curved geometry

$$\frac{\partial}{\partial r}\left((r+R)\, v\right) + R\frac{\partial u}{\partial s} = 0. \tag{1.4}$$

1.3.2 Linear momentum conservation law

This law declares that the total linear momentum of a system remains conserved. Mathematically it can be expressed by Newton's second law as

$$\rho_f \frac{d\mathbf{V}}{dt} = \boldsymbol{\nabla} \cdot \boldsymbol{\tau} + \rho_f \mathbf{b}, \tag{1.5}$$

where first term on right hand side of Eq. (1.5) represents surface forces and second term represents body forces while left hand side is the inertial forces per unit volume. $\boldsymbol{\tau} = -p\mathbf{I} + \mathbf{S}$ is the Cauchy stress tensor for the case of incompressible flow. Generally, Cauchy stress tensor and velocity are

$$\boldsymbol{\tau} = \begin{bmatrix} \sigma_{xx} & \tau_{xy} & \tau_{xz} \\ \tau_{yx} & \sigma_{yy} & \tau_{yz} \\ \tau_{zx} & \tau_{zy} & \sigma_{zz} \end{bmatrix}, \tag{1.6}$$

$$\mathbf{V} = [u(x,y,z,t), v(x,y,z,t), w(x,y,z,t)]. \tag{1.7}$$

Eq. (1.5) in component form can be written as

$$\rho_f \left(u\frac{\partial u}{\partial x} + v\frac{\partial u}{\partial y} + w\frac{\partial u}{\partial z} + \frac{\partial u}{\partial t} \right) = \frac{\partial (\sigma_{xx})}{\partial x} + \frac{\partial (\tau_{xy})}{\partial y} + \frac{\partial (\tau_{xz})}{\partial z} + \rho_f b_x, \tag{1.8}$$

$$\rho_f \left(u\frac{\partial v}{\partial x} + v\frac{\partial u}{\partial y} + w\frac{\partial v}{\partial z} + \frac{\partial v}{\partial t} \right) = \frac{\partial (\tau_{yx})}{\partial x} + \frac{\partial (\sigma_{yy})}{\partial y} + \frac{\partial (\tau_{yz})}{\partial z} + \rho_f b_y, \tag{1.9}$$

$$\rho_f \left(u\frac{\partial w}{\partial x} + v\frac{\partial w}{\partial y} + w\frac{\partial w}{\partial z} + \frac{\partial w}{\partial t} \right) = \frac{\partial (\tau_{zx})}{\partial x} + \frac{\partial (\tau_{zy})}{\partial y} + \frac{\partial (\sigma_{zz})}{\partial z} + \rho_f b_z. \tag{1.10}$$

For two-dimensional flow the above equations become

$$\rho_f \left(u\frac{\partial u}{\partial x} + v\frac{\partial u}{\partial y} + \frac{\partial u}{\partial t} \right) = \frac{\partial (\sigma_{xx})}{\partial x} + \frac{\partial (\tau_{xy})}{\partial y} + \rho_f b_x, \tag{1.11}$$

$$\rho_f \left(u\frac{\partial v}{\partial x} + v\frac{\partial v}{\partial y} + \frac{\partial v}{\partial t} \right) = \frac{\partial (\tau_{yx})}{\partial x} + \frac{\partial (\sigma_{yy})}{\partial y} + \rho_f b_y, \tag{1.12}$$

However for curved geometry in two-dimension, the velocity field is given by

$$\mathbf{V} = [u(r+R,s), v(r+R,s), 0] \tag{1.13}$$

and the momentum equations under boundary layer approximation in component form are

$$\frac{1}{r+R}u^2 = \frac{1}{\rho_f}\frac{\partial p}{\partial r}, \tag{1.14}$$

$$\begin{aligned} v\frac{\partial u}{\partial r} + \frac{R}{r+R}u\frac{\partial u}{\partial s} + \frac{1}{r+R}uv &= -\frac{1}{\rho_f}\frac{R}{r+R}\frac{\partial p}{\partial s} \\ &\quad +\nu\left(\frac{\partial^2 u}{\partial r^2} + \frac{1}{r+R}\frac{\partial u}{\partial r} - \frac{1}{(r+R)^2}u\right), \end{aligned} \tag{1.15}$$

where $\nu\left(=\frac{\mu}{\rho_f}\right)$ represents the kinematic viscosity. Moreover it is noticed that for the case of curved surface pressure is no longer consistent within the boundary layer.

1.3.3 Energy conservation law

Energy conservation law states that total energy of the system remains conserved. Mathematically first law of thermodynamics elaborates the heat transfer equation and is given as

$$\rho c_p \frac{dT}{dt} = \boldsymbol{\tau}\cdot\mathbf{L} + \rho r_h - \boldsymbol{\nabla}\cdot\mathbf{q}. \tag{1.16}$$

Left hand side of Eq. (1.16) represents internal energy while on right hand side first term depicts viscous dissipation whereas the last two terms represent radiative and thermal heat fluxes respectively. Thermal heat flux is expressed by Fourier's law of heat conduction. In absence of radiative heating above equation takes the following form

$$\rho c_p \frac{dT}{dt} = \boldsymbol{\tau}\cdot\boldsymbol{\nabla}\mathbf{V} + k_f\boldsymbol{\nabla}^2 T. \tag{1.17}$$

1.3.4 Mass transport equation

It elaborates that the total concentration of the system under consideration remains conserved. Fick's first law is given as

$$\mathbf{j} = -D_m \boldsymbol{\nabla} C, \tag{1.18}$$

where $\mathbf{j}$ denotes the mass flux, D_m the mass diffusivity and C the concentration of species. Fick's second law is given as

$$\frac{dC}{dt} = -\boldsymbol{\nabla}.\mathbf{j}, \tag{1.19}$$

Now by inserting Eq. (1.18) into Eq. (1.19), equation of mass transport is given as

$$\frac{dC}{dt} = D_m \boldsymbol{\nabla}^2 C. \tag{1.20}$$

1.4 Mathematical description of some fluid models

Current dissertation is focused for the analysis of boundary layer flows of incompressible viscous, Micropolar, Powell-Eyring, Jeffrey and Second grade fluid models. Therefore we explain the mathematically models of these fluids briefly.

1.4.1 Viscous fluid

Shear stress and rate of deformation is directly and linearly proportional to each other, which is the Newton's law of viscosity that obeyed by viscous fluids. Extra stress tensor for such fluids is given as:

$$\mathbf{S} = \mu \mathbf{A}_1^*. \tag{1.21}$$

Mathematical expression for first Rivlin-Ericksen $\mathbf{A}_1^*$ is

$$\mathbf{A}_1^* = \operatorname{grad} \mathbf{V} + (\operatorname{grad} \mathbf{V})^{T^t}. \tag{1.22}$$

In Cartesian coordinates, gradient of velocity vector $\mathbf{V} = [u(x,u,z), v(x,u,z), w(x,u,z)]$

is given as:

$$\operatorname{grad}\mathbf{V}=\begin{bmatrix} \frac{\partial u}{\partial x} & \frac{\partial u}{\partial y} & \frac{\partial u}{\partial z} \\ \frac{\partial v}{\partial x} & \frac{\partial v}{\partial y} & \frac{\partial v}{\partial z} \\ \frac{\partial w}{\partial x} & \frac{\partial w}{\partial y} & \frac{\partial w}{\partial z} \end{bmatrix}. \tag{1.23}$$

1.4.2 Micropolar fluid

These fluids $[25-35]$ exhibit the micro-inertia and micro-rotational effects. The extra stress tensor $\boldsymbol{\tau}_1$ and couple stress tensor $\mathbf{M}$ are defined as

$$\boldsymbol{\tau}_1=2\lambda_1^*\left(tr\mathbf{A}_1^*\right)\mathbf{I}+\mu\mathbf{A}_1^*+2k_v\boldsymbol{\epsilon}.\left(\boldsymbol{\omega}-\boldsymbol{\Omega}\right), \tag{1.24}$$

$$\mathbf{M}=\alpha_\nu\left(\nabla.\Omega\right)\mathbf{I}+\beta_\nu\left(\nabla\Omega\right)^{T^t}+\gamma_\nu\nabla\boldsymbol{\Omega}, \tag{1.25}$$

where λ_1^* denotes the bulk viscosity, k_v the vortex viscosity, tr the trace of the matrix, $\boldsymbol{\epsilon}$ the third rank tensor with Levi-Civita symbol, $\boldsymbol{\omega}\left(=\frac{1}{2}\left(\nabla\times\mathbf{V}\right)\right)$ the vorticity vector, $\boldsymbol{\Omega}$ the angular velocity, α_ν, β_ν and γ_ν are the spin viscosities. The basic equations for Micropolar fluid are

$$\rho_f\frac{d\mathbf{V}}{dt}=\boldsymbol{\nabla}\cdot\boldsymbol{\tau}_1+\rho_f\mathbf{b} \tag{1.26}$$

and

$$\rho_f j\frac{d\boldsymbol{\Omega}}{dt}=\boldsymbol{\nabla}\cdot\mathbf{M}+\boldsymbol{\epsilon}, \tag{1.27}$$

where j denotes the micro-inertia per unit mass.

1.4.3 Powell-Eyring fluid

Mathematical expression for extra stress tensor of Powell-Eyring fluid $[36-41]$ is:

$$\boldsymbol{\tau}_{ij}=\mu\frac{\partial u_i}{\partial x_j}+\frac{1}{\beta^*}\sinh^{-1}\left(\frac{1}{C^*}\frac{\partial u_i}{\partial x_j}\right), \tag{1.28}$$

in which β^* and C^* stands for material constants. Powell-Eyring fluid obeys the following conditions

$$\sinh^{-1}\left(\frac{1}{C^*}\frac{\partial u_i}{\partial x_j}\right)\tilde{=}\frac{1}{C^*}\frac{\partial u_i}{\partial x_j}-\frac{1}{6}\left(\frac{1}{C^*}\frac{\partial u_i}{\partial x_j}\right)^3,\ \ \left|\frac{1}{C^*}\frac{\partial u_i}{\partial x_j}\right|\ll 1. \tag{1.29}$$

1.4.4 Jeffrey fluid

The category of non-Newtonian fluid model which belongs to the class of rate type fluids and describes the features of both relaxation and retardation times is Jeffrey fluid. Instead of time derivative here substantive derivative is used. Mathematical expression for extra stress tensor of Jeffrey fluid [42 – 46] can be presented as:

$$\mathbf{S}_J = \frac{\mu}{1+\lambda_1}\left(\mathbf{A}_1^* + \lambda_2 \frac{d\mathbf{A}_1^*}{dt}\right). \tag{1.30}$$

Moreover in scalar form this extra stress tensor $\mathbf{S}_J$ takes the form

$$S_{xx} = \frac{\mu}{1+\lambda_1}\left(2\frac{\partial u}{\partial x} + \lambda_2\left(u\frac{\partial}{\partial x} + v\frac{\partial}{\partial y} + w\frac{\partial}{\partial z}\right)2\frac{\partial u}{\partial x}\right), \tag{1.31}$$

$$S_{xy} = \frac{\mu}{1+\lambda_1}\left(\lambda_2\left(\frac{\partial u}{\partial y} + \frac{\partial v}{\partial x}\right)\left(u\frac{\partial}{\partial x} + v\frac{\partial}{\partial y} + w\frac{\partial}{\partial z}\right) + \left(\frac{\partial u}{\partial y} + \frac{\partial v}{\partial x}\right)\right) = S_{yx}, \tag{1.32}$$

$$S_{xz} = \frac{\mu}{1+\lambda_1}\left(\lambda_2\left(\frac{\partial u}{\partial z} + \frac{\partial w}{\partial x}\right)\left(u\frac{\partial}{\partial x} + v\frac{\partial}{\partial y} + w\frac{\partial}{\partial z}\right) + \left(\frac{\partial u}{\partial z} + \frac{\partial w}{\partial x}\right)\right) = S_{zx}, \tag{1.33}$$

$$S_{yy} = \frac{\mu}{1+\lambda_1}\left(2\frac{\partial v}{\partial y} + \lambda_2\left(u\frac{\partial}{\partial x} + v\frac{\partial}{\partial y} + w\frac{\partial}{\partial z}\right)2\frac{\partial v}{\partial y}\right), \tag{1.34}$$

$$S_{yz} = \frac{\mu}{1+\lambda_1}\left(\lambda_2\left(\frac{\partial v}{\partial z} + \frac{\partial w}{\partial y}\right)\left(u\frac{\partial}{\partial x} + v\frac{\partial}{\partial y} + w\frac{\partial}{\partial z}\right) + \left(\frac{\partial v}{\partial z} + \frac{\partial w}{\partial y}\right)\right) = S_{zy}, \tag{1.35}$$

$$S_{zz} = \frac{\mu}{1+\lambda_1}\left(2\frac{\partial w}{\partial z} + \lambda_2\left(u\frac{\partial}{\partial x} + v\frac{\partial}{\partial y} + w\frac{\partial}{\partial z}\right)2\frac{\partial w}{\partial z}\right). \tag{1.36}$$

The momentum conservation law for a Jeffrey fluid model yields

$$\rho_f\left(u\frac{\partial u}{\partial x} + v\frac{\partial u}{\partial y} + w\frac{\partial u}{\partial z}\right) = \frac{\partial}{\partial x}S_{xx} + \frac{\partial}{\partial y}S_{xy} + \frac{\partial}{\partial z}S_{xz}, \tag{1.37}$$

$$\rho_f\left(u\frac{\partial v}{\partial x} + v\frac{\partial v}{\partial y} + w\frac{\partial v}{\partial z}\right) = \frac{\partial}{\partial x}S_{yx} + \frac{\partial}{\partial y}S_{yy} + \frac{\partial}{\partial z}S_{yz}, \tag{1.38}$$

$$\rho_f\left(u\frac{\partial w}{\partial x} + v\frac{\partial w}{\partial y} + w\frac{\partial w}{\partial z}\right) = \frac{\partial}{\partial x}S_{zx} + \frac{\partial}{\partial y}S_{zy} + \frac{\partial}{\partial z}S_{zz}, \tag{1.39}$$

here the body forces and pressure gradient are neglected. Now by incorporating the expressions of S_{xx}, S_{yy}, S_{zz}, S_{xy}, S_{yx}, S_{xz}, S_{zx}, S_{yz} and S_{zy} into Eqs. (1.37) – (1.39) and subsequently by

applying the boundary layer approximations we ultimately obtain

$$u\frac{\partial u}{\partial x}+v\frac{\partial u}{\partial y}+w\frac{\partial u}{\partial z}=\frac{\nu}{1+\lambda_1}\left(\lambda_2\left(\begin{array}{c}u\frac{\partial^3 u}{\partial x\partial z^2}+v\frac{\partial^3 u}{\partial y\partial z^2}+w\frac{\partial^3 u}{\partial z^3}\\+\frac{\partial u}{\partial z}\frac{\partial^2 u}{\partial x\partial z}+\frac{\partial v}{\partial z}\frac{\partial^2 u}{\partial y\partial z}+\frac{\partial w}{\partial z}\frac{\partial^2 u}{\partial z^2}\end{array}\right)+\frac{\partial^2 u}{\partial z^2}\right), \tag{1.40}$$

$$u\frac{\partial v}{\partial x}+v\frac{\partial v}{\partial y}+w\frac{\partial v}{\partial z}=\frac{\nu}{1+\lambda_1}\left(\lambda_2\left(\begin{array}{c}u\frac{\partial^3 v}{\partial x\partial z^2}+v\frac{\partial^3 v}{\partial y\partial z^2}+w\frac{\partial^3 v}{\partial z^3}\\+\frac{\partial u}{\partial z}\frac{\partial^2 v}{\partial x\partial z}+\frac{\partial v}{\partial z}\frac{\partial^2 v}{\partial y\partial z}+\frac{\partial w}{\partial z}\frac{\partial^2 v}{\partial z^2}\end{array}\right)+\frac{\partial^2 v}{\partial z^2}\right). \tag{1.41}$$

Two-dimensional boundary layer Jeffrey fluid flow can be presented by the equation

$$u\frac{\partial u}{\partial x}+v\frac{\partial u}{\partial y}=\frac{\nu}{1+\lambda_1}\left(\frac{\partial^2 u}{\partial y^2}+\lambda_2\left(u\frac{\partial^3 u}{\partial x\partial y^2}+v\frac{\partial^3 u}{\partial y^3}-\frac{\partial u}{\partial x}\frac{\partial^2 u}{\partial y^2}+\frac{\partial u}{\partial y}\frac{\partial^2 u}{\partial x\partial y}\right)\right) \tag{1.42}$$

and in curved geometry it can be expressed as

$$\begin{aligned}v\frac{\partial u}{\partial r}+\frac{R}{r+R}u\frac{\partial u}{\partial s}+\frac{1}{r+R}uv &= -\frac{1}{\rho_f}\frac{R}{r+R}\frac{\partial p}{\partial s}+\frac{\nu}{1+\lambda_1}\left(\begin{array}{c}\frac{\partial^2 u}{\partial r^2}+\frac{1}{r+R}\frac{\partial u}{\partial r}\\-\frac{1}{(r+R)^2}u\end{array}\right)\\ &\quad+\frac{\nu\lambda_2}{1+\lambda_1}\left(\begin{array}{c}\frac{\partial v}{\partial r}\frac{\partial^2 u}{\partial r^2}+v\frac{\partial^3 u}{\partial r^3}\\+\frac{R}{r+R}\frac{\partial u}{\partial r}\frac{\partial^2 u}{\partial s\partial r}+\frac{R}{r+R}u\frac{\partial^3 u}{\partial s\partial r^2}\\+\frac{1}{r+R}v\frac{\partial^2 u}{\partial r^2}-\frac{R}{(r+R)^2}\frac{\partial u}{\partial r}\frac{\partial u}{\partial s}\\-\frac{1}{r+R}\frac{\partial v}{\partial r}\frac{\partial u}{\partial r}+\frac{1}{(r+R)^2}u\frac{\partial v}{\partial r}\end{array}\right).\end{aligned} \tag{1.43}$$

1.4.5 Second grade fluid

Second grade fluid model $[47-51]$ having extra stress tensor $\mathbf{S}_2$ is expressed as

$$\mathbf{S}_2=\mu\mathbf{A}_1^*+\alpha_1\mathbf{A}_2^*+\alpha_2\left(\mathbf{A}_1^*\right)^2 \tag{1.44}$$

where α_1 and α_2^* are the normal stress moduli and $\mathbf{A}_2^*$ the second Rivilin-Erickson tensor is

$$\mathbf{A}_2^*=\frac{d\mathbf{A}_1^*}{dt}+\mathbf{A}_1^*\mathbf{L}+\mathbf{L}^{T^t}\mathbf{A}_1^*. \tag{1.45}$$

Moreover second grade fluid model obey the following conditions

$$\mu\geq 0,\ \alpha_1\geq 0,\ \alpha_1+\alpha_2=0, \tag{1.46}$$

for the thermodynamic stability. Two-dimensional boundary layer equation for second grade fluid in Cartesian coordinate system is

$$u\frac{\partial u}{\partial x}+v\frac{\partial u}{\partial y}=\nu_f\frac{\partial^2 u}{\partial y^2}+\frac{\alpha_1}{\rho_f}\left(\begin{array}{c} u\frac{\partial^3 u}{\partial x\partial y^2}+\frac{\partial u}{\partial y}\frac{\partial^2 v}{\partial y^2} \\ +\frac{\partial u}{\partial x}\frac{\partial^2 u}{\partial y^2}+v\frac{\partial^3 u}{\partial y^3} \end{array}\right). \tag{1.47}$$

1.5 Methodologies

1.5.1 Homotopy

In topology if one function can be transformed continuously into the other then such functions are called homotopic.

Definition

Let f_1 and g_1 be two continuous functions and X and Y be two topological spaces, then a homotopy between f_1 and g_1 from X to Y is defined to be continuous function

$$H : X * t^* \to Y, \tag{1.48}$$

from the product of X with the unit interval $t^* \in [0,1]$ to Y such that for all point x in X and

$$H(x,0) = f_1(x), \qquad H(x,1) = g_1(x). \tag{1.49}$$

The map H is called a homotopy between f_1 and g_1. Any function f_1 which is homotopic to g_1 can be written as

$$f_1 \simeq g_1. \tag{1.50}$$

We think of a homotopy as a continuous one parameter family of maps from X to Y. If we consider the parameter t^* as representing time, at time $t^* = 0$, we have the map f_1 and as t^* varies the map H varies continuously so that at $t^* = 1$ we have the map g_1.

Homotopy analysis method (HAM)

In order to solve various types of nonlinear problems analytically, Liao proposed a general method namely the homotopy analysis method (HAM) [132, 134, 61, 46]. To present fundamental idea of HAM, we assume the following differential equation:

$$\mathcal{N}[u\,(y)] = 0, \tag{1.51}$$

In above equation y indicates an independent variable. Liao [132] constructs the following zeroth-order deformation equation

$$(1-\breve{p})\,\mathcal{L}[\Phi\,(y;\breve{p}) - u_0(y)] = \breve{p}\mathcal{N}[\Phi\,(y;\breve{p})], \tag{1.52}$$

where $\breve{p} \in [0,1]$ and $\hbar(\neq 0)$ are the embedding and auxiliary parameters respectively. It is obvious that when $\breve{p} = 0$ and $\breve{p} = 1$, the following holds

$$\Phi\,(y;0) = u_0(y), \qquad \Phi\,(y;1) = u(y), \tag{1.53}$$

respectively. When $\breve{p}$ varies such that it starts from 0 and ends at 1, $\Phi\,(y;\breve{p})$ varies from $u_0(y)$ to $u(y)$. Now by Taylor series expansion

$$\Phi\,(y;\breve{p}) = u_0(y) + \sum_{i=1}^{\infty} u_i(y)\breve{p}^i, \tag{1.54}$$

$$u_i(y) = \frac{1}{i!}\frac{\partial^i \Phi(y,\breve{p})}{\partial \breve{p}^i}\bigg|_{\breve{p}=0}, \tag{1.55}$$

where the term on the right hand side of above equation can be evaluated by differentiating the zeroth-order deformation Eq. (1.53) $i-$times with respect to $\breve{p}$ and then dividing them by $i!$ and hence setting $\breve{p} = 0$.

If the appropriate values of $u_0(y)$, $\mathcal{L}$ and $\hbar$ are chosen so that the series (1.55) converges at $\breve{p} = 1$, one obtains

$$u(y) = u_0(y) + \sum_{i=1}^{\infty} u_i(y), \tag{1.56}$$

which must be the solution of the original non-linear problem (1.52) .

1.5.2 Shooting technique

This technique is employed using software Mathematica with Wolfram Language function using a built-in tool named as NDSolve. NDSolve generate solutions in terms of interpolating function objects. This tool/command has huge potential for solving nonlinear partial differential equations.

Chapter 2

On MHD nonlinear stretching flow of Powell-Eyring nanomaterial

This chapter describes flow of Powell-Eyring nanomaterial bounded by a nonlinear stretching surface. Novel features regarding thermophoresis and Brownian motion are taken into consideration. Powell-Eyring fluid is electrically conducted subject to applied magnetic field. Assumptions of small magnetic Reynolds number and boundary layer approximation are utilized in the mathematical development. Zero nanoparticles mass flux condition at the sheet is selected. Adequate transformation yield nonlinear ordinary differential systems. The developed nonlinear problems are computed through the homotopic approach. Influence of numerous effective variables on velocity, temperature and concentration are studied. Further numerical data of skin friction and heat transfer rate is also tabulated and interpreted.

2.1 Formulation

Let us consider two dimensional (2D) magnetohydrodynamic flow of Powell-Eyring nanomaterial. The flow is due to nonlinear stretchable surface. Features of thermophoresis and Brownian motion are taken into consideration. The $x-$ and $y-$axes are taken parallel and transverse to the stretching surface. The sheet at $y = 0$ is stretching along the $x-$direction with velocity $u_w(x) = a_1 x^n$ where a_1 and n are positive constants. Powell-Eyring fluid is electrically conducting subject to non-uniform magnetic field in $y-$direction (see Fig. 2.1). Induced magnetic

field for low magnetic Reynolds number is omitted.

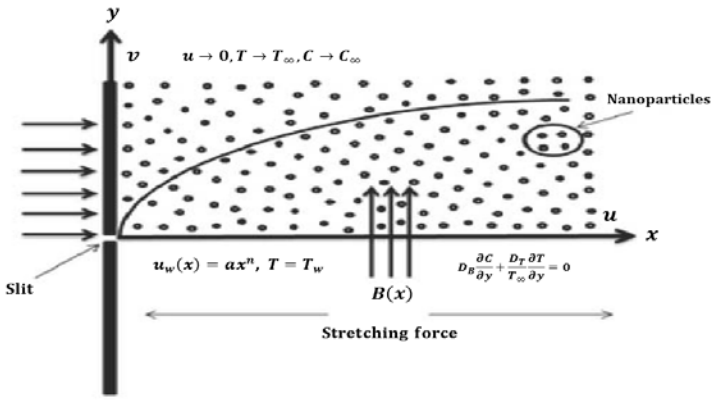

Fig. 2.1. Geometry of the problem.

The boundary layer expressions for two-dimensional (2D) magnetohydrodynamic flow of Powell-Eyring nanofluid are [39, 9] :

$$\frac{\partial u}{\partial x} + \frac{\partial v}{\partial y} = 0, \tag{2.1}$$

$$u\frac{\partial u}{\partial x} + v\frac{\partial u}{\partial y} = \left(\nu + \frac{1}{\rho_f \beta^* C^*}\right)\frac{\partial^2 u}{\partial y^2} - \frac{1}{2\rho_f \beta^* C^{*3}}\left(\frac{\partial u}{\partial y}\right)^2 \frac{\partial^2 u}{\partial y^2} - \frac{\sigma\left(B_1^*(x)\right)^2}{\rho_f}u, \tag{2.2}$$

$$u\frac{\partial T}{\partial x} + v\frac{\partial T}{\partial y} = \alpha\frac{\partial^2 T}{\partial y^2} + \frac{(\rho c)_p}{(\rho c)_f}\left(\frac{D_T}{T_\infty}\left(\frac{\partial T}{\partial y}\right)^2 + D_B\left(\frac{\partial T}{\partial y}\frac{\partial C}{\partial y}\right)\right), \tag{2.3}$$

$$u\frac{\partial C}{\partial x} + v\frac{\partial C}{\partial y} = \frac{D_T}{T_\infty}\left(\frac{\partial^2 T}{\partial y^2}\right) + D_B\left(\frac{\partial^2 C}{\partial y^2}\right). \tag{2.4}$$

Here $B_1^*(x) = B_0 x^{\frac{n-1}{2}}$ represents the non-uniform magnetic field. The associated boundary conditions are [59, 9] :

$$u = u_w(x) = a_1 x^n,\ v = 0,\ T = T_w,\ D_B\frac{\partial C}{\partial y} + \frac{D_T}{T_\infty}\frac{\partial T}{\partial y} = 0 \text{ at } y = 0, \tag{2.5}$$

$$u \to 0, \quad T \to T_\infty, \quad C \to C_\infty \quad \text{as } y \to \infty. \tag{2.6}$$

Introducing the suitable transformations

$$\left.\begin{aligned} u = a_1 x^n f'(\zeta),\ v = -\left(\tfrac{a_1\nu(n+1)}{2}\right)^{1/2} x^{\frac{n-1}{2}}\left(f + \tfrac{n-1}{n+1}\zeta f'\right), \\ \zeta = \left(\tfrac{a_1(n+1)}{2\nu}\right)^{1/2} x^{\frac{n-1}{2}} y,\ \theta(\zeta) = \tfrac{T-T_\infty}{T_w-T_\infty},\ \phi(\zeta) = \tfrac{C-C_\infty}{C_\infty}. \end{aligned}\right\} \tag{2.7}$$

Eq. (2.1) is vanishes symmetrically while Eqs. (2.2) – (2.6) yield

$$(1+K)\, f''' + f f'' - \left(\frac{n+1}{2}\right) K\Lambda f''^2 f''' - \left(\frac{2n}{n+1}\right) f'^2 - \left(\frac{2}{n+1}\right) M^2 f' = 0, \tag{2.8}$$

$$\theta'' + \Pr\left(f\theta' + N_b\theta'\phi' + N_t\theta'^2\right) = 0, \tag{2.9}$$

$$\phi'' + Le\,\Pr f\phi' + \frac{N_t}{N_b}\theta'' = 0, \tag{2.10}$$

$$\left.\begin{aligned} f = 0,\quad f' = 1,\quad \theta = 1,\quad N_b\phi' + N_t\theta' = 0 \ \text{ at } \ \zeta = 0, \\ f' \to 0,\quad \theta \to 0,\quad \phi \to 0 \ \text{ as } \ \zeta \to \infty. \end{aligned}\right\} \tag{2.11}$$

The parameters appearing in Eqs. (2.8) – (2.11) are defined by

$$\left.\begin{aligned} K = \tfrac{1}{\mu\beta_1^* C^*},\ \Lambda = \tfrac{u_w^3}{2\nu x C^{*2}},\ M^2 = \tfrac{\sigma B_0^2}{\rho_f a_1},\ \Pr = \tfrac{\nu}{\alpha_1^*}, \\ N_t = \tfrac{(\rho c)_p D_T(T_w - T_\infty)}{(\rho c)_f \nu T_\infty},\ N_b = \tfrac{(\rho c)_p D_B C_\infty}{(\rho c)_f \nu},\ Le = \tfrac{\alpha_1^*}{D_B}. \end{aligned}\right\} \tag{2.12}$$

Expression of coefficient of skin friction and local Nusselt number are

$$C_{f_{x_1}} = \frac{\tau_{w_1}}{\rho_f u_w^2},\ Nu_{x_1} = \frac{x q_{w_1}}{k_f\,(T_w - T_\infty)}, \tag{2.13}$$

in which wall shear stress (τ_{w_1}) and heat flux (q_{w_1}) satisfy

$$\left.\begin{aligned} \tau_{w_1} = \left(\left(1 + \tfrac{1}{\beta^* C^*}\right)\tfrac{\partial u}{\partial y} - \tfrac{1}{6\beta^* C^{*3}}\left(\tfrac{\partial u}{\partial y}\right)^3\right)\Big|_{y=0}, \\ q_{w_1} = -k_f\left(\tfrac{\partial T}{\partial y}\right)\Big|_{y=0}. \end{aligned}\right\} \tag{2.14}$$

In dimensionless variables

$$\left.\begin{aligned} \mathrm{Re}_{x_1}^{1/2}\, C_{fx_1} = \sqrt{\tfrac{n+1}{2}}\left((1+K)f''(0) - \tfrac{1}{3}(\tfrac{n+1}{2})K\Lambda f''^3(0)\right), \\ \mathrm{Re}_{x_1}^{-1/2}\, Nu_{x_1} = -\sqrt{\tfrac{n+1}{2}}\theta'(0), \end{aligned}\right\} \tag{2.15}$$

where $\mathrm{Re}_{x_1} = u_w x/\nu$ stands for local Reynolds number.

2.2 Homotopy analysis solutions

The appropriate primary approximations $\left(f_{0_1}, \theta_{0_1}, \phi_{0_1}\right)$ in homotopic solutions are defined as

$$f_{0_1}(\zeta) = 1 - \exp(-\zeta),\ \theta_{0_1}(\zeta) = \exp(-\zeta),\ \phi_{0_1}(\zeta) = -\frac{N_t}{N_b}\exp(-\zeta) \tag{2.16}$$

and auxiliary linear operators $\left(\mathcal{L}_{f_1},\ \mathcal{L}_{\theta_1},\ \mathcal{L}_{\phi_1}\right)$ are

$$\mathcal{L}_{f_1} = \frac{d^3 f}{d\zeta^3} - \frac{df}{d\zeta},\ \mathcal{L}_{\theta_1} = \frac{d^2\theta}{d\zeta^2} - \theta,\ \mathcal{L}_{\phi_1} = \frac{d^2\phi}{d\zeta^2} - \phi. \tag{2.17}$$

The above auxiliary linear operators satisfy the following characteristics:

$$\left.\begin{array}{c} \mathcal{L}_{f_1}\left[C_1^* + C_2^*\exp(\zeta) + C_3^*\exp(-\zeta)\right] = 0,\ \mathcal{L}_{\theta_1}\left[C_4^*\exp(\zeta) + C_5^*\exp(-\zeta)\right] = 0, \\ \mathcal{L}_{\phi_1}\left[C_6^*\exp(\zeta) + C_7^*\exp(-\zeta)\right] = 0, \end{array}\right\} \tag{2.18}$$

in which C_i^* $(i = 1 - 7)$ elucidate the random constants.

2.2.1 Deformation problems at zeroth-order

$$(1-\breve{p})\mathcal{L}_{f_1}\left[\hat{f}(\zeta,\breve{p}) - f_{0_1}(\zeta)\right] = \breve{p}\hbar\mathcal{N}_{f_1}[\hat{f}(\zeta,\breve{p})], \tag{2.19}$$

$$(1-\breve{p})\mathcal{L}_{\theta_1}\left[\hat{\theta}(\zeta,\breve{p}) - \theta_{0_1}(\zeta)\right] = \breve{p}\hbar\mathcal{N}_{\theta_1}[\hat{f}(\zeta,\breve{p}),\ \hat{\theta}(\zeta,\breve{p}),\ \hat{\phi}(\zeta,\breve{p})], \tag{2.20}$$

$$(1-\breve{p})\mathcal{L}_{\phi_1}\left[\hat{\phi}(\zeta,\breve{p}) - \phi_{0_1}(\zeta)\right] = \breve{p}\hbar\mathcal{N}_{\phi_1}[\hat{f}(\zeta,\breve{p}),\ \hat{\theta}(\zeta,\breve{p}),\ \hat{\phi}(\zeta,\breve{p})], \tag{2.21}$$

$$\left.\begin{array}{c} \hat{f}(0,\breve{p}) = 0,\ \hat{\theta}(0,\breve{p}) = 1,\ \hat{f}'(0,\breve{p}) = 1,\ N_b\hat{\phi}'(0,\breve{p}) + N_t\hat{\theta}'(0,\breve{p}) = 0, \\ \hat{f}'(\infty,\breve{p}) = 0,\ \hat{\theta}(\infty,\breve{p}) = 0,\ \hat{\phi}(\infty,\breve{p}) = 0, \end{array}\right\} \tag{2.22}$$

$$\begin{aligned} \mathcal{N}_{f_1}\left[\hat{f}(\zeta,\breve{p})\right] &= (1+K)\frac{\partial^3\hat{f}}{\partial\zeta^3} + \breve{f}\frac{\partial^2\hat{f}}{\partial\zeta^2} - \left(\frac{n+1}{2}\right)K\Lambda\left(\frac{\partial^2\hat{f}}{\partial\zeta^2}\right)^2\frac{\partial^3\hat{f}}{\partial\zeta^3} \\ &\quad - \left(\frac{2n}{n+1}\right)\left(\frac{\partial\hat{f}}{\partial\zeta}\right)^2 - \left(\frac{2}{n+1}\right)M^2\frac{\partial\hat{f}}{\partial\zeta}, \end{aligned} \tag{2.23}$$

$$\mathcal{N}_{\theta_1}\left[\hat{f}(\zeta,\breve{p}),\hat{\theta}(\zeta,\breve{p}),\hat{\phi}(\zeta,\breve{p})\right]=\frac{\partial^2\hat{\theta}}{\partial\zeta^2}+\Pr\left(\hat{f}\frac{\partial\hat{\theta}}{\partial\zeta}+N_b\frac{\partial\hat{\theta}}{\partial\zeta}\frac{\partial\hat{\phi}}{\partial\zeta}+N_t\left(\frac{\partial\hat{\theta}}{\partial\zeta}\right)^2\right), \tag{2.24}$$

$$\mathcal{N}_{\phi_1}\left[\hat{f}(\zeta,\breve{p}),\hat{\theta}(\zeta,\breve{p}),\hat{\phi}(\zeta,\breve{p})\right]=\frac{\partial^2\hat{\phi}}{\partial\zeta^2}+Le\Pr\hat{f}\frac{\partial\hat{\phi}}{\partial\zeta}+\frac{N_t}{N_b}\frac{\partial^2\hat{\theta}}{\partial\zeta^2}. \tag{2.25}$$

Setting $\breve{p}=0$ and $\breve{p}=1$ one obtains

$$\hat{f}(\zeta,0)=f_{0_1}(\zeta),\ \hat{f}(\zeta,1)=f(\zeta), \tag{2.26}$$

$$\hat{\theta}(\zeta,0)=\theta_{0_1}(\zeta),\ \hat{\theta}(\zeta,1)=\theta(\zeta), \tag{2.27}$$

$$\hat{\phi}(\zeta,0)=\phi_{0_1}(\zeta),\ \hat{\phi}(\zeta,1)=\phi(\zeta). \tag{2.28}$$

When $\breve{p}$ changes from 0 to 1 then $\hat{f}(\zeta,\breve{p})$, $\hat{\theta}(\zeta,\breve{p})$ and $\hat{\phi}(\zeta,\breve{p})$ display alteration from primary approximations $f_{0_1}(\zeta)$, $\theta_{0_1}(\zeta)$ and $\phi_{0_1}(\zeta)$ to desired ultimate solutions $f(\zeta)$, $\theta(\zeta)$ and $\phi(\zeta)$.

2.2.2 Deformation problems at $\hat{m}$th-order

$$\mathcal{L}_{f_1}\left[f_{\hat{m}}(\zeta)-\chi_{\hat{m}}f_{\hat{m}-1}(\zeta)\right]=\hbar\tilde{\mathcal{R}}^{\hat{m}}_{f_1}(\zeta), \tag{2.29}$$

$$\mathcal{L}_{\theta_1}\left[\theta_{\hat{m}}(\zeta)-\chi_{\hat{m}}\theta_{\hat{m}-1}(\zeta)\right]=\hbar\tilde{\mathcal{R}}^{\hat{m}}_{\theta_1}(\zeta), \tag{2.30}$$

$$\mathcal{L}_{\phi_1}\left[\phi_{\hat{m}}(\zeta)-\chi_{\hat{m}}\phi_{\hat{m}-1}(\zeta)\right]=\hbar\tilde{\mathcal{R}}^{\hat{m}}_{\phi_1}(\zeta), \tag{2.31}$$

$$\left.\begin{array}{c} f_{\hat{m}}(0)=\theta_{\hat{m}}(0)=f'_{\hat{m}}(0)=0,\ N_b\phi'_{\hat{m}}(0)+N_t\theta'_{\hat{m}}(0)=0,\\ f'_{\hat{m}}(\infty)=\theta_{\hat{m}}(\infty)=\phi_{\hat{m}}(\infty)=0, \end{array}\right\} \tag{2.32}$$

$$\begin{aligned}\tilde{\mathcal{R}}^{\hat{m}}_{f_1}(\zeta) &= (1+K)\,f'''_{\hat{m}-1}+\sum_{\hat{k}=0}^{\hat{m}-1}\left(f_{\hat{m}-1-\hat{k}}f''_{\hat{k}}\right)-\left(\frac{n+1}{2}\right)K\Lambda\sum_{\hat{k}=0}^{\hat{m}-l}f'''_{\hat{m}-1-\hat{k}}\sum_{l=0}^{\hat{k}}f''_{\hat{k}-l}f''_{l}\\ &\quad-\left(\frac{2n}{n+1}\right)\sum_{\hat{k}=0}^{\hat{m}-1}\left(f'_{\hat{m}-1-\hat{k}}f'_{\hat{k}}\right)-\left(\frac{2}{n+1}\right)M^2f'_{\hat{m}-1},\end{aligned} \tag{2.33}$$

$$\tilde{\mathcal{R}}^{\hat{m}}_{\theta_1}(\zeta)=\theta''_{\hat{m}-1}+\Pr\left(\sum_{\hat{k}=0}^{\hat{m}-1}f_{\hat{m}-1-\hat{k}}\theta'_{\hat{k}}+N_b\sum_{\hat{k}=0}^{\hat{m}-1}\theta'_{\hat{m}-1-\hat{k}}\phi'_{\hat{k}}+N_t\sum_{\hat{k}=0}^{\hat{m}-1}\theta'_{\hat{m}-1-\hat{k}}\theta'_{\hat{k}}\right), \tag{2.34}$$

$$\tilde{\mathcal{R}}^{\hat{m}}_{\phi_1}(\zeta) = \phi''_{\hat{m}-1} + Le\,\mathrm{Pr}\sum_{\hat{k}=0}^{\hat{m}-1} f_{\hat{m}-1-\hat{k}}\phi'_{\hat{k}} + \frac{N_t}{N_b}\theta''_{\hat{m}-1}, \tag{2.35}$$

$$\boldsymbol{\chi}_{\hat{m}} = \begin{cases} 0, & \hat{m} \leq 1, \\ 1, & \hat{m} > 1, \end{cases} \tag{2.36}$$

The following expressions are derived via Taylor's series expansion:

$$\hat{f}(\zeta,\breve{p}) = f_{0_1}(\zeta) + \sum_{\hat{m}=1}^{\infty} f_{\hat{m}}(\zeta)\breve{p}^{\hat{m}},\ f_{\hat{m}}(\zeta) = \frac{1}{\hat{m}!}\frac{\partial^{\hat{m}}\hat{f}(\zeta,\breve{p})}{\partial\breve{p}^{\hat{m}}}\bigg|_{\breve{p}=0}, \tag{2.37}$$

$$\hat{\theta}(\zeta,\breve{p}) = \theta_{0_1}(\zeta) + \sum_{\hat{m}=1}^{\infty} \theta_{\hat{m}}(\zeta)\breve{p}^{\hat{m}},\ \theta_{\hat{m}}(\zeta) = \frac{1}{\hat{m}!}\frac{\partial^{\hat{m}}\hat{\theta}(\zeta,\breve{p})}{\partial\breve{p}^{\hat{m}}}\bigg|_{\breve{p}=0}, \tag{2.38}$$

$$\hat{\phi}(\zeta,\breve{p}) = \phi_{0_1}(\zeta) + \sum_{\hat{m}=1}^{\infty} \phi_{\hat{m}}(\zeta)\breve{p}^{\hat{m}},\ \phi_{\hat{m}}(\zeta) = \frac{1}{\hat{m}!}\frac{\partial^{\hat{m}}\hat{\phi}(\zeta,\breve{p})}{\partial\breve{p}^{\hat{m}}}\bigg|_{\breve{p}=0}. \tag{2.39}$$

The convergence regarding Eqs. $(2.37)-(2.39)$ is solidly based upon the suitable selections of $\hbar_f$, $\hbar_\theta$ and $\hbar_\phi$. Choosing suitable values of $\hbar_f$, $\hbar_\theta$ and $\hbar_\phi$ so that Eqs. $(2.37)-(2.39)$ converge at $\breve{p}=1$ then

$$f(\zeta) = f_{0_1}(\zeta) + \sum_{\hat{m}=1}^{\infty} f_{\hat{m}}(\zeta), \tag{2.40}$$

$$\theta(\zeta) = \theta_{0_1}(\zeta) + \sum_{\hat{m}=1}^{\infty} \theta_{\hat{m}}(\zeta), \tag{2.41}$$

$$\phi(\zeta) = \phi_{0_1}(\zeta) + \sum_{\hat{m}=1}^{\infty} \phi_{\hat{m}}(\zeta). \tag{2.42}$$

In terms of special solutions $(f^*_{\hat{m}}, \theta^*_{\hat{m}}, \phi^*_{\hat{m}})$, the general solutions $(f_{\hat{m}}, \theta_{\hat{m}}, \phi_{\hat{m}})$ of the Eqs. $(2.29)-(2.31)$ are defined by the following expressions:

$$f_{\hat{m}}(\zeta) = f^*_{\hat{m}}(\zeta) + C^*_1 + C^*_2\exp(\zeta) + C^*_3\exp(-\zeta), \tag{2.43}$$

$$\theta_{\hat{m}}(\zeta) = \theta^*_{\hat{m}}(\zeta) + C^*_4\exp(\zeta) + C^*_5\exp(-\zeta), \tag{2.44}$$

$$\phi_{\hat{m}}(\zeta) = \phi^*_{\hat{m}}(\zeta) + C^*_6\exp(\zeta) + C^*_7\exp(-\zeta), \tag{2.45}$$

in which C_i^* $(i = 1 - 7)$ through the boundary conditions (2.32) are given by

$$C_2^* = C_4^* = C_6^* = 0,\ C_3^* = \left.\frac{\partial f_{\hat{m}}^*(\zeta)}{\partial \zeta}\right|_{\zeta=0},\ C_1^* = -C_3^* - f_{\hat{m}}^*(0), \tag{2.46}$$

$$C_5^* = -\theta_{\hat{m}}^*(0),\ C_7^* = \left.\frac{\partial \phi_{\hat{m}}^*(\zeta)}{\partial \zeta}\right|_{\zeta=0} + \frac{N_t}{N_b}\left(-C_5^* + \left.\frac{\partial \theta_{\hat{m}}^*(\zeta)}{\partial \zeta}\right|_{\zeta=0}\right). \tag{2.47}$$

2.2.3 Convergence analysis

Here the homotopic solutions $(2.40) - (2.42)$ contain the nonzero auxiliary variables $\hbar_f$, $\hbar_\theta$ and $\hbar_\phi$. Such auxiliary variables play a significant role to tune and govern the region of convergence. For appropriate auxiliary variables, the $\hbar-$curves are sketched at 25th order of deformations. Fig. 2.2 displays that the convergence zone lies within the ranges $-1.8 \leq \hbar_f \leq -0.1$, $-1.75 \leq \hbar_\theta \leq -0.15$ and $-1.7 \leq \hbar_\phi \leq -0.2$. The residual errors of velocity, temperature and concentration distributions are given by

$$\Delta_{\hat{m}}^f = \int_0^1 \left[\tilde{\mathcal{R}}_{f_1}^{\hat{m}}(\zeta, \hbar_f)\right]^2 d\zeta, \tag{2.48}$$

$$\Delta_{\hat{m}}^\theta = \int_0^1 \left[\tilde{\mathcal{R}}_{\theta_1}^{\hat{m}}(\zeta, \hbar_\theta)\right]^2 d\zeta, \tag{2.49}$$

$$\Delta_{\hat{m}}^\phi = \int_0^1 \left[\tilde{\mathcal{R}}_{\phi_1}^{\hat{m}}(\zeta, \hbar_\phi)\right]^2 d\zeta. \tag{2.50}$$

For suitable ranges of $\hbar$, the $\hbar-$curves for the residual errors of velocity, temperature and concentration distributions have been sketched in Figs. $2.3 - 2.5$. It is observed that the correct results up to fifth decimal place are deduced through selection of $\hbar$ in this range. HAM solutions

convergence via Table 2.1 is satisfactorily achieved by considering 20th orders of approximation.

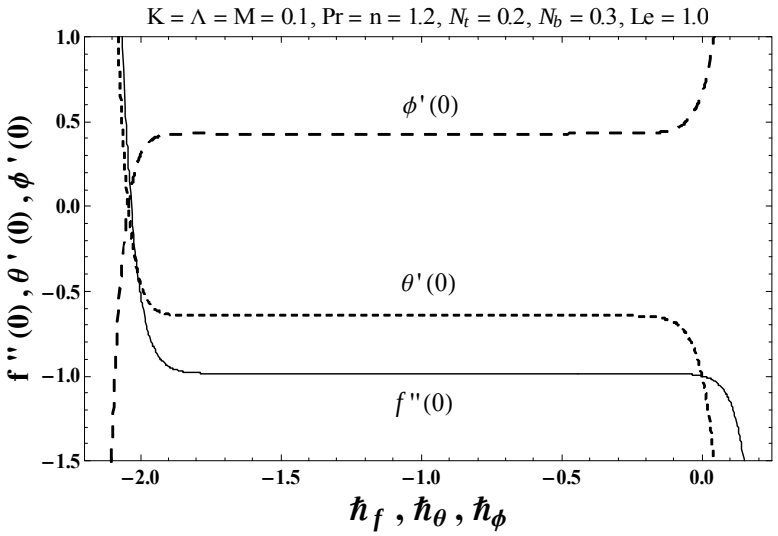

Fig. 2.2. The $\hbar-$ curves for $f(\zeta)$, $\theta(\zeta)$ and $\phi(\zeta)$.

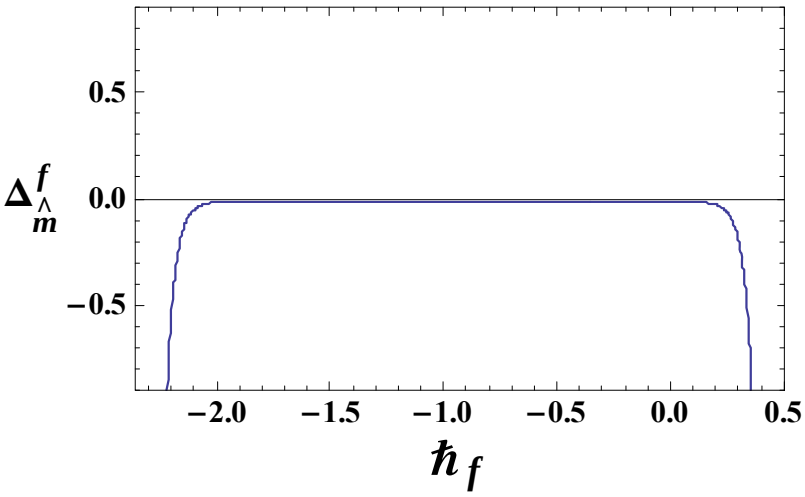

Fig. 2.3. $\hbar_f-$curve for the residual error $\Delta^f_{\hat{m}}$.

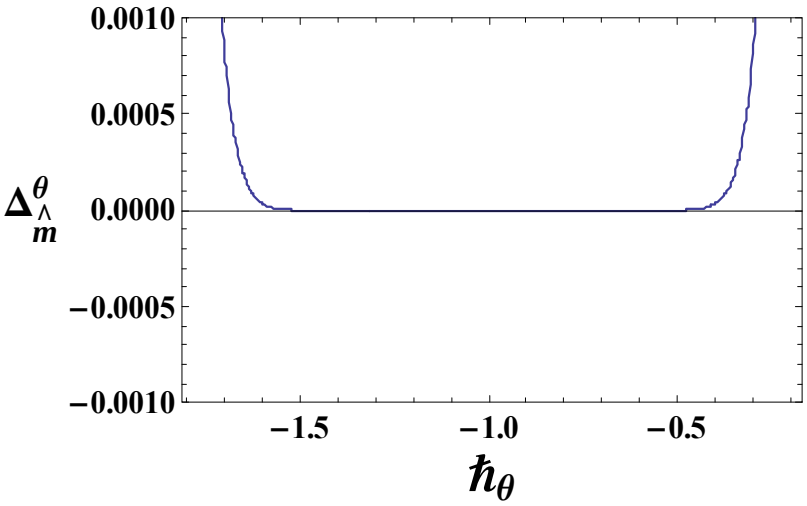

Fig. 2.4. $\hbar_\theta-$curve for the residual error $\Delta^{\theta}_{\hat{m}}$.

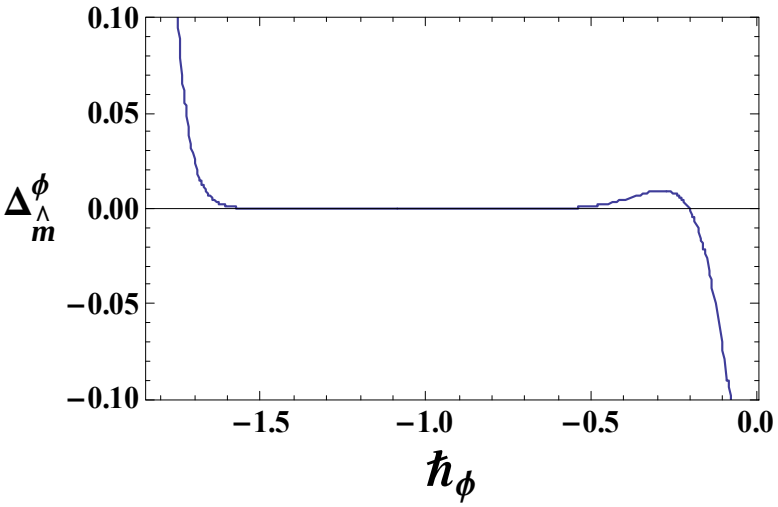

Fig. 2.5. $\hbar_\phi-$curve for the residual error $\Delta^{\phi}_{\hat{m}}$.

Table 2.1. Homotopic solutions convergence when $K = \Lambda = M = 0.1$, $n = \Pr = 1.2$, $N_t = 0.2$, $Le = 1.0$ and $N_b = 0.3$.

Order of approximations	$-f''(0)$	$-\theta'(0)$	$\phi'(0)$
1	0.98485	0.70000	0.46667
5	0.98476	0.64522	0.43015
10	0.98475	0.64301	0.42867
15	0.98475	0.64292	0.42862
20	0.98475	0.64294	0.42863
25	0.98475	0.64294	0.42863
30	0.98475	0.64294	0.42863
35	0.98475	0.64294	0.42863

2.3 Discussion

Current portion has been organized to explore the impacts of several effective parameters including magnetic parameter M, fluid parameter K, thermophoresis parameter N_t, Prandtl number Pr, Brownian motion parameter N_b, Lewis number Le and power-law index n on velocity $f'(\zeta)$, temperature $\theta(\zeta)$ and concentration $\phi(\zeta)$ distributions. Fig. 2.6 depicts the impact of fluid parameter K on velocity distribution $f'(\zeta)$. Both velocity field and momentum layer thickness have been increased for K. Behavior of M on velocity distribution $f'(\zeta)$ is presented in Fig. 2.7. Here both velocity and momentum boundary layer thickness decay for M. Fig. 2.8 shows influence of power-law index n for velocity $f'(\zeta)$. By increasing n, both the velocity and momentum boundary layer thickness have been reduced. Here $n = 1$ corresponds to linear stretching surface case and $n \neq 1$ for nonlinear stretching surface. The impacts of fluid parameter K, magnetic parameter M, thermophoresis parameter N_t, Prandtl number Pr and power-law index n for temperature $\theta(\zeta)$ have been displayed in the Figs. $2.9 - 2.13$ respectively. It is observed that by increasing magnetic parameter M, thermophoresis parameter N_t and power-law index n, both the temperature and related layer thickness are higher whereas reverse trend is noticed for fluid parameter K and Prandtl number Pr. It is a valuable fact to mention here that the properties of liquid metals are characterized by small values of Prandtl number ($\Pr < 1$), which

have larger thermal conductivity but smaller viscosity, whereas higher values of Prandtl number ($\mathrm{Pr} > 1$) associate with high-viscosity oils. Particularly Prandtl number $\mathrm{Pr} = 0.72$, 1.0 and 6.2 are associated to air, electrolyte solution such as salt water and water respectively. Moreover it is also observed that N_t portrays the strength of thermophoresis effects. Higher N_t leads to more strength to thermophoresis. Impacts of concentration field $\phi(\zeta)$ via material variable K, magnetic M, thermophoresis N_t, Brownian motion N_b, Lewis number Le, Prandtl number Pr and power-law index n are displayed in the Figs. $2.14 - 2.20$. Concentration field through these sketches enhances for larger magnetic parameter M, thermophoresis parameter N_t and power-law index n whereas reverse trend is observed for fluid parameter K, Brownian motion parameter N_b, Lewis number Le and Prandtl number Pr . Table 2.2 depicts the numerical data of skin friction coefficient for several effective parameters K, Λ, M and n. Skin friction coefficient is higher for larger K, M and n while the reverse behavior is noticed through n. Table 2.3 is presented to analyze the numerical data of local Nusselt numbers via different parameters. Here local Nusselt number increases for larger fluid parameter K, Prandtl number Pr and power-law index n whereas opposite result holds for magnetic parameter M, thermophoresis parameter N_t and Lewis number Le. There is no significant change of N_b on local Nusselt number.

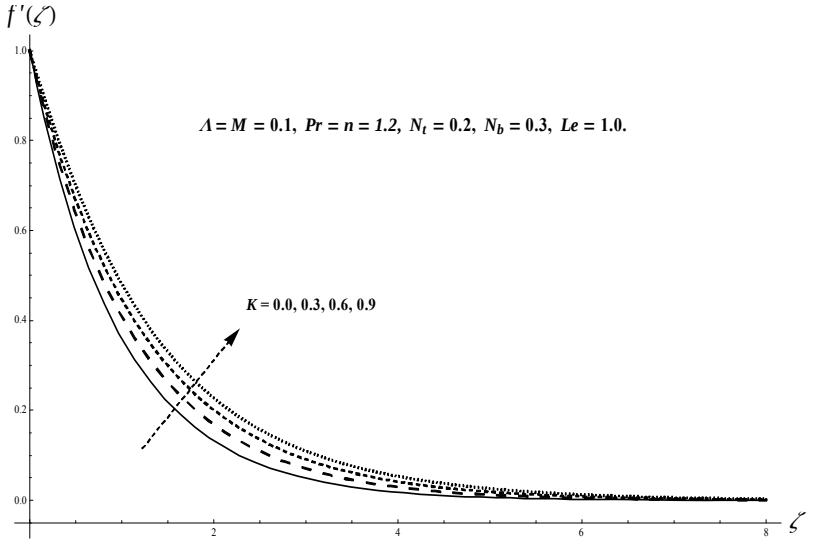

Fig. 2.6. Plots of $f'(\zeta)$ for K.

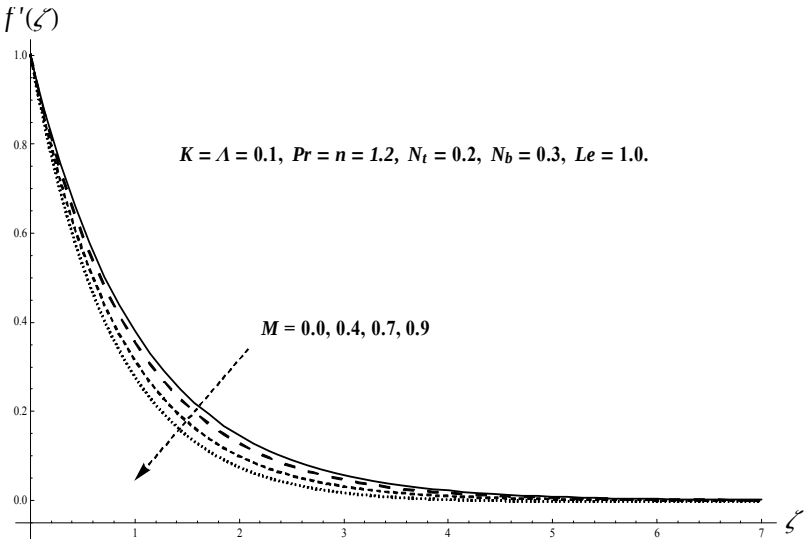

Fig. 2.7. Plots of $f'(\zeta)$ for M.

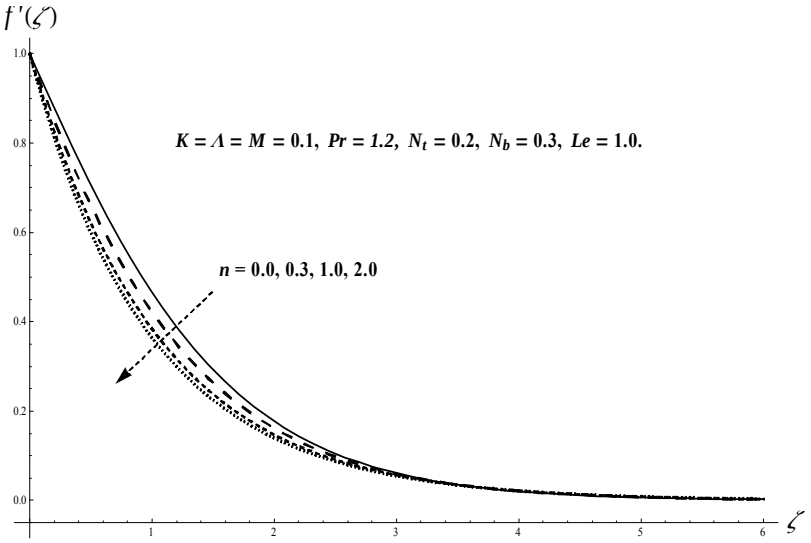

Fig. 2.8. Plots of $f'(\zeta)$ for n.

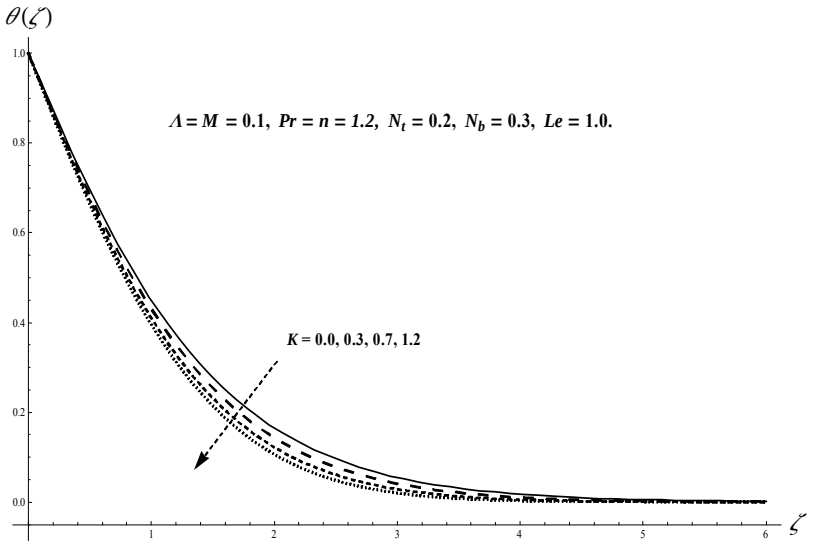

Fig. 2.9. Plots of $\theta(\zeta)$ for K.

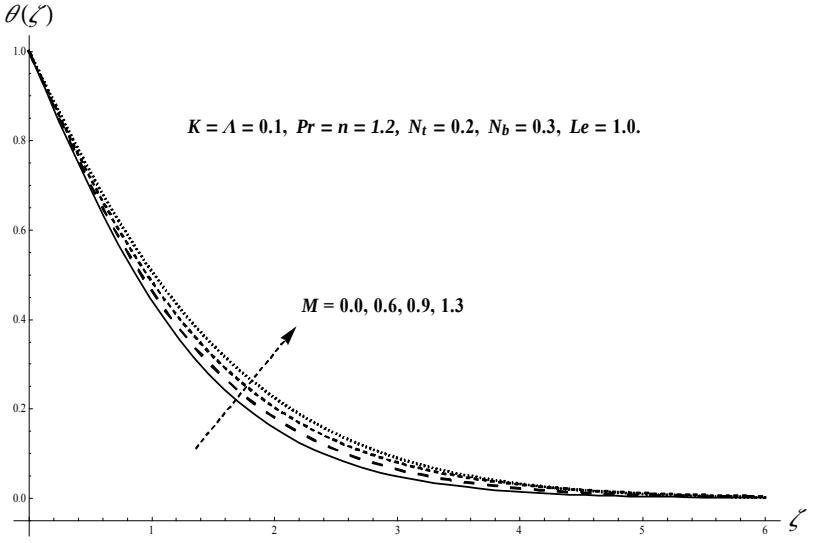

Fig. 2.10. Plots of $\theta(\zeta)$ for M.

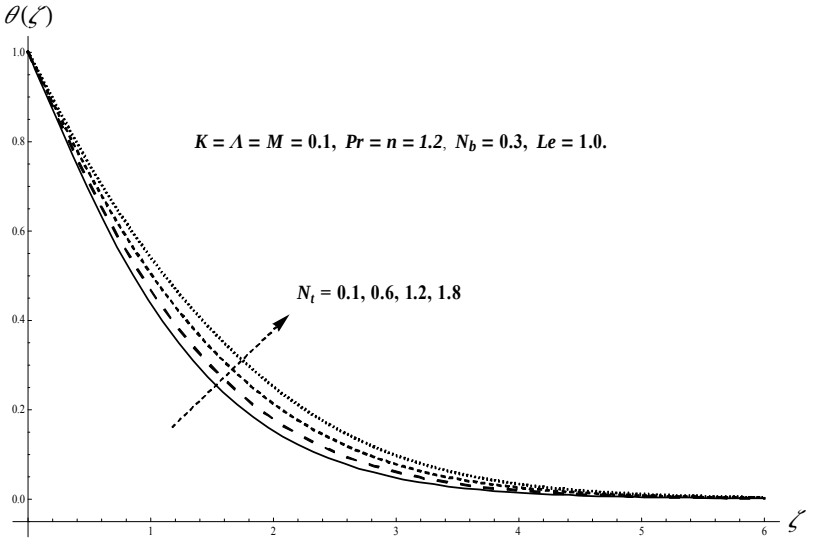

Fig. 2.11. Plots of $\theta(\zeta)$ for N_t.

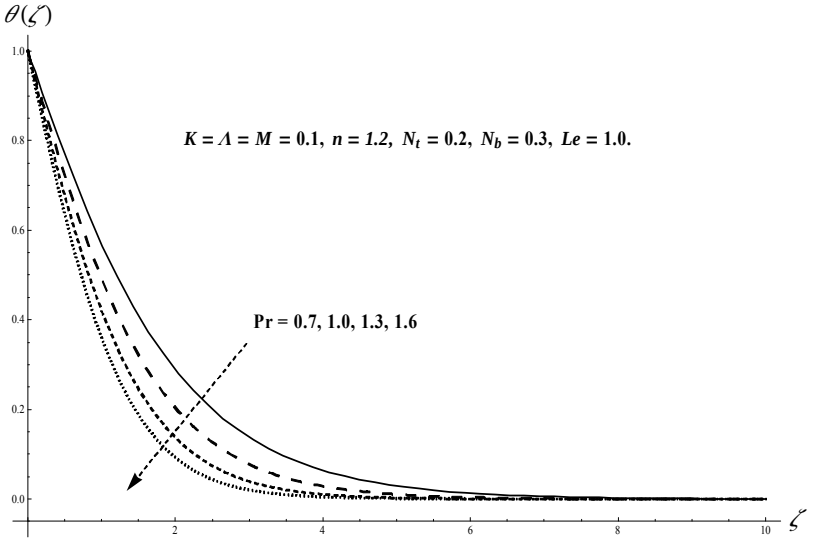

Fig. 2.12. Plots of $\theta(\zeta)$ for Pr.

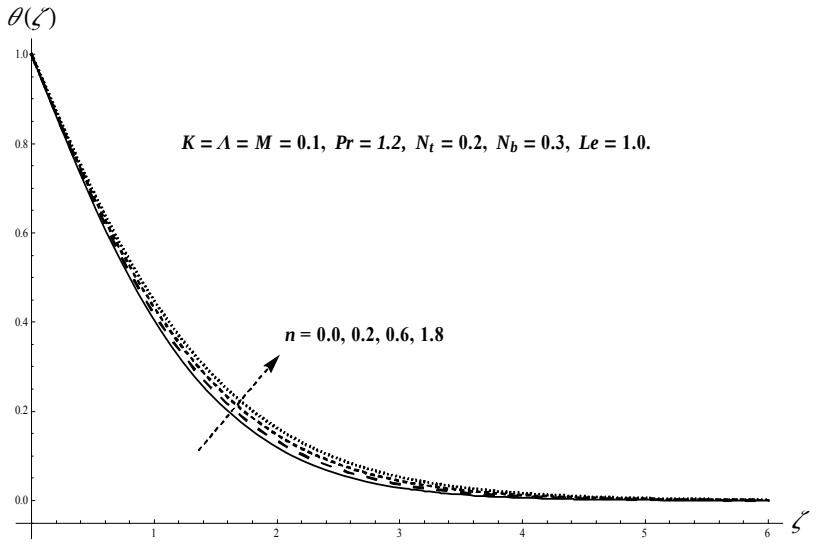

Fig. 2.13. Plots of $\theta(\zeta)$ for n.

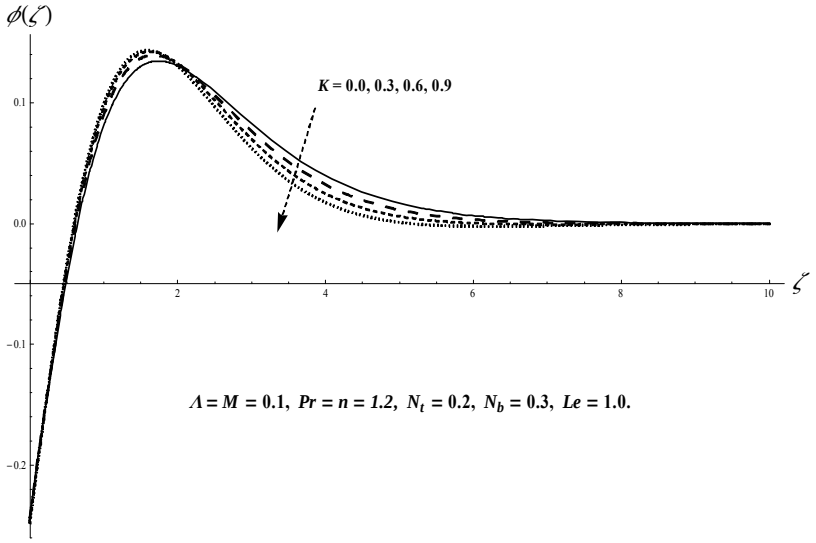

Fig. 2.14. Plots of $\phi(\zeta)$ for K.

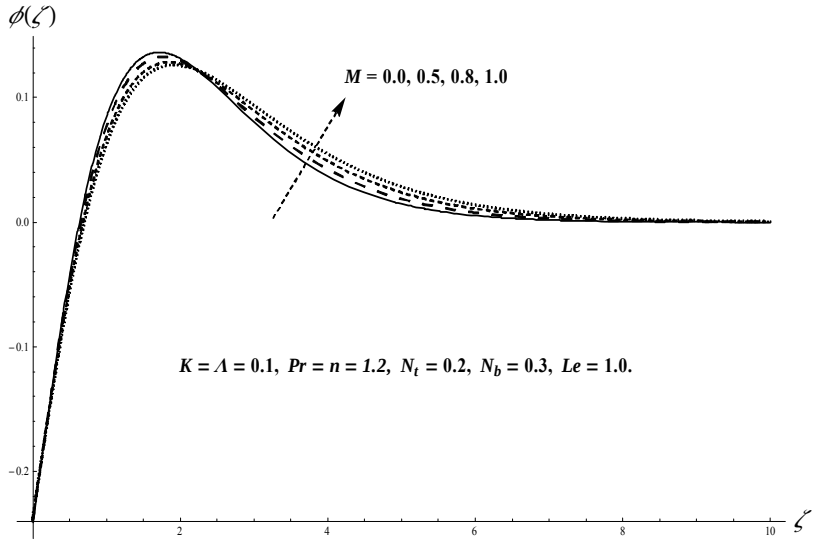

Fig. 2.15. Plots of $\phi(\zeta)$ for M.

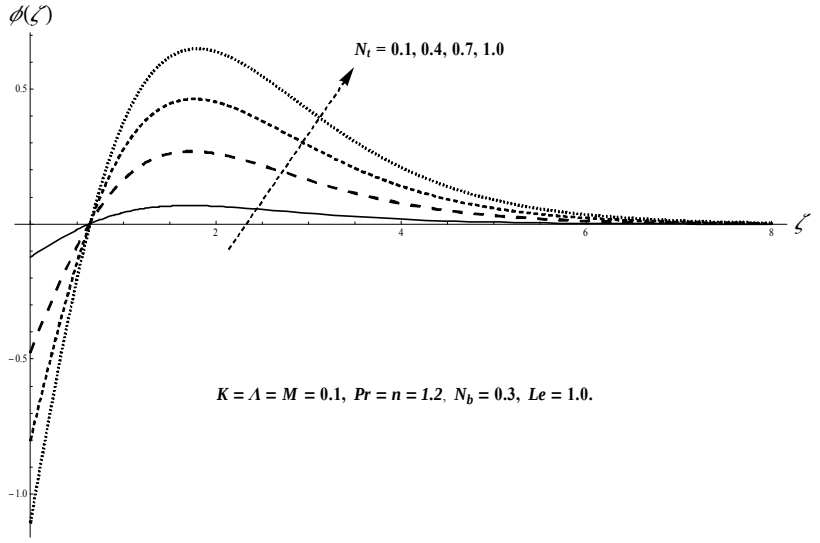

Fig. 2.16. Plots of $\phi(\zeta)$ for N_t.

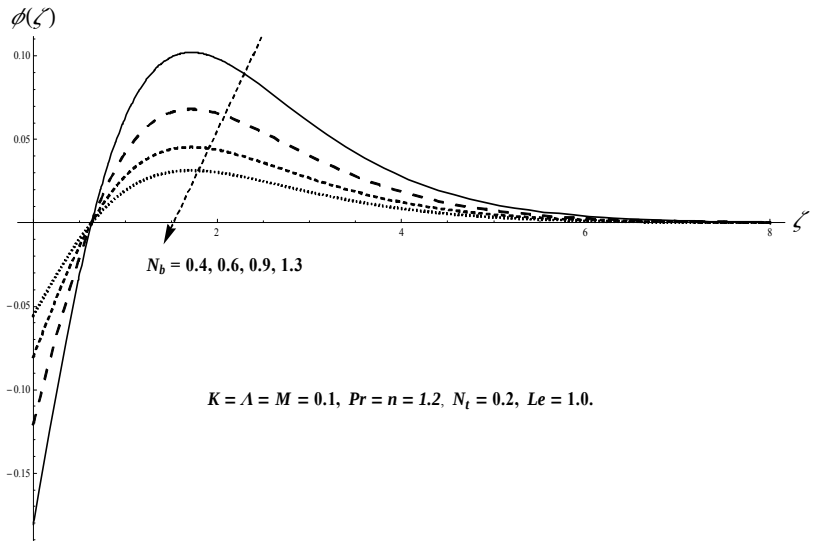

Fig. 2.17. Plots of $\phi(\zeta)$ for N_b.

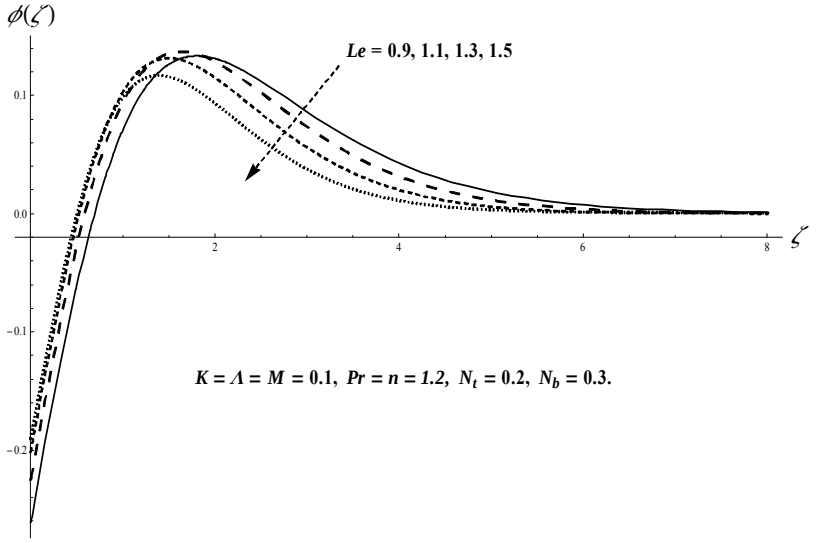

Fig. 2.18. Plots of $\phi(\zeta)$ for Le.

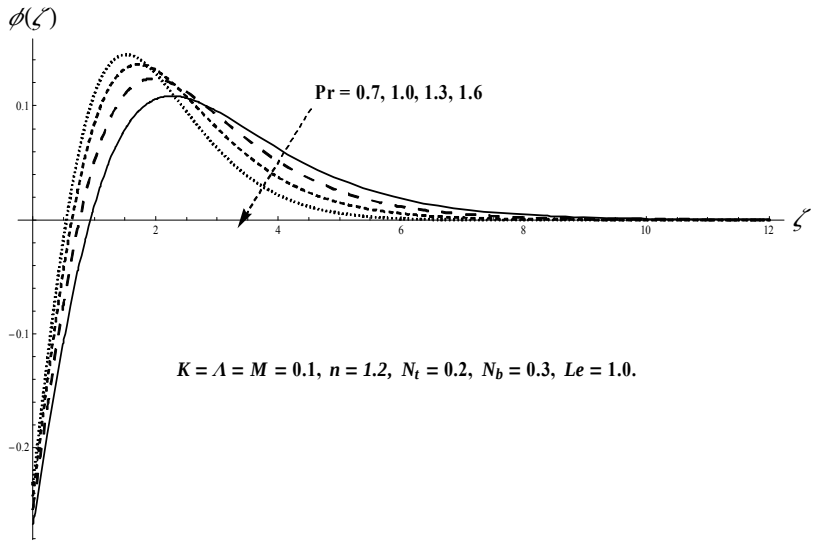

Fig. 2.19. Plots of $\phi(\zeta)$ for Pr .

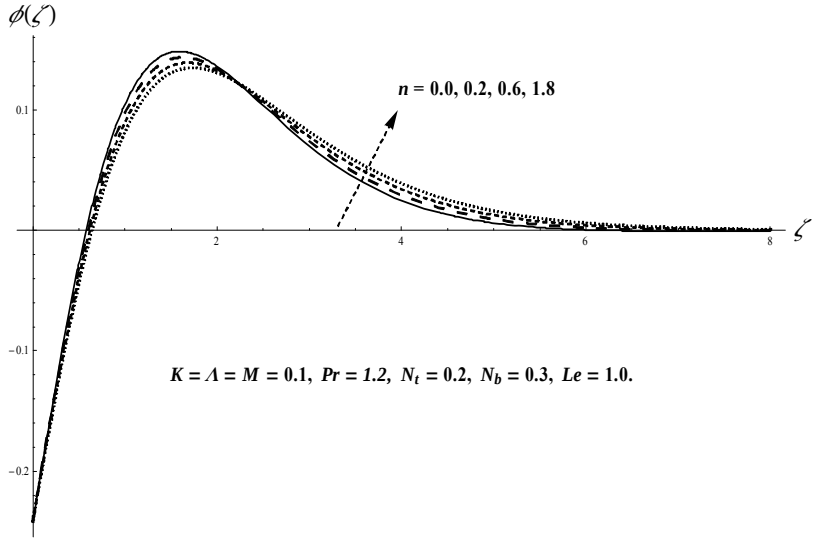

Fig. 2.20. Plots of $\phi(\zeta)$ for n.

Table 2.2. Skin friction for K, Λ, M and n.

K	Λ	M	n	$-\mathrm{Re}_x^{1/2} C_{fx}$
0.0	0.1	0.1	1.2	1.0832
0.1				1.1324
0.2				1.1802
0.1	0.0	0.1	1.2	1.1361
	0.2			1.1288
	0.4			1.1214
0.1	0.1	0.0	1.2	1.1276
		0.1		1.1324
		0.2		1.1468
0.1	0.1	0.1	0.8	0.9629
			1.0	1.0511
			1.2	1.1324

Table 2.3. Numerical data of local Nusselt number for K, M, N_t, N_b, Le, Pr and n when $\Lambda = 0.1$.

K	M	N_t	N_b	Le	Pr	n	$-\mathrm{Re}_x^{-1/2} Nu_x$
0.0	0.1	0.2	0.3	1.0	1.2	1.2	0.6638
0.1							0.6742
0.2							0.6836
0.1	0.0	0.2	0.3	1.0	1.2	1.2	0.6753
	0.1						0.6743
	0.2						0.6715
0.1	0.1	0.1	0.3	1.0	1.2	1.2	0.6848
		0.2					0.6743
		0.3					0.6639
0.1	0.1	0.2	0.1	1.0	1.2	1.2	0.6743
			0.2				0.6743
			0.3				0.6743
0.1	0.1	0.2	0.3	0.0	1.2	1.2	0.6951
				0.5			0.6824
				1.0			0.6743
0.1	0.1	0.2	0.3	1.0	0.8	1.2	0.5177
					1.0		0.6001
					1.2		0.6743
0.1	0.1	0.2	0.3	1.0	1.2	0.8	0.6172
						1.0	0.6463
						1.2	0.6743

2.4 Conclusions

Flow of Powell-Eyring nanomaterial due to nonlinear stretching velocity and magnetic field is discussed. Main observations of presented analysis are:

- Through larger K, increasing behavior of velocity field and decaying behavior of temperature and concentration are noted.
- Impact of magnetic parameter M on temperature and concentration fields is reverse to that of velocity field.
- Temperature and concentration fields through Prandtl number Pr are qualitatively similar.
- Larger Lewis number Le show decay in concentration field and corresponding layer thickness.
- Behaviors of N_b and N_t on concentration field are different.
- Skin friction coefficient is higher through larger K, M and n while the reverse trend is noticed through Λ.
- At the surface the rate of heat transfer is lower for higher M and N_t.

Chapter 3

Outcome of melting heat and internal heat generation in stagnation point Jeffrey fluid flow

Current chapter investigates the magnetohydrodynamic (MHD) stagnation point flow of Jeffrey material. Flow is caused due to a nonlinear stretchable surface of variable surface thickness. Heat transfer characteristics are examined through the melting process, viscous dissipation and internal heat generation. A nonuniform applied magnetic field is considered. Boundary-layer and low magnetic Reynolds number approximations are employed in the problem formulation. Both the momentum and energy equations are converted into the non-linear ordinary differential system using appropriate transformations. Convergent solutions for resulting problems are computed. Velocity and temperature profiles have been studied in detail. Further the heat transfer rate is also computed and analyzed.

3.1 Formulation

Here stagnation point Jeffrey fluid flow is considered which is generated by a non-linear stretching sheet. The $x-$ and $y-$axes are along and perpendicular to the stretchable sheet. A variable magnetic field of strength B_0 is injected in the $y-$ direction (see Fig. 3.1). We assume that the surface has variable thickness. The surface is at $y = \varepsilon (x + a^*)^{\frac{1-n}{2}}$, where ε is taken as an

extremely small constant so that the surface is almost very thin, a^* is a constant and shape parameter is represented by n which has a great significance in the present problem. It is obvious that our problem is valid only for $n \neq 1$. For $n = 1$, the surface is not of variable thickness. Moreover, melting heat transfer effects are also taken into consideration. The temperature of melting sheet is considered to be T_m while free stream temperature is T_∞ $(> T_m)$. Here T_0 denotes the constant temperature of the solid medium far from the interface such that $T_0 < T_m$.

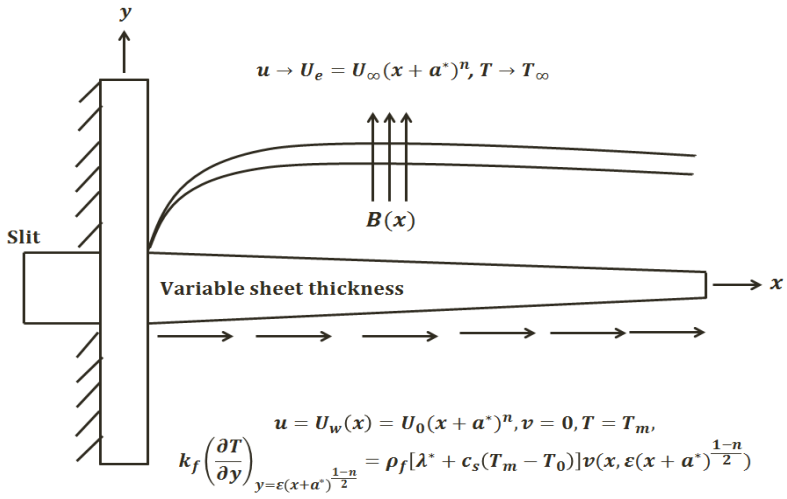

Fig. 3.1 : Geometry of the problem.

The flow equations for Jeffrey fluid satisfy

$$\frac{\partial u}{\partial x} + \frac{\partial v}{\partial y} = 0, \tag{3.1}$$

$$\begin{aligned} u\frac{\partial u}{\partial x} + v\frac{\partial u}{\partial y} &= U_e\frac{dU_e}{dx} + \frac{\nu}{1+\lambda_1}\left(\frac{\partial^2 u}{\partial y^2} + \lambda_2\left(\begin{array}{c}\frac{\partial u}{\partial y}\frac{\partial^2 u}{\partial x \partial y} + u\frac{\partial^3 u}{\partial x \partial y^2} \\ -\frac{\partial u}{\partial x}\frac{\partial^2 u}{\partial y^2} + v\frac{\partial^3 u}{\partial y^3}\end{array}\right)\right) \\ &\quad -\frac{\sigma\left(B_2^*(x)\right)^2}{\rho_f}\left(u - U_e\right), \end{aligned} \tag{3.2}$$

$$u\frac{\partial T}{\partial x}+v\frac{\partial T}{\partial y} = \alpha_1^*\frac{\partial^2 T}{\partial y^2}+\frac{\mu}{\rho_f c_p\left(1+\lambda_1\right)}\left(\left(\frac{\partial u}{\partial y}\right)^2+\lambda_2\left(\begin{array}{c} u\frac{\partial u}{\partial y}\frac{\partial^2 u}{\partial x\partial y} \\ +v\frac{\partial u}{\partial y}\frac{\partial^2 u}{\partial y^2}\end{array}\right)\right) + \frac{Q_0}{\rho_f c_p}\left(T-T_m\right). \tag{3.3}$$

The boundary conditions are

$$\left.\begin{array}{c} u\left(x,y\right)=U_w\left(x,y\right)=U_0\left(x+a^*\right)^n,\quad v\left(x,y\right)=0, \\ T\left(x,y\right)=T_m \ \text{ at } \ y=\varepsilon\left(x+a^*\right)^{\frac{1-n}{2}}, \\ k_f\left(\frac{\partial T}{\partial y}\right)_{y=\varepsilon(x+a^*)^{\frac{1-n}{2}}}=\rho\left[\lambda^*+c_s\left(T_m-T_0\right)\right]v\left(x,\varepsilon\left(x+a^*\right)^{\frac{1-n}{2}}\right), \\ u\left(x,y\right)=U_e\left(x,y\right)\rightarrow U_\infty\left(x+a^*\right)^n,\ T\left(x,y\right)\rightarrow T_\infty \ \text{ as } \ y\rightarrow\infty. \end{array}\right\} \tag{3.4}$$

In above expressions $B_2^*(x)=B_0\left(x+a^*\right)^{\frac{n-1}{2}}$ the nonuniform magnetic field and $Q_0\left(x\right)=Q_1\left(x+a^*\right)^{n-1}$ the heat generation coefficient. Moreover the boundary conditions for heat transport phenomena depicts that the sensible heat required to increase the temperature of the solid T_0 to its melting temperature T_m plus the heat due to melting is equal to the heat conduction of the melting surface. The velocity components and transformations are considered in the forms:

$$\left.\begin{array}{c} u=\frac{\partial\psi}{\partial y},\ v=-\frac{\partial\psi}{\partial x},\ \eta=\sqrt{\left(\frac{n+1}{2\nu}\right)U_0\left(x+a^*\right)^{n-1}}y, \\ \psi=\sqrt{\left(\frac{2\nu}{n+1}\right)U_0\left(x+a^*\right)^{n+1}}F_1\left(\zeta\right),\ \theta_1\left(\zeta\right)=\frac{T-T_m}{T_\infty-T_m}, \end{array}\right\} \tag{3.5}$$

in which ψ denotes the stream function. Now Eq. (3.1) is automatically satisfied and Eqs. $(3.2)-(3.4)$ become

$$F_1'''+\left(1+\lambda_1\right)\left(\begin{array}{c} F_1F_1''+\frac{2n}{n+1}\left(A^2+MA-F_1'^2\right) \\ -\left(\frac{2}{n+1}\right)MF_1'\end{array}\right)+\beta\left(\begin{array}{c}\left(\frac{3n-1}{2}\right)F_1''^2+\left(n-1\right)F_1'F_1''' \\ -\left(\frac{n+1}{2}\right)F_1F_1^{iv}\end{array}\right)=0, \tag{3.6}$$

$$\theta_1''+\Pr F_1\theta_1'+\frac{\Pr Ec}{1+\lambda_1}\left(F_1''^2+\beta\left(\begin{array}{c}\left(\frac{3n-1}{2}\right)F_1'F_1''^2 \\ -\left(\frac{n+1}{2}\right)F_1F_1''F_1'''\end{array}\right)\right)+\Pr\delta\left(\frac{2}{n+1}\right)\theta_1=0, \tag{3.7}$$

$$\left.\begin{array}{c} F_1'\left(\alpha\right)=1,\ Me\theta_1'\left(\alpha\right)+\Pr\left[F_1\left(\alpha\right)+\alpha\left(\frac{n-1}{n+1}\right)\right]=0,\ \theta_1(\alpha)=0, \\ F_1'\left(\infty\right)\rightarrow A,\ \theta_1\left(\infty\right)\rightarrow 1, \end{array}\right\} \tag{3.8}$$

where $A = \frac{U_\infty}{U_0}$ represents the ratio parameter of free stream velocity and stretching velocity, $M = \frac{\sigma B_0^2}{\rho_f U_0}$ the magnetic parameter, $\beta = \lambda_2 U_0 (x + a^*)^{n-1}$ the local Deborah number, $\Pr = \frac{\nu}{\alpha_1^*}$ the Prandtl number, $Ec = \frac{U_w^2}{c_p(T_\infty - T_m)}$ the Eckert number, $\delta = \frac{Q_1}{U_0 \rho_f c_p}$ the heat generation parameter, $Me = \frac{c_p(T_\infty - T_m)}{\lambda^* + c_s(T_m - T_0)}$ the melting parameter which is a combination of Stefan numbers $\frac{c_s(T_m - T_0)}{\lambda^*}$ and $\frac{c_f(T_\infty - T_m)}{\lambda^*}$ for the solid and liquid phases respectively, $\alpha = \varepsilon \sqrt{\left(\frac{n+1}{2}\right) \frac{U_0}{\nu}}$ the surface thickness parameter and $\eta = \alpha = \varepsilon \sqrt{\left(\frac{n+1}{2}\right) \frac{U_0}{\nu}}$ indicates the plate surface. Moreover the domain of Eqs. $(3.6) - (3.8)$ is $[\alpha, \infty[$ and to facilitate the computation we transform the domain to $[0, \infty[$ by defining $F_1(\eta) = F_1(\zeta - \alpha) = f(\zeta)$ and $\theta_1(\eta) = \theta_1(\zeta - \alpha) = \theta(\zeta)$. Hence Eqs. $(3.6) - (3.8)$ yield

$$f''' + (1 + \lambda_1) \left(\begin{array}{c} f f'' + \frac{2n}{n+1} \left(A^2 + MA - f'^2 \right) \\ - \left(\frac{2}{n+1} \right) M f' \end{array} \right) + \beta \left(\begin{array}{c} \left(\frac{3n-1}{2} \right) f''^2 + (n-1) f' f''' \\ - \left(\frac{n+1}{2} \right) f f^{iv} \end{array} \right) = 0, \tag{3.9}$$

$$\theta'' + \Pr f \theta' + \frac{\Pr Ec}{1 + \lambda_1} \left(f''^2 + \beta \left(\begin{array}{c} \left(\frac{3n-1}{2} \right) f' f''^2 \\ - \left(\frac{n+1}{2} \right) f f'' f''' \end{array} \right) \right) + \Pr \delta \left(\frac{2}{n+1} \right) \theta = 0, \tag{3.10}$$

$$\left. \begin{array}{c} f'(0) = 1, \ Me\theta'(0) + \Pr \left[f(0) + \alpha \left(\frac{n-1}{n+1} \right) \right] = 0, \ \theta(0) = 0, \\ f'(\infty) \to A, \ \theta(\infty) \to 1. \end{array} \right\} \tag{3.11}$$

Local Nusselt number is defined by

$$Nu_{x_2} = \frac{(x + a^*) q_{w_2}}{k_f (T_\infty - T_m)}, \tag{3.12}$$

where q_{w_2} denotes the surface heat flux given by

$$q_{w_2} = -k_f \left(\frac{\partial T}{\partial y} \right)_{y = \varepsilon (x + a^*)^{\frac{1-n}{2}}}. \tag{3.13}$$

Local Nusselt number in non-dimensional scale is given by

$$Nu_{x_2} / \sqrt{Re_{x_2}} = -\sqrt{\frac{n+1}{2}} \theta'(0), \tag{3.14}$$

where $Re_{x_2} = \frac{U_w (x + a^*)}{\nu} = \frac{U_0 (x + a^*)^{n+1}}{\nu}$ represents the local Reynolds number.

3.2 Homotopy solutions

Here

$$f_{0_2}(\zeta) = A\zeta + (1-A)\left(1-e^{-\zeta}\right) - \frac{Me}{\mathrm{Pr}} - \alpha\left(\frac{n-1}{n+1}\right), \quad \theta_{0_2}(\zeta) = 1-e^{-\zeta}, \tag{3.15}$$

$$\mathcal{L}_{f_1} = \frac{d^3 f}{d\zeta^3} - \frac{df}{d\zeta},\ \mathcal{L}_{\theta_1} = \frac{d^2\theta}{d\zeta^2} - \theta. \tag{3.16}$$

These above linear operators $(\mathcal{L}_{f_1}, \mathcal{L}_{\theta_1})$ satisfy

$$\mathcal{L}_{f_1}\left[C_8^* + C_9^* e^{\zeta} + C_{10}^* e^{-\zeta}\right] = 0, \quad \mathcal{L}_{\theta_1}\left[C_{11}^* e^{\zeta} + C_{12}^* e^{-\zeta}\right] = 0, \tag{3.17}$$

in which C_i^* $(i = 8-12)$ are the random constants.

3.2.1 Deformation problems at zeroth-order

$$(1-\breve{p})\mathcal{L}_{f_1}\left[\hat{f}(\zeta,\breve{p}) - f_{0_2}(\zeta)\right] = \breve{p}\hbar\mathcal{N}_{f_2}[\hat{f}(\zeta,\breve{p})], \tag{3.18}$$

$$(1-\breve{p})\mathcal{L}_{\theta_1}\left[\hat{\theta}(\zeta,\breve{p}) - \theta_{0_2}(\zeta)\right] = \breve{p}\hbar\mathcal{N}_{\theta_2}[\hat{f}(\zeta,\breve{p}),\ \hat{\theta}(\zeta,\breve{p})], \tag{3.19}$$

$$\left.\begin{array}{c} \hat{f}(0,\breve{p}) = 1,\ \hat{\theta}(0,\breve{p}) = 0, \\ Pr\left(\hat{f}\,(0,p) + \alpha\left(\frac{n-1}{n+1}\right)\right) + Me\hat{\theta}'\,(0,p) = 0, \\ \hat{f}'(\infty,\breve{p}) = A,\ \hat{\theta}(\infty,\breve{p}) = 1, \end{array}\right\} \tag{3.20}$$

$$\begin{aligned} \mathcal{N}_{f_2}\left[\hat{f}(\zeta,\breve{p})\right] &= \frac{\partial^3\hat{f}}{\partial\zeta^3} + (1+\lambda_1)\left(\begin{array}{c} \hat{f}\frac{\partial^2\hat{f}}{\partial\zeta^2} - \left(\frac{2}{n+1}\right)M\frac{\partial\hat{f}}{\partial\zeta} \\ +\frac{2n}{n+1}\left(A^2 + MA - \left(\frac{\partial\hat{f}}{\partial\zeta}\right)^2\right) \end{array}\right) \\ &\quad +\beta\left(\begin{array}{c} \left(\frac{3n-1}{2}\right)\left(\frac{\partial^2\hat{f}}{\partial\zeta^2}\right)^2 + (n-1)\frac{\partial\hat{f}}{\partial\zeta}\frac{\partial^3\hat{f}}{\partial\zeta^3} \\ -\left(\frac{n+1}{2}\right)\hat{f}\frac{\partial^4\hat{f}}{\partial\zeta^4} \end{array}\right), \end{aligned} \tag{3.21}$$

$$\mathcal{N}_{\theta_2}\left[\hat{f}(\zeta,\breve{p}),\hat{\theta}(\zeta,\breve{p})\right] = \frac{\partial^2\hat{\theta}}{\partial\zeta^2}+\Pr\hat{f}\frac{\partial\hat{\theta}}{\partial\zeta} + \frac{\Pr Ec}{1+\lambda_1}\left(\left(\frac{\partial^2\hat{f}}{\partial\zeta^2}\right)^2-\beta\left(\begin{array}{c}\left(\frac{n+1}{2}\right)\hat{f}\frac{\partial^2\hat{f}}{\partial\zeta^2}\frac{\partial^3\hat{f}}{\partial\zeta^3}\\ -\left(\frac{3n-1}{2}\right)\frac{\partial\hat{f}}{\partial\zeta}\left(\frac{\partial^2\hat{f}}{\partial\zeta^2}\right)^2\end{array}\right)\right) + \Pr\delta\left(\frac{2}{n+1}\right)\hat{\theta}. \tag{3.22}$$

For $\breve{p}=0$ and $\breve{p}=1$ one obtains

$$\hat{f}(\zeta,0)=f_{0_2}(\zeta),\ \hat{f}(\zeta,1)=f(\zeta), \tag{3.23}$$

$$\hat{\theta}(\zeta,0)=\theta_{0_2}(\zeta),\ \hat{\theta}(\zeta,1)=\theta(\zeta), \tag{3.24}$$

when $\breve{p}$ changes from 0 to 1 then $\hat{f}(\zeta,\breve{p})$ and $\hat{\theta}(\zeta,\breve{p})$ display alteration from primary approximations $f_{0_2}(\zeta)$ and $\theta_{0_2}(\zeta)$ to desired ultimate solutions $f(\zeta)$ and $\theta(\zeta)$.

3.2.2 Deformation problems at $\hat{m}$th-order

$$\mathcal{L}_{f_1}\left[f_{\hat{m}}(\zeta)-\chi_{\hat{m}}f_{\hat{m}-1}(\zeta)\right]=\hbar\tilde{\mathcal{R}}^{\hat{m}}_{f_2}(\zeta), \tag{3.25}$$

$$\mathcal{L}_{\theta_1}\left[\theta_{\hat{m}}(\zeta)-\chi_{\hat{m}}\theta_{\hat{m}-1}(\zeta)\right]=\hbar\tilde{\mathcal{R}}^{\hat{m}}_{\theta_2}(\zeta), \tag{3.26}$$

$$\left.\begin{array}{c} f_{\hat{m}}(0)=Me\,\theta'_{\hat{m}}(0)+Pr\left(f_{\hat{m}}(0)+\alpha\left(\frac{n-1}{n+1}\right)\right)=\theta_{\hat{m}}(0)=0,\\ f'_{\hat{m}}(\infty)=\theta_{\hat{m}}(\infty)=0,\end{array}\right\} \tag{3.27}$$

$$\tilde{\mathcal{R}}^{\hat{m}}_{f_2}(\zeta) = f'''_{\hat{m}-1}+(1+\lambda_1)\left(\begin{array}{c}\sum\limits_{\hat{k}=0}^{\hat{m}-1}\left(f_{\hat{m}-1-\hat{k}}f''_{\hat{k}}\right)\\ +\frac{2n}{n+1}\left(A^2+MA-\sum\limits_{\hat{k}=0}^{\hat{m}-1}\left(f'_{\hat{m}-1-\hat{k}}f'_{\hat{k}}\right)\right)\\ -\left(\frac{2}{n+1}\right)Mf'_{\hat{m}-1}\end{array}\right) + \beta\left(\begin{array}{c}\left(\frac{3n-1}{2}\right)\sum\limits_{\hat{k}=0}^{\hat{m}-1}\left(f''_{\hat{m}-1-\hat{k}}f''_{\hat{k}}\right)+(n-1)\sum\limits_{\hat{k}=0}^{\hat{m}-1}\left(f'_{\hat{m}-1-\hat{k}}f'''_{\hat{k}}\right)\\ -\left(\frac{n+1}{2}\right)\sum\limits_{\hat{k}=0}^{\hat{m}-1}\left(f_{\hat{m}-1-\hat{k}}f''''_{\hat{k}}\right)\end{array}\right), \tag{3.28}$$

$$\tilde{\mathcal{R}}^{\hat{m}}_{\theta_2}(\zeta) = \theta''_{\hat{m}-1} + \Pr\left(\sum_{k=0}^{\hat{m}-1} f_{\hat{m}-1-\hat{k}}\theta'_{\hat{k}}\right) \tag{3.29}$$

$$+\frac{\Pr Ec}{1+\lambda_1}\left(\begin{array}{c}\beta\left(\begin{array}{c}\left(\frac{3n-1}{2}\right)\sum\limits_{\hat{k}=0}^{\hat{m}-1}\left(f'_{\hat{m}-1-\hat{k}}\right)\sum\limits_{l=0}^{\hat{k}} f''_{\hat{k}-l}f''_{l}\\ -\left(\frac{n+1}{2}\right)\sum\limits_{\hat{k}=0}^{\hat{m}-1}\left(f_{\hat{m}-1-\hat{k}}\right)\sum\limits_{l=0}^{\hat{k}} f''_{\hat{k}-l}f'''_{l}\end{array}\right)\\ +\sum\limits_{\hat{k}=0}^{\hat{m}-1} f''_{\hat{m}-1-\hat{k}}f''_{\hat{k}}\end{array}\right) \tag{3.30}$$

$$+\Pr\delta\left(\frac{2}{n+1}\right)\theta_{\hat{m}-1}, \tag{3.31}$$

The following expressions are derived via Taylor's series expansion:

$$\hat{f}(\zeta,\breve{p}) = f_{0_2}(\zeta) + \sum_{m=1}^{\infty} f_m(\zeta)\breve{p}^m,\ f_m(\zeta) = \left.\frac{1}{m!}\frac{\partial^m \hat{f}(\zeta,\breve{p})}{\partial\breve{p}^m}\right|_{\breve{p}=0}, \tag{3.32}$$

$$\hat{\theta}(\zeta,\breve{p}) = \theta_{0_2}(\zeta) + \sum_{m=1}^{\infty} \theta_m(\zeta)\breve{p}^m,\ \theta_m(\zeta) = \left.\frac{1}{m!}\frac{\partial^m \hat{\theta}(\zeta,\breve{p})}{\partial\breve{p}^m}\right|_{\breve{p}=0}. \tag{3.33}$$

The convergence regarding Eqs. (3.32) and (3.33) is solidly based upon the suitable selections of $\hbar_f$ and $\hbar_\theta$. Choosing suitable values of $\hbar_f$ and $\hbar_\theta$ so that Eqs. (3.32) and (3.33) converge at $\breve{p} = 1$ then

$$f(\zeta) = f_{0_2}(\zeta) + \sum_{\hat{m}=1}^{\infty} f_{\hat{m}}(\zeta), \tag{3.34}$$

$$\theta(\zeta) = \theta_{0_2}(\zeta) + \sum_{\hat{m}=1}^{\infty} \theta_{\hat{m}}(\zeta). \tag{3.35}$$

In terms of special solutions $(f^*_{\hat{m}}, \theta^*_{\hat{m}})$, the general solutions $(f_{\hat{m}}, \theta_{\hat{m}})$ of the Eqs. (3.25) and (3.26) are defined by the following expressions:

$$f_{\hat{m}}(\zeta) = f^*_{\hat{m}}(\zeta) + C^*_8 + C^*_9\exp(\zeta) + C^*_{10}\exp(-\zeta), \tag{3.36}$$

$$\theta_{\hat{m}}(\zeta) = \theta^*_{\hat{m}}(\zeta) + C^*_{11}\exp(\zeta) + C^*_{12}\exp(-\zeta), \tag{3.37}$$

in which C_i^* $(i = 8 - 12)$ through the boundary conditions (3.27) are given by

$$\begin{aligned} C_9^* &= C_{11}^* = 0,\ C_{10}^* = \left.\frac{\partial f_{\hat{m}}^*(\zeta)}{\partial \zeta}\right|_{\zeta=0},\ C_{12}^* = -\theta_{\hat{m}}^*(0), \\ C_8^* &= -C_{10}^* - f_{\hat{m}}^*(0) - \frac{Me}{\Pr}\left(\left.\frac{\partial \theta_{\hat{m}}^*(\zeta)}{\partial \zeta}\right|_{\zeta=0} - C_{12}^*\right). \end{aligned} \tag{3.38}$$

3.2.3 Convergence

Clearly homotopic solutions contain nonzero auxiliary variables $\hbar_f$ and $\hbar_\theta$. Such auxiliary variables can tune and restrict convergence of obtained series results. To get the acceptable values, the $\hbar-$ curves at 13th order of approximations are plotted. Figs. 3.2 and 3.3 clearly indicate that the convergence zone lies within the ranges $-1.55 \leq \hbar_f \leq -0.4$ and $-1.45 \leq \hbar_\theta \leq -0.45$. Table 3.1 ensures that 16th order of deformations are enough for meaningful solutions.

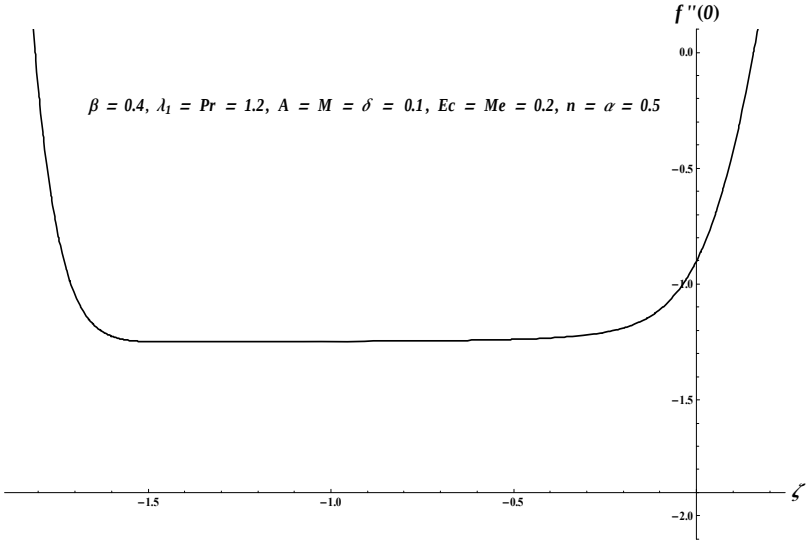

Fig. 3.2. $\hbar_f-$curve for $f(\zeta)$.

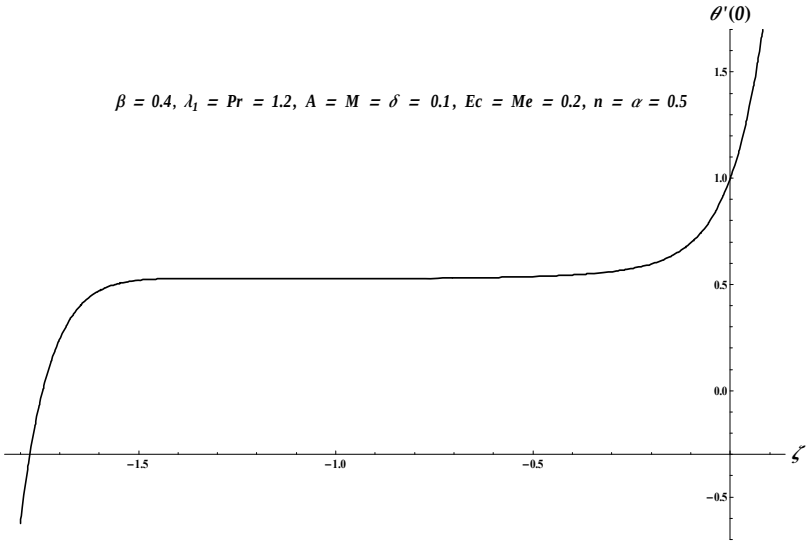

Fig. 3.3. $\hbar_\theta-$curve for $\theta(\zeta)$.

Table 3.1. Convergence of HAM solutions when $\lambda_1 = \Pr = 1.2$, $A = M = \delta = 0.1$, $Ec = Me = 0.2$, $n = \alpha = 0.5$ and $\beta = 0.4$.

Order of approximations	$-f''(0)$	$\theta'(0)$
1	1.1193	0.6053
5	1.2341	0.5416
10	1.2448	0.5289
16	1.2469	0.5281
25	1.2469	0.5281
35	1.2469	0.5281
50	1.2469	0.5281

3.3 Discussion

Here effects of several pertinent parameters like ratio parameter A, ratio of relaxation to retardation times λ_1, local Deborah number β, magnetic parameter M, Prandtl number Pr, Eckert number Ec, heat generation parameter δ, melting parameter Me, surface thickness parameter α and shape parameter n on velocity $f'(\zeta)$ and temperature $\theta(\zeta)$. Fig. 3.4 shows the impact of ratio parameter A on velocity distribution. Here $A < 1$ corresponds to the fact that free stream velocity is less than the stretching velocity whereas $A > 1$ corresponds to the reverse

phenomenon. Both velocity distribution and the momentum boundary layer are increased for higher A (when $A < 1$) whereas for $A > 1$ the velocity distribution increases and opposite trend is noticed in momentum boundary layer. Boundary layer vanishes for $A = 1$. Fig. 3.5 depicts the behavior of ratio of relaxation to retardation times λ_1 on velocity. Both the velocity and momentum layer are reduced for increasing values of λ_1. Fig. 3.6 displays the influence of local Deborah number β on velocity distribution. Velocity and associated layer thickness are enhanced for higher β. Impact of magnetic parameter M on velocity profile is sketched in Fig. 3.7. Both the velocity and momentum layer are decreasing functions of magnetic parameter. In fact more resistance is offered by the magnetic field to the fluid flow which results in the decay of velocity. Influence of surface thickness variable α on velocity distribution is shown in Fig. 3.8. Increasing values of α lead to higher velocity distribution. Effect of shape variable n on velocity distribution is depicted in Fig. 3.9. It is noted that larger n lead to more velocity distribution and momentum layer thickness. Especially analysis is based on the shape parameter n that is associated with the type of motion, namely, the shape of surface and the nature of boundary layer. For $n = 1$, the analysis reduces to the flat surface with constant thickness whereas for $n < 1$ the behavior of surface transformed to increasing thickness with convex outer shape and for $n > 1$ the behavior of surface changes to decreasing thickness with concave outer shape. Further, the type of motion can also be controlled by the shape parameter n. For $n = 0$ the motion becomes linear with constant velocity. If $n < 1$ the motion behaves as a decelerated motion and accelerated motion for $n > 1$. Fig. 3.10 presents the influence of ratio variable A on temperature distribution. Here temperature distribution is an increasing function of ratio parameter. Figs. $3.11 - 3.13$ show the behaviors of ratio of relaxation to retardation times λ_1, local Deborah number β and magnetic parameter M on temperature respectively. Temperature and related layer thickness are reducing functions of λ_1, β and M. Fig. 3.14 elaborates the characteristics of Prandtl number Pr on temperature. Higher Prandtl number Pr lead to stronger temperature. Effect of Eckert number Ec on temperature profile is sketched in Fig. 3.15. Temperature is larger for increasing values of Eckert number. In fact more heat is produced due to viscous forces between the fluid particles and thus the temperature distribution enhances. Impact of heat generation variable δ on temperature profile is displayed in Fig. 3.16. Here temperature profile enhances for increasing values of heat generation parameter. Fig. 3.17

depicts the influence of melting parameter Me on temperature profile. Temperature profile reduces with an increase in the values of melting paramter. Table 3.2 is generated to validate the current analysis with the earlier published outcomes in a limiting sense. Here current HAM solutions have nice resemblance with the previous numerical solutions by Sharma and Singh [36] in a limiting sense. Effects of λ_1, A, M, β, Pr, Me, Ec and δ on the local Nusselt number are presented in Table 3.3. The local Nusselt number is higher for A, β, Ec, Pr and δ while the reverse trend is noticed through λ_1, M and Me.

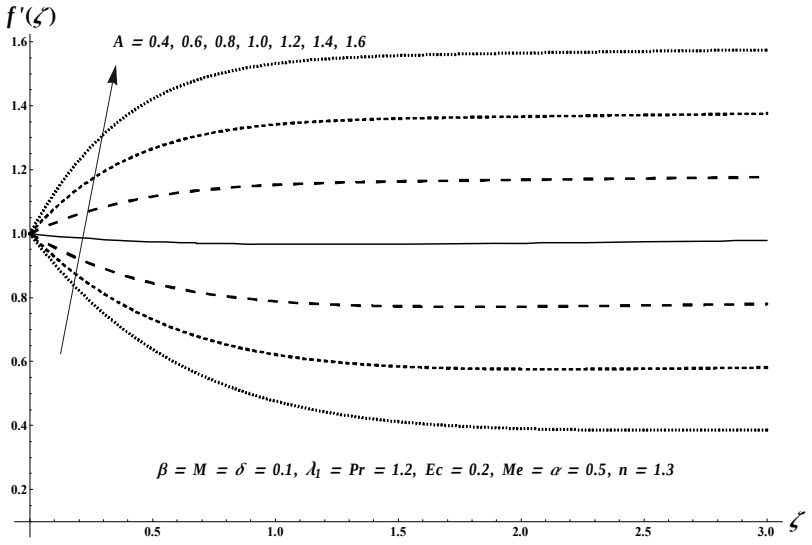

Fig. 3.4. Plots of $f'(\zeta)$ for A.

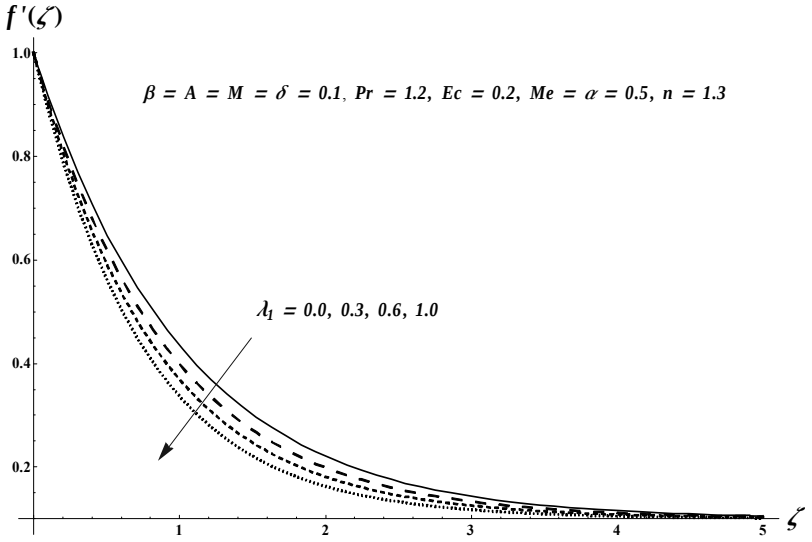

Fig. 3.5. Plots of $f'(\zeta)$ for λ_1.

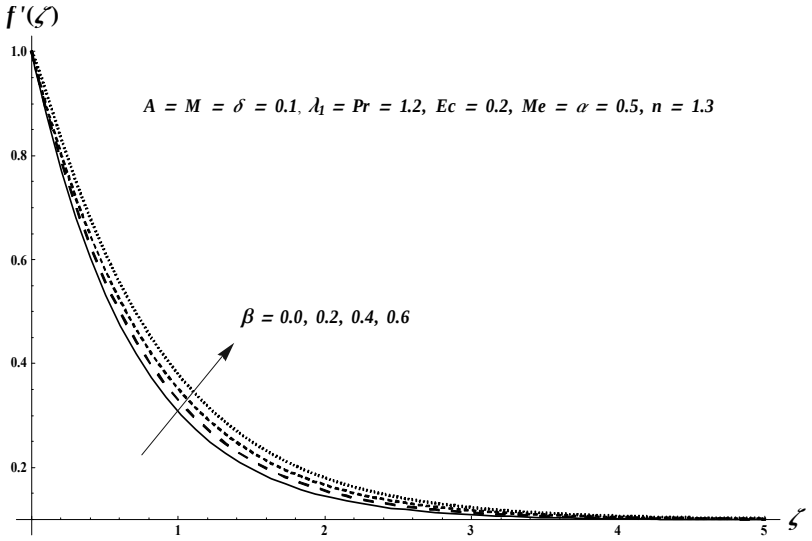

Fig. 3.6. Plots of $f'(\zeta)$ for β.

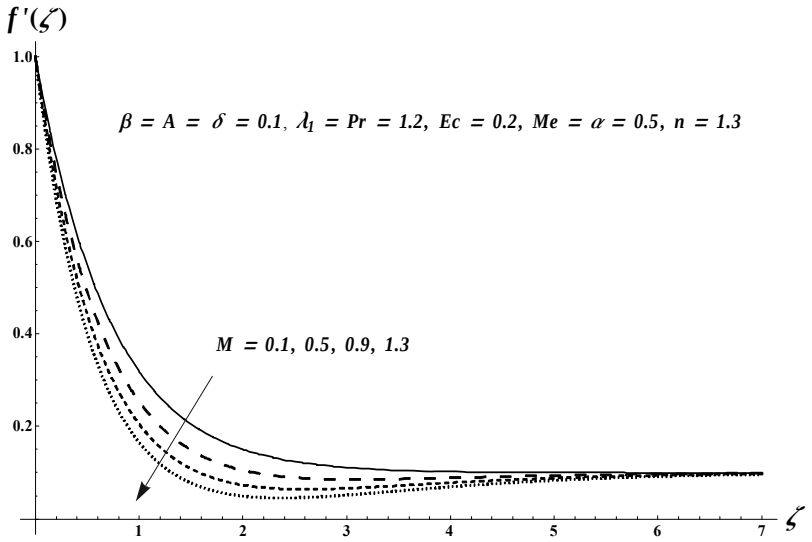

Fig. 3.7. Plots of $f'(\zeta)$ for M.

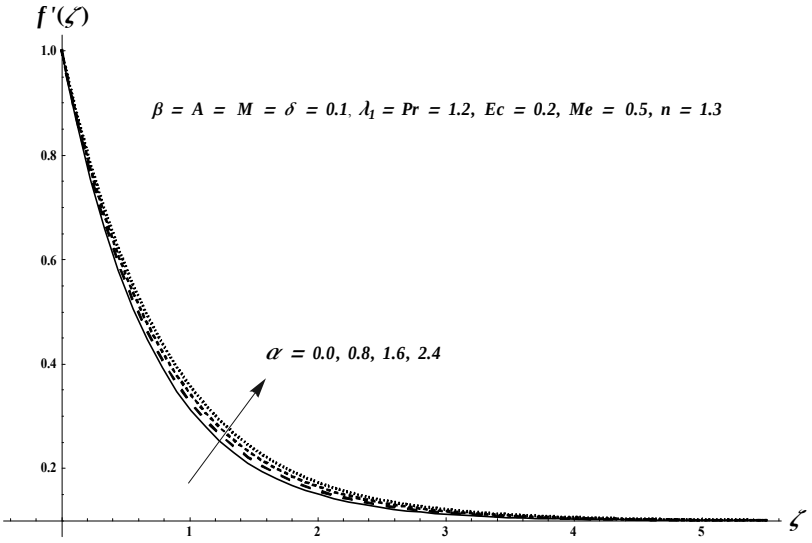

Fig. 3.8. Plots of $f'(\zeta)$ for α.

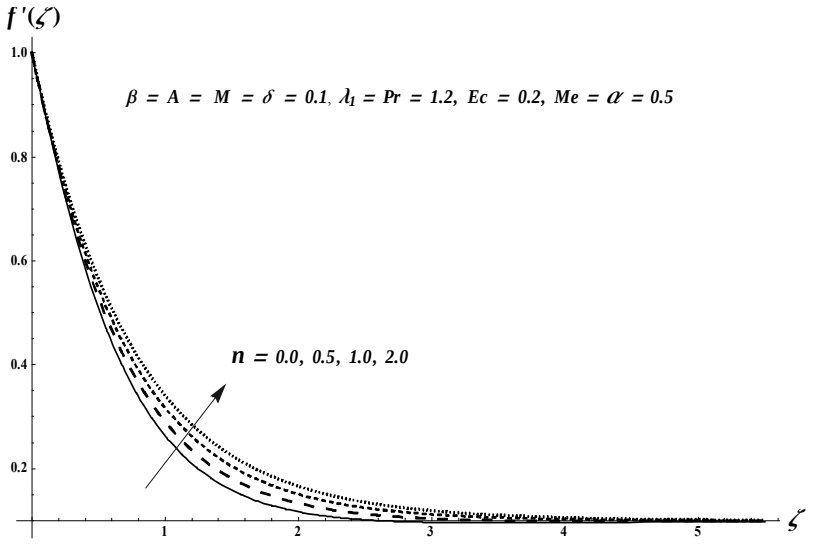

Fig. 3.9. Plots of $f'(\zeta)$ for n.

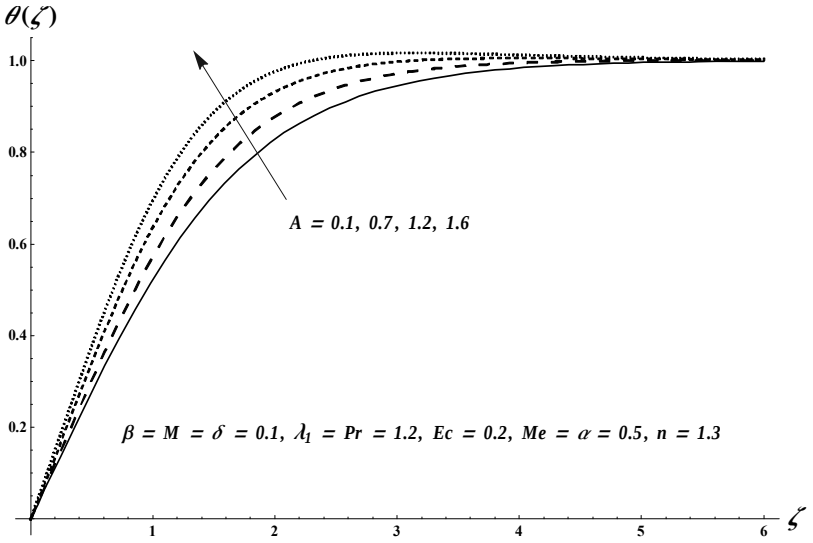

Fig. 3.10. Plots of $\theta(\zeta)$ for A.

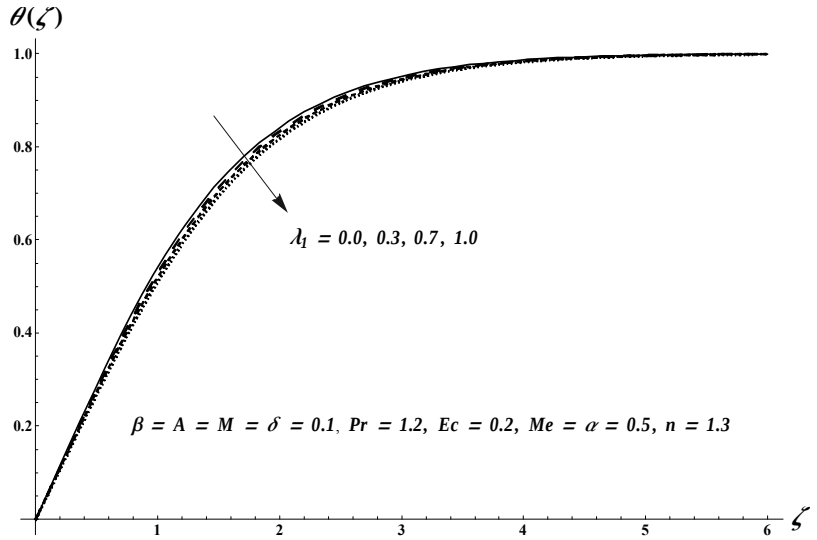

Fig. 3.11. Plots of $\theta(\zeta)$ for λ_1.

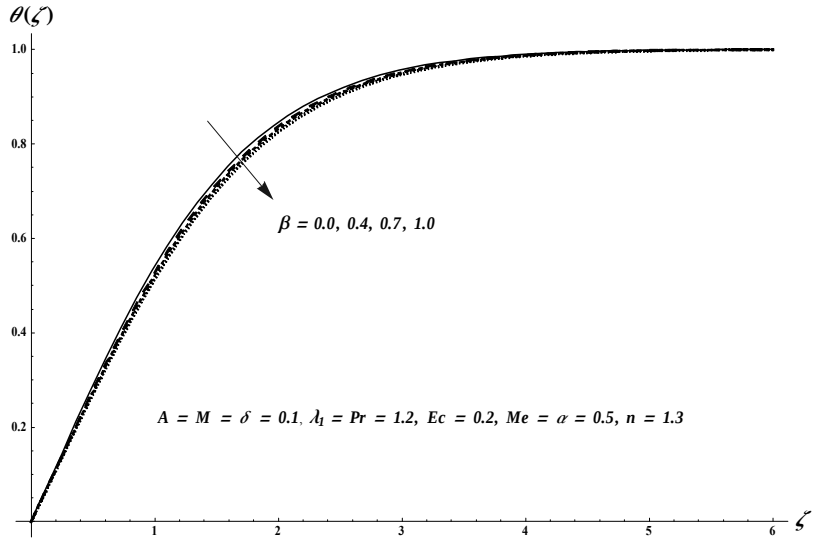

Fig. 3.12. Plots of $\theta(\zeta)$ for β.

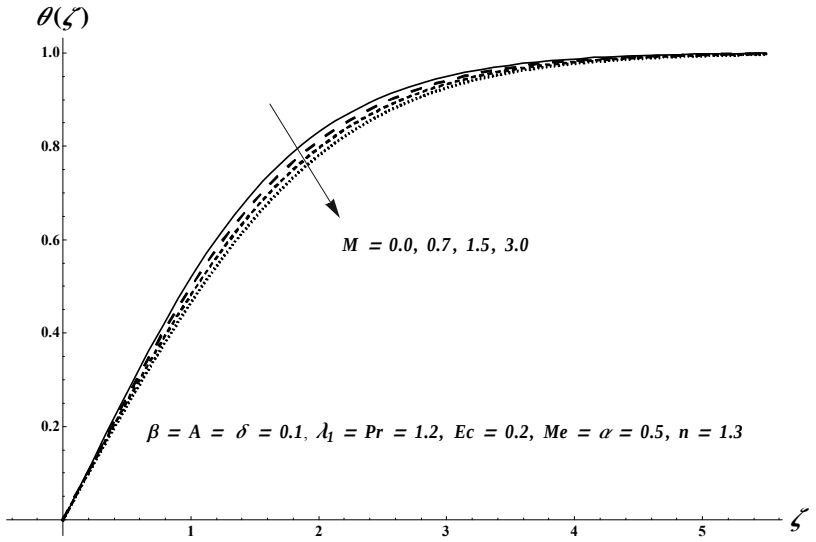

Fig. 3.13. Plots of $\theta(\zeta)$ for M.

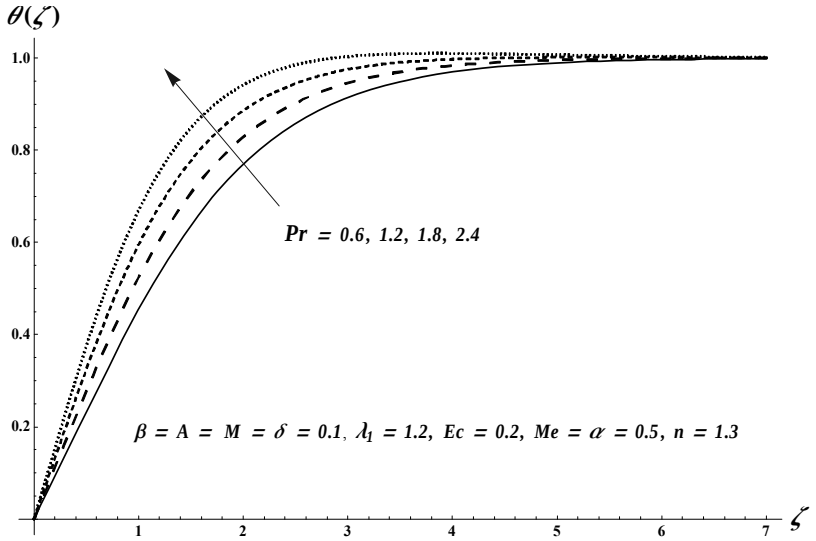

Fig. 3.14. Plots of $\theta(\zeta)$ for Pr.

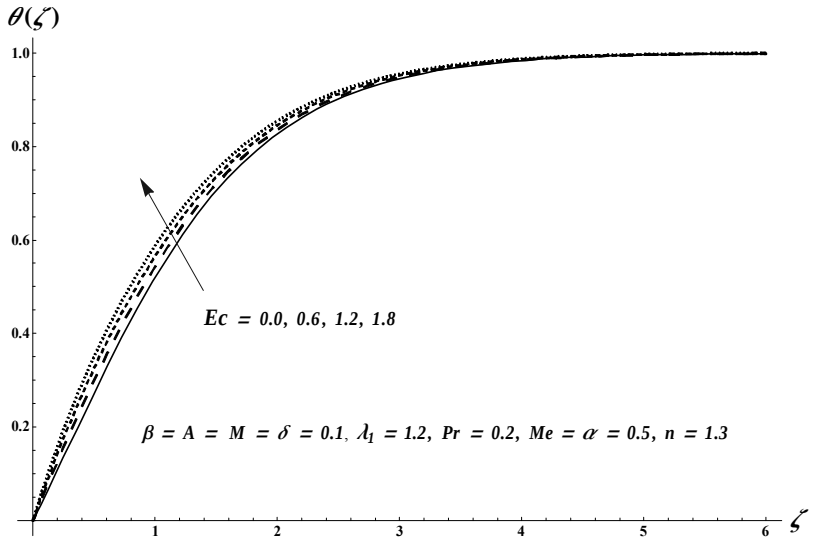

Fig. 3.15. Plots of $\theta(\zeta)$ for Ec.

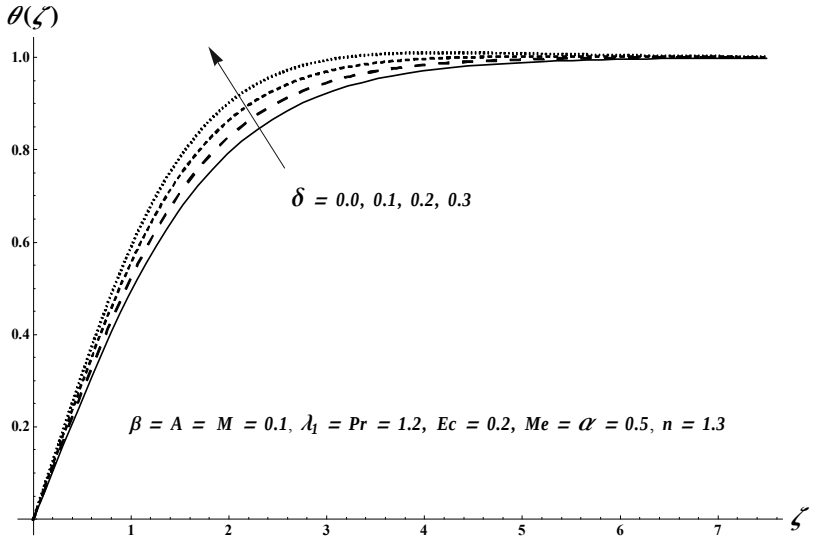

Fig. 3.16. Plots of $\theta(\zeta)$ for δ.

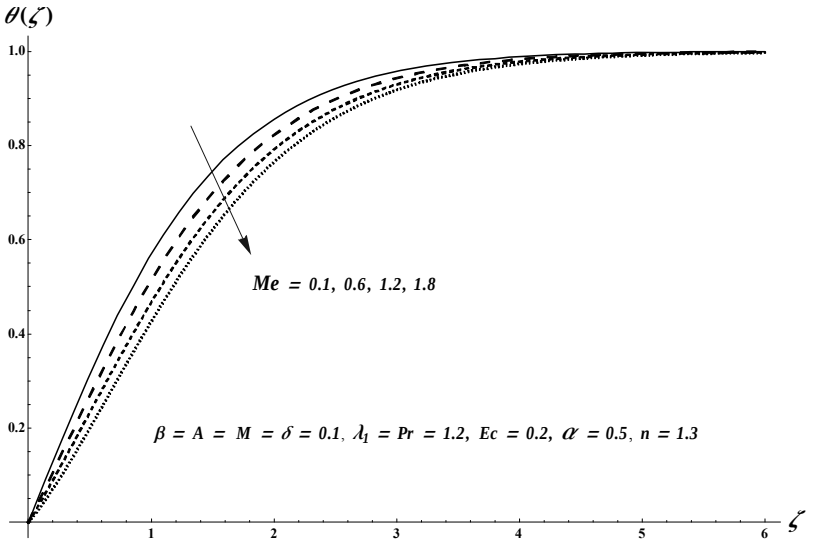

Fig. 3.17. Plots of $\theta(\zeta)$ for Me.

Table 3.2. Comparative values of $-f''(0)$ via A when $n = 1$ and $\alpha = \beta = \lambda_1 = M = Me = 0$.

A	HAM	Numerical [133]
0.1	0.96939	0.969386
0.2	0.91811	0.9181069
0.5	0.66726	0.667263

Table 3.3. Numerical data for local Nusselt number when $\alpha = 0.5$ and $n = 1.3$.

λ_1	A	M	β	Pr	Ec	δ	Me	$Nu_{w_2}/\sqrt{Re_{x_2}}$
1.1	0.1	0.1	0.1	1.2	0.1	0.1	0.5	0.5307
1.2								0.5281
1.3								0.5258
1.2	0.1	0.1	0.1	1.2	0.1	0.1	0.5	0.5281
	0.2							0.5363
	0.3							0.5473
1.2	0.1	0.1	0.1	1.2	0.1	0.1	0.5	0.5281
		0.3						0.5200
		0.5						0.5122
1.2	0.1	0.1	0.1	1.2	0.1	0.1	0.5	0.5281
			0.3					0.5329
			0.5					0.5395
1.2	0.1	0.1	0.1	1.2	0.1	0.1	0.5	0.5281
				1.4				0.5718
				1.6				0.6105
1.2	0.1	0.1	0.1	1.2	0.1	0.1	0.5	0.5281
					0.3			0.5685
					0.5			0.6075
1.2	0.1	0.1	0.1	1.2	0.1	0.1	0.5	0.5281
						0.2		0.5787
						0.3		0.6575
1.2	0.1	0.1	0.1	1.2	0.1	0.1	0.4	0.5522
							0.7	0.4865
							1.0	0.4365

3.4 Conclusions

Combined characteristics of melting heat and internal heat generation in stagnation point flow of Jeffrey material towards a nonlinear stretchable surface of variable surface thickness is studied. Main observations are

- Larger Deborah number β elucidates an increase in velocity field while opposite trend is noticed for temperature.
- Larger values of λ_1 leads to lower velocity and temperature distributions.
- Melting parameter Me indicates decreasing behavior for temperature distribution.
- Temperature distribution is an increasing function of heat generation parameter δ.
- Local Nusselt number reduces for melting parameter while reverse trend is seen for heat generation parameter.

Chapter 4

Stagnation-point second grade nanofluid flow over a nonlinear stretchable surface of variable thickness with melting heat process

Ongoing chapter addresses mixed convection stagnation point second grade nanofluid flow along with melting heat phenomena. Novel features regarding Brownian motion and thermophoresis are incorporated. Boundary-layer approximation is employed in the problem formulation. Momentum, energy and concentration equations are converted into the non-linear ordinary differential system through the appropriate transformations. Convergent solutions for resulting problem are computed. Behaviors of various sundry variables on temperature and concentration are studied in detail. The skin friction coefficient and heat and mass transfer rates are also computed and analyzed. Our results indicate that the temperature and concentration have been increased for larger thermophoresis parameter.

4.1 Formulation

Here the steady stagnation point flow of second grade nanomaterial is considered. The flow is caused by a non-linear stretched surface. The $x-$ and $y-$axes are chosen along and perpendicular to the stretched surface. Mixed convection, Brownian motion and thermophoresis effects have been included. We assume that the surface has variable thickness. The surface is at $y = \varepsilon\,(x + a^*)^{\frac{1-n}{2}}$, where ε is taken as an extremely small constant so that the surface is almost very thin, a^* is a constant and shape parameter is represented by n which has a great significance in the present flow. Clearly our problem holds only for $n \neq 1$. For $n = 1$, the surface is not of variable thickness. Moreover melting heat transfer effect is also accounted. The temperature of melting sheet is assumed to be T_m while the temperature in free stream is T_∞ $(> T_m)$ (see Fig. 4.1). Here T_0 denotes the constant temperature of the solid medium far from the interface such that $T_0 < T_m$. The flow is governed by [9, 20] :

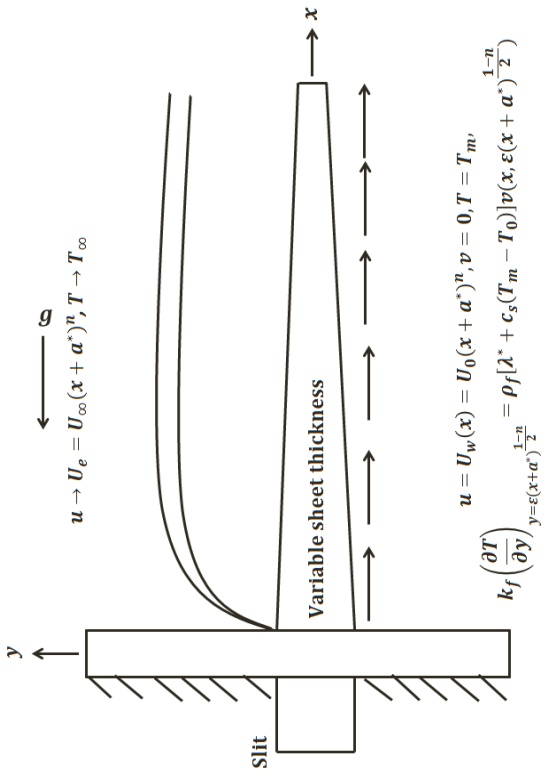

Fig. 4.1. Flow configuration.

$$\frac{\partial u}{\partial x}+\frac{\partial v}{\partial y}=0, \tag{4.1}$$

$$\begin{aligned} u\frac{\partial u}{\partial x}+v\frac{\partial u}{\partial y} &= U_e\frac{dU_e}{dx}+\nu\frac{\partial^2 u}{\partial y^2}+\frac{\alpha_1}{\rho_f}\begin{pmatrix} u\frac{\partial^3 u}{\partial x\partial y^2}+\frac{\partial u}{\partial y}\frac{\partial^2 v}{\partial y^2} \\ +\frac{\partial u}{\partial x}\frac{\partial^2 u}{\partial y^2}+v\frac{\partial^3 u}{\partial y^3}\end{pmatrix} \\ &\quad +\mathbf{g}\beta_t\left(T-T_m\right)+\mathbf{g}\beta_c\left(C-C_m\right), \end{aligned} \tag{4.2}$$

$$u\frac{\partial T}{\partial x}+v\frac{\partial T}{\partial y}=\alpha_1^*\frac{\partial^2 T}{\partial y^2}+\tau\left(\frac{D_T}{T_\infty}\left(\frac{\partial T}{\partial y}\right)^2+D_B\left(\frac{\partial C}{\partial y}\frac{\partial T}{\partial y}\right)\right), \tag{4.3}$$

$$u\frac{\partial C}{\partial x}+v\frac{\partial C}{\partial y}=\frac{D_T}{T_\infty}\left(\frac{\partial^2 T}{\partial y^2}\right)+D_B\left(\frac{\partial^2 C}{\partial y^2}\right). \tag{4.4}$$

The subjected boundary conditions are [20, 109] :

$$\left.\begin{aligned} u=U_w=U_0\left(x+a^*\right)^n,\quad v=0,\quad T=T_m\quad C=C_m\quad \text{at}\quad y=\varepsilon\left(x+a^*\right)^{\frac{1-n}{2}}, \\ k_f\left(\frac{\partial T}{\partial y}\right)_{y=\varepsilon(x+a^*)^{\frac{1-n}{2}}}=\rho_f\left[\lambda^*+c_s\left(T_m-T_0\right)\right]v\left(x,\varepsilon\left(x+a^*\right)^{\frac{1-n}{2}}\right), \end{aligned}\right\} \tag{4.5}$$

$$u\to U_e=U_\infty\left(x+a^*\right)^n,\quad T\to T_\infty\quad C\to C_\infty\quad \text{as}\quad y\to\infty, \tag{4.6}$$

in which $\tau\left(=\frac{(\rho c)_p}{(\rho c)_f}\right)$ the ratio of heat capacity of the nanoparticles to the heat capacity of the fluid. The velocity components and transformations are considered in the forms:

$$\left.\begin{aligned} u=\tfrac{\partial\psi}{\partial y},\quad v=-\tfrac{\partial\psi}{\partial x},\quad \eta=\sqrt{\left(\tfrac{n+1}{2\nu}\right)U_0\left(x+a^*\right)^{n-1}}y, \\ \psi=\sqrt{\left(\tfrac{2\nu}{n+1}\right)U_0\left(x+a^*\right)^{n+1}}F_1\left(\zeta\right),\quad \theta_1\left(\zeta\right)=\tfrac{T-T_m}{T_\infty-T_m},\quad \phi_1\left(\zeta\right)=\tfrac{C-C_m}{C_\infty-C_m}. \end{aligned}\right\} \tag{4.7}$$

Now Eq. (4.1) is automatically verified and Eqs. $(4.2)-(4.6)$ become

$$\begin{aligned} &F_1'''+F_1F_1''+\left(\tfrac{2n}{n+1}\right)\left(A^2-F_1'^2\right)+\tfrac{2}{n+1}\lambda_G\left(\theta_1+N_r\phi_1\right) \\ &+\alpha_2\begin{pmatrix}\left(3n-1\right)F_1'F_1'''- \\ \left(\frac{3n-1}{2}\right)F_1''^2-\left(\frac{n+1}{2}\right)F_1F_1^{iv}\end{pmatrix}=0, \end{aligned} \tag{4.8}$$

$$\theta_1''+\Pr\left(F_1\theta_1'+N_b\theta_1'\phi_1'+N_t\theta_1'^2\right)=0, \tag{4.9}$$

$$\phi_1''+Le\Pr F_1\phi_1'+\frac{N_t}{N_b}\theta_1''=0, \tag{4.10}$$

$$\left.\begin{array}{c} F_1'(\alpha)=1,\quad Me\theta_1'(\alpha)+Pr\left[F_1(\alpha)+\alpha\left(\frac{n-1}{n+1}\right)\right]=0,\quad \theta_1(\alpha)=0,\quad \phi_1(\alpha)=0,\\ F_1'(\infty)\to A,\quad \theta_1(\infty)\to 1,\quad \phi_1(\infty)\to 1, \end{array}\right\} \tag{4.11}$$

where $\lambda_G = \frac{G_{r_x}}{\mathrm{Re}_{x_2}^2}$ the Grashof number, $N_r = \frac{\beta_c(C_\infty - C_m)}{\beta_t(T_\infty - T_m)}$ the buoyancy ratio parameter, $\alpha_2 = \frac{U_0\alpha_1(x+a)^{n-1}}{\mu}$ the local second grade parameter, $N_b = \frac{\tau D_B(C_\infty - C_m)}{\nu}$ the Brownian motion parameter, $Le = \frac{\alpha_1^*}{D_B}$ the Lewis number and $N_t = \frac{\tau D_T(T_\infty - T_m)}{T_\infty \nu}$ the thermophoresis parameter. Moreover the domain of Eqs. $(4.8)-(4.11)$ is $[\alpha,\infty[$ and to facilitate the computation we transform the domain to $[0,\infty[$ by defining

$$\left.\begin{array}{l} F_1(\eta)=F_1(\zeta-\alpha)=f(\zeta),\\ \theta_1(\eta)=\theta_1(\zeta-\alpha)=\theta(\zeta),\\ \phi_1(\eta)=\phi_1(\zeta-\alpha)=\phi(\zeta). \end{array}\right\} \tag{4.12}$$

Hence Eqs. $(4.8)-(4.11)$ yield

$$\begin{array}{c} f'''+ff''+\left(\frac{2n}{n+1}\right)\left(A^2-f'^2\right)+\frac{2}{n+1}\lambda_G(\theta+N_r\phi)\\ +\alpha_2\left(\begin{array}{c}(3n-1)f'f'''-\\ \left(\frac{3n-1}{2}\right)f''^2-\left(\frac{n+1}{2}\right)ff^{iv}\end{array}\right)=0, \end{array} \tag{4.13}$$

$$\theta''+\mathrm{Pr}\left(f\theta'+N_b\theta'\phi'+N_t\theta'^2\right)=0, \tag{4.14}$$

$$\phi''+Le\,\mathrm{Pr}\,f\phi'+\frac{N_t}{N_b}\theta''=0, \tag{4.15}$$

$$\left.\begin{array}{c} f'(0)=1,\ Me\theta'(0)+\mathrm{Pr}\left(f(0)+\alpha\left(\frac{n-1}{n+1}\right)\right)=0,\ \theta(0)=0,\ \phi(0)=0,\\ f'(\infty)\to A,\ \theta(\infty)\to 1,\ \phi(\infty)\to 1, \end{array}\right\} \tag{4.16}$$

Expressions of skin friction coefficient and local Sherwood and Nusselt numbers are

$$C_{f_{x_2}}=\frac{\tau_{w_2}}{\rho_f U_w^2},\quad Sh_{x_1}=\frac{(x+a^*)\,j_{w_1}}{D_B(C_\infty-C_m)},\quad Nu_{x_2}=\frac{(x+a^*)\,q_{w_2}}{k_f(T_\infty-T_m)}, \tag{4.17}$$

in which τ_{w_2} denotes the wall shear stress, j_{w_1} the wall mass flux and q_{w_2} the wall heat flux. These are

$$\left.\begin{aligned} \tau_{w_2} &= \left(\mu\frac{\partial u}{\partial y}+\alpha_2\left(u\frac{\partial^2 u}{\partial x\partial y}+2\frac{\partial u}{\partial x}\frac{\partial u}{\partial y}+v\frac{\partial^2 u}{\partial y^2}\right)\right)_{y=\varepsilon(x+a^*)^{\frac{1-n}{2}}}, \\ j_{w_1} &= -D_B\left(\frac{\partial C}{\partial y}\right)_{y=\varepsilon(x+a^*)^{\frac{1-n}{2}}}, \\ q_{w_2} &= -k_f\left(\frac{\partial T}{\partial y}\right)_{y=\varepsilon(x+a^*)^{\frac{1-n}{2}}}. \end{aligned}\right\} \tag{4.18}$$

The related dimensionless definitions are

$$\left.\begin{aligned} \sqrt{Re_{x_2}}C_{f_{x_2}} &= \sqrt{\tfrac{n+1}{2}}\left(f''(0)+\alpha_2\left(\left(\tfrac{7n-1}{2}\right)f'(0)f''(0)-\left(\tfrac{n+1}{2}\right)f(0)f'''(0)\right)\right), \\ Sh_{x_1}/\sqrt{Re_{x_2}} &= -\sqrt{\tfrac{n+1}{2}}\phi'(0), \\ Nu_{x_2}/\sqrt{Re_{x_2}} &= -\sqrt{\tfrac{n+1}{2}}\theta'(0). \end{aligned}\right\} \tag{4.19}$$

4.2 Homotopic solutions

Our objective now is to calculate the local similar solutions via homotopy analysis method (HAM). The appropriate initial assumptions $\left(f_{0_2},\ \theta_{0_2},\ \phi_{0_2}\right)$ and the corresponding auxiliary operators $\left(\mathcal{L}_{f_1},\ \mathcal{L}_{\theta_1},\ \mathcal{L}_{\phi_1}\right)$ are

$$\left.\begin{aligned} f_{0_2}(\zeta) &= A\zeta+(1-A)\left(1-e^{-\zeta}\right)-\tfrac{Me}{\Pr}-\alpha\left(\tfrac{n-1}{n+1}\right), \\ \theta_{0_2}(\zeta) &= 1-e^{-\zeta},\quad \phi_{0_2}(\zeta)=1-e^{-\zeta}, \end{aligned}\right\} \tag{4.20}$$

$$\mathcal{L}_{f_1}=f'''-f',\quad \mathcal{L}_{\theta_1}=\theta''-\theta,\quad \mathcal{L}_{\phi_1}=\phi''-\phi. \tag{4.21}$$

The linear operators have properties

$$\left.\begin{aligned} \mathcal{L}_{f_1}\ \left[C_{13}^*+C_{14}^*e^{\zeta}+C_{15}^*e^{-\zeta}\right]&=0, \\ \mathcal{L}_{\theta_1}\ \left[C_{16}^*e^{\zeta}+C_{17}^*e^{-\zeta}\right]&=0, \\ \mathcal{L}_{\phi_1}\ \left[C_{18}^*e^{\zeta}+C_{19}^*e^{-\zeta}\right]&=0. \end{aligned}\right\} \tag{4.22}$$

Here C_i^* $(i=13-19)$ denote the random constants.

4.2.1 Deformation problems at zeroth-order

$$(1-\breve{p})\,\mathcal{L}_{f_1}\left[\hat{f}(\zeta,\breve{p})-f_{0_2}(\zeta)\right]=\breve{p}\hbar_f\mathcal{N}_{f_3}\left[\hat{f}(\zeta,\breve{p}),\ \hat{\theta}(\zeta,\breve{p}),\ \hat{\phi}(\zeta,\breve{p})\right], \tag{4.23}$$

$$(1-\breve{p})\,\mathcal{L}_{\theta_1}\left[\hat{\theta}\,(\zeta,\breve{p})-\theta_{0_2}\,(\zeta)\right]=\breve{p}\hbar_\theta\mathcal{N}_{\theta_3}\left[\hat{f}(\zeta,\breve{p}),\ \hat{\theta}(\zeta,\breve{p}),\ \hat{\phi}(\zeta,\breve{p})\right], \tag{4.24}$$

$$(1-\breve{p})\,\mathcal{L}_{\phi_1}\left[\hat{\phi}\,(\zeta,\breve{p})-\phi_{0_2}\,(\zeta)\right]=\breve{p}\hbar_\phi\mathcal{N}_{\phi_2}\left[\hat{f}(\zeta,\breve{p}),\ \hat{\theta}(\zeta,\breve{p}),\ \hat{\phi}(\zeta,\breve{p})\right], \tag{4.25}$$

$$\left.\begin{array}{c}\hat{f}'\,(0,\breve{p})=1,\quad \hat{\theta}\,(0,\breve{p})=0,\quad \hat{\phi}\,(0,\breve{p})=0,\\ Me\ \hat{\theta}'\,(0,\breve{p})+\Pr\left(\hat{f}\,(0,\breve{p})+\alpha\left(\frac{n-1}{n+1}\right)\right)=0,\end{array}\right\} \tag{4.26}$$

$$\hat{f}'\,(\infty,\breve{p})=A,\quad \hat{\theta}\,(\infty,\breve{p})=1,\quad \hat{\phi}\,(\infty,\breve{p})=1, \tag{4.27}$$

$$\begin{aligned}\mathcal{N}_{f_3}\left[\hat{f}(\zeta,\breve{p}),\ \hat{\theta}(\zeta,\breve{p}),\ \hat{\phi}(\zeta,\breve{p})\right] \;=\;& \frac{\partial^3\hat{f}}{\partial\zeta^3}+\frac{\partial\hat{f}}{\partial\zeta}\frac{\partial^2\hat{f}}{\partial\zeta^2}+\frac{2n}{n+1}\left(A^2-\frac{\partial\hat{f}}{\partial\zeta}\frac{\partial\hat{f}}{\partial\zeta}\right)\\ &+\frac{2n}{n+1}\lambda_G\left(\hat{\theta}+N_r\hat{\phi}\right)\\ &+\alpha_2\left(\begin{array}{c}(3n-1)\,\frac{\partial\hat{f}}{\partial\zeta}\frac{\partial^3\hat{f}}{\partial\zeta^3}-\\ \left(\frac{3n-1}{2}\right)\frac{\partial^2\hat{f}}{\partial\zeta^2}\frac{\partial^2\hat{f}}{\partial\zeta^2}-\left(\frac{n+1}{2}\right)\hat{f}\frac{\partial^4\hat{f}}{\partial\zeta^4}\end{array}\right),\end{aligned} \tag{4.28}$$

$$\mathcal{N}_{\theta_3}\left[\hat{f}(\zeta,\breve{p}),\ \hat{\theta}(\zeta,\breve{p}),\ \hat{\phi}(\zeta,\breve{p})\right]=\frac{\partial^2\hat{\theta}}{\partial\zeta^2}+\Pr\left(\hat{f}\frac{\partial\hat{\theta}}{\partial\zeta}+N_b\frac{\partial\hat{\theta}}{\partial\zeta}\frac{\partial\hat{\phi}}{\partial\zeta}+N_t\left(\frac{\partial\hat{\theta}}{\partial\zeta}\right)^2\right), \tag{4.29}$$

$$\mathcal{N}_{\phi_2}\left[\hat{f}(\zeta,\breve{p}),\ \hat{\theta}(\zeta,\breve{p}),\ \hat{\phi}(\zeta,\breve{p})\right]=\frac{\partial^2\hat{\phi}}{\partial\zeta^2}+Le\Pr\hat{f}\frac{\partial\hat{\phi}}{\partial\zeta}+\frac{N_t}{N_b}\frac{\partial^2\hat{\theta}}{\partial\zeta^2}. \tag{4.30}$$

Setting $\breve{p}=0$ and $\breve{p}=1$ one obtains

$$\hat{f}(\zeta,0)=f_{0_2}(\zeta),\quad \hat{f}(\zeta,1)=f(\zeta), \tag{4.31}$$

$$\hat{\theta}(\zeta,0)=\theta_{0_2}(\zeta),\quad \hat{\theta}(\zeta,1)=\theta(\zeta), \tag{4.32}$$

$$\hat{\phi}(\zeta,0)=\phi_{0_2}(\zeta),\quad \hat{\phi}(\zeta,1)=\phi(\zeta). \tag{4.33}$$

When $\breve{p}$ changes from 0 to 1 then $\hat{f}(\zeta,\breve{p})$, $\hat{\theta}(\zeta,\breve{p})$ and $\hat{\phi}(\zeta,\breve{p})$ vary from primary approximations $f_{0_2}(\zeta)$, $\theta_{0_2}(\zeta)$ and $\phi_{0_2}(\zeta)$ to desired ultimate results $f(\zeta)$, $\theta(\zeta)$ and $\phi(\zeta)$.

4.2.2 Deformation problems at $\hat{m}$th-order

$$\mathcal{L}_{f_1}\left[f_{\hat{m}}\,(\zeta)-\chi_{\hat{m}}f_{\hat{m}-1}\,(\zeta)\right]=\hbar_f\mathcal{R}^{\hat{m}}_{f_3}(\zeta), \tag{4.34}$$

$$\mathcal{L}_{\theta 1}\left[\theta_{\hat{m}}\left(\zeta\right)-\chi_{\hat{m}}\theta_{\hat{m}-1}\left(\zeta\right)\right]=\hbar_{\theta}\mathcal{R}_{\theta 3}^{\hat{m}}(\zeta), \tag{4.35}$$

$$\mathcal{L}_{\phi_1}\left[\phi_{\hat{m}}\left(\zeta\right)-\chi_{\hat{m}}\phi_{\hat{m}-1}\left(\zeta\right)\right]=\hbar_{\phi}\mathcal{R}_{\phi_2}^{\hat{m}}(\zeta), \tag{4.36}$$

$$f'_{\hat{m}}\left(0\right)=Pr\left(f_{\hat{m}}\left(0\right)+\alpha\left(\frac{n-1}{n+1}\right)\right)+Me\theta'_{\hat{m}}\left(0\right)=\phi_{\hat{m}}\left(0\right)=\theta_{\hat{m}}\left(0\right)=0, \tag{4.37}$$

$$f'_{\hat{m}}\left(\infty\right)=\theta_{\hat{m}}\left(\infty\right)=\phi_{\hat{m}}\left(\infty\right)=0, \tag{4.38}$$

$$\begin{aligned}\mathcal{R}_{f_3}^{\hat{m}}(\zeta) &= f'''_{\hat{m}-1}+\sum_{\hat{k}=0}^{\hat{m}-1}f'_{\hat{m}-1-\hat{k}}f''_{\hat{k}}+\frac{2n}{n+1}\left(A^2-\sum_{k=0}^{\hat{m}-1}f'_{\hat{m}-1-\hat{k}}f'_{\hat{k}}\right)\\ &+\frac{2n}{n+1}\lambda_G\left(\theta_{\hat{m}-1}+N_r\phi_{\hat{m}-1}\right)\\ &+\alpha_2\left(\begin{array}{c}(3n-1)\sum_{\hat{k}=0}^{\hat{m}-1}f'_{\hat{m}-1-\hat{k}}f'''_{\hat{k}}-\\ \left(\frac{3n-1}{2}\right)\sum_{\hat{k}=0}^{\hat{m}-1}f''_{\hat{m}-1-\hat{k}}f''_{\hat{k}}-\left(\frac{n+1}{2}\right)\sum_{\hat{k}=0}^{\hat{m}-1}f_{\hat{m}-1-\hat{k}}f_{\hat{k}}^{(iv)}\end{array}\right),\end{aligned} \tag{4.39}$$

$$\mathcal{R}_{\theta_3}^{\hat{m}}(\zeta)=\theta''_{\hat{m}-1}+\Pr\left(\sum_{\hat{k}=0}^{\hat{m}-1}f_{\hat{m}-1-\hat{k}}\theta'_{\hat{k}}+N_b\sum_{\hat{k}=0}^{\hat{m}-1}\theta'_{\hat{m}-1-\hat{k}}\phi'_{\hat{k}}+N_t\sum_{\hat{k}=0}^{\hat{m}-1}\theta'_{\hat{m}-1-\hat{k}}\theta'_{\hat{k}}\right), \tag{4.40}$$

$$\mathcal{R}_{\phi_2}^{\hat{m}}(\zeta)=\phi''_{\hat{m}-1}+Le\Pr\sum_{\hat{k}=0}^{\hat{m}-1}f_{\hat{m}-1-\hat{k}}\phi'_{\hat{k}}+\frac{N_t}{N_b}\theta''_{\hat{m}-1}, \tag{4.41}$$

The following expressions are derived via Taylor's series expansion:

$$\hat{f}(\zeta,\breve{p})=f_{0_2}(\zeta)+\sum_{\hat{m}=1}^{\infty}f_{\hat{m}}(\zeta)\breve{p}^{\hat{m}},\ f_{\hat{m}}(\zeta)=\left.\frac{1}{\hat{m}!}\frac{\partial^{\hat{m}}\hat{f}(\zeta,\breve{p})}{\partial\breve{p}^{\hat{m}}}\right|_{\breve{p}=0}, \tag{4.42}$$

$$\hat{\theta}(\zeta,\breve{p})=\theta_{0_2}(\zeta)+\sum_{\hat{m}=1}^{\infty}\theta_{\hat{m}}(\zeta)\breve{p}^{\hat{m}},\ \theta_{\hat{m}}(\zeta)=\left.\frac{1}{\hat{m}!}\frac{\partial^{\hat{m}}\hat{\theta}(\zeta,\breve{p})}{\partial\breve{p}^{\hat{m}}}\right|_{\breve{p}=0}, \tag{4.43}$$

$$\hat{\phi}(\zeta,\breve{p})=\phi_{0_2}(\zeta)+\sum_{\hat{m}=1}^{\infty}\phi_{\hat{m}}(\zeta)\breve{p}^{\hat{m}},\ \phi_{\hat{m}}(\zeta)=\left.\frac{1}{\hat{m}!}\frac{\partial^{\hat{m}}\hat{\phi}(\zeta,\breve{p})}{\partial\breve{p}^{\hat{m}}}\right|_{\breve{p}=0}. \tag{4.44}$$

The convergence regarding Eqs. $(4.42)-(4.44)$ solidly depends on suitable values of $\hbar_f$, $\hbar_\theta$ and $\hbar_\phi$. Choosing appropriate $\hbar_f$, $\hbar_\theta$ and $\hbar_\phi$ so that Eqs. $(4.42)-(4.44)$ converge at $\breve{p}=1$ then

$$f\left(\zeta\right)=f_{0_2}(\zeta)+\sum_{\hat{m}=1}^{\infty}f_{\hat{m}}(\zeta), \tag{4.45}$$

$$\theta(\zeta) = \theta_{0_2}(\zeta) + \sum_{\hat{m}=1}^{\infty} \theta_{\hat{m}}(\zeta), \tag{4.46}$$

$$\phi(\zeta) = \phi_{0_2}(\zeta) + \sum_{\hat{m}=1}^{\infty} \phi_{\hat{m}}(\zeta). \tag{4.47}$$

In terms of special solutions $(f^*_{\hat{m}}, \theta^*_{\hat{m}}, \phi^*_{\hat{m}})$, the general solutions $(f_{\hat{m}}, \theta_{\hat{m}}, \phi_{\hat{m}})$ of the Eqs. (4.34)$-$(4.36) are defined by the following expressions:

$$f_{\hat{m}}(\zeta) = f^*_{\hat{m}}(\zeta) + C^*_{13} + C^*_{14}\exp(\zeta) + C^*_{15}\exp(-\zeta), \tag{4.48}$$

$$\theta_{\hat{m}}(\zeta) = \theta^*_{\hat{m}}(\zeta) + C^*_{16}\exp(\zeta) + C^*_{17}\exp(-\zeta), \tag{4.49}$$

$$\phi_{\hat{m}}(\zeta) = \phi^*_{\hat{m}}(\zeta) + C^*_{18}\exp(\zeta) + C^*_{19}\exp(-\zeta), \tag{4.50}$$

in which C^*_i $(i = 13 - 19)$ through the boundary conditions (4.37) and (4.38) are given by

$$\begin{aligned} C^*_{14} &= C^*_{16} = C^*_{18} = 0,\ C^*_{15} = \left.\frac{\partial f^*_{\hat{m}}(\zeta)}{\partial \zeta}\right|_{\zeta=0},\ C^*_{17} = -\theta^*_{\hat{m}}(0), \\ C^*_{13} &= -C^*_{15} - f^*_{\hat{m}}(0) - \frac{Me}{\mathrm{Pr}}\left(\left.\frac{\partial \theta^*_{\hat{m}}(\zeta)}{\partial \zeta}\right|_{\zeta=0} - C^*_{17}\right),\ C^*_{19} = -\phi^*_{\hat{m}}(0). \end{aligned} \tag{4.51}$$

4.2.3 Convergence analysis

No doubt the homotopic solutions (4.45) $-$ (4.47) have the nonzero auxiliary variables $\hbar_f$, $\hbar_\theta$ and $\hbar_\phi$. These variables are important to tune and govern the convergence of obtained approximate homotopic expressions. For meaningful values of such variables, we have drawn the $\hbar-$ curves at 16th order of deformations. Fig. 4.2 indicates that the convergence region satisfies $-1.75 \leq \hbar_f \leq -0.5$, $-1.9 \leq \hbar_\theta \leq -0.3$ and $-1.85 \leq \hbar_\phi \leq -0.4$. Table 4.1 depicts that

the 35th order of deformation is sufficient for convergent solutions.

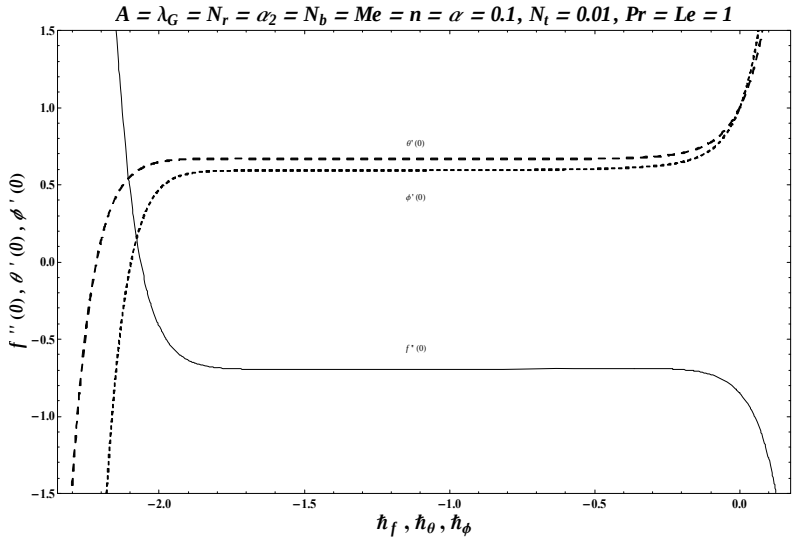

Fig. 4.2. The $\hbar-$plots for f, θ and ϕ.

Table 4.1. HAM solutions convergence when $A = \lambda_G = N_r = \alpha_2 = N_b = Me = n = \alpha = 0.1$, $N_t = 0.01$ and $Le = \Pr = 1.0$.

Order of approximations	$f''(0)$	$\theta'(0)$	$\phi'(0)$
1	-0.743	0.752	0.728
5	-0.730	0.671	0.617
10	-0.749	0.661	0.596
15	-0.762	0.658	0.588
20	-0.772	0.655	0.583
25	-0.782	0.653	0.579
30	-0.786	0.651	0.576
35	-0.791	0.649	0.574
40	-0.791	0.649	0.574
50	-0.791	0.649	0.574

4.3 Interpretation

This portion organizes effects of several pertinent parameters like ratio parameter A, Grashof number λ_G, buoyancy ratio parameter N_r, local second grade parameter α_2, thermophoresis parameter N_t, Brownian motion parameter N_b, Lewis number Le, Prandtl number Pr, melting parameter Me, shape parameter n and surface thickness parameter α on temperature $\theta(\eta)$ and concentration $\phi(\eta)$ distributions. Fig. 4.3 presents the influence of ratio parameter A on temperature profile. Here temperature distribution is an increasing function of ratio parameter while the thermal layer thickness decreases. Note that $A < 1$ corresponds to the fact that the free stream velocity is less than the stretching velocity whereas $A > 1$ corresponds to the reverse phenomenon. For $A = 1$ boundary layer vanishes as both velocities (free stream velocity and stretching velocity) balanced each other. Fig. 4.4 depicts the behavior of Grashof number λ_G on temperature $\theta(\eta)$. Temperature decreases whereas thermal layer thickness enhances for increasing values of λ_G. Fig. 4.5 displays the behavior of buoyancy ratio parameter N_r on temperature distribution. Here temperature decreases and associated layer thickness enhances via N_r. Effect of local second grade variable α_2 on temperature distribution is plotted in Fig. 4.6. Temperature decreases and related layer thickness enhances for local second grade parameter α_2. Figs. $4.7 - 4.12$ show the behaviors of thermophoresis parameter N_t, Brownian motion parameter N_b, Prandtl number Pr, melting parameter Me, shape parameter n and surface thickness parameter α on temperature respectively. Temperature enhances and thermal layer thickness reduces by increasing values of N_t, N_b and Pr whereas temperature decreases and thermal layer thickness increases by increasing values of Me, n and α. Here especially the analysis is based on the shape parameter n that is associated with the type of motion, namely, the shape of surface and the nature of boundary layer. For $n = 1$, the analysis reduces to the flat surface with constant thickness whereas for $n < 1$ the behavior of surface transformed to increasing thickness with convex outer shape and for $n > 1$ the behavior of surface changes to decreasing thickness with concave outer shape. Further, the type of motion can also be controlled by the shape parameter n. For $n = 0$ the motion becomes linear with constant velocity. If $n < 1$ the motion behaves as a decelerated motion and accelerated motion for $n > 1$. It is a valuable fact to focus here that the properties of liquid metals are characterized by small values of Prandtl number ($\mathrm{Pr} < 1$), which have larger thermal conductivity but smaller

viscosity, whereas higher values of Prandtl number ($\mathrm{Pr} > 1$) associate with high-viscosity oils. Particularly Prandtl number $\mathrm{Pr} = 0.72$, 1.0 and 6.2 associate to electrolyte solution, air such as water and salt water respectively. In heat transfer, Prandtl number is used to control the thicknesses of momentum and thermal boundary layers. Further it is also observed that N_t and N_b portray the vitalities of thermophoresis and Brownian motion phenomenons respectively. The higher the values of N_b and N_t, the larger will be the vitality of the corresponding effects. Larger N_b gives stronger thermophoretic force which encourages the nanoparticles to move from hot to cold areas. Ultimately the temperature and thermal layer are increased. In addition, larger Brownian motion parameter has higher Brownian diffusion coefficient and smaller viscous force. It increases temperature and thermal layer thickness. The change in concentration field $\phi(\eta)$ for several values of ratio parameter A, dimensionless second grade parameter α_2, thermophoresis parameter N_t, Brownian motion parameter N_b, Lewis number Le, Prandtl number Pr, melting parameter Me, shape parameter n and surface thickness parameter α are displayed in the Figs. $4.13 - 4.21$ respectively. It is observed that by increasing α_2, N_b and Pr the concentration field $\phi(\eta)$ decreases while it increases by increasing A, N_t, Le, Me, n and α. There is low concentration gradient and more concentration for larger N_b. Table 4.2 depicts skin friction coefficient for several effective parameters A, λ_G, N_r, α_2 and Me. Skin friction coefficient is higher for λ_G, N_r and α_2 while the reverse trend is noticed through A and Me. Table 4.3 is generated to analyze the numerical data of local Nusselt and Sherwood numbers for distinct values of embedding parameters. Here it is examined that local Nusselt number reduces for larger buoyancy ratio parameter N_r, local second grade parameter α_2, Lewis number Le and melting parameter Me whereas opposite trend is seen for ratio parameter A, Grashof number λ_G, thermophoresis parameter N_t and Brownian motion parameter N_b. However the local Nusselt number enhances for Prandtl number Pr . A larger Prandtl number containing higher convection in contrast to pure conduction and effective in transmitting energy through unit area. Hence local Nusselt number enhances for Prandtl number. Further local Sherwood number is higher for A, λ_r, N_b, and Le while the reverse trend is noticed through N_r, α_2, N_t,

Pr and Me.

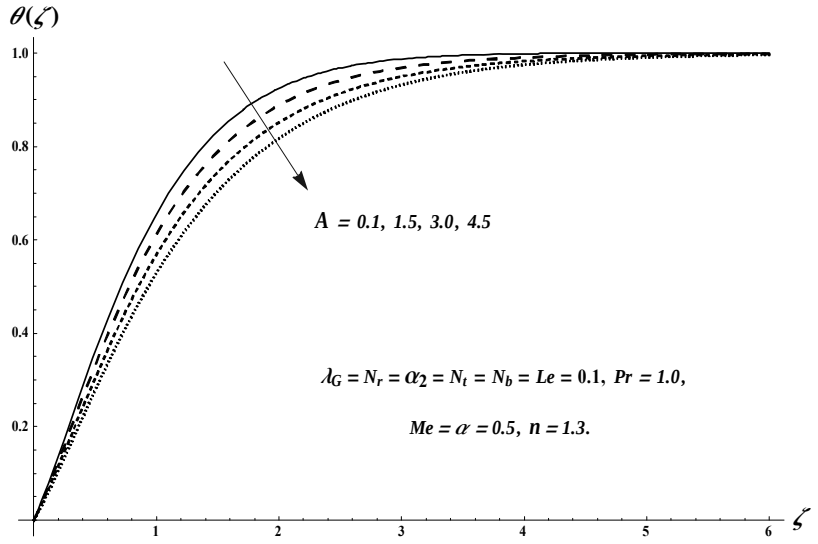

Fig. 4.3. Plots of $\theta(\zeta)$ for A.

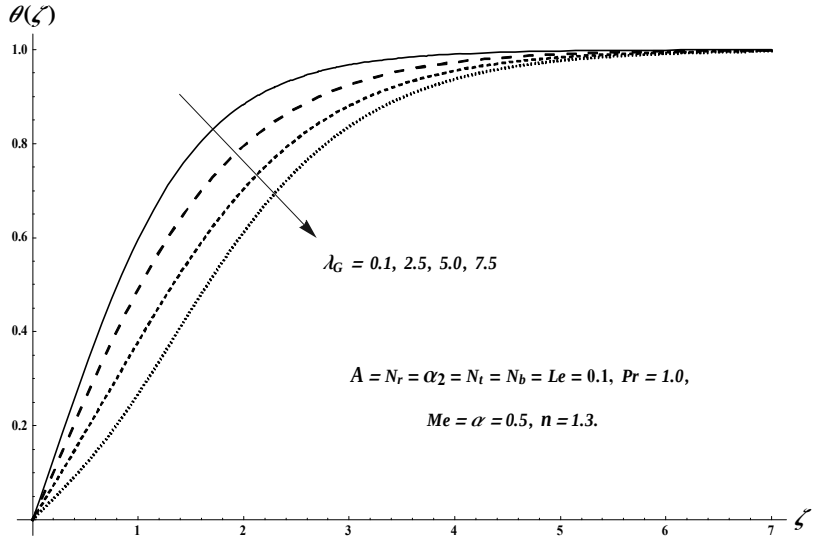

Fig. 4.4. Plots of $\theta(\zeta)$ for λ_G.

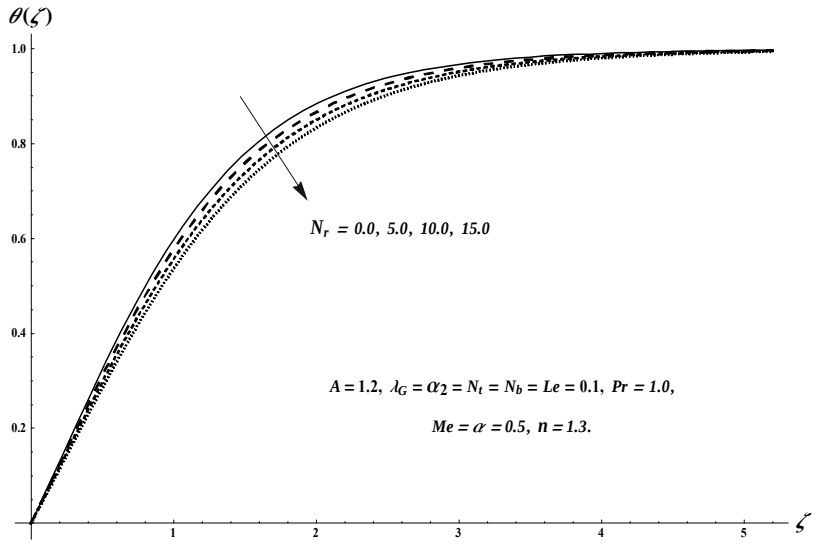

Fig. 4.5. Plots of $\theta(\zeta)$ for N_r.

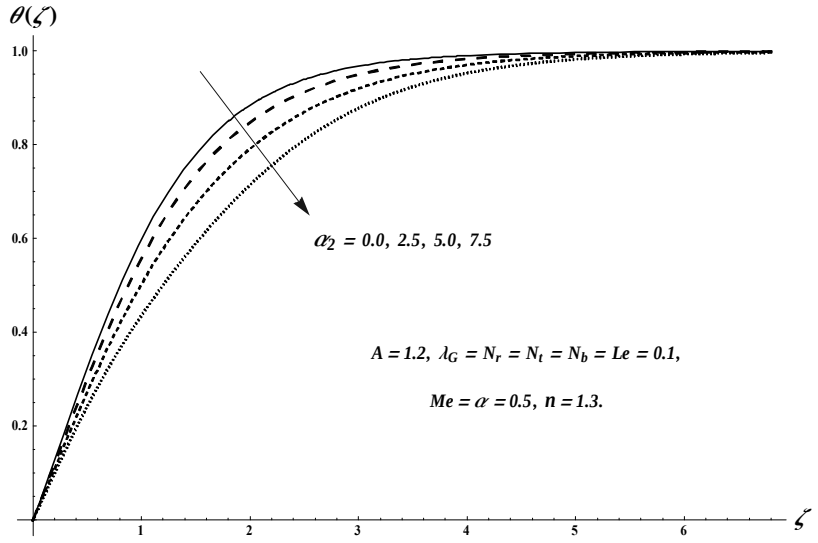

Fig. 4.6. Plots of $\theta(\zeta)$ for α_2.

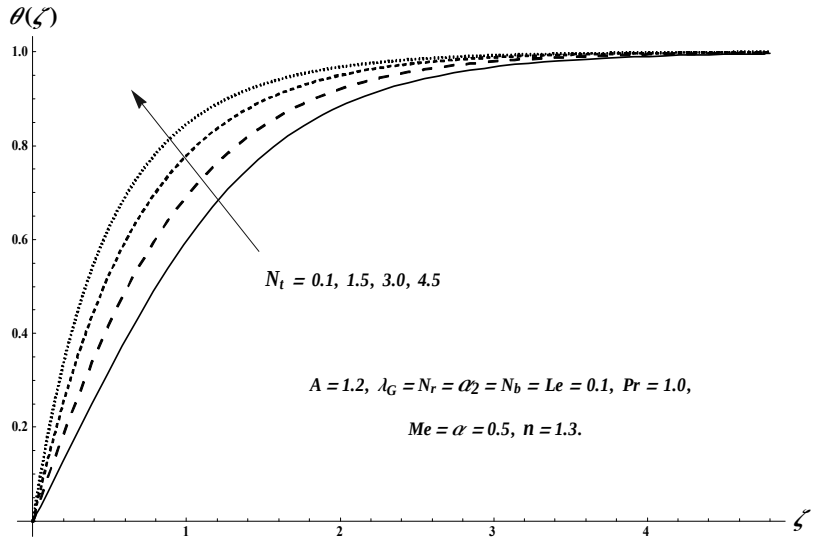

Fig. 4.7. Plots of $\theta(\zeta)$ for N_t.

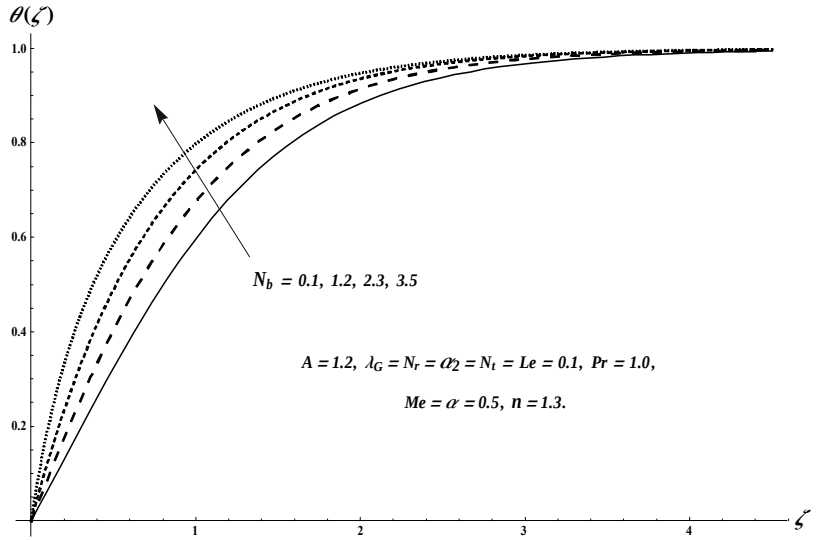

Fig. 4.8. Plots of $\theta(\zeta)$ for N_b.

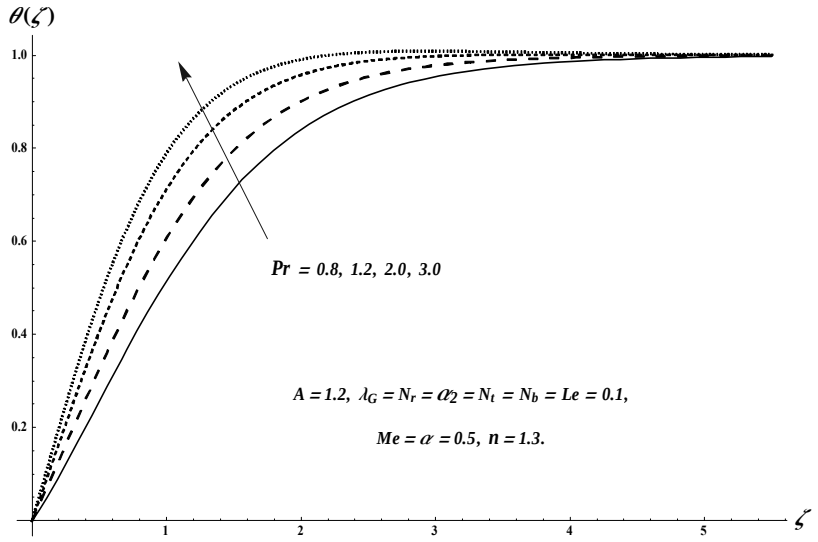

Fig. 4.9. Plots of $\theta(\zeta)$ for Pr .

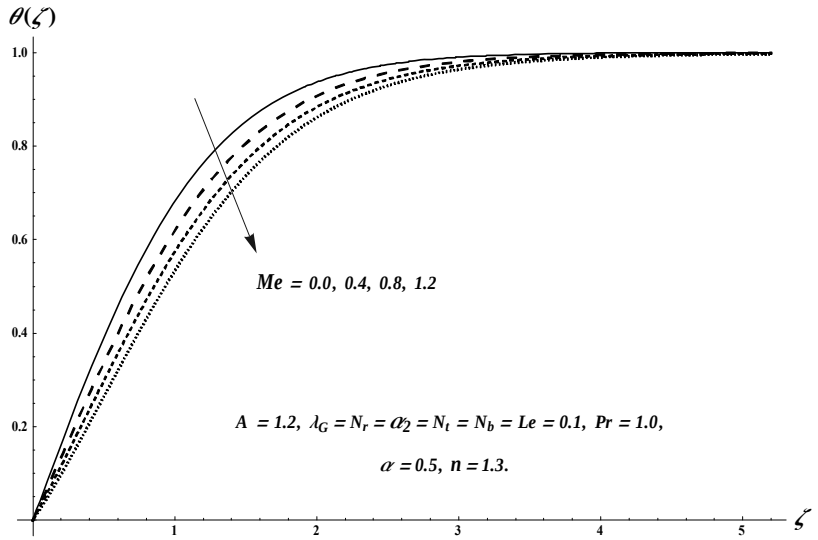

Fig. 4.10. Plots of $\theta(\zeta)$ for Me.

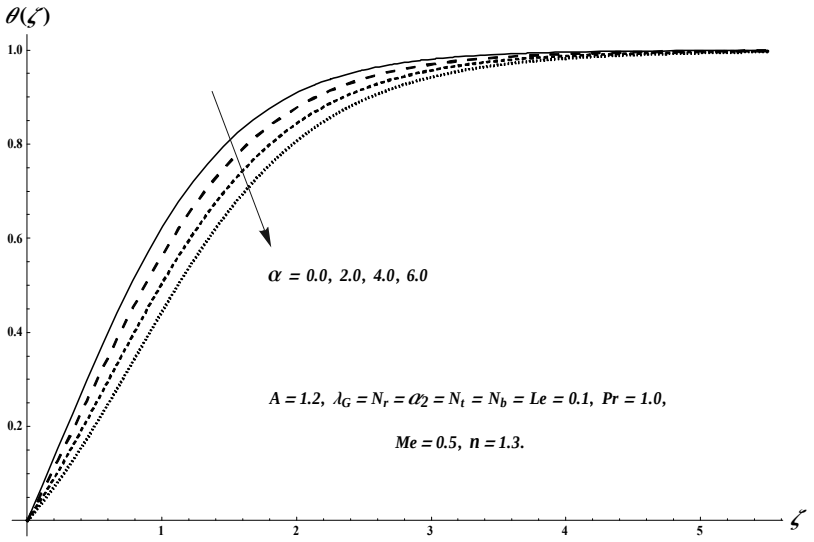

Fig. 4.11. Plots of $\theta(\zeta)$ for α.

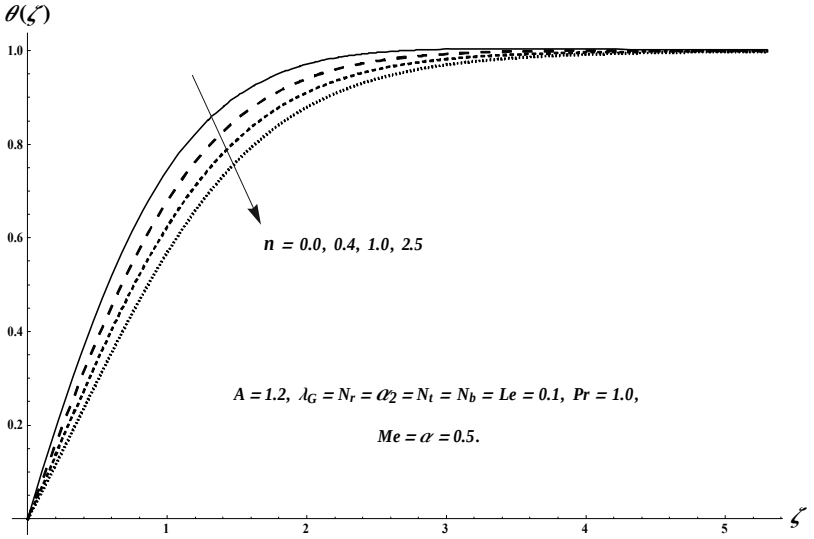

Fig. 4.12. Plots of $\theta(\zeta)$ for n.

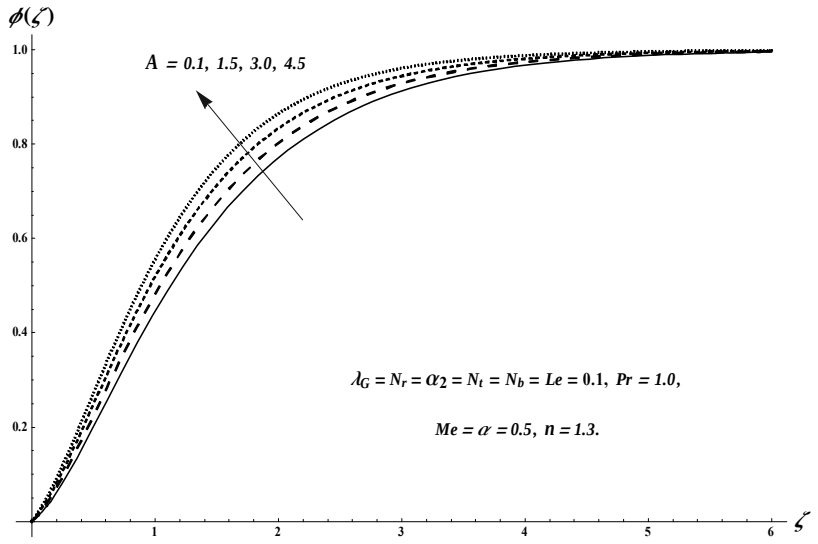

Fig. 4.13. Plots of $\phi(\zeta)$ for A.

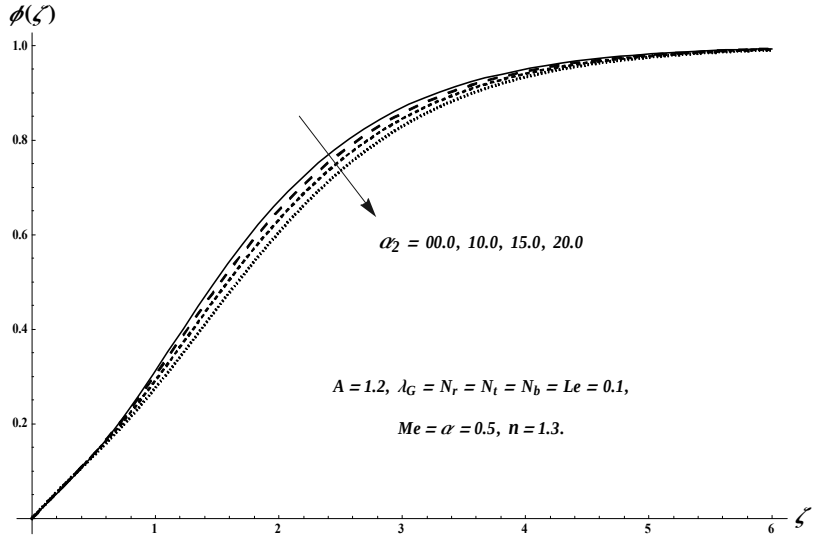

Fig. 4.14. Plots of $\phi(\zeta)$ for α_2.

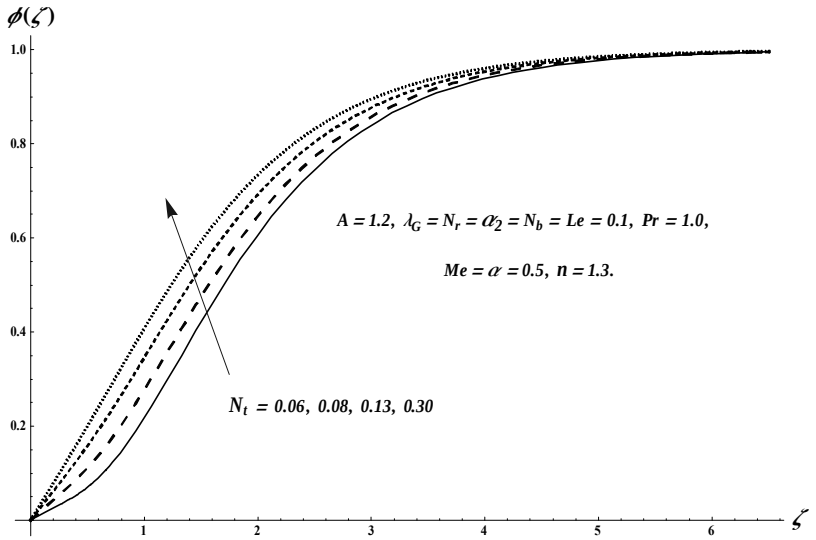

Fig. 4.15. Plots of $\phi(\zeta)$ for N_t.

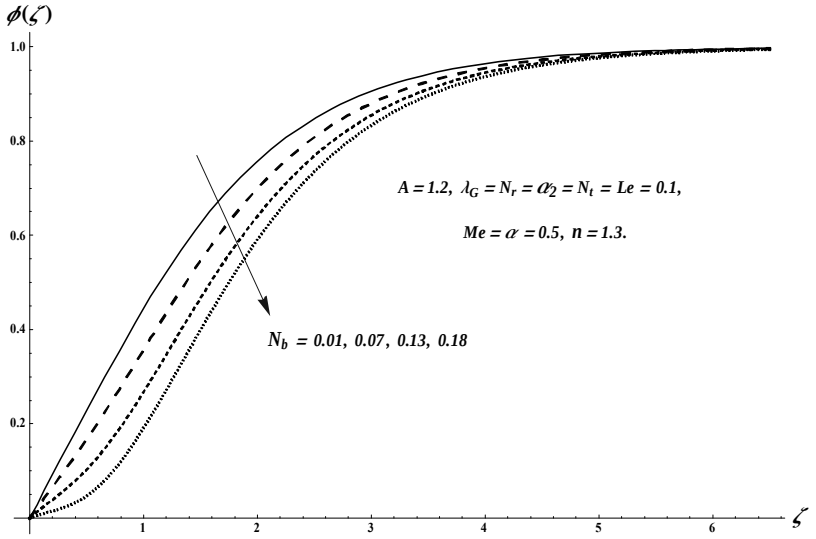

Fig. 4.16. Plots of $\phi(\zeta)$ for N_b.

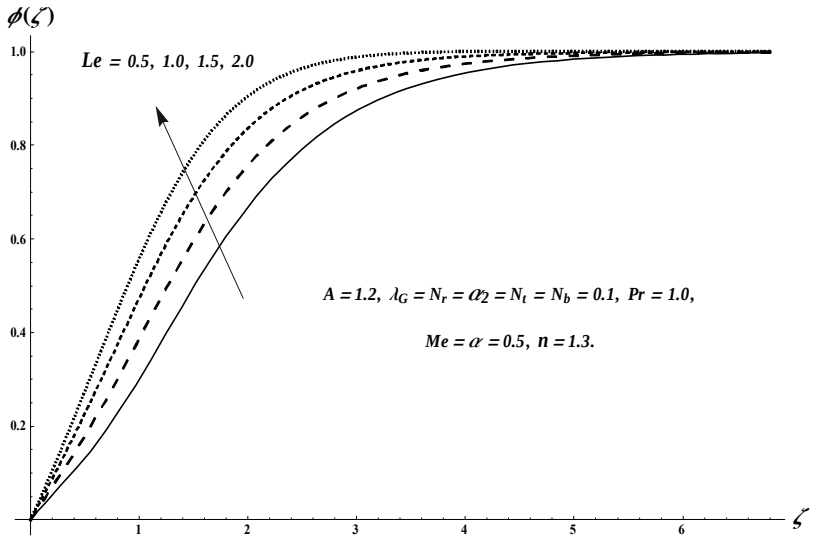

Fig. 4.17. Plots of $\phi(\zeta)$ for Le.

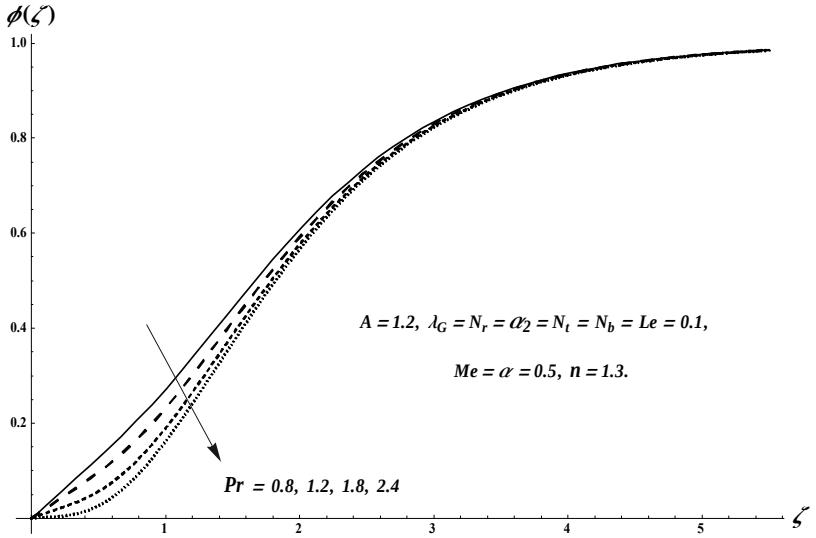

Fig. 4.18. Plots of $\phi(\zeta)$ for Pr .

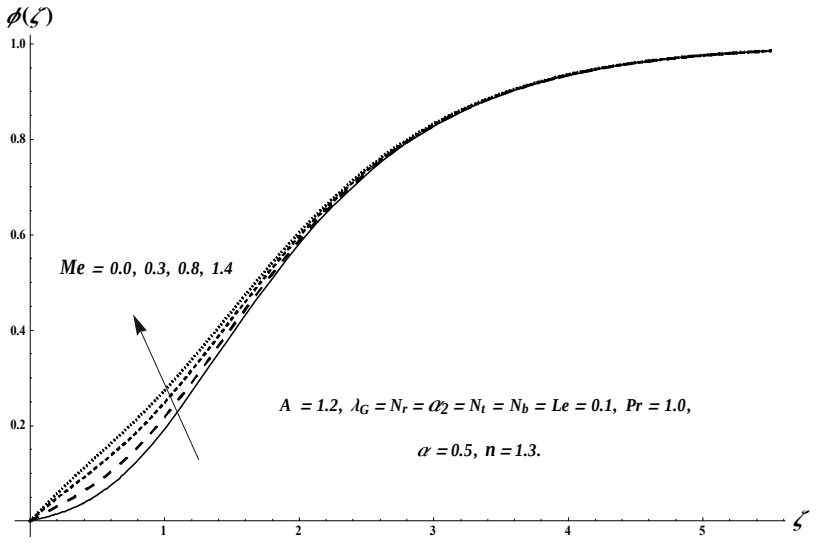

Fig. 4.19. Plots of $\phi(\zeta)$ for Me.

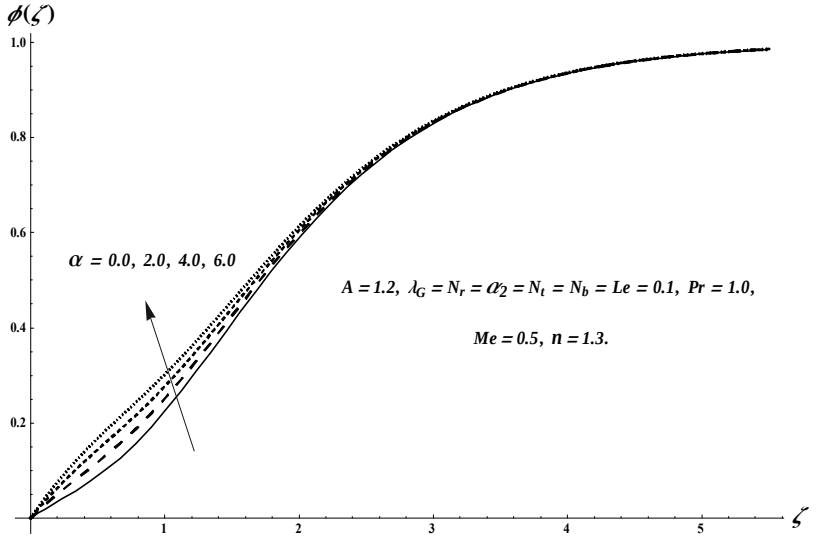

Fig. 4.20. Plots of $\phi(\zeta)$ for α.

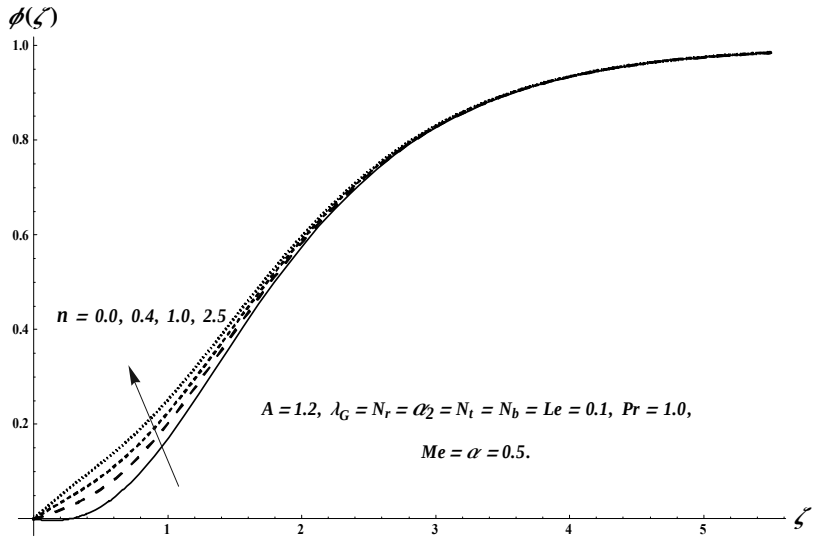

Fig. 4.21. Plots of $\phi(\zeta)$ for n.

Table 4.2. Computed values of $C_{f_{x_2}}$ when $N_b = \alpha = 0.1$, $Le = \Pr = 1.0$, $N_t = 0.01$ and $n = 0.9$.

A	λ_G	N_r	α_2	Me	$-C_{f_{x_2}}$
0.0	0.1	0.1	0.1	0.1	1.270
0.1					1.256
0.2					1.250
0.1	0.0	0.1	0.1	0.1	1.258
	0.2				1.263
	0.4				1.268
0.1	0.1	0.0	0.1	0.1	1.253
		0.3			1.255
		0.6			1.261
0.1	0.1	0.1	0.0	0.1	0.916
			0.1		1.257
			0.2		1.621
0.1	0.1	0.1	0.1	0.0	1.311
				0.2	1.214
				0.4	1.141

Table 4.3. Numerical data for local Nusselt and Sherwood numbers through pertinent parameters when $\alpha = 0.1$ and $n = 0.9$.

A	λ_G	N_r	α_2	N_t	N_b	Le	Pr	Me	$-Nu_{x_2}$	$-Sh_{x_2}$
0.0	0.1	0.1	0.1	0.01	0.1	1.0	1.0	0.1	0.555	0.491
0.1									0.568	0.509
0.2									0.573	0.513
0.1	0.0	0.1	0.1	0.01	0.1	1.0	1.0	0.1	0.563	0.504
	0.2								0.566	0.505
	0.4								0.569	0.506
0.1	0.1	0.0	0.1	0.01	0.1	1.0	1.0	0.1	0.568	0.512
		0.3							0.566	0.510
		0.6							0.565	0.505
0.1	0.1	0.1	0.0	0.01	0.1	1.0	1.0	0.1	0.583	0.522
			0.1						0.568	0.510
			0.2						0.550	0.493
0.1	0.1	0.1	0.1	0.0	0.1	1.0	1.0	0.1	0.563	0.537
				0.1					0.580	0.220
				0.2					0.583	0.011
0.1	0.1	0.1	0.1	0.01	0.1	1.0	1.0	0.1	0.580	0.224
					0.3				0.644	0.407
					0.5				0.711	0.441
0.1	0.1	0.1	0.1	0.01	0.1	0.0	1.0	0.1	0.566	0.266
						0.5			0.565	0.380
						1.0			0.564	0.506
0.1	0.1	0.1	0.1	0.01	0.1	1.0	0.9	0.1	0.532	0.509
							1.0		0.565	0.506
							1.1		0.598	0.504
0.1	0.1	0.1	0.1	0.01	0.1	1.0	1.0	0.0	0.598	0.535
								0.2	0.535	0.482
								0.4	0.489	0.443

4.4 Conclusions

Melting heat and mixed convection in stagnation point second grade nanofluid flow towards a nonlinear stretchable surface of variable surface thickness are investigated. Main results are:

- An increment in both Grashof number λ_G and buoyancy ratio parameter N_r elucidate a decreasing behavior for temperature field while dual behavior is noticed for concentration field.
- Increasing trend is noticed for both temperature and concentration distributions for larger N_t while opposite trend is seen for Brownian motion parameter N_b.
- Larger values of shape parameter n illustrates opposite trend for temperature and concentration fields.
- Melting parameter Me indicates decreasing trend for temperature distribution while opposite trend is noticed for concentration field.
- The skin friction coefficient is higher for λ_G, N_r and α_2 while the reverse trend is seen for A and Me.
- Local Nusselt number reduces for larger buoyancy ratio parameter N_r, second grade parameter α_2, Lewis number Le and melting parameter Me whereas opposite trend is observed for ratio parameter A, Grashof number λ_G, thermophoresis parameter N_t, Brownian motion parameter N_b and Prandtl number Pr .
- Local Sherwood number is higher for A, λ_G, N_b and Le while the reverse trend is noticed for N_r, α_2, N_t, Pr and Me.

Chapter 5

Numerical study for Darcy-Forchheimer flow due to a curved stretching surface with homogeneous-heterogeneous reactions and Cattaneo-Christov heat flux

The current chapter investigates Darcy-Forchheimer flow generated by curved stretchable surface. Flow for porous space is illustrated by Darcy-Forchheimer relation. Concept of homogeneous and heterogeneous reactions is also utilized. Heat transfer for Cattaneo–Christov theory characterizing the feature of thermal relaxation is incorporated. Nonlinear differential systems are derived. Shooting algorithm is employed to construct the solutions for the resulting nonlinear system. The characteristics of various sundry parameters are studied and discussed. Numerical data of skin friction and local Nusselt number is prepared.

5.1 Formulation

Two-dimensional (2D) flow by a curved stretchable sheet (coiled in a circle having radius R with linear stretching velocity $u = u_w$) is addressed. The distance R of curved stretchable surface from the origin determines the shape of curved surface (see Fig. 5.1). Flow in porous medium is characterized by Darcy-Forchheimer relation. Moreover heat transfer via Cattaneo–Christov theory characterizing the feature of thermal relaxation is examined. Further homogeneous and heterogeneous reactions with two chemical species A_1 and B_1 respectively are also taken into account. For cubic autocatalysis, the homogenous reaction is

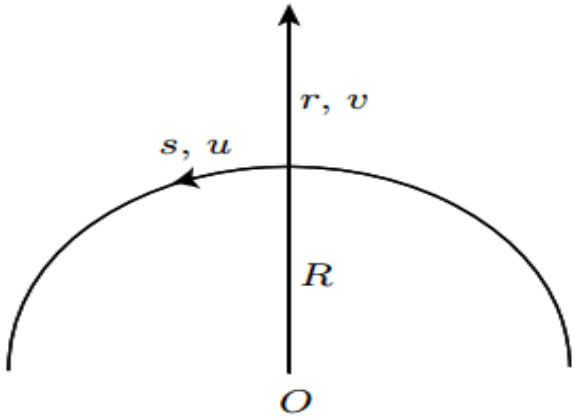

Fig. 5.1. Physical model.

$$A_1 + 2B_1 \rightarrow 3B_1, \qquad \text{rate} = k_c a b^2, \tag{5.1}$$

whereas heterogeneous reaction on catalyst surface is

$$A_1 \rightarrow B_1, \qquad \text{rate} = k_s a, \tag{5.2}$$

in which a and b are the concentrations of chemical species A_1 and B_1 respectively and rate constants are defined by k_c and k_s. Equations governing the flow are

$$\frac{\partial}{\partial r}\left((r+R)\,v\right) + R\frac{\partial u}{\partial s} = 0, \tag{5.3}$$

$$\frac{1}{r+R}u^2 = \frac{1}{\rho_f}\frac{\partial p}{\partial r}, \tag{5.4}$$

$$
\begin{aligned}
v\frac{\partial u}{\partial r}+\frac{R}{r+R}u\frac{\partial u}{\partial s}+\frac{1}{r+R}uv &= -\frac{1}{\rho_f}\frac{R}{r+R}\frac{\partial p}{\partial s} \\
&\quad +\nu\left(\frac{\partial^2 u}{\partial r^2}+\frac{1}{r+R}\frac{\partial u}{\partial r}-\frac{1}{(r+R)^2}u\right) \\
&\quad -Fu^2-\frac{\upsilon}{K_p}u, \qquad (5.5)
\end{aligned}
$$

$$
\rho_f c_p\left(v\frac{\partial T}{\partial r}+\frac{R}{r+R}u\frac{\partial T}{\partial s}\right)=-\nabla.\mathbf{q}, \qquad (5.6)
$$

$$
v\frac{\partial a}{\partial r}+\frac{R}{r+R}u\frac{\partial a}{\partial s}=D_{A_1}\left(\frac{\partial^2 a}{\partial r^2}+\frac{1}{r+R}\frac{\partial a}{\partial r}\right)-k_c ab^2, \qquad (5.7)
$$

$$
v\frac{\partial b}{\partial r}+\frac{R}{r+R}u\frac{\partial b}{\partial s}=D_{B_1}\left(\frac{\partial^2 b}{\partial r^2}+\frac{1}{r+R}\frac{\partial b}{\partial r}\right)+k_c ab^2, \qquad (5.8)
$$

with the boundary conditions

$$
u=u_w(s)=a_1 s,\ v=0,\ T=T_w,\ D_{A_1}\frac{\partial a}{\partial r}=k_s a,\ D_{B_1}\frac{\partial b}{\partial r}=-k_s a \text{ at } r=0, \qquad (5.9)
$$

$$
u\to 0,\ \ \frac{\partial u}{\partial r}\to 0,\ \ T\to T_\infty,\ \ a\to a_0,\ \ b\to 0 \text{ as } \ r\to\infty. \qquad (5.10)
$$

Here $F\left(=\frac{C_b}{s\sqrt{K_1}}\right)$ the porous medium variable inertia coefficient, C_b the drag coefficient, K_p the permeability of porous medium, D_{A_1} and D_{B_1} the diffusion coefficients of chemical species A_1 and B_1 respectively, $a_0>0$ the dimensional constant and $\mathbf{q}$ the heat flux whose mathematical expression as per Cattaneo-Christov theory is

$$
\mathbf{q}+\lambda_t\left(\mathbf{V}.\nabla\mathbf{q}-\mathbf{q}.\nabla\mathbf{V}+(\nabla.\mathbf{V})\,\mathbf{q}\right)=-k_f\nabla T, \qquad (5.11)
$$

where λ_t the relaxation time of heat flux. By considering incompressible fluid $(\nabla.\mathbf{V}=0)$, Eq. (5.11) yields

$$
\mathbf{q}+\lambda_t\left(\mathbf{V}.\nabla\mathbf{q}-\mathbf{q}.\nabla\mathbf{V}\right)=-k_f\nabla T. \qquad (5.12)
$$

Then the temperature equation becomes

$$\begin{aligned} v\frac{\partial T}{\partial r}+\frac{R}{r+R}u\frac{\partial T}{\partial s} &= \frac{k_f}{\rho_f c_p}\left(\frac{\partial^2 T}{\partial r^2}+\frac{1}{r+R}\frac{\partial T}{\partial r}+\left(\frac{R}{r+R}\right)^2\frac{\partial^2 T}{\partial s^2}\right) \\ &\quad -\lambda_t\left(\begin{array}{c} v^2\frac{\partial^2 T}{\partial r^2}+u^2\left(\frac{R}{r+R}\right)^2\frac{\partial^2 T}{\partial s^2} \\ +\left(v\frac{\partial v}{\partial r}+\frac{R}{r+R}u\frac{\partial v}{\partial s}\right)\frac{\partial T}{\partial r} \\ +\left(\frac{R}{r+R}v\frac{\partial u}{\partial s}+u\left(\frac{R}{r+R}\right)^2\frac{\partial u}{\partial s}\right)\frac{\partial T}{\partial s}+2\frac{R}{r+R}uv\frac{\partial^2 T}{\partial r\partial s} \end{array}\right). \end{aligned} \tag{5.13}$$

Moreover for the case of curved surface, pressure is no longer consistent within the boundary layer. Using the following transformations

$$\left.\begin{array}{c} u=a_1 s f'(\zeta), \quad v=-\frac{R}{r+R}\sqrt{a_1 \upsilon}f(\zeta), \quad \zeta=\sqrt{\frac{a_1}{\upsilon}}r, \\ p=\rho_f a_1^2 s^2 P(\zeta), \quad k=\sqrt{\frac{a_1}{\upsilon}}R, \quad \theta(\zeta)=\frac{T-T_\infty}{T_w-T_\infty}, \quad a=a_0\phi(\zeta), \quad b=a_0 h(\zeta), \end{array}\right\} \tag{5.14}$$

Eq. (5.3) is symmetrically verified and Eqs. (5.4) – (5.13) yield

$$\frac{\partial P}{\partial \zeta}=\frac{f'^2}{\zeta+k}, \tag{5.15}$$

$$\frac{2k}{\zeta+k}P=f'''+\frac{1}{\zeta+k}f''-\frac{1}{(\zeta+k)^2}f'+\frac{k}{\zeta+k}ff''-\frac{k}{\zeta+k}f'^2+\frac{k}{(\zeta+k)^2}ff'-F_r f'^2-\lambda f', \tag{5.16}$$

$$\frac{1}{\mathrm{Pr}}\left(\theta''+\frac{\theta'}{\zeta+k}\right)-\gamma\left(\frac{k^2}{(\zeta+k)^2}\left(f^2\theta''+ff'\theta'\right)-k^2f^2\theta'\right)+\frac{k}{\zeta+k}f\theta'=0, \tag{5.17}$$

$$\frac{1}{Sc}\left(\phi''+\frac{\phi'}{\zeta+k}\right)+\frac{k}{\zeta+k}f\phi'-k_1\phi h^2=0, \tag{5.18}$$

$$\frac{\delta}{Sc}\left(h''+\frac{h'}{\zeta+k}\right)+\frac{k}{\zeta+k}fh'+k_1\phi h^2=0, \tag{5.19}$$

$$\left.\begin{array}{c} f=0, \quad f'=1, \quad \theta=1, \quad \phi'=k_2\phi, \quad \delta_1 h'=-k_2\phi \quad \text{at} \quad \zeta=0, \\ f'\to 0, \quad f''\to 0, \quad \theta\to 0, \quad \phi\to 1, \quad h\to 0 \quad \text{as} \quad \zeta\to\infty, \end{array}\right\} \tag{5.20}$$

where k stands for dimensionless curvature parameter, F_r for inertia coefficient, λ for porosity parameter, γ for dimensionless thermal relaxation parameter, Sc for Schmidt number, k_1 for intensity of homogeneous reaction, k_2 for intensity of heterogeneous reaction and δ_1 for ratio of

diffusion coefficients. These parameters can be expressed as follows:

$$\left.\begin{array}{c} k = R\sqrt{\frac{a_1}{v}},\ \lambda = \frac{v}{K_p a_1},\ F_r = \frac{C_b}{\sqrt{K_p}},\ \gamma = a_1\lambda_t, \\ Sc = \frac{v}{D_{A_1}},\ k_1 = \frac{a_0^2 k_c}{a_1},\ k_2 = \frac{k_s}{D_{A_1}}\sqrt{\frac{v}{a_1}},\ \delta_1 = \frac{D_{B_1}}{D_{A_1}}. \end{array}\right\} \tag{5.21}$$

Now eliminating pressure P from Eqs. (5.15) and (5.16), we get

$$f^{iv} + \frac{2f'''}{\zeta+k} - \frac{f''}{(\zeta+k)^2} + \frac{f'}{(\zeta+k)^3} + \frac{k}{(\zeta+k)}\left(ff''' - f'f''\right) + \frac{k}{(\zeta+k)^2}\left(ff'' - f'^2\right)$$

$$-\frac{k}{(\zeta+k)^3}ff' - F_r\left(2f'f'' + \frac{f'^2}{\zeta+k}\right) - \lambda\left(f'' + \frac{f'}{\zeta+k}\right) = 0. \tag{5.22}$$

Pressure P can be calculated from Eq. (5.16) as

$$P = \frac{\zeta+k}{2k}\left(\begin{array}{c} f''' + \frac{1}{\zeta+k}f'' - \frac{1}{(\zeta+k)^2}f' + \frac{k}{\zeta+k}ff'' \\ -\frac{k}{\zeta+k}f'^2 + \frac{k}{(\zeta+k)^2}ff' - F_r f'^2 - \lambda f' \end{array}\right). \tag{5.23}$$

When $D_{A_1} = D_{B_1}$ then $\delta_1 = 1$ and thus

$$\phi(\zeta) + h(\zeta) = 1. \tag{5.24}$$

Now Eqs. (5.18) and (5.19) yield

$$\frac{1}{Sc}\left(\phi'' + \frac{\phi'}{\zeta+k}\right) + \frac{k}{\zeta+k}f\phi' - k_1\phi(1-\phi)^2 = 0, \tag{5.25}$$

with the boundary conditions

$$\phi'(0) = k_2\phi(0), \quad \phi(\infty) \to 1. \tag{5.26}$$

Definitions of $C_{f_{s_1}}$ and Nu_s are

$$C_{f_{s_1}} = \frac{\tau_{rs_1}}{\rho_f u_w^2}, \qquad Nu_s = \frac{sq_{w_r}}{k_f(T_w - T_\infty)}, \tag{5.27}$$

in which (τ_{rs_1}) stands for wall shear stress and (q_{w_r}) for wall heat flux which are given by

$$\left.\begin{aligned} \tau_{rs_1} &= \mu\left(\frac{\partial u}{\partial r}-\frac{u}{r+R}\right)\Big|_{r=0}, \\ q_{w_r} &= -k_f\left(\frac{\partial T}{\partial r}\right)\Big|_{r=0}. \end{aligned}\right\} \tag{5.28}$$

In non-dimensional coordinates

$$\left.\begin{aligned} C_{fs_1}Re_{s_1}^{1/2} &= f''(0)-\tfrac{1}{k}f'(0), \\ Nu_sRe_{s_1}^{-1/2} &= -\theta'(0), \end{aligned}\right\} \tag{5.29}$$

where $\mathrm{Re}_{s_1}=\frac{a_1s^2}{\upsilon}$ stands for local Reynolds number.

5.2 Discussion

The system of Eqs. (5.17), (5.22) and (5.25) subject to (5.20) and (5.26) are computed numerically by shooting method. Main interest here is to examine the velocity $f'(\zeta)$, temperature $\theta(\zeta)$ and concentration $\phi(\zeta)$ profiles for several influential variables like dimensionless radius of curvature parameter k, inertia coefficient F_r, porosity parameter λ, Prandtl number Pr, thermal relaxation parameter γ, Schmidt number Sc and strength of homogeneous reaction k_1. Effects of curvature parameter k, inertia coefficient F_r and porosity parameter λ on dimensionless velocity distribution $f'(\zeta)$ are presented in the Figs. $5.2-5.4$ respectively. Fig. 5.2 elucidates the impact of dimensionless radius of curvature k on velocity distribution $f'(\zeta)$. Both velocity and momentum layer thickness are higher when curvature parameter k is increased. Variation of inertia coefficient F_r on velocity $f'(\zeta)$ is displayed in Fig. 5.3. Larger inertia coefficient F_r shows a decay in velocity $f'(\zeta)$ and momentum layer thickness. Fig. 5.4 elaborates the influence of porosity parameter λ on velocity $f'(\zeta)$. Larger porosity parameter λ shows a reduction in velocity field $f'(\zeta)$ and related layer thickness. Impacts of curvature parameter k, inertia coefficient F_r, porosity parameter λ, Prandtl number Pr and thermal relaxation parameter γ on dimensionless temperature profile $\theta(\zeta)$ are displayed in the Figs. $5.5-5.9$ respectively. Fig. 5.5 elucidates the variation of dimensionless radius of curvature parameter k on temperature profile $\theta(\zeta)$. Both temperature $\theta(\zeta)$ and thermal layer thickness are increased for larger curvature k. Fig. 5.6 elaborates the influence of inertia coefficient F_r on temperature $\theta(\zeta)$. Larger inertia

coefficient F_r shows an increment in temperature $\theta(\zeta)$ and related layer thickness. Outcome of porosity parameter λ on temperature $\theta(\zeta)$ is displayed in Fig. 5.7. Larger porosity parameter λ shows more temperature $\theta(\zeta)$ and thermal layer thickness. Existence of porous media opposes the fluid flow which ultimately enhances temperature $\theta(\zeta)$ and corresponding layer thickness. Fig. 5.8 depicts the effect of Prandtl number Pr on temperature profile $\theta(\zeta)$. Clearly both temperature and thermal layer thickness are lower for larger Pr. Fig. 5.9 shows the variation of thermal relaxation parameter γ on temperature $\theta(\zeta)$. Larger thermal relaxation parameter γ shows a reduction in temperature field and related layer thickness. Contributions of dimensionless radius of curvature parameter k, inertia coefficient F_r, porosity parameter λ, Schmidt number Sc and strength of homogeneous reaction k_1 on dimensionless concentration profile $\phi(\zeta)$ are presented in the Figs. $5.10 - 5.14$ respectively. Fig. 5.10 elucidates the impact of dimensionless radius of curvature parameter k on concentration $\phi(\zeta)$. It is noted that concentration $\phi(\zeta)$ is reduced via k. Variation in $\phi(\zeta)$ for different inertia coefficient F_r is illustrated in Fig. 5.11. Larger values of F_r correspond to higher concentration $\phi(\zeta)$. Effects of porosity parameter λ on concentration $\phi(\zeta)$ is displayed in Fig. 5.12. Larger porosity parameter λ causes an enhancement in concentration $\phi(\zeta)$. Fig. 5.13 shows the impact of Schmidt number Sc on concentration $\phi(\zeta)$. Larger Schmidt number Sc shows an enhancement in concentration $\phi(\zeta)$. Impact of k_1 on concentration $\phi(\zeta)$ is shown in Fig. 5.14. Concentration $\phi(\zeta)$ is reduced for higher strength of homogeneous reaction k_1. Table 5.1 elucidates the numerical data of skin friction coefficient for numerous values of curvature parameter k, inertia coefficient F_r and porosity parameter λ. It is examined that skin friction coefficient is enhanced for larger F_r and λ while reverse trend is noticed for k. Table 5.2 is displayed to analyze the numerical data of local Nusselt number for curvature parameter k, inertia coefficient F_r, porosity parameter λ, Prandtl number Pr and thermal relaxation variable γ. Clearly local Nusselt number is increased for higher Prandtl number Pr and thermal relaxation γ whereas the opposite trend is seen via

curvature parameter k, inertia coefficient F_r and porosity parameter λ.

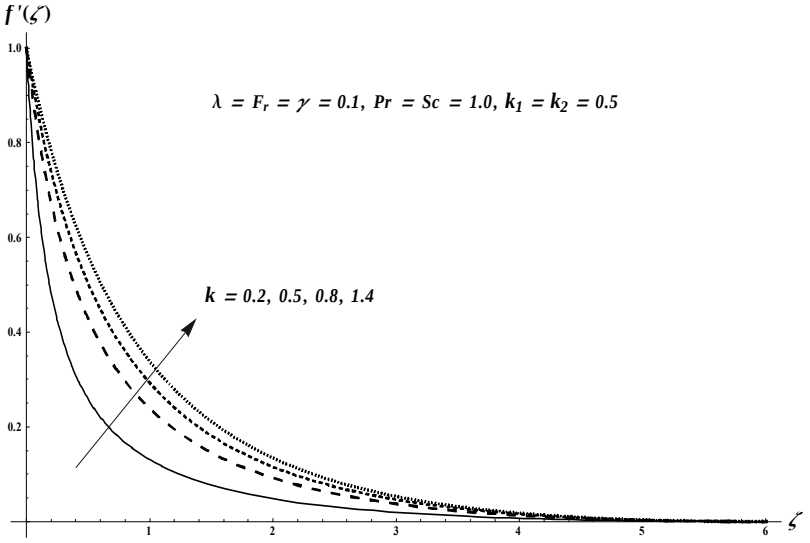

Fig. 5.2. Plots of $f'(\zeta)$ for k.

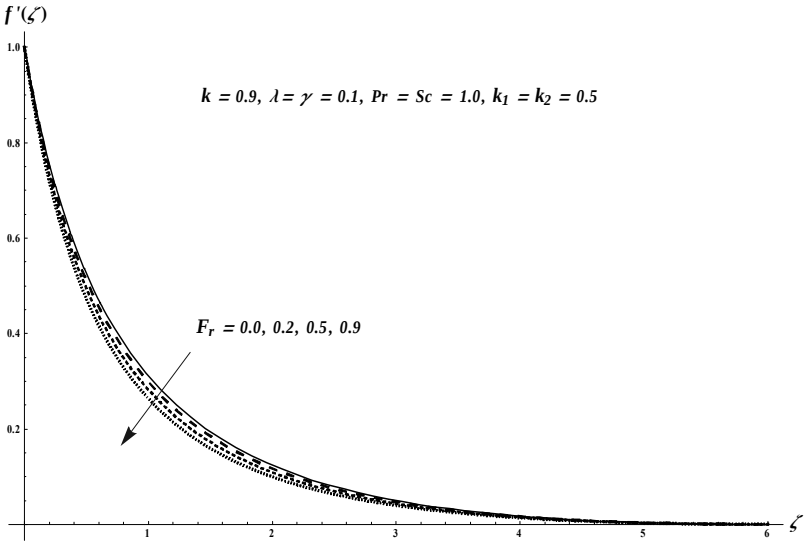

Fig. 5.3. Plots of $f'(\zeta)$ for F_r.

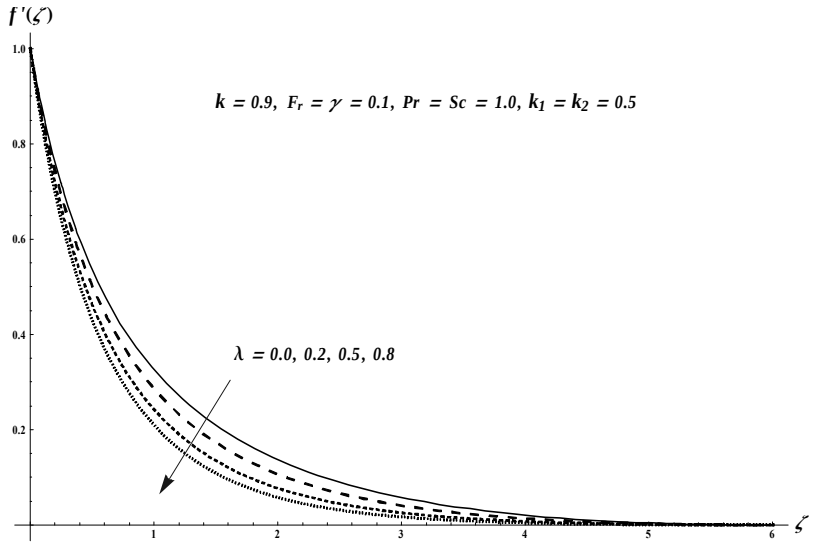

Fig. 5.4. Plots of $f'(\zeta)$ for λ.

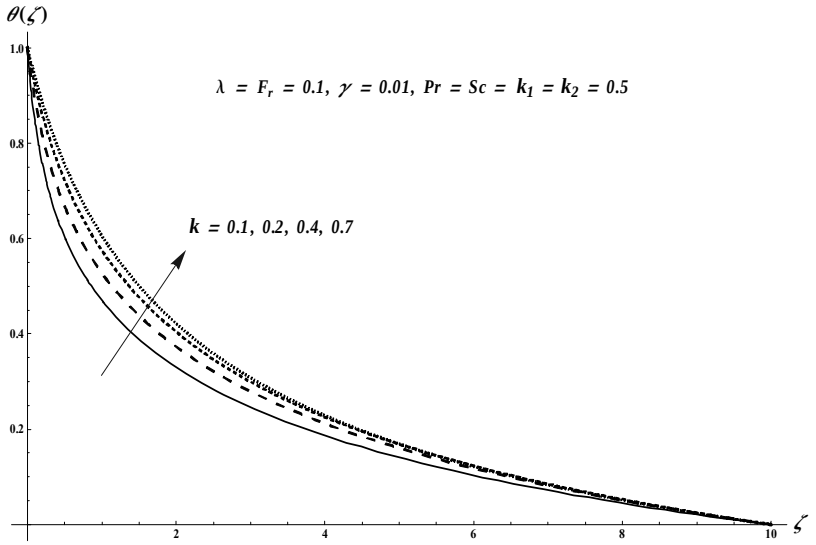

Fig. 5.5. Plots of $\theta(\zeta)$ for k.

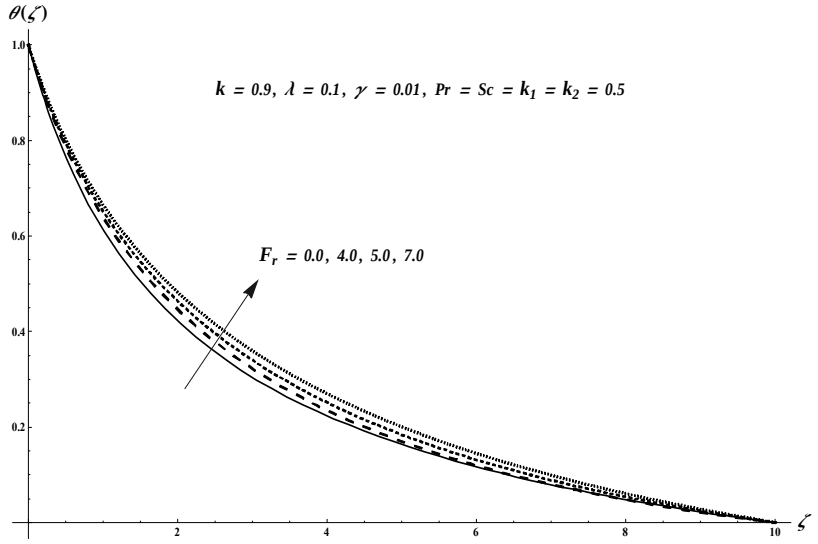

Fig. 5.6. Plots of $\theta(\zeta)$ for F_r.

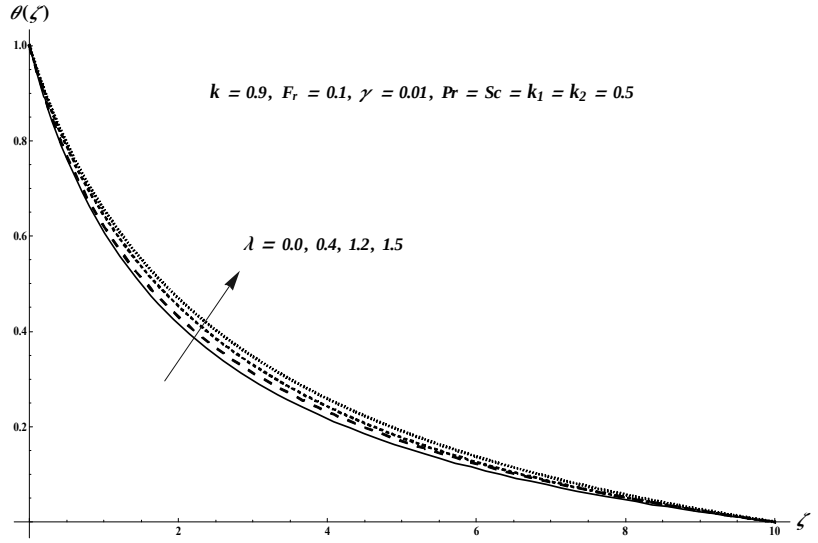

Fig. 5.7. Plots of $\theta(\zeta)$ for λ.

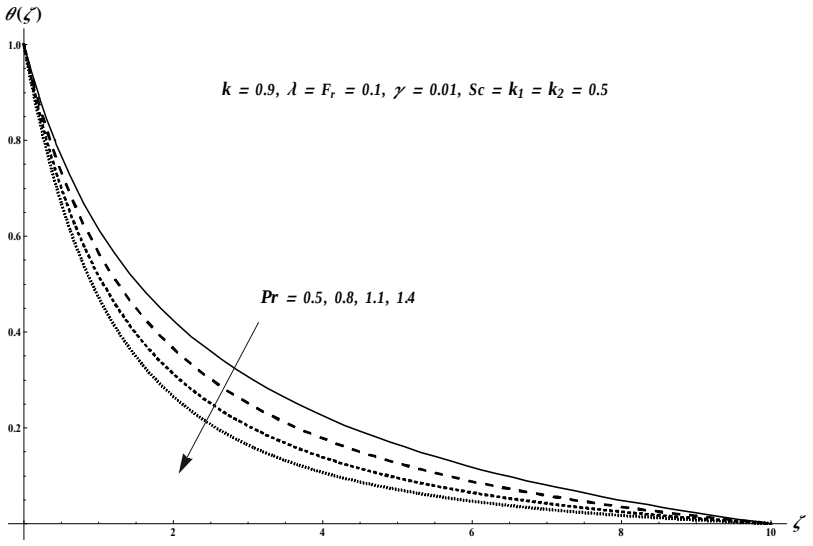

Fig. 5.8. Plots of $\theta(\zeta)$ for Pr.

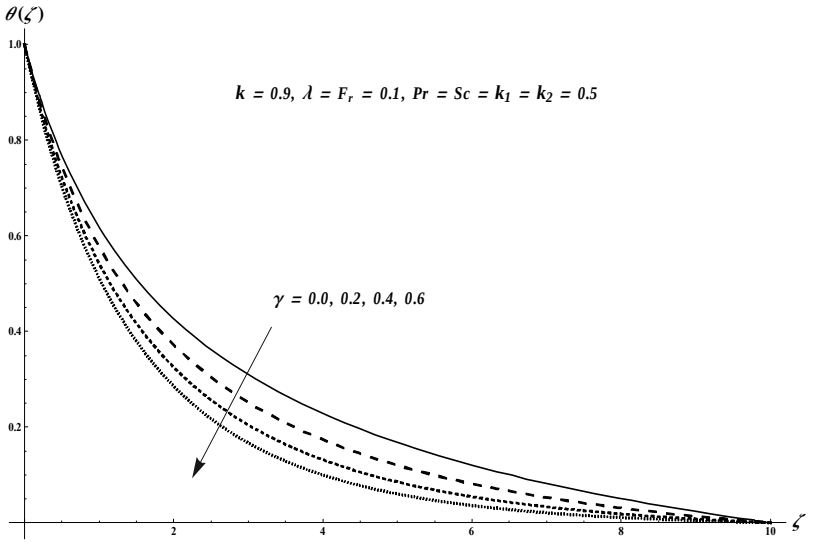

Fig. 5.9. Plots of $\theta(\zeta)$ for γ.

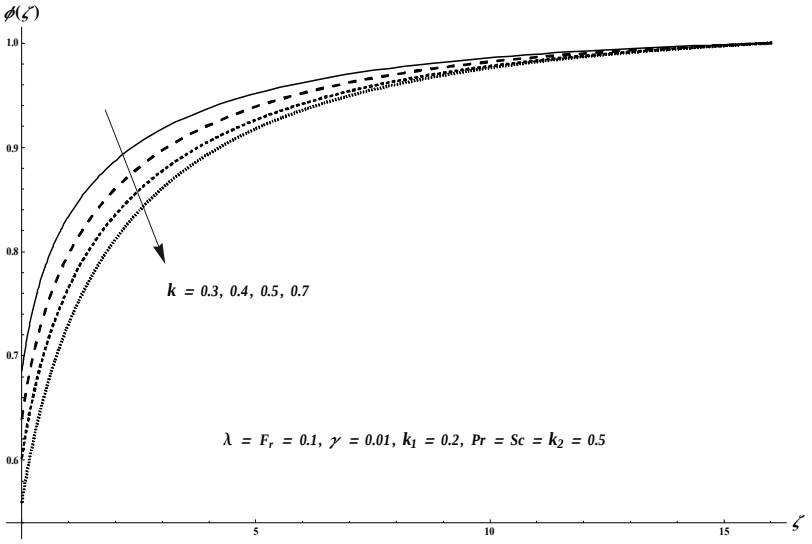

Fig. 5.10. Plots of $\phi(\zeta)$ for k.

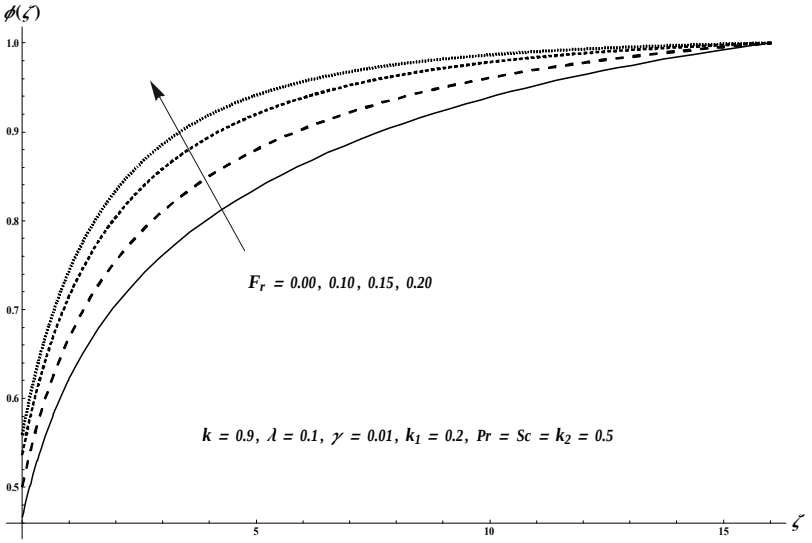

Fig. 5.11. Plots of $\phi(\zeta)$ for F_r.

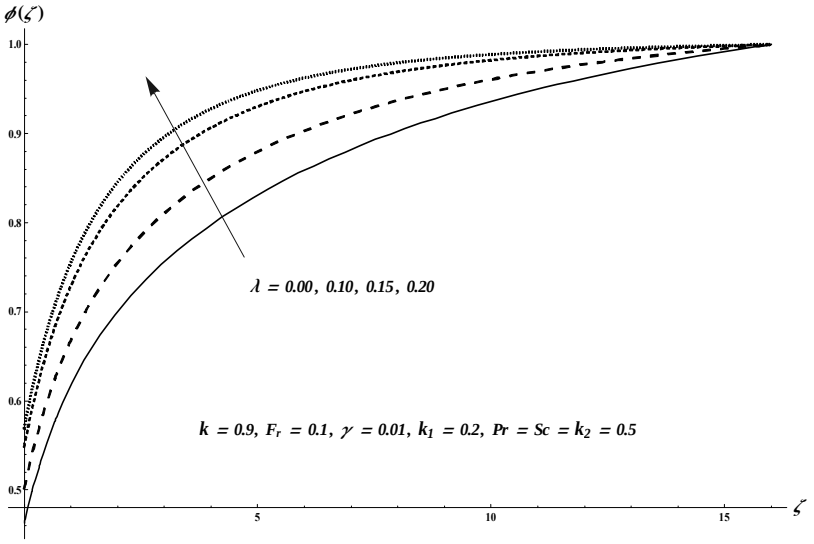

Fig. 5.12. Plots of $\phi(\zeta)$ for λ.

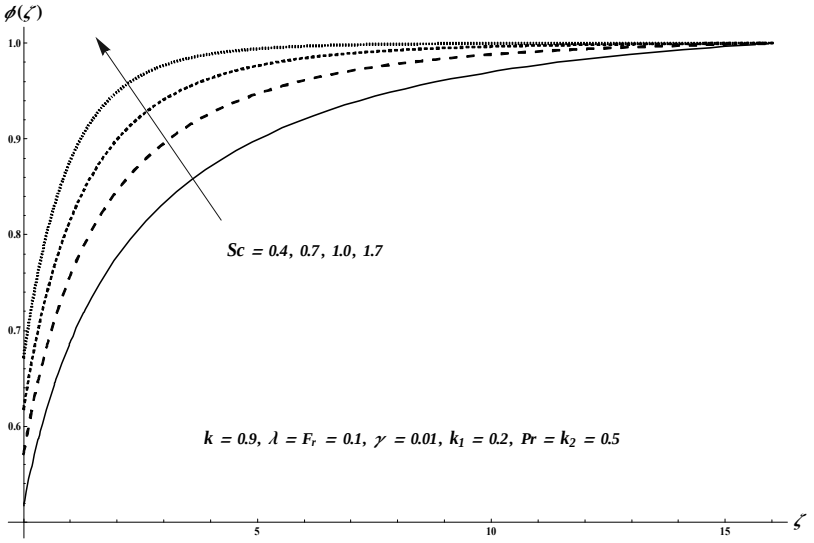

Fig. 5.13. Plots of $\phi(\zeta)$ for Sc.

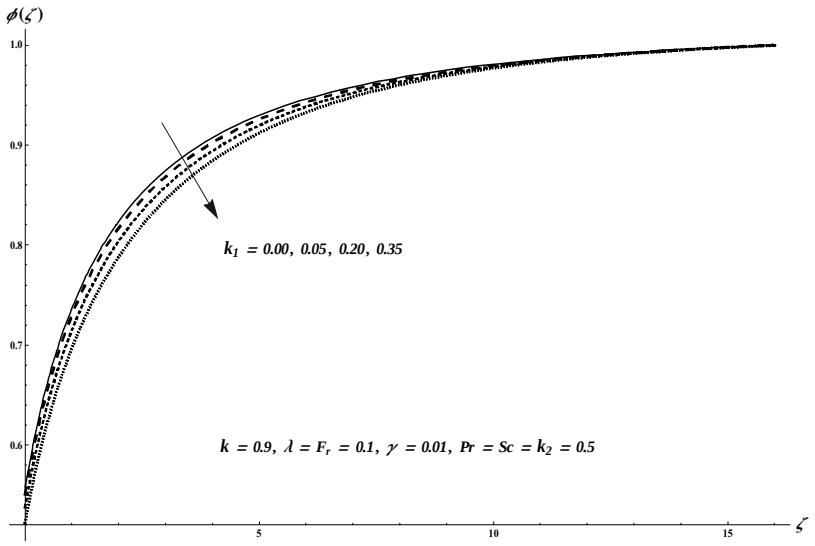

Fig. 5.14. Plots of $\phi(\zeta)$ for k_1.

Table 5.1. Numerical data of skin friction coefficient for varying values of k, F_r and λ.

k	F_r	λ	$-C_{fs_1}Re_{s_1}^{1/2}$
0.7	0.1	0.1	3.20889
0.8			2.88705
0.9			2.64211
0.9	0.0	0.1	2.60608
	0.1		2.64211
	0.2		2.67674
0.9	0.1	0.0	2.57554
		0.1	2.64211
		0.2	2.70364

Table 5.2. Numerical data of local Nusselt number for varying k, F_r, λ, Pr and β when $Sc = k_1 = k_2 = 0.5$.

k	F_r	λ	Pr	γ	$-Nu_s Re_{s_1}^{-1/2}$
0.7	0.1	0.1	0.5	0.01	0.654355
0.9					0.592607
1.1					0.553641
0.9	0.0	0.1	0.5	0.01	0.595138
	0.2				0.590294
	0.4				0.586189
0.9	0.1	0.0	0.5	0.01	0.603132
		0.2			0.584795
		0.4			0.579865
0.9	0.1	0.1	0.8	0.01	0.683539
			1.0		0.744031
			1.2		0.803885
0.9	0.1	0.1	1.0	0.0	0.589278
				0.1	0.621643
				0.2	0.651962

5.3 Conclusions

Darcy-Forchheimer flow by a curved stretching surface with homogeneous and heterogeneous reactions and Cattaneo-Christov heat flux is addressed. Main observations of presented research are listed below.

- Velocity $f'(\zeta)$ is enhanced for curvature parameter k whereas reverse trend is noticed for porosity parameter λ and inertia coefficient F_r.
- Larger curvature parameter k, inertia coefficient F_r and porosity parameter λ produce higher temperature field $\theta(\zeta)$ while reverse trend is seen for Prandtl number Pr and thermal relaxation parameter γ.
- Concentration field $\phi(\zeta)$ is higher for larger inertia coefficient F_r, porosity parameter λ and Schmidt number Sc. However opposite behavior of $\phi(\zeta)$ is found for curvature parameter k and strength of homogeneous reaction k_1.
- Skin friction coefficient is enhanced for larger F_r and λ while reverse trend is noticed for k.
- Local Nusselt number is enhanced for larger Prandtl number Pr and thermal relaxation parameter γ whereas opposite trend is seen via curvature parameter k, inertia coefficient F_r and porosity parameter λ.

Chapter 6

Numerical study for Darcy-Forchheimer nanofluid flow due to curved stretchable sheet with convective heat and mass conditions

This chapter addresses Darcy-Forchheimer flow of viscous nanofluid. Flow induced by a curved stretchable sheet. Flow for porous space is illustrated by Darcy-Forchheimer relation. Attributes of Brownian diffusion and thermophoresis are incorporated. Convective conditions are employed at the curved stretchable sheet. Boundary layer assumption is employed in the mathematical development. The system of ordinary differential equations is developed by mean of suitable variables. Shooting algorithm is employed to construct the numerical solutions of resulting nonlinear systems. The characteristics of various sundry parameters are examined and discussed. Physical quantities of interest are examined.

6.1 Formulation

Ongoing consideration is the steady viscous nanofluid flow by a curved stretchable sheet. The curved stretchable sheet is coiled in a circle having radius R with linear stretching velocity $u =$

u_w. The s and $r-$ directions are perpendicular to each other. The distance R of the stretchable curved sheet from the origin determines the shape of the curved surface, i.e., for higher value of $R\,(\to\infty)$ the surface tends to flat. Flow for porous space is illustrated by Darcy-Forchheimer relation. Influences of Brownian diffusion and thermophoresis are incorporated. Moreover convective mass and heat boundary conditions are also employed at the curved stretchable surface. Surface is heated through the hot fluid having temperature T_f and concentration C_f that give heat and mass transfer coefficients h_f and k_m respectively. The governing boundary-layer expressions are

$$\frac{\partial}{\partial r}\left(\left(r+R\right)v\right)+R\frac{\partial u}{\partial s}=0, \tag{6.1}$$

$$\frac{1}{r+R}u^2=\frac{1}{\rho_f}\frac{\partial p}{\partial r}, \tag{6.2}$$

$$\begin{aligned} v\frac{\partial u}{\partial r}+\frac{R}{r+R}u\frac{\partial u}{\partial s}+\frac{1}{r+R}uv &= -\frac{1}{\rho_f}\frac{R}{r+R}\frac{\partial p}{\partial s} \\ &\quad +\upsilon\left(\frac{\partial^2 u}{\partial r^2}+\frac{1}{r+R}\frac{\partial u}{\partial r}-\frac{1}{\left(r+R\right)^2}u\right) \\ &\quad -\frac{\upsilon}{K_p}u-Fu^2, \end{aligned} \tag{6.3}$$

$$\begin{aligned} v\frac{\partial T}{\partial r}+\frac{R}{r+R}u\frac{\partial T}{\partial s} &= \frac{k_f}{\left(\rho c\right)_f}\left(\frac{\partial^2 T}{\partial r^2}+\frac{1}{r+R}\frac{\partial T}{\partial r}\right) \\ &\quad +\tau\left(D_B\left(\frac{\partial C}{\partial r}\frac{\partial T}{\partial r}\right)+\frac{D_T}{T_\infty}\left(\frac{\partial T}{\partial r}\right)^2\right), \end{aligned} \tag{6.4}$$

$$v\frac{\partial C}{\partial r}+\frac{R}{r+R}u\frac{\partial C}{\partial s}=\frac{D_T}{T_\infty}\left(\frac{\partial^2 T}{\partial r^2}+\frac{1}{r+R}\frac{\partial T}{\partial r}\right)+D_B\left(\frac{\partial^2 C}{\partial r^2}+\frac{1}{r+R}\frac{\partial C}{\partial r}\right), \tag{6.5}$$

with the boundary conditions

$$u=u_w\left(s\right)=a_1 s,\ v=0,\ -k_f\frac{\partial T}{\partial r}=h_f\left(T_f-T\right),\ -D_B\frac{\partial C}{\partial r}=k_m\left(C_f-C\right)\ \text{at}\ r=0, \tag{6.6}$$

$$u\to 0,\ \frac{\partial u}{\partial r}\to 0,\ T\to T_\infty,\ C\to C_\infty\ \text{as}\ r\to\infty. \tag{6.7}$$

For the case of curved surface, the pressure is no longer consistent within the boundary layer. Using the following transformations

$$\left.\begin{array}{c} u = a_1 s f'(\zeta), \quad v = -\frac{R}{r+R}\sqrt{a_1 \upsilon} f(\zeta), \quad \zeta = \sqrt{\frac{a_1}{\upsilon}} r, \\ p = \rho_f a_1^2 s^2 P(\zeta), \quad \theta(\zeta) = \frac{T-T_\infty}{T_f - T_\infty}, \quad \phi(\zeta) = \frac{C-C_\infty}{C_f - C_\infty}, \end{array}\right\} \tag{6.8}$$

Eq. (6.1) is symmetrically verified and Eqs. (6.2) – (6.7) give

$$\frac{\partial P}{\partial \zeta} = \frac{f'^2}{\zeta + k}, \tag{6.9}$$

$$\frac{2k}{\zeta+k}P = f''' + \frac{1}{\zeta+k}f'' - \frac{1}{(\zeta+k)^2}f' + \frac{k}{\zeta+k}ff'' - \frac{k}{\zeta+k}f'^2 + \frac{k}{(\zeta+k)^2}ff' - \lambda f' - F_r f'^2, \tag{6.10}$$

$$\theta'' + \frac{\theta'}{\zeta+k} + \Pr\left(\frac{k}{\zeta+k}f\theta' + N_t\theta'^2 + N_b\theta'\phi'\right) = 0, \tag{6.11}$$

$$\phi'' + \frac{1}{\zeta+k}\phi' + \frac{k}{\zeta+k}Scf\phi' + \frac{N_t}{N_b}\left(\theta'' + \frac{1}{\zeta+k}\theta'\right) = 0, \tag{6.12}$$

$$\left.\begin{array}{c} f = 0, \quad f' = 1, \quad \theta' = -\gamma_t(1-\theta), \quad \phi' = -\gamma_c(1-\phi) \quad \text{at} \quad \zeta = 0, \\ f' \to 0, \quad f'' \to 0, \quad \theta \to 0, \quad \phi \to 0, \quad \text{as} \quad \zeta \to \infty. \end{array}\right\} \tag{6.13}$$

Here N_t thermophoresis parameter, N_b Brownian motion parameter, γ_t the thermal Biot number and γ_c the concentration Biot number. These dimensionless parameters can be expressed as follows:

$$\left.\begin{array}{c} N_t = \frac{\tau D_T\left(T_f - T_\infty\right)}{T_\infty \upsilon}, \ N_b = \frac{\tau D_B\left(C_f - C_\infty\right)}{\upsilon}, \\ \gamma_t = \frac{h_f}{k_f}\sqrt{\frac{\upsilon}{a_1}}, \ \gamma_c = \frac{k_m}{D_B}\sqrt{\frac{\upsilon}{a_1}}. \end{array}\right\} \tag{6.14}$$

Now eliminating pressure P from Eqs. (6.9) and (6.10), we get

$$f^{iv} + \frac{2f'''}{\zeta+k} - \frac{f''}{(\zeta+k)^2} + \frac{f'}{(\zeta+k)^3} + \frac{k}{(\zeta+k)}\left(ff''' - f'f''\right) + \frac{k}{(\zeta+k)^2}\left(ff'' - f'^2\right) - \frac{k}{(\zeta+k)^3}ff'$$

$$-\lambda\left(f'' + \frac{f'}{\zeta+k}\right) - F_r\left(2f'f'' + \frac{f'^2}{\zeta+k}\right) = 0. \tag{6.15}$$

Pressure P can be calculated from Eq. (6.10) as

$$P=\frac{\zeta+k}{2k}\left(\begin{array}{c} f'''+\frac{1}{\zeta+k}f''-\frac{1}{(\zeta+k)^2}f'+\frac{k}{\zeta+k}ff'' \\ -\frac{k}{\zeta+k}f'^2+\frac{k}{(\zeta+k)^2}ff'-\lambda f'-F_rf'^2 \end{array}\right). \tag{6.16}$$

Skin friction and local Nusselt and Sherwood numbers can be given by

$$C_{f_{s_1}}=\frac{\tau_{rs_1}}{\rho_f u_w^2}, \qquad Nu_s=\frac{sq_{w_r}}{k_f\left(T_w-T_\infty\right)}, \qquad Sh_{s_1}=\frac{sj_{w_1}}{D_B\left(C_w-C_\infty\right)}. \tag{6.17}$$

Here τ_{rs_1} stands for wall shear stress, q_{w_r} for wall heat flux and j_{w_1} for wall mass flux. We can write

$$\left.\begin{array}{c} \tau_{rs_1}=\mu\left(\frac{\partial u}{\partial r}-\frac{u}{r+R}\right)\Big|_{r=0}, \\ q_{w_r}=-k_f\left(\frac{\partial T}{\partial r}\right)\Big|_{r=0}, \\ j_{w_1}=-D_B\left(\frac{\partial C}{\partial r}\right)\Big|_{r=0}. \end{array}\right\} \tag{6.18}$$

Dimensionless skin friction coefficient and local Nusselt and Sherwood numbers are

$$\left.\begin{array}{c} C_{f_{s_1}}Re_{s_1}^{1/2}=f''(0)-\frac{1}{k}f'(0), \\ Nu_sRe_{s_1}^{-1/2}=-\theta'(0), \\ Sh_{s_1}Re_{s_1}^{-1/2}=-\phi'(0). \end{array}\right\} \tag{6.19}$$

6.2 Numerical results

The systems of Eqs. (6.11) − (6.13) and (6.15) are numerically solved by employing shooting technique. Main interest here is to examine velocity $f'(\zeta)$, temperature $\theta(\zeta)$ and concentration $\phi(\zeta)$ profiles for several influential variables like dimensionless radius of curvature parameter k, porosity parameter λ, Prandtl number Pr, inertia coefficient F_r, thermophoresis parameter N_t, Brownian motion parameter N_b, Schmidt number Sc, thermal Biot number γ_t and concentration Biot number γ_c. Effects of curvature parameter k, porosity parameter λ and inertia coefficient F_r on velocity distribution $f'(\zeta)$ are presented in the Figs. 6.1 − 6.3 respectively. Fig. 6.1 elucidates the impact of dimensionless radius of curvature k on velocity distribution $f'(\zeta)$. Both velocity and related layer thickness are higher for larger curvature parameter k. Variation of porosity parameter λ on velocity $f'(\zeta)$ is displayed in Fig. 6.2. Larger porosity

parameter λ shows a reduction in velocity $f'(\zeta)$ and momentum layer thickness. Fig. 6.3 elaborates the effect of inertia coefficient F_r on velocity $f'(\zeta)$. Larger inertia coefficient F_r shows a lower velocity field $f'(\zeta)$ as well as momentum layer thickness. Impacts of curvature parameter k, porosity parameter λ, inertia coefficient F_r, Prandtl number Pr, thermophoresis parameter N_t, Brownian motion parameter N_b and thermal Biot number γ_t on dimensionless temperature profile $\theta(\zeta)$ are displayed in the Figs. $6.4 - 6.10$ respectively. Fig. 6.4 elucidates the variation of dimensionless radius of curvature parameter k on temperature profile $\theta(\zeta)$. Both temperature $\theta(\zeta)$ and corresponding layer thickness are increased for larger curvature parameter k. Variation of porosity parameter λ on temperature $\theta(\zeta)$ is displayed in Fig. 6.5. Larger porosity parameter λ shows an increment in temperature $\theta(\zeta)$ and related layer thickness. Fig. 6.6 elaborates the influence of inertia coefficient F_r on temperature $\theta(\zeta)$. Larger inertia coefficient F_r give rise to enhance in temperature $\theta(\zeta)$ and related layer thickness. Fig. 6.7 depicts the impact of Prandtl number Pr on temperature distribution $\theta(\zeta)$. Clearly both temperature and thermal layer thickness are lower for larger Pr. Fig. 6.8 shows the variation of thermophoresis parameter N_t on temperature $\theta(\zeta)$. Larger thermophoresis parameter N_t shows an enhance in temperature field and related thermal layer thickness. Influence of Brownian motion variable N_b on temperature profile $\theta(\zeta)$ is displayed in Fig. 6.9. Both temperature $\theta(\zeta)$ and corresponding layer thickness are higher for larger N_b. Variation of thermal Biot number γ_t on temperature profile $\theta(\zeta)$ is presented in Fig. 6.10. For larger thermal Biot number γ_t, both temperature $\theta(\zeta)$ and associated layer thickness are enhanced. Contributions of curvature parameter k, porosity parameter λ, inertia coefficient F_r, Schmidt number Sc, thermophoresis parameter N_t, Brownian motion parameter N_b and concentration Biot number γ_c on dimensionless concentration profile $\phi(\zeta)$ are presented in the Figs. $6.11 - 6.17$ respectively. Fig. 6.11 elucidates the impact of dimensionless radius of curvature parameter k on concentration $\phi(\zeta)$. It is noted that concentration $\phi(\zeta)$ is enhanced for larger curvature parameter k. Effect of porosity parameter λ on concentration $\phi(\zeta)$ is displayed in Fig. 6.12. Larger porosity parameter λ causes an enhancement in concentration $\phi(\zeta)$. Variation in concentration $\phi(\zeta)$ for distinct values of inertia coefficient F_r is illustrated in Fig. 6.13. Larger values of F_r correspond to higher concentration $\phi(\zeta)$. Fig. 6.14 illustrates the influence of Schmidt number Sc on concentration $\phi(\zeta)$. Higher Schmidt number Sc shows a decay in concentration $\phi(\zeta)$. Impact of thermophoresis parameter

N_t on concentration $\phi(\zeta)$ is shown in Fig. 6.15. Concentration $\phi(\zeta)$ is enhanced for higher thermophoresis parameter N_t. Fig. 6.16 elaborates the influence of Brownian motion variable N_b on concentration $\phi(\zeta)$. Larger Brownian motion variable N_b depicts a reduction in concentration field $\phi(\zeta)$. Impact of concentration Biot number γ_c on concentration $\phi(\zeta)$ is sketched in Fig. 6.17. For larger concentration Biot number γ_c, the concentration $\phi(\zeta)$ is enhanced. Table 6.1 elucidates the numerical data of skin friction coefficient for numerous values of curvature parameter k, porosity parameter λ and inertia coefficient F_r. It is examined that skin friction coefficient is enhanced for larger λ and F_r while reverse trend is noticed for k. Table 6.2 is displayed to analyze the numerical data of local Nusselt number for distinct values of curvature parameter k, porosity parameter λ, Prandtl number Pr, inertia coefficient F_r, thermal Biot number γ_t, Brownian motion parameter N_b and thermophoresis parameter N_t. Local Nusselt number is increased for higher Prandtl number Pr and thermal Biot number γ_t whereas the opposite trend is seen via curvature parameter k, porosity parameter λ, inertia coefficient F_r, thermophoresis parameter N_t and Brownian motion parameter N_b. Table 6.3 describes the numerical data of local Sherwood number for curvature parameter k, porosity parameter λ, inertia coefficient F_r, Schmidt number Sc, thermophoresis parameter N_t, Brownian motion parameter N_b and concentration Biot number γ_c. It is seen that local Sherwood number is enhanced via Schmidt number Sc, N_b and concentration Biot number γ_c while reverse trend is noticed for curvature parameter k, porosity parameter λ, inertia coefficient F_r and thermophoresis parameter

N_t.

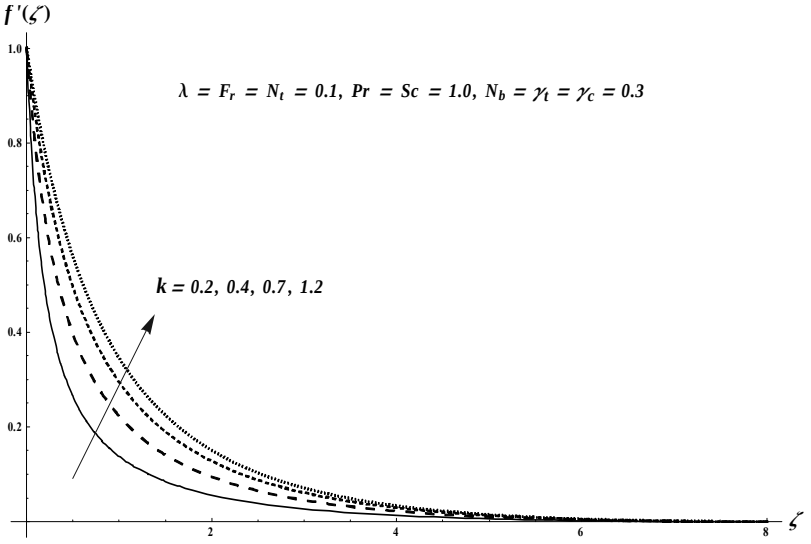

Fig. 6.1. Plots of $f'(\zeta)$ for k.

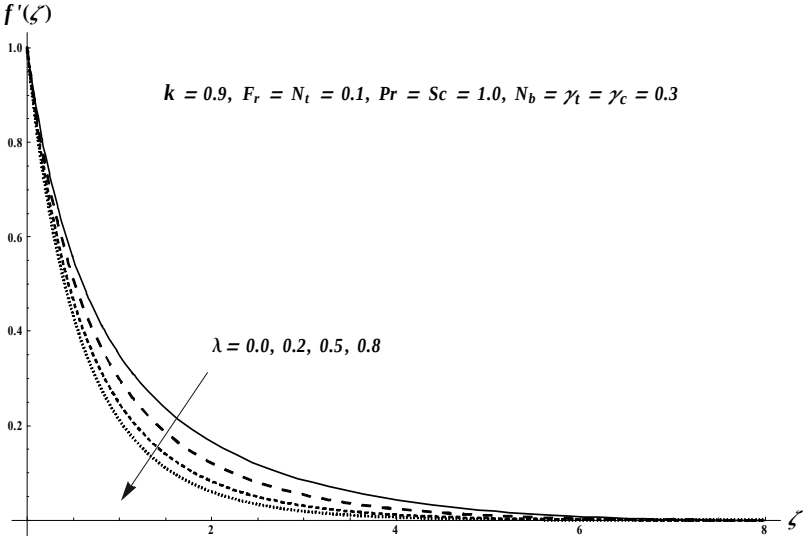

Fig. 6.2. Plots of $f'(\zeta)$ for λ.

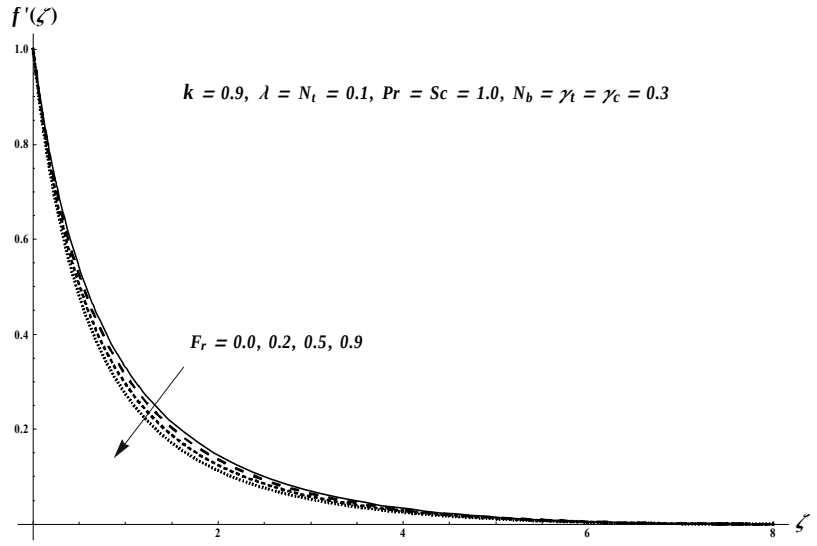

Fig. 6.3. Plots of $f'(\zeta)$ for F_r.

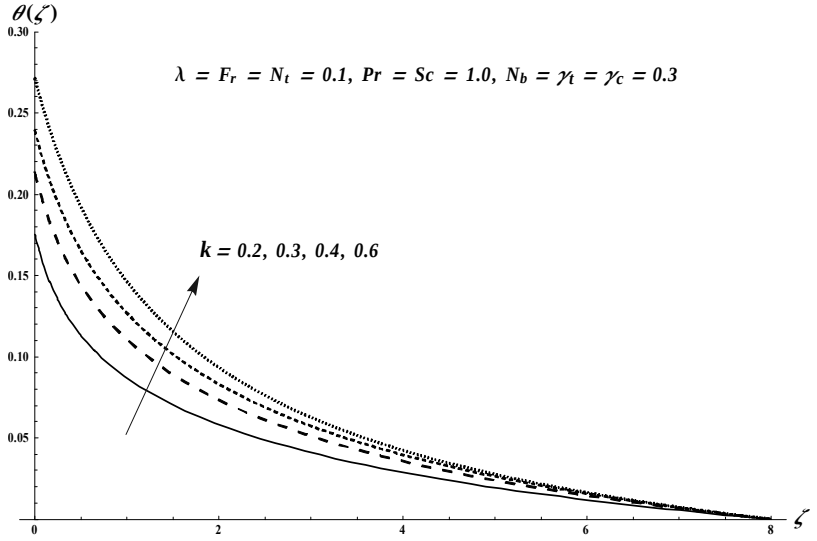

Fig. 6.4. Plots of $\theta(\zeta)$ for k.

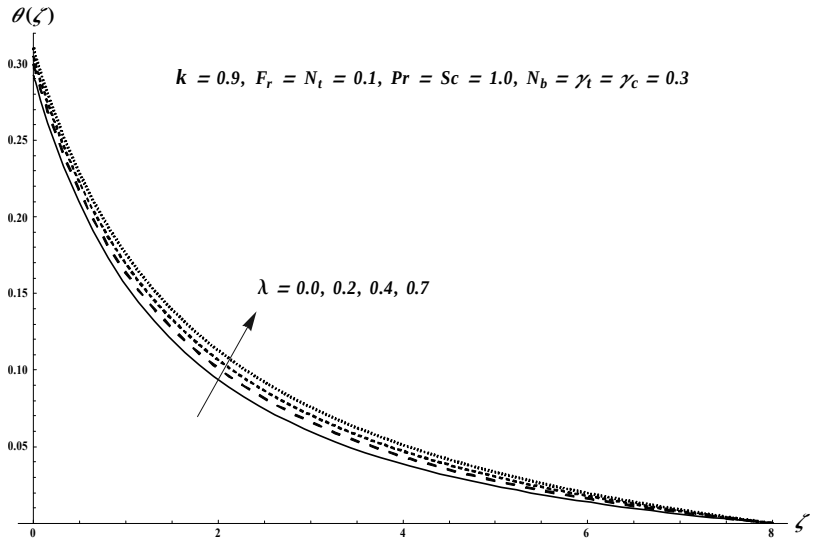

Fig. 6.5. Plots of $\theta(\zeta)$ for λ.

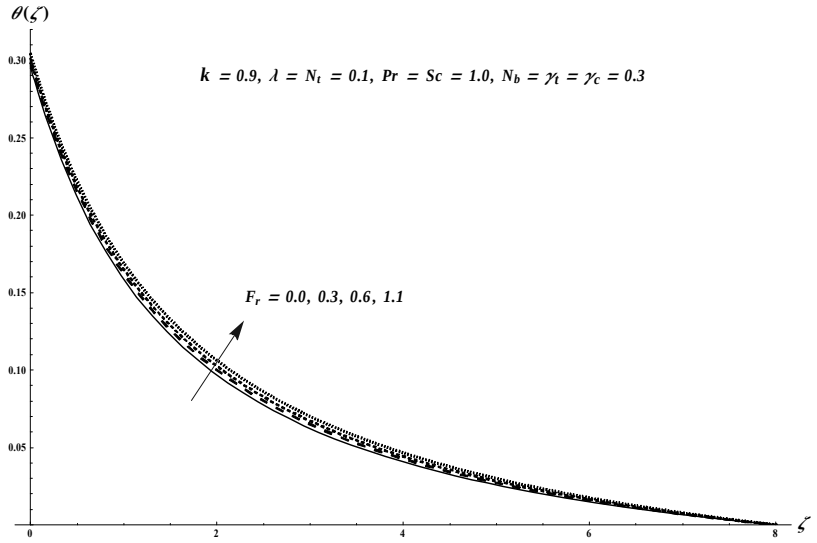

Fig. 6.6. Plots of $\theta(\zeta)$ for F_r.

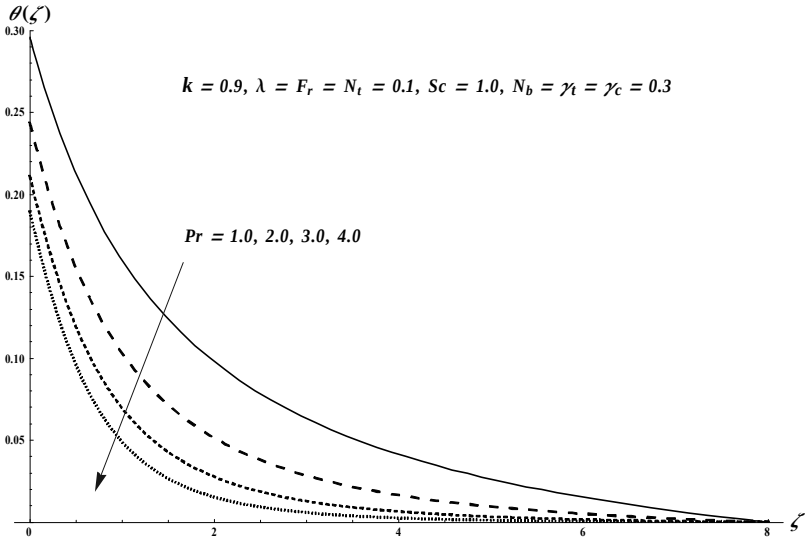

Fig. 6.7. Plots of $\theta(\zeta)$ for Pr.

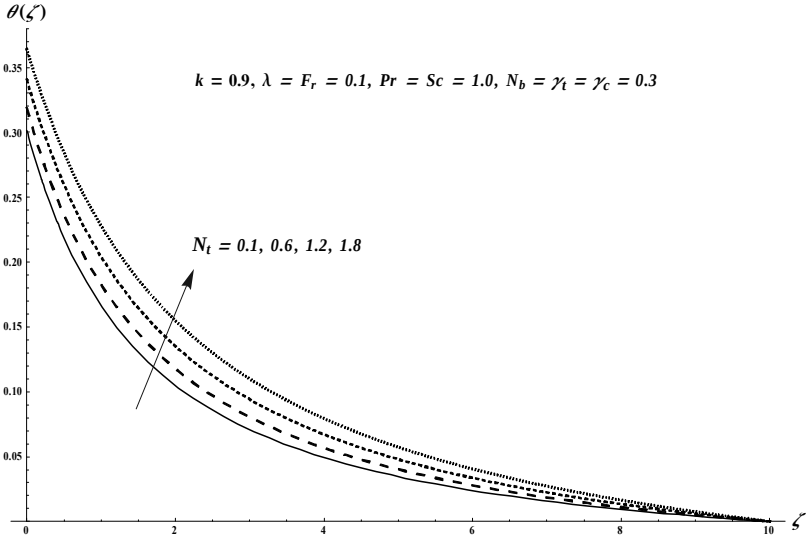

Fig. 6.8. Plots of $\theta(\zeta)$ for N_t.

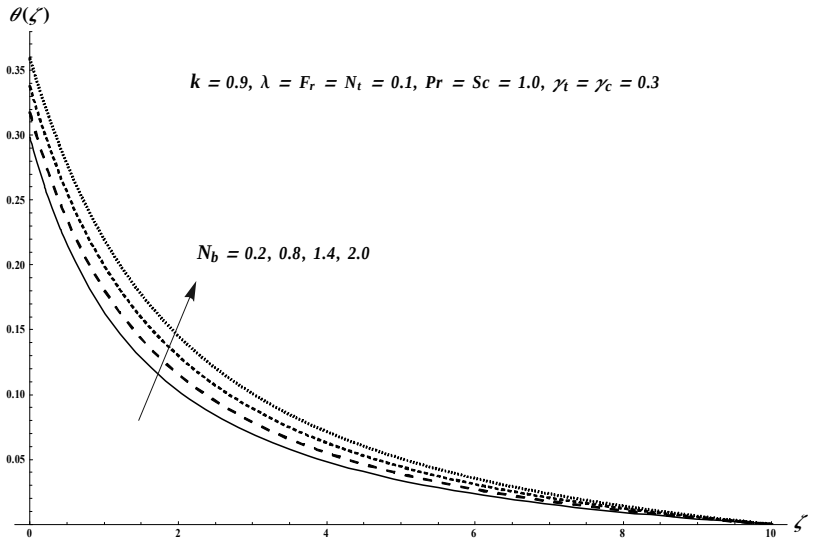

Fig. 6.9. Plots of $\theta(\zeta)$ for N_b.

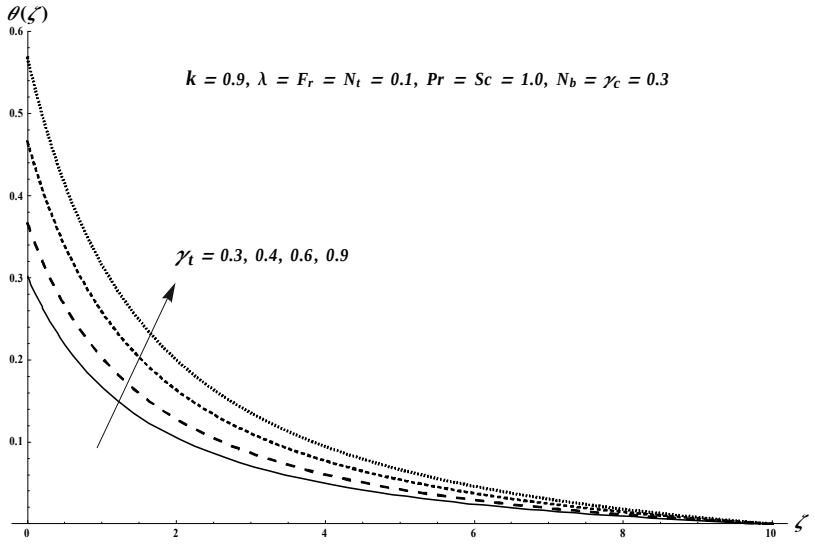

Fig. 6.10. Plots of $\theta(\zeta)$ for γ_t.

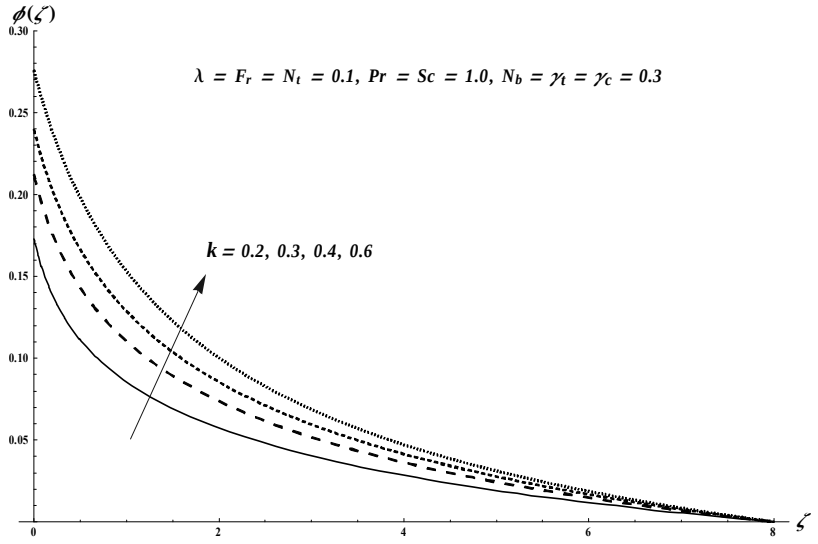

Fig. 6.11. Plots of $\phi(\zeta)$ for k.

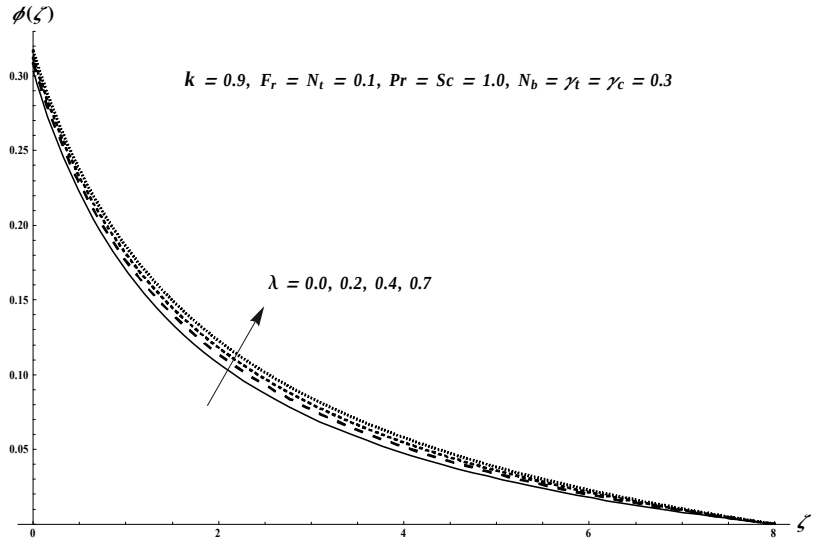

Fig. 6.12. Plots of $\phi(\zeta)$ for λ.

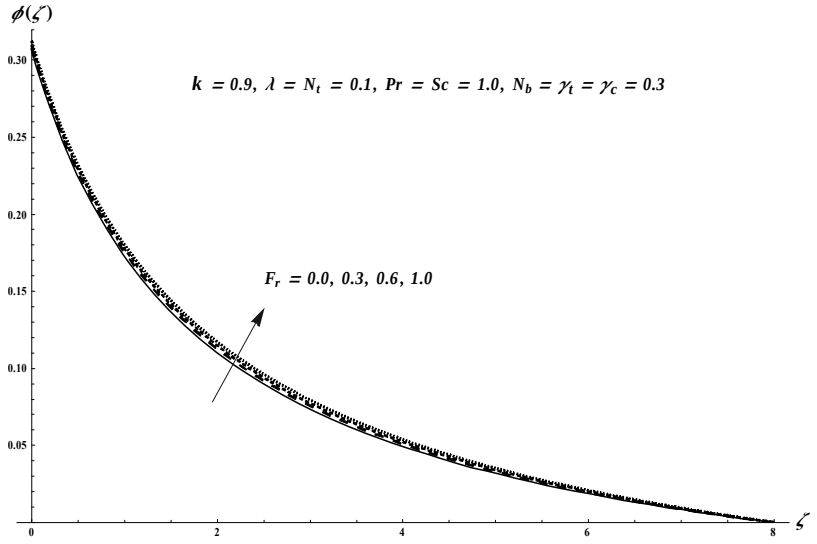

Fig. 6.13. Plots of $\phi(\zeta)$ for F_r.

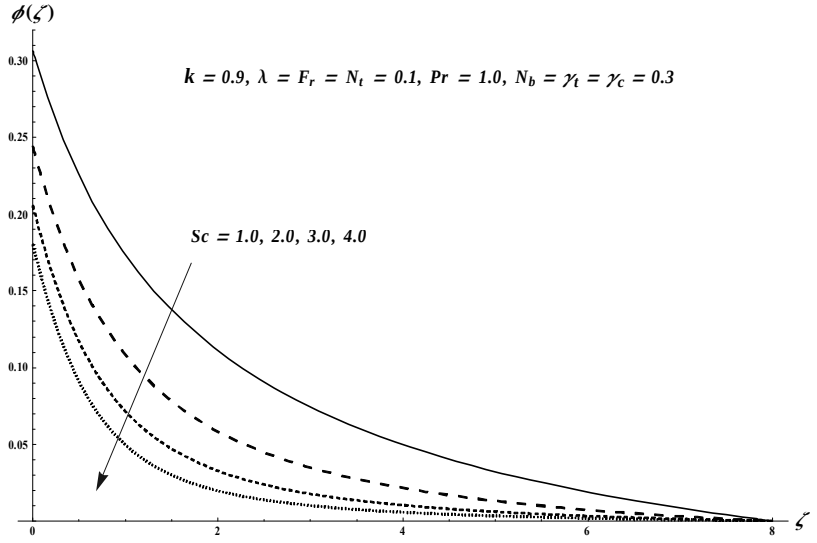

Fig. 6.14. Plots of $\phi(\zeta)$ for Sc.

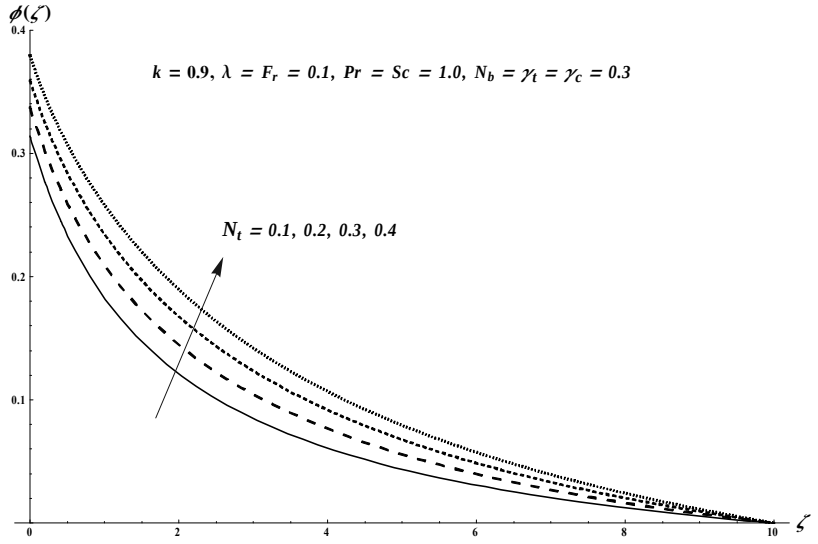

Fig. 6.15. Plots of $\phi(\zeta)$ for N_t.

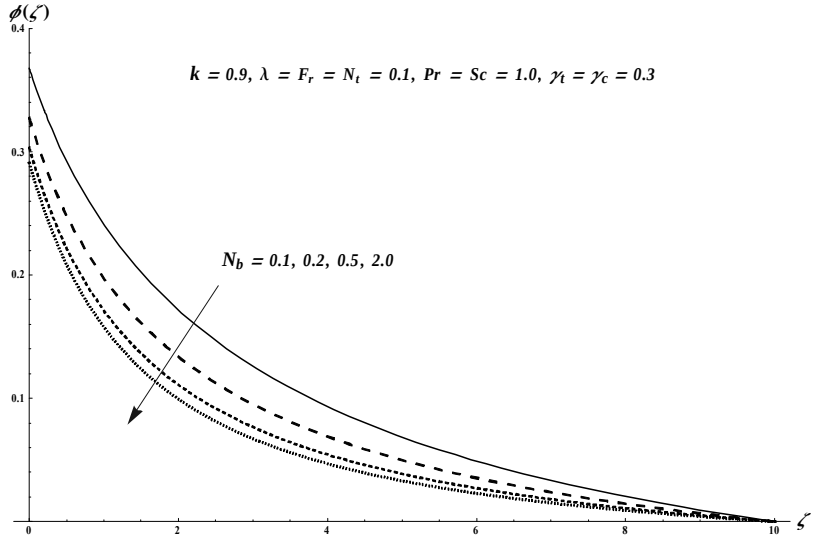

Fig. 6.16. Plots of $\phi(\zeta)$ for N_b.

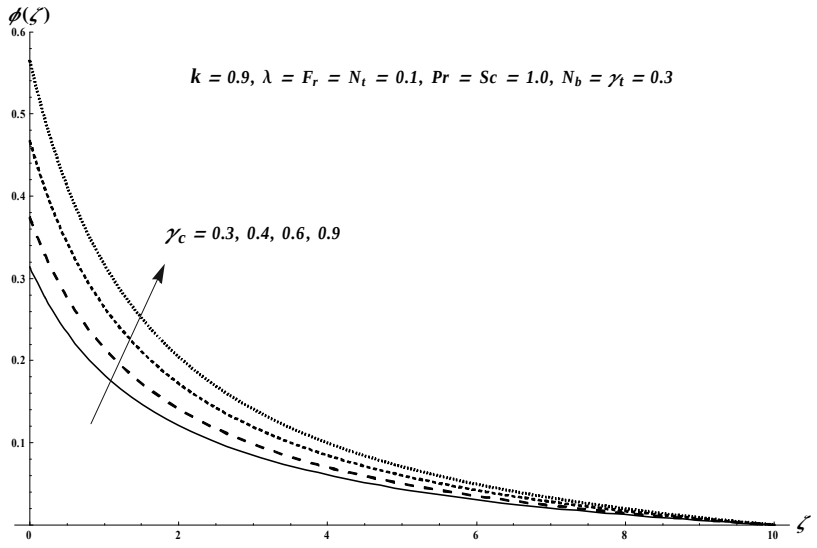

Fig. 6.17. Plots of $\phi(\zeta)$ for γ_c.

Table 6.1. Numerical data of skin friction coefficient for distinct values of k, λ and F_r.

k	λ	F_r	$-C_{fs_1}Re_{s_1}^{1/2}$
0.7	0.1	0.1	3.16892
0.8			2.84704
0.9			2.60252
0.9	0.0	0.1	2.52094
	0.1		2.60252
	0.2		2.67420
0.9	0.1	0.0	2.56300
		0.1	2.60252
		0.2	2.64013

Table 6.2. Numerical data of local Nusselt number for k, Pr, F_r, γ_t, N_t, λ and N_b when $\gamma_c = 0.3$ and $Sc = 1.0$.

k	λ	F_r	Pr	N_t	N_b	γ_t	$-Nu_s Re_{s_1}^{-1/2}$
0.7	0.1	0.1	1.0	0.1	0.3	0.3	0.215569
0.9							0.211194
1.1							0.208271
0.9	0.0	0.1	1.0	0.1	0.3	0.3	0.212310
	0.2						0.210257
	0.4						0.208745
0.9	0.1	0.0	1.0	0.1	0.3	0.3	0.211520
		0.3					0.210605
		0.6					0.209840
0.9	0.1	0.1	1.0	0.1	0.3	0.3	0.211194
			2.0				0.226898
			3.0				0.236688
0.9	0.1	0.1	1.0	0.1	0.3	0.3	0.211194
				0.3			0.209241
				0.5			0.207238
0.9	0.1	0.1	1.0	0.1	0.1	0.3	0.212986
					0.5		0.209364
					0.9		0.205587
0.9	0.1	0.1	1.0	0.1	0.3	0.2	0.156347
						0.3	0.211194
						0.4	0.255999

Table 6.3. Local Sherwood number for distinct k, λ, F_r, Sc, N_t, N_b and γ_c when $Pr = 1.0$ and $\gamma_t = 0.3$.

k	λ	F_r	Sc	N_t	N_b	γ_c	$-Sh_{s_1}Re_{s_1}^{-1/2}$
0.7	0.1	0.1	1.0	0.1	0.3	0.3	0.213683
0.9							0.208197
1.1							0.204364
0.9	0.0	0.1	1.0	0.1	0.3	0.3	0.209099
	0.2						0.207453
	0.4						0.206278
0.9	0.1	0.0	1.0	0.1	0.3	0.3	0.208455
		0.3					0.207734
		0.6					0.207139
0.9	0.1	0.1	1.0	0.1	0.3	0.3	0.208197
			2.0				0.226932
			3.0				0.238458
0.9	0.1	0.1	1.0	0.1	0.3	0.3	0.208197
				0.3			0.196394
				0.5			0.186509
0.9	0.1	0.1	1.0	0.1	0.1	0.3	0.193746
					0.5		0.211093
					0.9		0.213033
0.9	0.1	0.1	1.0	0.1	0.3	0.2	0.142562
						0.3	0.208197
						0.4	0.253753

6.3 Conclusions

Darcy-Forchheimer nanofluid flow due to a curved stretchable sheet is explored. Convective heat and mass conditions are addressed. Flow in porous medium is characterized by Darcy-Forchheimer relation. Impacts of Brownian diffusion and thermophoresis are also taken into account. Main observations of presented research are listed below.

- Velocity distribution $f'(\zeta)$ is enhanced for higher values of curvature parameter k whereas reverse trend is noticed for porosity parameter λ and inertia coefficient F_r.

- Larger curvature parameter k, porosity parameter λ, thermal Biot number γ_t, inertia coefficient F_r, thermophoresis parameter N_t and Brownian motion parameter N_b show higher temperature field $\theta(\zeta)$ while reverse trend is seen for Prandtl number Pr.

- Concentration field $\phi(\zeta)$ is higher for larger curvature parameter k, porosity parameter λ, inertia coefficient F_r, thermophoresis parameter N_t and concentration Biot number γ_c. However opposite trend is found for Schmidt number Sc and Brownian motion parameter N_b.

- Skin friction coefficient is enhanced for larger λ and F_r while reverse trend is noticed for k.

- Local Nusselt number is enhanced for higher Prandtl number Pr and thermal Biot number γ_t whereas the opposite trend is seen via curvature parameter k, porosity parameter λ, inertia coefficient F_r, Brownian motion parameter N_b and thermophoresis parameter N_t.

- Local Sherwood number is enhanced for Schmidt number Sc, Brownian motion parameter N_b and concentration Biot number γ_c while reverse trend is noticed for curvature parameter k, porosity parameter λ, inertia coefficient F_r and thermophoresis parameter N_t.

Chapter 7

Homogeneous-heterogeneous reactions in MHD micropolar fluid flow by a curved stretchable sheet with heat generation/absorption

The purpose of present chapter is to provide analysis of magnetohydrodynamic (MHD) flow of micropolar fluid by curved stretchable sheet. Homogeneous-heterogeneous reactions are taken into consideration. Heat transfer process is explored through heat generation/absorption effects. Micropolar liquid is electrically conducted subject to uniform applied magnetic field. Boundary layer approximation and small magnetic Reynolds number assumptions are employed in the mathematical development. The reduction of partial differential system to nonlinear ordinary differential system has been made by employing suitable variables. The obtained nonlinear systems have been computed and analyzed. The characteristics of various sundry parameters are studied through graphically and numerically. Moreover the physical quantities like surface drag and couple stress coefficients and local Nusselt number are described by numerical data.

7.1 Formulation

An incompressible 2D flow of micropolar fluid is examined. The concept of curvature is employed. Magnetic field of strength B_0 is injected in the radial axis (see Fig. 7.1). Induced magnetic field is neglected due to low magnetic Reynolds number assumption. Heat generation/absorption effects are present. Further homogeneous-heterogeneous reactions of two chemical species A_1 and B_1 are considered. Homogeneous reaction for cubic autocatalysis is given by

$$A_1 + 2B_1 \rightarrow 3B_1, \qquad \text{rate} = k_c a b^2, \tag{7.1}$$

whereas the heterogeneous reaction on the catalyst surface is

$$A_1 \rightarrow B_1, \qquad \text{rate} = k_s a, \tag{7.2}$$

in which the chemical species A_1 and B_1 have concentrations a and b respectively and rate constants are defined by k_c and k_s. The governing boundary layer expressions for present flow are [10, 35] :

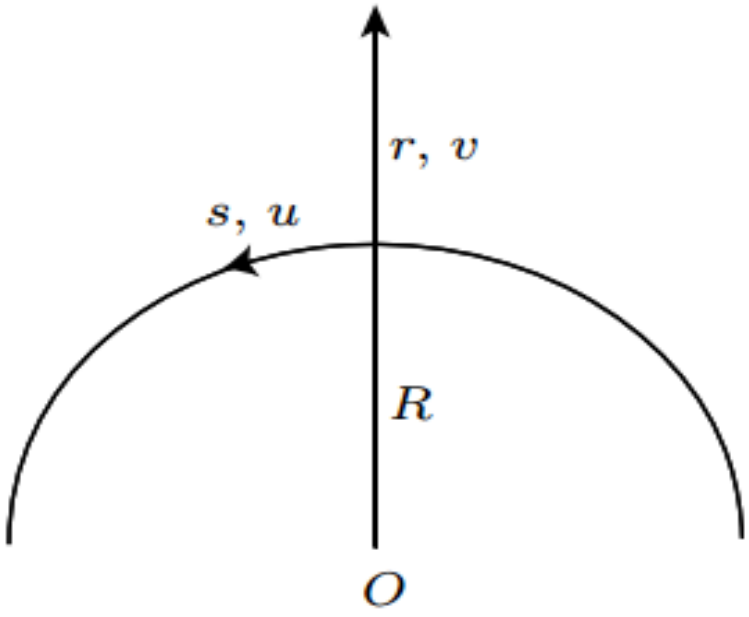

Fig. 7.1. Geometry of the problem.

$$\frac{\partial}{\partial r}\left(\left(r+R\right)v\right)+R\frac{\partial u}{\partial s}=0, \tag{7.3}$$

$$\frac{1}{r+R}u^2=\frac{1}{\rho_f}\frac{\partial p}{\partial r}, \tag{7.4}$$

$$\begin{aligned} v\frac{\partial u}{\partial r}+\frac{R}{r+R}u\frac{\partial u}{\partial s}+\frac{1}{r+R}uv &= -\frac{1}{\rho}\frac{R}{r+R}\frac{\partial p}{\partial s} \\ &\quad +\left(\nu+\frac{\kappa}{\rho_f}\right)\left(\frac{\partial^2 u}{\partial r^2}+\frac{1}{r+R}\frac{\partial u}{\partial r}-\frac{1}{\left(r+R\right)^2}u\right) \\ &\quad -\frac{\kappa}{\rho_f}\frac{\partial N}{\partial r}-\frac{\sigma B_0^2}{\rho_f}u, \end{aligned} \tag{7.5}$$

$$v\frac{\partial N}{\partial r}+\frac{R}{r+R}u\frac{\partial N}{\partial s}=\frac{\gamma_s}{\rho_f j}\left(\frac{\partial^2 N}{\partial r^2}+\frac{1}{r+R}\frac{\partial N}{\partial r}\right)-\frac{\kappa}{\rho_f j}\left(2N+\frac{\partial u}{\partial r}+\frac{1}{r+R}u\right), \tag{7.6}$$

$$\rho_f c_p\left(v\frac{\partial T}{\partial r}+\frac{R}{r+R}u\frac{\partial T}{\partial s}\right)=k_f\left(\frac{\partial^2 T}{\partial r^2}+\frac{1}{r+R}\frac{\partial T}{\partial r}\right)+Q_0\left(T-T_\infty\right), \tag{7.7}$$

$$v\frac{\partial a}{\partial r}+\frac{R}{r+R}u\frac{\partial a}{\partial s}=D_{A_1}\left(\frac{\partial^2 a}{\partial r^2}+\frac{1}{r+R}\frac{\partial a}{\partial r}\right)-k_c ab^2, \tag{7.8}$$

$$v\frac{\partial b}{\partial r}+\frac{R}{r+R}u\frac{\partial b}{\partial s}=D_{B_1}\left(\frac{\partial^2 b}{\partial r^2}+\frac{1}{r+R}\frac{\partial b}{\partial r}\right)+k_c ab^2, \tag{7.9}$$

with the boundary conditions

$$u=u_w\left(s\right)=a_1 s,\ v=0,\ N=-m_0\frac{\partial u}{\partial r},\ T=T_w,\ D_{A_1}\frac{\partial a}{\partial r}=k_s a,\ D_{B_1}\frac{\partial b}{\partial r}=-k_s a \text{ at } r=0, \tag{7.10}$$

$$u\to 0,\ \ \frac{\partial u}{\partial r}\to 0,\ \ N\to 0,\ \ T\to T_\infty,\ \ a\to a_0,\ \ b\to 0\ \ as\ \ r\to\infty. \tag{7.11}$$

Here s and r represent the directions of the velocity components u and v respectively, κ the vortex viscosity, N the micro-rotation in the $rs-$ plane, γ_s the spin gradient viscosity, Q_0 the heat generation/absorption coefficient and m_0 $(0\leq m_0\leq 1)$ the constant. Here $m_0=0$ represents strong concentration of microelements and $m_0=\frac{1}{2}$ is for weak concentration of microelements. Moreover for a curved surface pressure is no longer constant inside the boundary layer. We further simplified the above expressions by invoking a linear relationship between

micro-inertial per unit mass j and spin gradient viscosity γ_s given by

$$\gamma_s = \left(\mu + \frac{\kappa}{2}\right) j. \tag{7.12}$$

Using the following transformations

$$\left.\begin{aligned} u = a_1 s f'(\zeta), \quad v = -\tfrac{R}{r+R}\sqrt{a_1 \upsilon} f(\zeta), \quad N = a_1 s \sqrt{\tfrac{a_1}{\upsilon}} g(\zeta), \quad \zeta = \sqrt{\tfrac{a_1}{\upsilon}} r, \\ p = \rho_f a_1^2 s^2 P(\zeta), \quad \theta(\zeta) = \tfrac{T-T_\infty}{T_w - T_\infty}, \quad a = a_0 \phi(\zeta), \quad b = a_0 h(\zeta). \end{aligned}\right\} \tag{7.13}$$

Now Eq. (7.3) is symmetrically verified and Eqs. (7.4) – (7.12) yield

$$\frac{\partial P}{\partial \zeta} = \frac{f'^2}{\zeta + k}, \tag{7.14}$$

$$\begin{aligned} \frac{2k}{\zeta+k} P &= (1+K^*)\left(f''' + \frac{f''}{\zeta+k} - \frac{f'}{(\zeta+k)^2}\right) - \frac{k}{\zeta+k} f'^2 \\ &\quad + \frac{k}{\zeta+k} f f'' + \frac{k}{(\zeta+k)^2} f f' - K^* g' - M^2 f', \end{aligned} \tag{7.15}$$

$$\left(1 + \frac{K^*}{2}\right)\left(g'' + \frac{g'}{\zeta+k}\right) + \frac{k}{\zeta+k} f g' - \frac{k}{\zeta+k} f' g - K^*\left(2g + f'' + \frac{f'}{\zeta+k}\right) = 0, \tag{7.16}$$

$$\frac{1}{\mathrm{Pr}}\left(\theta'' + \frac{\theta'}{\zeta+k}\right) + \frac{k}{\zeta+k} f\theta' + \delta\theta = 0, \tag{7.17}$$

$$\frac{1}{Sc}\left(\phi'' + \frac{\phi'}{\zeta+k}\right) + \frac{k}{\zeta+k} f\phi' - k_1 \phi h^2 = 0, \tag{7.18}$$

$$\frac{\delta_1}{Sc}\left(h'' + \frac{h'}{\zeta+k}\right) + \frac{k}{\zeta+k} f h' + k_1 \phi h^2 = 0, \tag{7.19}$$

$$\left.\begin{aligned} f = 0, \quad f' = 1, \quad g = -m_0 f'', \quad \theta = 1, \quad \phi' = k_2 \phi, \quad \delta_1 h' = -k_2 \phi \quad \text{at} \quad \zeta = 0, \\ f' \to 0, \quad f'' \to 0, \quad g \to 0, \quad \theta \to 0, \quad \phi \to 1, \quad h \to 0 \quad \text{as} \quad \zeta \to \infty, \end{aligned}\right\} \tag{7.20}$$

where $K^*\left(=\frac{\kappa}{\upsilon}\right)$ stands for material parameter.

Now eliminating pressure P from Eqs. (7.14) and (7.15), we get

$$f^{iv} + \frac{2f'''}{\zeta+k} - \frac{f''}{(\zeta+k)^2} + \frac{f'}{(\zeta+k)^3} - \frac{k}{\zeta+k}\left(f'f'' - ff'''\right)$$

$$-\frac{k}{(\zeta+k)^2}\left(f'^2-ff''\right)-\frac{k}{(\zeta+k)^3}ff'-M^2\left(f''+\frac{f'}{\zeta+k}\right)=0. \tag{7.21}$$

Pressure P can be calculated from Eq. (7.15) as

$$P=\frac{\zeta+k}{2k}\left(\begin{array}{c}(1+K^*)\left(f'''+\frac{f''}{\zeta+k}-\frac{f'}{(\zeta+k)^2}\right)-\frac{k}{\zeta+k}f'^2\\ +\frac{k}{\zeta+k}ff''+\frac{k}{(\zeta+k)^2}ff'-K^*g'-M^2f'\end{array}\right). \tag{7.22}$$

When $D_{A_1}=D_{B_1}$ then $\delta_1=1$ and thus

$$\phi(\zeta)+h(\zeta)=1. \tag{7.23}$$

Now Eqs. (7.18) and (7.19) yield

$$\frac{1}{Sc}\left(\phi''+\frac{\phi'}{\zeta+k}\right)+\frac{k}{\zeta+k}f\phi'-k_1\phi(1-\phi)^2=0, \tag{7.24}$$

with the boundary conditions

$$\phi'(0)=k_2\phi(0), \quad \phi(\infty)\to 1. \tag{7.25}$$

The dimensionless expressions of skin friction and couple stress coefficients and local Nusselt number are given by

$$\left.\begin{array}{c}C_{fs_2}Re_{s_1}^{1/2}=(1+K^*)\left(f''(0)-\frac{f'(0)}{k}\right),\\ C_{m_1}Re_{s_1}=\left(1+\frac{K^*}{2}\right)g'(0),\\ Nu_sRe_{s_1}^{-1/2}=-\theta'(0),\end{array}\right\} \tag{7.26}$$

Here the results are obtained for strong concentration of microelements ($m_0=0$) case only.

7.2 Solutions

The appropriate initial guesses $\left(f_{0_3}, g_{0_1}, \theta_{0_1}, \phi_{0_3}\right)$ in homotopic solutions are defined by

$$\left.\begin{aligned} f_{0_3}(\zeta) &= \exp(-\zeta) - \exp(-2\zeta), \\ g_{0_1}(\zeta) &= m_0 \exp(-\zeta), \\ \theta_{0_1}(\zeta) &= \exp(-\zeta), \\ \phi_{0_3}(\zeta) &= 1 - \tfrac{1}{2}\exp(-k_2\zeta), \end{aligned}\right\} \tag{7.27}$$

and auxiliary linear operators $\left(\mathcal{L}_{f_2},\ \mathcal{L}_{g_1},\ \mathcal{L}_{\theta_1},\ \mathcal{L}_{\phi_1}\right)$ are

$$\mathcal{L}_{f_2} = \frac{d^4 f}{d\zeta^4} - 5\frac{d^2 f}{d\zeta^2} + 4\frac{df}{d\zeta}, \quad \mathcal{L}_{g_1} = \frac{d^2 g}{d\zeta^2} - g, \quad \mathcal{L}_{\theta_1} = \frac{d^2\theta}{d\zeta^2} - \theta, \quad \mathcal{L}_{\phi_1} = \frac{d^2\phi}{d\zeta^2} - \phi. \tag{7.28}$$

The operators satisfy

$$\left.\begin{aligned} \mathcal{L}_{f_2}\left[C^*_{20}\exp(\zeta) + C^*_{21}\exp(-\zeta) + C^*_{22}\exp(2\zeta) + C^*_{23}\exp(-2\zeta)\right] &= 0, \\ \mathcal{L}_{g_1}\left[C^*_{24}\exp(\zeta) + C^*_{25}\exp(-\zeta)\right] &= 0, \\ \mathcal{L}_{\theta_1}\left[C^*_{26}\exp(\zeta) + C^*_{27}\exp(-\zeta)\right] &= 0, \\ \mathcal{L}_{\phi_1}\left[C^*_{28}\exp(\zeta) + C^*_{29}\exp(-\zeta)\right] &= 0, \end{aligned}\right\} \tag{7.29}$$

where C^*_i $(i = 20 - 29)$ elucidate the arbitrary constants.

7.2.1 Deformation problems at zeroth-order

$$(1-\breve{p})\mathcal{L}_{f_2}\left[\hat{f}(\zeta,\ \breve{p}) - f_{0_3}(\zeta)\right] = \breve{p}\hbar_f \mathcal{N}_{f_4}[\hat{f}(\zeta,\ \breve{p})], \tag{7.30}$$

$$(1-\breve{p})\mathcal{L}_{g_1}\left[\hat{g}(\zeta,\ \breve{p}) - g_{0_1}(\zeta)\right] = \breve{p}\hbar_g \mathcal{N}_{g_1}[\hat{f}(\zeta,\ \breve{p}),\ \hat{g}(\zeta,\ \breve{p})], \tag{7.31}$$

$$(1-\breve{p})\mathcal{L}_{\theta_1}\left[\hat{\theta}(\zeta,\ \breve{p}) - \theta_{0_1}(\zeta)\right] = \breve{p}\hbar_\theta \mathcal{N}_{\theta_4}[\hat{f}(\zeta,\ \breve{p}),\ \hat{\theta}(\zeta,\ \breve{p})], \tag{7.32}$$

$$(1-\breve{p})\mathcal{L}_{\phi_1}\left[\hat{\phi}(\zeta,\ \breve{p}) - \phi_{0_3}(\zeta)\right] = \breve{p}\hbar_\phi \mathcal{N}_{\phi_3}[\hat{f}(\zeta,\ \breve{p}),\ \hat{\phi}(\zeta,\ \breve{p})], \tag{7.33}$$

$$\left.\begin{aligned} &\hat{f}(0,\ \breve{p}) = 0, \quad \hat{g}(0,\ \breve{p}) = 0, \quad \hat{f}'(0,\ \breve{p}) = 1, \quad \hat{\theta}(0,\ \breve{p}) = 1, \quad \hat{\phi}'(0,\ \breve{p}) = k_2\hat{\phi}(0,\ \breve{p}) \\ &\hat{f}'(\infty,\ \breve{p}) = 0, \quad \hat{g}(\infty,\ \breve{p}) = 0, \quad \hat{f}''(\infty,\ \breve{p}) = 0, \quad \hat{\theta}(\infty,\ \breve{p}) = 0,\ \hat{\phi}(\infty,\ \breve{p}) = 1, \end{aligned}\right\} \tag{7.34}$$

$$\mathcal{N}_{f_4}\left[\hat{f}(\zeta,\ \breve{p})\right] = \frac{\partial^4\hat{f}}{\partial\zeta^4}+\left(\frac{2}{\zeta+k}\right)\frac{\partial^3\hat{f}}{\partial\zeta^3}-\left(\frac{1}{\zeta+k}\right)^2\frac{\partial^2\hat{f}}{\partial\zeta^2}+\left(\frac{1}{\zeta+k}\right)^3\frac{\partial\hat{f}}{\partial\zeta}$$
$$-\left(\frac{k}{\zeta+k}\right)\left(\frac{\partial\hat{f}}{\partial\zeta}\frac{\partial^2\hat{f}}{\partial\zeta^2}-\hat{f}\frac{\partial^3\hat{f}}{\partial\zeta^3}\right)-\left(\frac{k}{(\zeta+k)^2}\right)\left(\frac{\partial\hat{f}}{\partial\zeta}\frac{\partial\hat{f}}{\partial\zeta}-\hat{f}\frac{\partial^2\hat{f}}{\partial\zeta^2}\right)$$
$$-\left(\frac{k}{(\zeta+k)^3}\right)\hat{f}\frac{\partial\hat{f}}{\partial\zeta}-M^2\left(\frac{\partial^2\hat{f}}{\partial\zeta^2}+\frac{1}{\zeta+k}\frac{\partial\hat{f}}{\partial\zeta}\right), \tag{7.35}$$

$$\mathcal{N}_{g_1}[\hat{f}(\zeta,\ \breve{p}),\ \hat{g}(\zeta,\ \breve{p})] = \left(1+\frac{K^*}{2}\right)\left(\frac{\partial^2\hat{g}}{\partial\zeta^2}+\frac{1}{\zeta+k}\frac{\partial\hat{g}}{\partial\zeta}\right)$$
$$+\frac{k}{\zeta+k}\left(\hat{f}\frac{\partial\hat{g}}{\partial\zeta}-\hat{g}\frac{\partial\hat{f}}{\partial\zeta}\right)-K^*\left(2\hat{g}+\frac{\partial^2\hat{f}}{\partial\zeta^2}+\frac{1}{\zeta+k}\frac{\partial\hat{f}}{\partial\zeta}\right), \tag{7.36}$$

$$\mathcal{N}_{\theta_4}\left[\hat{f}(\zeta,\ \breve{p}),\ \hat{\theta}(\zeta,\ \breve{p})\right] = \frac{\partial^2\hat{\theta}}{\partial\zeta^2}+\frac{1}{\zeta+k}\frac{\partial\hat{\theta}}{\partial\zeta}+\Pr\frac{k}{\zeta+k}\hat{f}\frac{\partial\hat{\theta}}{\partial\zeta}+\Pr\delta\hat{\theta}, \tag{7.37}$$

$$\mathcal{N}_{\phi_3}\left[\hat{f}(\zeta,\ \breve{p}),\ \hat{\phi}(\zeta,\ \breve{p})\right] = \frac{1}{Sc}\left(\frac{\partial^2\hat{\phi}}{\partial\zeta^2}+\frac{1}{\zeta+k}\frac{\partial\hat{\phi}}{\partial\zeta}\right)+\frac{k}{\zeta+k}\hat{f}\frac{\partial\hat{\phi}}{\partial\zeta}-k_1\hat{\phi}\left(1-\hat{\phi}\right)^2. \tag{7.38}$$

Setting $\breve{p}=0$ and $\breve{p}=1$ one obtains

$$\hat{f}(\zeta,\ 0)=f_{0_3}(\zeta),\ \hat{f}(\zeta,\ 1)=f(\zeta), \tag{7.39}$$

$$\hat{g}(\zeta,\ 0)=g_{0_1}(\zeta),\ \hat{g}(\zeta,\ 1)=g(\zeta), \tag{7.40}$$

$$\hat{\theta}(\zeta,\ 0)=\theta_{0_1}(\zeta),\ \hat{\theta}(\zeta,\ 1)=\theta(\zeta), \tag{7.41}$$

$$\hat{\phi}(\zeta,\ 0)=\phi_{0_3}(\zeta),\ \hat{\phi}(\zeta,\ 1)=\phi(\zeta), \tag{7.42}$$

when $\breve{p}$ changes from 0 to 1 then $\hat{f}(\zeta,\breve{p})$, $\hat{g}(\zeta,\breve{p})$, $\hat{\theta}(\zeta,\breve{p})$ and $\hat{\phi}(\zeta,\breve{p})$ display alteration from primary approximations $f_{0_3}(\zeta)$, $g_{0_1}(\zeta)$, $\theta_{0_1}(\zeta)$ and $\phi_{0_3}(\zeta)$ to desired ultimate solutions $f(\zeta)$, $g(\zeta)$, $\theta(\zeta)$ and $\phi(\zeta)$.

7.2.2 Deformation problems at $\hat{m}$th-order

$$\mathcal{L}_{f_2}\left[f_{\hat{m}}(\zeta)-\chi_{\hat{m}}f_{\hat{m}-1}(\zeta)\right]=\hbar_f\tilde{\mathcal{R}}^{\hat{m}}_{f_4}(\zeta), \tag{7.43}$$

$$\mathcal{L}_{g_1}\left[g_{\hat{m}}(\zeta)-\chi_{\hat{m}}g_{\hat{m}-1}(\zeta)\right]=\hbar_g\tilde{\mathcal{R}}^{\hat{m}}_{g_1}(\zeta), \tag{7.44}$$

$$\mathcal{L}_{\theta_1}\left[\theta_{\hat{m}}(\zeta)-\chi_{\hat{m}}\theta_{\hat{m}-1}(\zeta)\right]=\hbar_\theta\tilde{\mathcal{R}}^{\hat{m}}_{\theta_4}(\zeta), \tag{7.45}$$

$$\mathcal{L}_{\phi_1}\left[\phi_{\hat{m}}(\zeta)-\chi_{\hat{m}}\phi_{\hat{m}-1}(\zeta)\right]=\hbar_\phi\tilde{\mathcal{R}}^{\hat{m}}_{\phi_3}(\zeta), \tag{7.46}$$

$$\left.\begin{array}{c} f_{\hat{m}}(0)=g_{\hat{m}}(0)=f'_{\hat{m}}(0)=\theta_{\hat{m}}(0)=\phi'_{\hat{m}}(0)-k_2\phi_{\hat{m}}(0)=0,\\ f'_{\hat{m}}(\infty)=g_{\hat{m}}(\infty)=f''_{\hat{m}}(\infty)=\theta_{\hat{m}}(\infty)=\phi_{\hat{m}}(\infty)=0, \end{array}\right\} \tag{7.47}$$

$$\begin{aligned}\tilde{\mathcal{R}}^{\hat{m}}_{f_4}(\zeta) &= f''''_{\hat{m}-1}+\left(\frac{2}{\zeta+k}\right)f'''_{\hat{m}-1}-\left(\frac{1}{\zeta+k}\right)^2 f''_{\hat{m}-1}+\left(\frac{1}{\zeta+k}\right)^3 f'_{\hat{m}-1}\\ &\quad-\left(\frac{k}{\zeta+k}\right)\left(\sum_{\hat{k}=0}^{\hat{m}-1}\left(f'_{\hat{m}-1-\hat{k}}f''_{\hat{k}}\right)-\sum_{\hat{k}=0}^{\hat{m}-1}\left(f_{\hat{m}-1-\hat{k}}f'''_{\hat{k}}\right)\right)\\ &\quad-\left(\frac{k}{(\zeta+k)^2}\right)\left(\sum_{\hat{k}=0}^{\hat{m}-1}\left(f'_{\hat{m}-1-\hat{k}}f'_{\hat{k}}\right)-\sum_{\hat{k}=0}^{\hat{m}-1}\left(f_{\hat{m}-1-\hat{k}}f''_{\hat{k}}\right)\right)\\ &\quad-\left(\frac{k}{(\zeta+k)^3}\right)\sum_{\hat{k}=0}^{\hat{m}-1}\left(f_{\hat{m}-1-\hat{k}}f'_{\hat{k}}\right)-M^2\left(f''_{\hat{m}-1}+\frac{1}{\zeta+k}f'_{\hat{m}-1}\right),\end{aligned} \tag{7.48}$$

$$\begin{aligned}\tilde{\mathcal{R}}^{\hat{m}}_{g_1}(\zeta) &= \left(1+\frac{K^*}{2}\right)\left(g''_{\hat{m}-1}+\frac{1}{\zeta+k}g'_{\hat{m}-1}\right)\\ &\quad+\frac{k}{\zeta+k}\left(\sum_{k=0}^{\hat{m}-1}f_{\hat{m}-1-k}g'_k-\sum_{k=0}^{\hat{m}-1}g_{\hat{m}-1-k}f'_k\right)\\ &\quad-K^*\left(2g_{\hat{m}-1}+f''_{\hat{m}-1}+\frac{1}{\zeta+k}f'_{\hat{m}-1}\right),\end{aligned} \tag{7.49}$$

$$\tilde{\mathcal{R}}^{\hat{m}}_{\theta_4}(\zeta)=\theta''_{\hat{m}-1}+\frac{1}{\zeta+k}\theta'_{\hat{m}-1}+\Pr\frac{k}{\zeta+k}\left(\sum_{\hat{k}=0}^{\hat{m}-1}f_{\hat{m}-1-\hat{k}}\theta'_{\hat{k}}\right)+\Pr\delta\theta_{\hat{m}-1}, \tag{7.50}$$

$$\begin{aligned}\tilde{\mathcal{R}}^{\hat{m}}_{\phi_3}(\zeta) &= \frac{1}{Sc}\left(\phi''_{\hat{m}-1}+\frac{1}{\zeta+k}\phi'_{\hat{m}-1}\right)+\frac{k}{\zeta+k}\left(\sum_{\hat{k}=0}^{\hat{m}-1}f_{\hat{m}-1-\hat{k}}\phi'_{\hat{k}}\right)\\ &\quad-k_1\left(\sum_{\hat{k}=0}^{\hat{m}-l}\phi_{\hat{m}-1-\hat{k}}\sum_{l=0}^{\hat{k}}\left(1-\phi_{\hat{k}-l}\right)(1-\phi_l)\right),\end{aligned} \tag{7.51}$$

The following expressions are derived via Taylor's series expansion:

$$\hat{f}(\zeta,\ \breve{p}) = f_{0_3}(\zeta) + \sum_{\hat{m}=1}^{\infty} f_{\hat{m}}(\zeta)\breve{p}^{\hat{m}},\ f_{\hat{m}}(\zeta) = \frac{1}{\hat{m}!}\frac{\partial^{\hat{m}}\hat{f}(\zeta,\ \breve{p})}{\partial\breve{p}^{\hat{m}}}\bigg|_{\breve{p}\,=\,0}, \tag{7.52}$$

$$\hat{g}(\zeta,\ \breve{p}) = g_{0_1}(\zeta) + \sum_{\hat{m}=1}^{\infty} g_{\hat{m}}(\zeta)\breve{p}^{\hat{m}},\ g_{\hat{m}}(\zeta) = \frac{1}{\hat{m}!}\frac{\partial^{\hat{m}}\hat{g}(\zeta,\ \breve{p})}{\partial\breve{p}^{\hat{m}}}\bigg|_{\breve{p}\,=\,0}, \tag{7.53}$$

$$\hat{\theta}(\zeta,\ \breve{p}) = \theta_{0_1}(\zeta) + \sum_{\hat{m}=1}^{\infty} \theta_{\hat{m}}(\zeta)\breve{p}^{\hat{m}},\ \theta_{\hat{m}}(\zeta) = \frac{1}{\hat{m}!}\frac{\partial^{\hat{m}}\hat{\theta}(\zeta,\ \breve{p})}{\partial\breve{p}^{\hat{m}}}\bigg|_{\breve{p}\,=\,0}, \tag{7.54}$$

$$\hat{\phi}(\zeta,\ \breve{p}) = \phi_{0_3}(\zeta) + \sum_{\hat{m}=1}^{\infty} \phi_{\hat{m}}(\zeta)\breve{p}^{\hat{m}},\ \phi_{\hat{m}}(\zeta) = \frac{1}{\hat{m}!}\frac{\partial^{\hat{m}}\hat{\phi}(\zeta,\ \breve{p})}{\partial\breve{p}^{\hat{m}}}\bigg|_{\breve{p}\,=\,0}. \tag{7.55}$$

The convergence regarding Eqs. $(7.52) - (7.55)$ is solidly based upon the suitable selections of $\hbar_f$, $\hbar_\theta$, $\hbar_g$ and $\hbar_\phi$. Choosing suitable values of $\hbar_f$, $\hbar_\theta$, $\hbar_g$ and $\hbar_\phi$ so that Eqs. $(7.52) - (7.55)$ converge at $\breve{p} = 1$ then

$$f(\zeta) = f_{0_3}(\zeta) + \sum_{\hat{m}=1}^{\infty} f_{\hat{m}}(\zeta), \tag{7.56}$$

$$g(\zeta) = g_{0_1}(\zeta) + \sum_{\hat{m}=1}^{\infty} g_{\hat{m}}(\zeta), \tag{7.57}$$

$$\theta(\zeta) = \theta_{0_1}(\zeta) + \sum_{\hat{m}=1}^{\infty} \theta_{\hat{m}}(\zeta), \tag{7.58}$$

$$\phi(\zeta) = \phi_{0_3}(\zeta) + \sum_{\hat{m}=1}^{\infty} \phi_{\hat{m}}(\zeta). \tag{7.59}$$

In terms of special solutions $(f^*_{\hat{m}},\ g^*_{\hat{m}},\ \theta^*_{\hat{m}},\ \phi^*_{\hat{m}})$, the general solutions $(f_{\hat{m}},\ g_{\hat{m}},\ \theta_{\hat{m}},\ \phi_{\hat{m}})$ of the Eqs. $(7.43) - (7.46)$ are defined by the following expressions:

$$f_{\hat{m}}(\zeta) = f^*_{\hat{m}}(\zeta) + C^*_{20}\exp(\zeta) + C^*_{21}\exp(-\zeta) + C^*_{22}\exp(2\zeta) + C^*_{23}\exp(-2\zeta), \tag{7.60}$$

$$g_{\hat{m}}(\zeta) = g^*_{\hat{m}}(\zeta) + C^*_{24}\exp(\zeta) + C^*_{25}\exp(-\zeta), \tag{7.61}$$

$$\theta_{\hat{m}}(\zeta) = \theta^*_{\hat{m}}(\zeta) + C^*_{26}\exp(\zeta) + C^*_{27}\exp(-\zeta), \tag{7.62}$$

$$\phi_{\hat{m}}(\zeta) = \phi^*_{\hat{m}}(\zeta) + C^*_{28}\exp(\zeta) + C^*_{29}\exp(-\zeta), \tag{7.63}$$

in which C_i^* $(i = 20 - 29)$ through the boundary conditions (7.47) are given by

$$C_{20}^* = C_{22}^* = C_{24}^* = C_{26}^* = C_{28}^* = 0,\ C_{23}^* = \left.\frac{\partial f_{\hat{m}}^*(\zeta)}{\partial \zeta}\right|_{\zeta\,=\,0} + f_{\hat{m}}^*(0),\ C_{21}^* = -C_{23}^* - f_{\hat{m}}^*(0), \quad (7.64)$$

$$C_{25}^* = -g_{\hat{m}}^*(0),\ C_{27}^* = -\theta_{\hat{m}}^*(0),\ C_{29}^* = \frac{1}{1+k_2}\left(\left.\frac{\partial \phi_{\hat{m}}^*(\zeta)}{\partial \zeta}\right|_{\zeta\,=\,0} - k_2\phi_{\hat{m}}^*(0)\right). \quad (7.65)$$

7.2.3 Convergence analysis

Here the homotopic solutions involve nonzero auxiliary parameters $\hbar_f$, $\hbar_g$, $\hbar_\theta$ and $\hbar_\phi$. Such auxiliary variables have significant role to tune and govern the convergence of obtained results. To get the acceptable values of such parameters, the $\hbar-$curves at 20th order of deformations are sketched. Fig. 7.2 shows that the convergence zone lies inside the ranges $-1.4 \leq \hbar_f \leq -0.1$, $-1.5 \leq \hbar_g \leq -0.1$, $-1.7 \leq \hbar_\theta \leq -0.5$ and $-1.8 \leq \hbar_\phi \leq 0.2$ for strong concentration of microelements ($m_0 = 0$) case. Table 7.1 indicates that the 10th order of deformation is sufficient for convergent results.

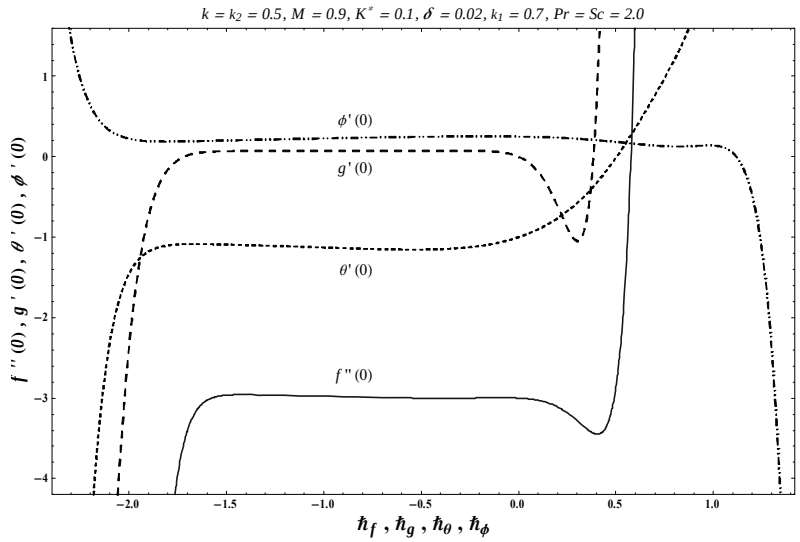

Fig. 7.2. The $\hbar-$plots for $f(\zeta)$, $g(\zeta)$, $\theta(\zeta)$ and $\phi(\zeta)$.

Table 7.1. Homotopic solutions convergence when $k = k_2 = 0.5$, $k_1 = 0.7$, $M = 0.9$, $K^* = 0.1$, $Pr = Sc = 2.0$ and $\delta = 0.02$.

Order of approximations	$-f''(0)$	$g'(0)$	$-\theta'(0)$	$\phi'(0)$
1	2.9932	0.0587	1.0472	0.2521
5	3.0023	0.0745	1.1415	0.2537
10	3.0032	0.0730	1.1571	0.2537
15	3.0032	0.0730	1.1571	0.2537
20	3.0032	0.0730	1.1571	0.2537
25	3.0032	0.0730	1.1571	0.2537
30	3.0032	0.0730	1.1571	0.2537

7.3 Discussion

This portion has been organized to explore the impacts of several effective parameters including dimensionless radius of curvature parameter k, material parameter K^*, magnetic parameter M, Prandtl number Pr, heat absorption/generation parameter δ, Schmidt parameter Sc, intensity of homogeneous reaction k_1 and intensity of heterogeneous reaction k_2 on $f'(\zeta)$, $g(\zeta)$, $\theta(\zeta)$ and $\phi(\zeta)$. Here the results are obtained for strong concentration of microelements ($m_0 = 0$) case only. Influences of curvature k and magnetic M parameters on velocity distribution $f'(\zeta)$ are presented in the Figs. 7.3 and 7.4 respectively. Fig. 7.3 elucidates the impact of dimensionless radius of curvature parameter k on velocity distribution $f'(\zeta)$. Both velocity field and momentum layer thickness are enhanced for larger curvature parameter k. Impact of magnetic parameter M on velocity $f'(\zeta)$ is sketched in Fig. 7.4. Here both velocity and momentum layer thickness are lower for larger M. Effects of curvature parameter k, magnetic parameter M and material parameter K^* on micro-rotation profile $g(\zeta)$ are displayed in the Figs. $7.5 - 7.7$ respectively. Fig. 7.5 depicts the variation of dimensionless radius of curvature parameter k on micro-rotation profile $g(\zeta)$. By enlarging radius of curvature parameter k, the micro-rotation field enhances. Influence of magnetic parameter M on micro-rotation profile $g(\zeta)$ is sketched in Fig. 7.6. By increasing magnetic parameter M, the micro-rotation field decreases. Fig. 7.7 depicts the effect of material parameter K^* on micro-rotation profile $g(\zeta)$. Larger material pa-

rameter K^* leads to higher micro-rotation field. Behaviors of curvature parameter k, magnetic parameter M, Prandtl number Pr and heat absorption/generation parameter δ on dimensionless temperature profile $\theta(\zeta)$ are presented in the Figs. $7.8-7.11$ respectively. Fig. 7.8 depicts variation of curvature parameter k on temperature $\theta(\zeta)$. Both temperature field and related layer thickness are enhanced for larger curvature parameter k. Influence of magnetic parameter M on temperature profile $\theta(\zeta)$ is plotted in Fig. 7.9. It is noticed that both temperature and corresponding layer thickness are larger when M is enhanced. Fig. 7.10 elucidates the effect of Prandtl number Pr on temperature $\theta(\zeta)$. Larger Prandtl number Pr show a decay in temperature field and thermal layer thickness. Influence of heat generation/absorption variable δ on temperature distribution $\theta(\zeta)$ is shown in Fig. 7.11. Here temperature and related layer thickness are larger for higher $\delta\ (>0)$ whereas opposite trend is observed for larger $\delta\ (<0)$. Effects of dimensionless curvature parameter k, magnetic parameter M, strength of homogeneous reaction k_1, Schmidt parameter Sc and strength of heterogeneous reaction k_2 on dimensionless concentration profile $\phi(\zeta)$ are presented in the Figs. $7.12-7.16$ respectively. By enhancing curvature parameter k, magnetic parameter M, strength of homogeneous reaction k_1 and Schmidt parameter Sc, the concentration distribution $\phi(\zeta)$ reduces while reverse behavior is seen for strength of heterogeneous reaction k_2. It is noticed that the strength of homogeneous reaction k_1 and strength of heterogeneous reaction k_2 have opposite impacts on concentration distribution $\phi(\zeta)$. Table 7.2 elucidates numerical data for skin friction and couple stress coefficients for distinct values of curvature parameter k, magnetic parameter M and material parameter K^*. It is examined that skin friction and couple stress coefficients are enhanced for larger magnetic M and material K^* parameters while the reverse trend is noticed through curvature parameter k. Table 7.3 validates the current outcomes with the earlier published observations in a limiting sense. By this Table, we have examined that the current HAM solution has nice resemblance with the earlier numerical solution by Sajid et al. [26] in a limiting sense. Further Table 7.4 is displayed to analyze the numerical data for local Nusselt number for distinct values of curvature parameter k, magnetic parameter M, Pr and δ when $k_1 = 0.7$, $k_2 = 0.5$, $K^* = 0.1$ and $Sc = 2.0$. It is examined that local Nusselt number is higher for larger material parameter K^* and Prandtl number Pr whereas opposite trend is seen for curvature k and heat generation/absorption δ

parameters.

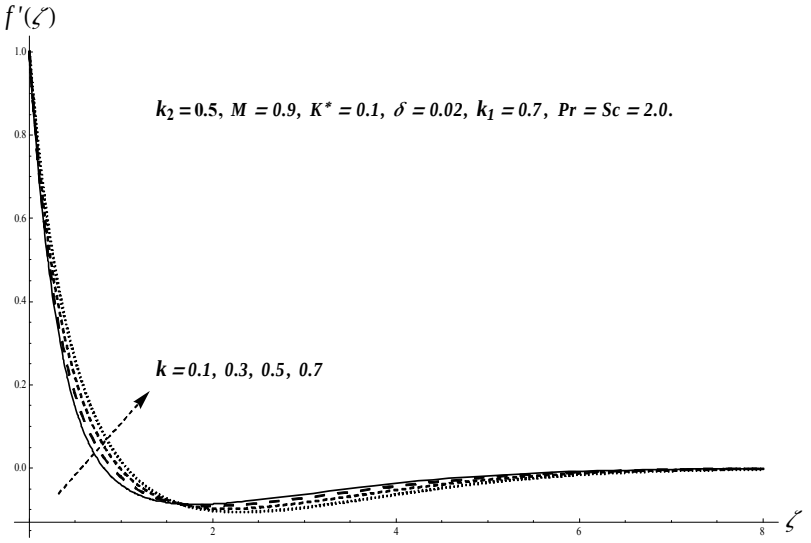

Fig. 7.3. Plots of $f'(\zeta)$ for k.

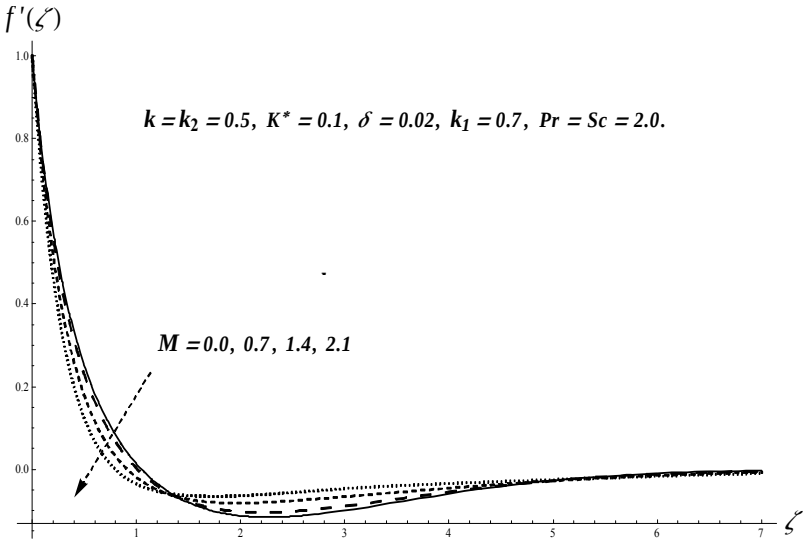

Fig. 7.4. Plots of $f'(\zeta)$ for M.

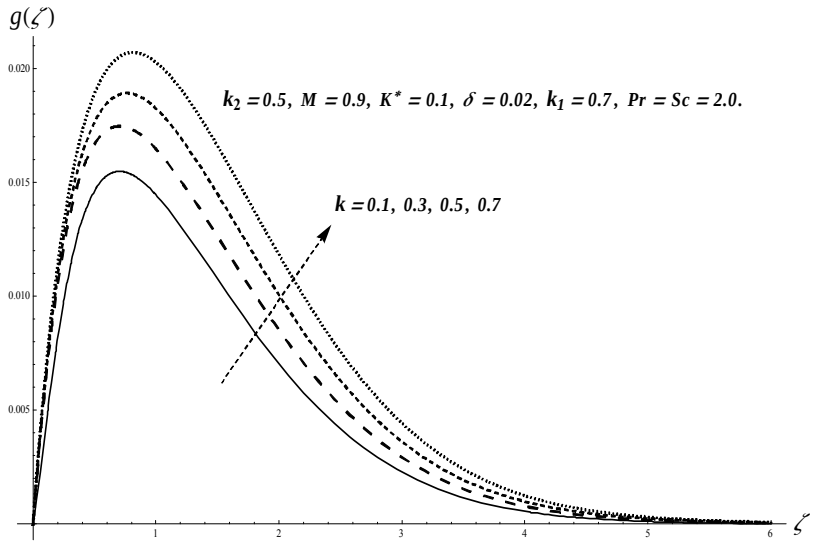

Fig. 7.5. Plots of $g(\zeta)$ for k.

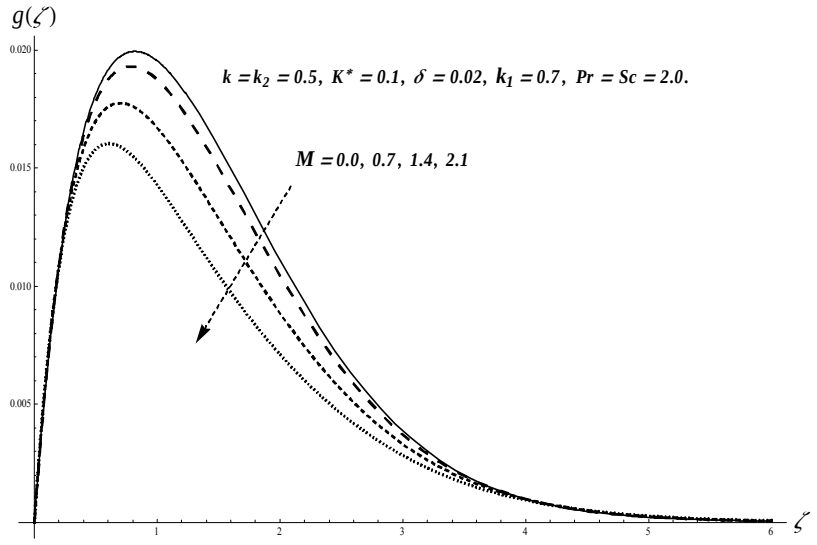

Fig. 7.6. Plots of $g(\zeta)$ for M.

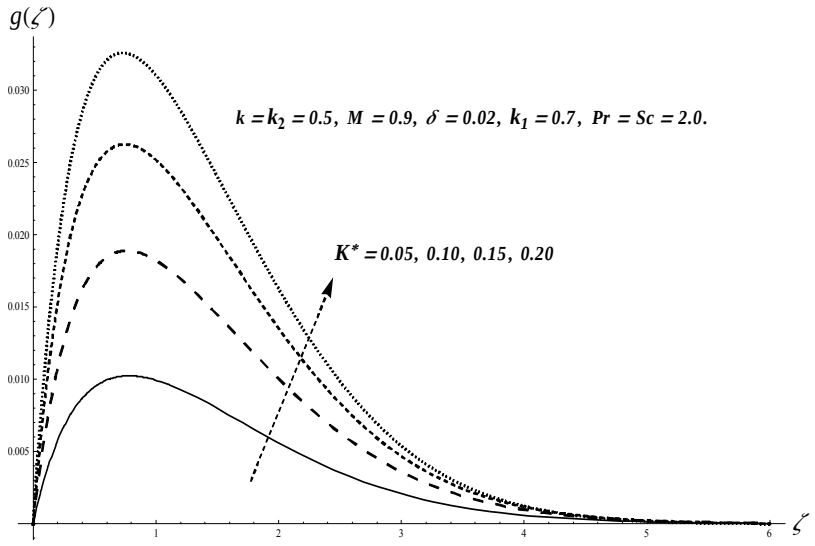

Fig. 7.7. Plots of $g(\zeta)$ for K.

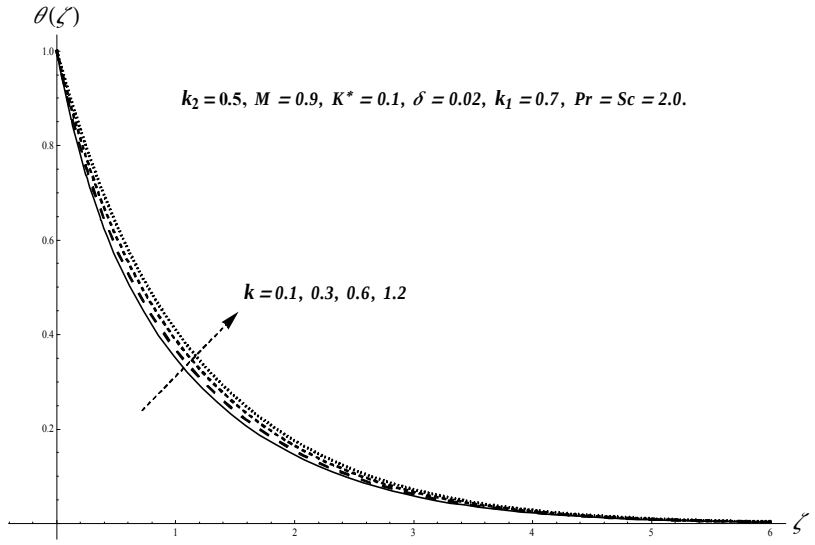

Fig. 7.8. Plots of $\theta(\zeta)$ for k.

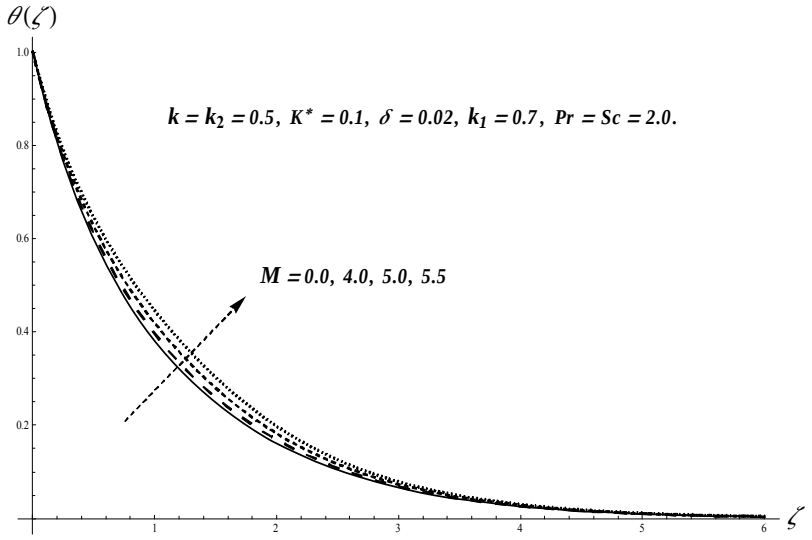

Fig. 7.9. Plots of $\theta(\zeta)$ for M.

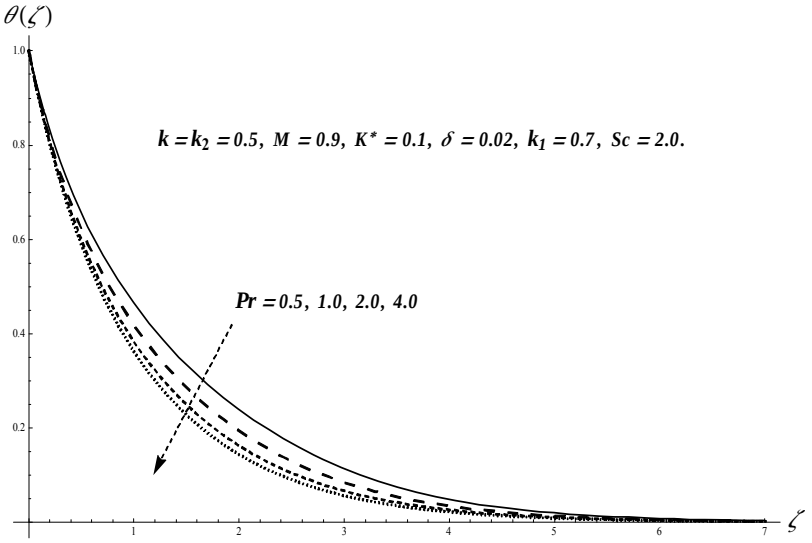

Fig. 7.10. Plots of $\theta(\zeta)$ for Pr.

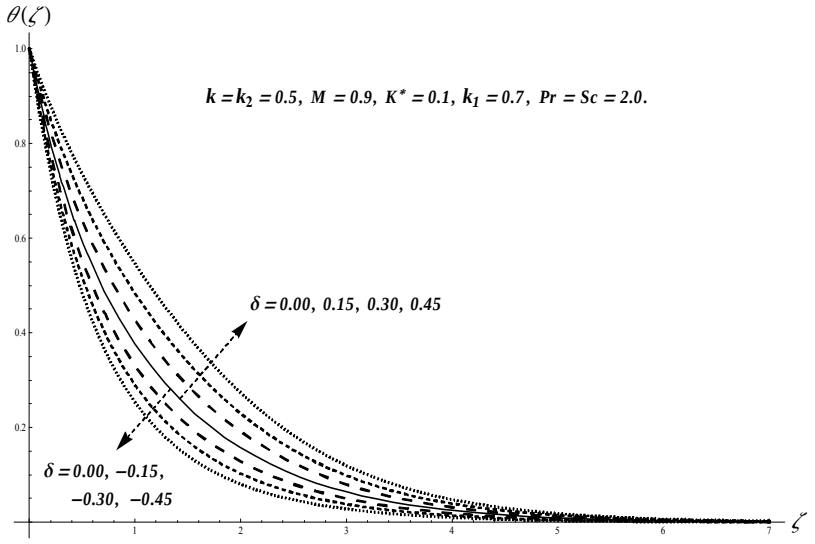

Fig. 7.11. Plots of $\theta(\zeta)$ for δ.

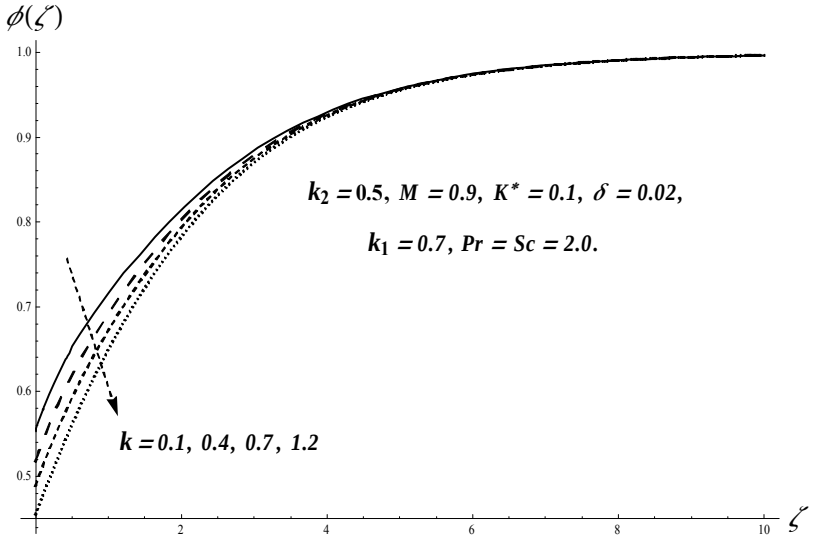

Fig. 7.12. Plots of $\phi(\zeta)$ for k.

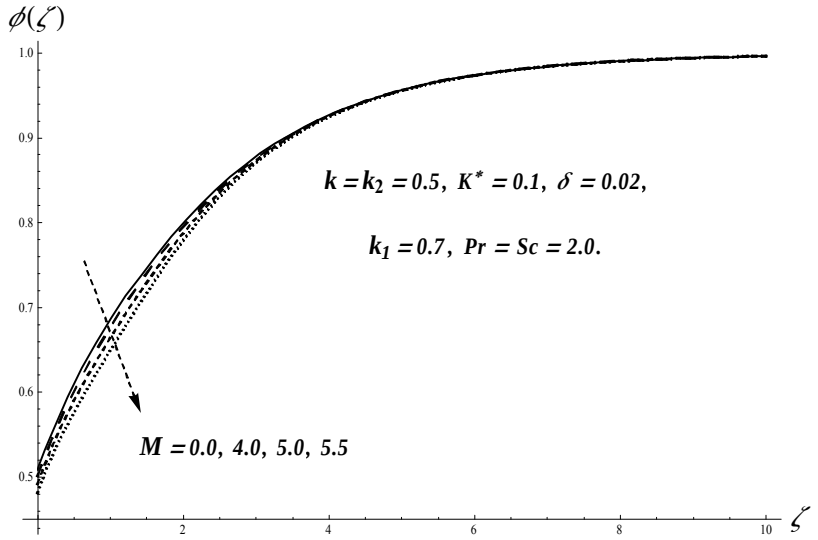

Fig. 7.13. Plots of $\phi(\zeta)$ for M.

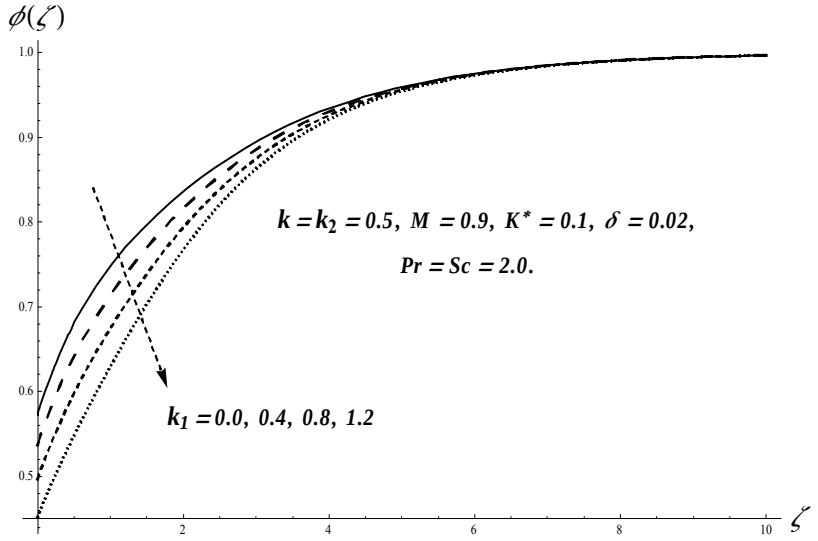

Fig. 7.14. Plots of $\phi(\zeta)$ for k_1.

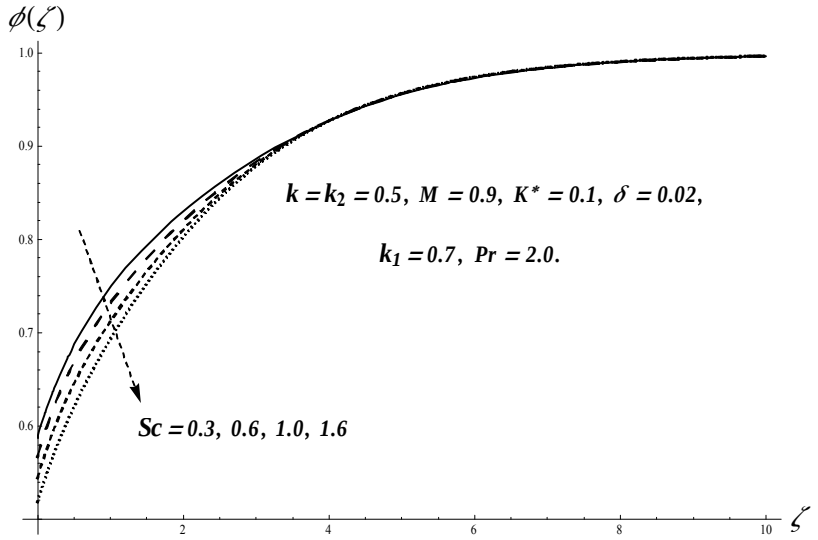

Fig. 7.15. Plots of $\phi(\zeta)$ for Sc.

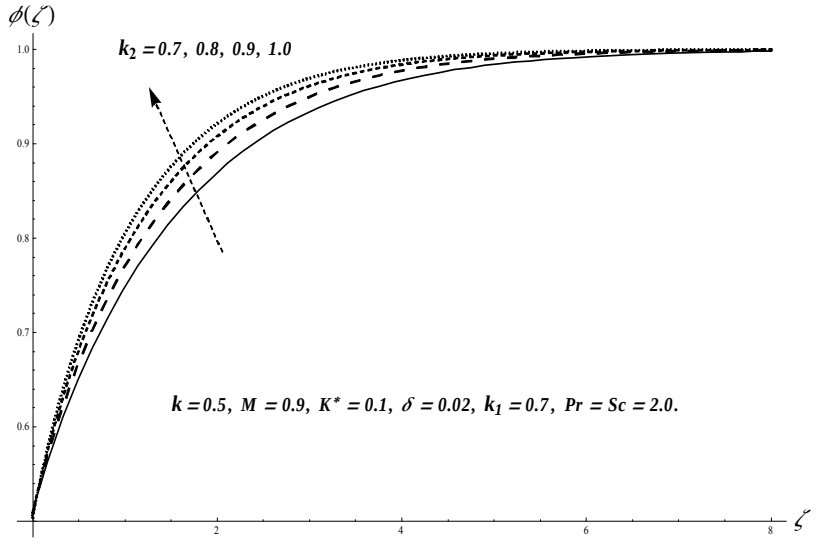

Fig. 7.16. Plots of $\phi(\zeta)$ for k_2.

Table 7.2. Numerical data for skin friction and couple stress coefficients for distinct values of k, M and K^*.

k	M	K^*	$-C_{fs_2}Re_{s_1}^{1/2}$	$C_mRe_{s_1}$
0.3	0.9	0.1	7.405	0.075
0.4			6.317	0.077
0.5			5.504	0.078
0.5	0.0	0.1	5.167	0.074
	0.5		5.289	0.075
	1.0		5.569	0.078
0.5	0.9	0.05	5.252	0.041
		0.10	5.502	0.077
		0.15	5.753	0.110

Table 7.3. Comparative values of $-C_{fs_2}Re_{s_1}^{1/2}$ for varying k when $K^* = M = m_0 = 0$.

k	$-C_{fs_2}Re_{s_1}^{1/2}$	
	HAM	Numerical [10]
5	0.7577	0.75763
10	0.8735	0.87349
20	0.9357	0.93561

Table 7.4. Numerical data for local Nusselt number for k, M, Pr and δ when $k_1 = 0.7$, $k_2 = 0.5$, $K^* = 0.1$ and $Sc = 2.0$.

k	M	Pr	δ	$Nu_s Re_{s_1}^{-1/2}$
0.3	0.9	2.0	0.02	1.399
0.4				1.255
0.5				1.158
0.5	0.0	2.0	0.02	1.163
	0.5			1.160
	1.0			1.153
0.5	0.9	1.0	0.02	1.023
		2.0		1.155
		3.0		1.207
0.5	0.9	2.0	0.00	1.192
			0.04	1.117
			0.08	1.037

7.4 Conclusions

Hydromagnetic flow of micropolar fluid due to a curved stretchable surface with homogeneous-heterogeneous reactions and heat generation/absorption are investigated. Main observations of presented research are listed below.

- Velocity distribution $f'(\zeta)$ shows reverse trend for curvature k and magnetic M parameters.
- Micro-rotation profile $g(\zeta)$ enhances for larger curvature k and material K^* parameters whereas opposite behavior is seen for magnetic paramter M.
- Temperature field $\theta(\zeta)$ is higher for larger curvature k and magnetic M parameters while opposite trend is seen for Prandtl number Pr.
- Effects of homogeneous k_1 and heterogeneous k_2 reaction parameters on concentration field $\phi(\zeta)$ are entirely reverse.

- Skin friction coefficient enlarges for higher magnetic M and material K^* parameters while reverse trend is noticed through curvature parameter k.
- Couple stress coefficient enhances for larger curvature k, magnetic M and material K^* parameters.
- Local Nusselt number is enhanced for larger material parameter K^* and Prandtl number Pr whereas opposite trend is seen for curvature k and heat generation/absorption δ parameters.

Chapter 8

Flow of Jeffrey nanofluid subject to MHD and heat generation/absorption

Current chapter investigates magnetohydrodynamic (MHD) flow of Jeffrey nanomaterial. Flow is due to a curved stretchable sheet. Novel features regarding thermophoresis and Brownian motion are considered. Heat transfer process is explored through heat generation/absorption effects. Jeffrey liquid is electrically conducted subject to uniform applied magnetic field. Boundary layer concept employed in mathematical development. The reduction of partial differential system to nonlinear ordinary differential system has been made by employing suitable variables. The obtained nonlinear systems have been computed and analyzed. The characteristics of various sundry parameters are studied through plots and numerical data. Moreover the physical quantities are numerically examined.

8.1 Formulation

Two-dimensional magnetohydrodynamic flow of Jeffrey nanomaterial fluid over a curved stretchable surface is examined. The curved stretchable sheet is coiled in a circle having radius R with stretching velocity $u = u_w$ and is taken in the $s-$direction. Brownian motion and thermophoresis effects are incorporated. Magnetic field (of strength B_0) is injected in radial direction.

There is no Hall current and electric field. Heat transfer process is explored through heat generation/absorption. The related expressions are

$$\frac{\partial}{\partial r}\left(\left(r+R\right)v\right)+R\frac{\partial u}{\partial s}=0, \tag{8.1}$$

$$\frac{1}{r+R}u^2=\frac{1}{\rho_f}\frac{\partial p}{\partial r}, \tag{8.2}$$

$$\begin{aligned} v\frac{\partial u}{\partial r}+\frac{R}{r+R}u\frac{\partial u}{\partial s}+\frac{1}{r+R}uv &= -\frac{1}{\rho_f}\frac{R}{r+R}\frac{\partial p}{\partial s} \\ &+\frac{\nu}{1+\lambda_1}\left(\begin{array}{c} \frac{\partial^2 u}{\partial r^2}+\frac{1}{r+R}\frac{\partial u}{\partial r}-\frac{1}{(r+R)^2}u \\ +\lambda_2\left(\begin{array}{c} \frac{\partial v}{\partial r}\frac{\partial^2 u}{\partial r^2}+v\frac{\partial^3 u}{\partial r^3} \\ +\frac{R}{r+R}\frac{\partial u}{\partial r}\frac{\partial^2 u}{\partial s\partial r}+\frac{R}{r+R}u\frac{\partial^3 u}{\partial s\partial r^2} \\ +\frac{1}{r+R}v\frac{\partial^2 u}{\partial r^2}-\frac{R}{(r+R)^2}\frac{\partial u}{\partial r}\frac{\partial u}{\partial s} \\ -\frac{1}{r+R}\frac{\partial v}{\partial r}\frac{\partial u}{\partial r}+\frac{1}{(r+R)^2}u\frac{\partial v}{\partial r} \end{array}\right) \end{array}\right) \\ &-\frac{\sigma B_0^2}{\rho_f}u, \end{aligned} \tag{8.3}$$

$$\begin{aligned} v\frac{\partial T}{\partial r}+\frac{R}{r+R}u\frac{\partial T}{\partial s} &= \frac{k_f}{\left(\rho c\right)_f}\left(\frac{\partial^2 T}{\partial r^2}+\frac{1}{r+R}\frac{\partial T}{\partial r}\right) \\ &+\tau\left(D_B\left(\frac{\partial C}{\partial r}\frac{\partial T}{\partial r}\right)+\frac{D_T}{T_\infty}\left(\frac{\partial T}{\partial r}\right)^2\right) \\ &+\frac{Q_0}{\left(\rho c\right)_f}\left(T-T_\infty\right), \end{aligned} \tag{8.4}$$

$$v\frac{\partial C}{\partial r}+\frac{R}{r+R}u\frac{\partial C}{\partial s}=D_B\left(\frac{\partial^2 C}{\partial r^2}+\frac{1}{r+R}\frac{\partial C}{\partial r}\right)+\frac{D_T}{T_\infty}\left(\frac{\partial^2 T}{\partial r^2}+\frac{1}{r+R}\frac{\partial T}{\partial r}\right), \tag{8.5}$$

with the boundary conditions

$$u=u_w=a_1 s,\ v=0,\ T=T_w,\ C=C_w \quad \text{at} \quad r=0, \tag{8.6}$$

$$u\to 0,\ \ \frac{\partial u}{\partial r}\to 0,\ \ T\to T_\infty,\ \ C\to C_\infty \quad \text{as} \quad r\to\infty. \tag{8.7}$$

Selecting

$$\left.\begin{array}{c} u = a_1 s f'(\zeta), \quad v = -\frac{R}{r+R}\sqrt{a_1 \upsilon} f(\zeta), \quad \zeta = \sqrt{\frac{a_1}{\upsilon}} r, \\ p = \rho_f a_1^2 s^2 P(\zeta), \quad \theta(\zeta) = \frac{T-T_\infty}{T_w - T_\infty}, \quad \phi(\zeta) = \frac{C-C_\infty}{C_w - C_\infty}. \end{array}\right\} \tag{8.8}$$

Expression (8.1) is identically verified and Eqs. $(8.2) - (8.7)$ yield

$$\frac{\partial P}{\partial \zeta} = \frac{f'^2}{\zeta + k}, \tag{8.9}$$

$$\begin{aligned} \frac{2k}{\zeta+k} P &= \frac{k}{\zeta+k} f f'' - \frac{k}{\zeta+k} f'^2 + \frac{k}{(\zeta+k)^2} f f' - M^2 f' \\ &\quad + \frac{1}{1+\lambda_1} \left(\begin{array}{c} f''' + \frac{1}{\zeta+k} f'' - \frac{1}{(\zeta+k)^2} f' \\ +\beta \left(\begin{array}{c} \frac{k}{\zeta+k} f''^2 - \frac{k}{\zeta+k} f f^{iv} \\ -\frac{k}{(\zeta+k)^3} \left(f f'' + f'^2 \right) + \frac{k}{(\zeta+k)^4} f f' \end{array} \right) \end{array} \right), \end{aligned} \tag{8.10}$$

$$\theta'' + \frac{\theta'}{\zeta+k} + \Pr \left(\frac{k}{\zeta+k} f\theta' + N_t \theta'^2 + N_b \theta' \phi' + \delta\theta \right) = 0, \tag{8.11}$$

$$\phi'' + \frac{1}{\zeta+k}\phi' + \frac{k}{\zeta+k} Sc f \phi' + \frac{N_t}{N_b} \left(\theta'' + \frac{1}{\zeta+k}\theta' \right) = 0, \tag{8.12}$$

$$\left.\begin{array}{c} f = 0, \quad f' = 1, \quad \theta = 1, \quad \phi = 1 \quad \text{at} \quad \zeta = 0, \\ f' \to 0, \quad f'' \to 0, \quad \theta \to 0, \quad \phi \to 0 \quad \text{as} \quad \zeta \to \infty. \end{array}\right\} \tag{8.13}$$

The parameters appearing in above equations can be expressed as follows:

$$\left.\begin{array}{c} k = R\sqrt{\frac{a_1}{\upsilon}}, \ M^2 = \frac{\sigma B_0^2}{a_1 \rho_f}, \ \Pr = \frac{\nu}{\alpha_1^*}, \ N_b = \frac{\tau D_B (C_w - C_\infty)}{\nu}, \\ \beta = a_1 \lambda_2, \ N_t = \frac{\tau D_T (T_w - T_\infty)}{T_\infty \nu}, \ \delta = \frac{Q_0}{a_1 (\rho c)_f}, \ Sc = \frac{\upsilon}{D_B}. \end{array}\right\} \tag{8.14}$$

Now eliminating pressure P from Eqs. (8.9) and (8.10), we get

$$\begin{aligned}
&f^{iv}+\frac{2}{\zeta+k}f'''-\frac{1}{(\zeta+k)^2}f''+\frac{1}{(\zeta+k)^3}f' \\
&+\beta\begin{pmatrix} \frac{k}{\zeta+k}\left(2f''f'''-ff^{v}-f'f^{iv}\right) \\ -\frac{k}{(\zeta+k)^3}\left(ff'''+3f'f''\right)+\frac{3k}{(\zeta+k)^4}\left(f'^2+ff''\right)-\frac{3k}{(\zeta+k)^5}ff' \end{pmatrix} \\
&+(1+\lambda_1)\begin{pmatrix} \frac{k}{\zeta+k}\left(ff'''-f'f''\right)+\frac{k}{(\zeta+k)^2}\left(ff''-f'^2\right) \\ -\frac{k}{(\zeta+k)^3}ff'-M^2\left(f''+\frac{1}{\zeta+k}f'\right) \end{pmatrix}=0.
\end{aligned} \tag{8.15}$$

Pressure P is given by

$$\begin{aligned}
P &= \frac{1}{2}\left(ff''-f'^2\right)+\frac{1}{2(\zeta+k)}ff' \\
&\quad+\frac{1}{1+\lambda_1}\begin{pmatrix} \frac{\zeta+k}{2k}f'''-\frac{1}{2k}f''-\frac{1}{2k(\zeta+k)}f' \\ +\beta\begin{pmatrix} \frac{1}{2}\left(f''^2-ff^{iv}\right) \\ -\frac{1}{2(\zeta+k)^2}\left(ff''+f'^2\right) \\ +\frac{1}{2(\zeta+k)^3}ff' \end{pmatrix}-M^2\frac{\zeta+k}{2k}f' \end{pmatrix}.
\end{aligned} \tag{8.16}$$

Physical quantities are

$$C_{f_{s_3}}=\frac{\tau_{rs_2}}{\frac{1}{2}\rho_f u_w^2}, \qquad Nu_s=\frac{sq_{w_r}}{k_f\left(T_w-T_\infty\right)}. \tag{8.17}$$

Here τ_{rs_2} and q_{w_r} stands for surface shear stress and heat flux respectively. These are

$$\left.\begin{aligned}
\tau_{rs_2}=\frac{\mu}{1+\lambda_1}\left(\begin{pmatrix} \frac{\partial u}{\partial r}-\frac{1}{r+R}u \\ +\lambda_2\begin{pmatrix} \frac{R}{r+R}u\frac{\partial^2 u}{\partial s\partial r}-\frac{R}{(r+R)^2}u\frac{\partial u}{\partial s}+v\frac{\partial^2 u}{\partial r^2} \\ -\frac{1}{r+R}v\frac{\partial u}{\partial r}+\frac{1}{(r+R)^2}uv \end{pmatrix} \end{pmatrix}\right|_{r=0}, \\
q_{w_r}=-k_f\left(\frac{\partial T}{\partial r}\right)\big|_{r=0}.
\end{aligned}\right\} \tag{8.18}$$

Dimensionless variables give

$$\left.\begin{aligned}
\frac{1}{2}C_{fs_3}\left(Re_{s_1}\right)^{1/2}=\frac{1}{1+\lambda_1}\left(f''(0)-\frac{1}{k}f'(0)+\beta\left(f'(0)f''(0)-\frac{1}{k^2}\left(f'(0)\right)^2\right)\right), \\
Nu_s\left(Re_{s_1}\right)^{-1/2}=-\theta'(0).
\end{aligned}\right\} \tag{8.19}$$

8.2 Solutions

The appropriate initial guesses $\left(f_{0_3},\ \theta_{0_1},\ \phi_{0_4}\right)$ in homotopic solutions are defined by

$$\left.\begin{aligned} f_{0_3}(\zeta) &= \exp(-\zeta) - \exp(-2\zeta), \\ \theta_{0_1}(\zeta) &= \exp(-\zeta), \\ \phi_{0_4}(\zeta) &= \exp(-\zeta), \end{aligned}\right\} \tag{8.20}$$

and auxiliary linear operators $\left(\mathcal{L}_{f_2},\ \mathcal{L}_{\theta_1},\ \mathcal{L}_{\phi_1}\right)$ are

$$\left.\begin{aligned} \mathcal{L}_{f_2} &= \tfrac{d^4 f}{d\zeta^4} - 5\tfrac{d^2 f}{d\zeta^2} + 4\tfrac{df}{d\zeta}, \\ \mathcal{L}_{\theta_1} &= \tfrac{d^2\theta}{d\zeta^2} - \theta, \\ \mathcal{L}_{\phi_1} &= \tfrac{d^2\phi}{d\zeta^2} - \phi. \end{aligned}\right\} \tag{8.21}$$

The above operators satisfy the following relations:

$$\left.\begin{aligned} \mathcal{L}_{f_2}\left[C_{30}^{*}\exp(\zeta) + C_{31}^{*}\exp(-\zeta) + C_{32}^{*}\exp(2\zeta) + C_{33}^{*}\exp(-2\zeta)\right] = 0, \\ \mathcal{L}_{\theta_1}\left[C_{34}^{*}\exp(\zeta) + C_{35}^{*}\exp(-\zeta)\right] = 0, \\ \mathcal{L}_{\phi_1}\left[C_{36}^{*}\exp(\zeta) + C_{37}^{*}\exp(-\zeta)\right] = 0, \end{aligned}\right\} \tag{8.22}$$

where C_i^{*} $(i = 30 - 37)$ elucidate the arbitrary constants.

8.2.1 Deformation problems at zeroth-order

$$(1-\breve{p})\mathcal{L}_{f_2}\left[\hat{f}(\zeta,\ \breve{p}) - f_{0_3}(\zeta)\right] = \breve{p}\hbar_f \mathcal{N}_{f_5}[\hat{f}(\zeta,\ \breve{p})], \tag{8.23}$$

$$(1-\breve{p})\mathcal{L}_{\theta_1}\left[\hat{\theta}(\zeta,\ \breve{p}) - \theta_{0_1}(\zeta)\right] = \breve{p}\hbar_\theta \mathcal{N}_{\theta_5}[\hat{f}(\zeta,\ \breve{p}),\ \hat{\theta}(\zeta,\ \breve{p}),\ \hat{\phi}(\zeta,\ \breve{p})], \tag{8.24}$$

$$(1-\breve{p})\mathcal{L}_{\phi_1}\left[\hat{\phi}(\zeta,\ \breve{p}) - \phi_{0_4}(\zeta)\right] = \breve{p}\hbar_\phi \mathcal{N}_{\phi_4}[\hat{f}(\zeta,\ \breve{p}),\ \hat{\theta}(\zeta,\ \breve{p}),\ \hat{\phi}(\zeta,\ \breve{p})], \tag{8.25}$$

$$\left.\begin{aligned} \hat{f}(0,\ \breve{p}) = 0, \quad \hat{f}'(\infty,\ \breve{p}) = 0, \quad \hat{f}'(0,\ \breve{p}) = 1, \quad \hat{f}''(\infty,\ \breve{p}) = 0, \\ \hat{\theta}(0,\ \breve{p}) = 1, \quad \hat{\theta}(\infty,\ \breve{p}) = 0, \quad \hat{\phi}(0,\ \breve{p}) = 1, \quad \hat{\phi}(\infty,\ \breve{p}) = 0, \end{aligned}\right\} \tag{8.26}$$

$$\mathcal{N}_{f_5}\left[\hat{f}(\zeta,\ \breve{p})\right] = \frac{\partial^4 \hat{f}}{\partial \zeta^4} + \left(\frac{2}{\zeta+k}\right)\frac{\partial^3 \hat{f}}{\partial \zeta^3} - \left(\frac{1}{\zeta+k}\right)^2 \frac{\partial^2 \hat{f}}{\partial \zeta^2} + \left(\frac{1}{\zeta+k}\right)^3 \frac{\partial \hat{f}}{\partial \zeta}$$
$$+\beta \begin{pmatrix} \frac{k}{\zeta+k}\left(2\frac{\partial^2 \hat{f}}{\partial \zeta^2}\frac{\partial^3 \hat{f}}{\partial \zeta^3} - \hat{f}\frac{\partial^5 \hat{f}}{\partial \zeta^5} - \frac{\partial \hat{f}}{\partial \zeta}\frac{\partial^4 \hat{f}}{\partial \zeta^4}\right) \\ -\frac{k}{(\zeta+k)^3}\left(3\frac{\partial \hat{f}}{\partial \zeta}\frac{\partial^2 \hat{f}}{\partial \zeta^2} + \hat{f}\frac{\partial^3 \hat{f}}{\partial \zeta^3}\right) + \frac{3k}{(\zeta+k)^4}\left(\hat{f}\frac{\partial^2 \hat{f}}{\partial \zeta^2} + \frac{\partial^2 \hat{f}}{\partial \zeta^2}\frac{\partial^2 \hat{f}}{\partial \zeta^2}\right) \\ -\frac{3k}{(\zeta+k)^5}\hat{f}\frac{\partial \hat{f}}{\partial \zeta} \end{pmatrix}$$
$$+(1+\lambda_1)\begin{pmatrix} \frac{k}{\zeta+k}\left(\hat{f}\frac{\partial^3 \hat{f}}{\partial \zeta^3} - \frac{\partial \hat{f}}{\partial \zeta}\frac{\partial^2 \hat{f}}{\partial \zeta^2}\right) + \frac{k}{(\zeta+k)^2}\left(\hat{f}\frac{\partial^2 \hat{f}}{\partial \zeta^2} - \frac{\partial \hat{f}}{\partial \zeta}\frac{\partial \hat{f}}{\partial \zeta}\right) \\ -\frac{k}{(\zeta+k)^3}\hat{f}\frac{\partial \hat{f}}{\partial \zeta} - M^2\left(\frac{1}{\zeta+k}\frac{\partial \hat{f}}{\partial \zeta} + \frac{\partial^2 \hat{f}}{\partial \zeta^2}\right) \end{pmatrix}, \quad (8.27)$$

$$\mathcal{N}_{\theta_5}\left[\hat{f}(\zeta,\ \breve{p}),\ \hat{\theta}(\zeta,\ \breve{p}),\ \hat{\phi}(\zeta,\ \breve{p})\right] = \frac{\partial^2 \hat{\theta}}{\partial \zeta^2} + \frac{1}{\zeta+k}\frac{\partial \hat{\theta}}{\partial \zeta} + \Pr\begin{pmatrix} \frac{k}{\zeta+k}\hat{f}\frac{\partial \hat{\theta}}{\partial \zeta} + N_b\frac{\partial \hat{\theta}}{\partial \zeta}\frac{\partial \hat{\phi}}{\partial \zeta} \\ +N_t\frac{\partial \hat{\theta}}{\partial \zeta}\frac{\partial \hat{\theta}}{\partial \zeta} + \delta\hat{\theta} \end{pmatrix}, \quad (8.28)$$

$$\mathcal{N}_{\phi_4}\left[\hat{f}(\zeta,\ \breve{p}),\ \hat{\theta}(\zeta,\ \breve{p}),\ \hat{\phi}(\zeta,\ \breve{p})\right] = \frac{\partial^2 \hat{\phi}}{\partial \zeta^2} + \frac{1}{\zeta+k}\frac{\partial \hat{\phi}}{\partial \zeta} + \frac{k}{\zeta+k}Sc\hat{f}\frac{\partial \hat{\phi}}{\partial \zeta}$$
$$+\frac{N_t}{N_b}\left(\frac{\partial^2 \hat{\theta}}{\partial \zeta^2} + \frac{1}{\zeta+k}\frac{\partial \hat{\theta}}{\partial \zeta}\right). \quad (8.29)$$

Setting $\breve{p}=0$ and $\breve{p}=1$ one obtains

$$\hat{f}(\zeta,\ 0) = f_{0_3}(\zeta), \qquad \hat{f}(\zeta,\ 1) = f(\zeta), \quad (8.30)$$

$$\hat{\theta}(\zeta,\ 0) = \theta_{0_1}(\zeta), \qquad \hat{\theta}(\zeta,\ 1) = \theta(\zeta), \quad (8.31)$$

$$\hat{\phi}(\zeta,\ 0) = \phi_{0_4}(\zeta), \qquad \hat{\phi}(\zeta,\ 1) = \phi(\zeta). \quad (8.32)$$

When $\breve{p}$ changes from 0 to 1 then $\hat{f}(\zeta,\breve{p})$, $\hat{\theta}(\zeta,\breve{p})$ and $\hat{\phi}(\zeta,\breve{p})$ display alteration from primary approximations $f_{0_3}(\zeta)$, $\theta_{0_1}(\zeta)$ and $\phi_{0_4}(\zeta)$ to desired ultimate solutions $f(\zeta)$, $\theta(\zeta)$ and $\phi(\zeta)$.

8.2.2 Deformation problems at $\hat{m}$th-order

$$\mathcal{L}_{f_2}\left[f_{\hat{m}}(\zeta) - \chi_{\hat{m}} f_{\hat{m}-1}(\zeta)\right] = \hbar_f \tilde{\mathcal{R}}^{\hat{m}}_{f_5}(\zeta), \quad (8.33)$$

$$\mathcal{L}_{\theta_1}\left[\theta_{\hat{m}}(\zeta) - \chi_{\hat{m}} \theta_{\hat{m}-1}(\zeta)\right] = \hbar_\theta \tilde{\mathcal{R}}^{\hat{m}}_{\theta_5}(\zeta), \quad (8.34)$$

$$\mathcal{L}_{\phi_1}\left[\phi_{\hat{m}}(\zeta) - \chi_{\hat{m}} \phi_{\hat{m}-1}(\zeta)\right] = \hbar_\phi \tilde{\mathcal{R}}^{\hat{m}}_{\phi_4}(\zeta), \quad (8.35)$$

$$\left.\begin{array}{c} f_{\hat{m}}(0) = \theta_{\hat{m}}(0) = \theta_{\hat{m}}(\infty) = \phi_{\hat{m}}(0) = \phi_{\hat{m}}(\infty) = 0, \\ f'_{\hat{m}}(0) = f'_{\hat{m}}(\infty) = f''_{\hat{m}}(\infty) = 0, \end{array}\right\} \tag{8.36}$$

$$\begin{aligned} \tilde{\mathcal{R}}^{\hat{m}}_{f_5}(\zeta) &= f''''_{\hat{m}-1} + \left(\frac{2}{\zeta+k}\right) f'''_{\hat{m}-1} - \left(\frac{1}{\zeta+k}\right)^2 f''_{\hat{m}-1} + \left(\frac{1}{\zeta+k}\right)^3 f'_{\hat{m}-1} \\ &+\beta \left(\begin{array}{c} \frac{k}{\zeta+k}\left(2\sum\limits_{\hat{k}=0}^{\hat{m}-1}\left(f''_{\hat{m}-1-\hat{k}} f'''_{\hat{k}}\right) - \sum\limits_{\hat{k}=0}^{\hat{m}-1}\left(f_{\hat{m}-1-`k} f^{v}_{k}\right) - \sum\limits_{k=0}^{\hat{m}-1}\left(f'_{\hat{m}-1-k} f^{iv}_{k}\right)\right) \\ -\frac{k}{(\zeta+k)^3}\left(3\sum\limits_{k=0}^{\hat{m}-1}\left(f'_{\hat{m}-1-k} f''_{k}\right) + \sum\limits_{k=0}^{\hat{m}-1}\left(f_{\hat{m}-1-k} f'''_{k}\right)\right) \\ +\frac{3k}{(\zeta+k)^4}\left(\sum\limits_{k=0}^{\hat{m}-1}\left(f''_{\hat{m}-1-k} f''_{k}\right) + \sum\limits_{k=0}^{\hat{m}-1}\left(f_{\hat{m}-1-k} f''_{k}\right)\right) \\ -\frac{3k}{(\zeta+k)^5}\sum\limits_{k=0}^{\hat{m}-1}\left(f_{\hat{m}-1-k} f'_{k}\right) \end{array} \right) \\ &+(1+\lambda_1) \left(\begin{array}{c} \frac{k}{\zeta+k}\left(\sum\limits_{k=0}^{\hat{m}-1}\left(f_{\hat{m}-1-k} f'''_{k}\right) - \sum\limits_{k=0}^{\hat{m}-1}\left(f'_{\hat{m}-1-k} f''_{k}\right)\right) \\ +\frac{k}{(\zeta+k)^2}\left(\sum\limits_{k=0}^{\hat{m}-1}\left(f_{\hat{m}-1-k} f''_{k}\right) - \sum\limits_{k=0}^{\hat{m}-1}\left(f'_{\hat{m}-1-k} f'_{k}\right)\right) \\ -\frac{k}{(\zeta+k)^3}\sum\limits_{k=0}^{\hat{m}-1}\left(f_{\hat{m}-1-k} f'_{k}\right) - M^2\left(\frac{1}{\zeta+k} f'_{\hat{m}-1} + f''_{\hat{m}-1}\right) \end{array} \right), \end{aligned} \tag{8.37}$$

$$\tilde{\mathcal{R}}^{\hat{m}}_{\theta_5}(\zeta) = \theta''_{\hat{m}-1} + \frac{1}{\zeta+k}\theta'_{\hat{m}-1} + \mathrm{Pr}\left(\begin{array}{c} \frac{k}{\zeta+k}\sum\limits_{k=0}^{\hat{m}-1} f_{\hat{m}-1-k}\theta'_k + N_b \sum\limits_{k=0}^{\hat{m}-1}\theta'_{\hat{m}-1-k}\phi'_k \\ +N_t \sum\limits_{k=0}^{\hat{m}-1}\theta'_{\hat{m}-1-k}\theta'_k + \delta\theta_{\hat{m}-1} \end{array} \right), \tag{8.38}$$

$$\begin{aligned} \tilde{\mathcal{R}}^{\hat{m}}_{\phi_4}(\zeta) &= \phi''_{\hat{m}-1} + \frac{1}{\zeta+k}\phi'_{\hat{m}-1} + \frac{k}{\zeta+k}\left(Sc\sum_{k=0}^{\hat{m}-1} f_{\hat{m}-1-k}\phi'_k\right) \\ &+\frac{N_t}{N_b}\left(\phi''_{\hat{m}-1} + \frac{1}{\zeta+k}\phi'_{\hat{m}-1}\right), \end{aligned} \tag{8.39}$$

The following expressions are derived via Taylor's series expansion:

$$\hat{f}(\zeta,\ \breve{p}) = f_{0_3}(\zeta) + \sum_{\hat{m}=1}^{\infty} f_{\hat{m}}(\zeta)\breve{p}^{\hat{m}},\ f_{\hat{m}}(\zeta) = \frac{1}{\hat{m}!}\frac{\partial^{\hat{m}}\hat{f}(\zeta,\ \breve{p})}{\partial\breve{p}^{\hat{m}}}\bigg|_{\breve{p}\,=\,0}, \tag{8.40}$$

$$\hat{\theta}(\zeta,\ \breve{p}) = \theta_{0_1}(\zeta) + \sum_{\hat{m}=1}^{\infty} \theta_{\hat{m}}(\zeta)\breve{p}^{\hat{m}},\ \theta_{\hat{m}}(\zeta) = \frac{1}{\hat{m}!}\frac{\partial^{\hat{m}}\hat{\theta}(\zeta,\ \breve{p})}{\partial\breve{p}^{\hat{m}}}\bigg|_{\breve{p}\,=\,0}, \tag{8.41}$$

$$\hat{\phi}(\zeta,\ \breve{p}) = \phi_{0_4}(\zeta) + \sum_{\hat{m}=1}^{\infty} \phi_{\hat{m}}(\zeta)\breve{p}^{\hat{m}},\ \phi_{\hat{m}}(\zeta) = \frac{1}{\hat{m}!}\frac{\partial^{\hat{m}}\hat{\phi}(\zeta,\ \breve{p})}{\partial \breve{p}^{\hat{m}}}\bigg|_{\breve{p}\,=\,0}. \tag{8.42}$$

The convergence concerning Eqs. (8.40) – (8.42) firmly depend for appropriate choices of $\hbar_f$, $\hbar_\theta$ and $\hbar_\phi$. Choosing appropriate values of $\hbar_f$, $\hbar_\theta$ and $\hbar_\phi$ so that Eqs. (8.40) – (8.42) converge at $\breve{p} = 1$ then

$$f(\zeta) = f_{0_3}(\zeta) + \sum_{\hat{m}=1}^{\infty} f_{\hat{m}}(\zeta), \tag{8.43}$$

$$\theta(\zeta) = \theta_{0_1}(\zeta) + \sum_{\hat{m}=1}^{\infty} \theta_{\hat{m}}(\zeta), \tag{8.44}$$

$$\phi(\zeta) = \phi_{0_4}(\zeta) + \sum_{\hat{m}=1}^{\infty} \phi_{\hat{m}}(\zeta). \tag{8.45}$$

In terms of special solutions ($f^*_{\hat{m}}$, $\theta^*_{\hat{m}}$, $\phi^*_{\hat{m}}$), the general solutions ($f_{\hat{m}}$, $\theta_{\hat{m}}$, $\phi_{\hat{m}}$) of the Eqs. (8.33) – (8.35) are defined by the following expressions:

$$f_{\hat{m}}(\zeta) = f^*_{\hat{m}}(\zeta) + C^*_{30}\exp(\zeta) + C^*_{31}\exp(-\zeta) + C^*_{32}\exp(2\zeta) + C^*_{33}\exp(-2\zeta), \tag{8.46}$$

$$\theta_{\hat{m}}(\zeta) = \theta^*_{\hat{m}}(\zeta) + C^*_{34}\exp(\zeta) + C^*_{35}\exp(-\zeta), \tag{8.47}$$

$$\phi_{\hat{m}}(\zeta) = \phi^*_{\hat{m}}(\zeta) + C^*_{36}\exp(\zeta) + C^*_{37}\exp(-\zeta), \tag{8.48}$$

in which the constants C^*_i $(i = 30 - 37)$ through the boundary conditions (8.36) are given by

$$\left.\begin{array}{c} C^*_{30} = C^*_{32} = C^*_{34} = C^*_{36} = 0, \\ C^*_{33} = \frac{\partial f^*_{\hat{m}}(\zeta)}{\partial \zeta}\Big|_{\zeta\,=\,0} + f^*_{\hat{m}}(0),\ C^*_{31} = -C^*_{33} - f^*_{\hat{m}}(0), \\ C^*_{35} = -\,\theta^*_{\hat{m}}(0),\ C^*_{37} = -\,\phi^*_{\hat{m}}(0). \end{array}\right\} \tag{8.49}$$

8.2.3 Convergence analysis

The derived homotopic solutions contain nonzero auxiliary parameters $\hbar_f$, $\hbar_\theta$ and $\hbar_\phi$. Such auxiliary variables have significant role to tune and govern the convergence of obtained homotopic results. To get the acceptable values of such parameters, the $\hbar-$ curves at 20th order of deformations are tabulated. Fig. 8.1 shows the appropriate ranges as $-1.5 \leq \hbar_f \leq 0.0$, $-1.7 \leq \hbar_\theta \leq -0.5$ and $-1.6 \leq \hbar_\phi \leq -0.2$. Table 8.1 indicates that the 10th order of deforma-

tion is sufficient for convergent approximate solutions.

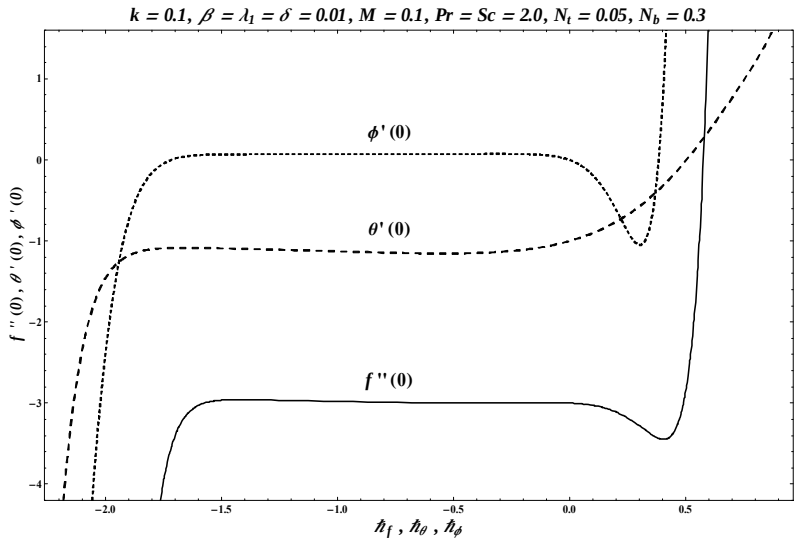

Fig. 8.1 : $\hbar-$plots of $f(\zeta)$, $\theta(\zeta)$ and $\phi(\zeta)$.

Table 8.1. Solutions convergence when $k = 0.1$, $\beta = \lambda_1 = \delta = 0.01$, $M = 0.1$, $\Pr = Sc = 2.0$, $N_t = 0.05$ and $N_b = 0.3$.

Order of approximations	$-f''(0)$	$-\theta'(0)$	$\phi'(0)$
1	2.9912	1.0461	0.2519
5	3.0028	1.1418	0.2532
10	3.0034	1.1573	0.2538
15	3.0034	1.1573	0.2538
20	3.0034	1.1573	0.2538

8.3 Discussion

This portion has been organized to explore the effects of several effective parameters including dimensionless radius of curvature parameter k, Deborah number β, the ratio of relaxation to retardation times λ_1, Prandtl number Pr, magnetic variable M, Brownian motion variable N_b, thermophoresis variable N_t, heat generation/absorption δ and Schmidt parameter Sc on dimensionless velocity $f'(\zeta)$, temperature $\theta(\zeta)$ and concentration $\phi(\zeta)$ profiles. Effects of curvature parameter k, Deborah number β, ratio of relaxation to retardation times λ_1 and

magnetic parameter M on velocity distribution $f'(\zeta)$ are presented in the Figs. $8.2-8.5$ respectively. Fig. 8.2 elucidates the impact of dimensionless radius of curvature parameter k on velocity distribution $f'(\zeta)$. Velocity and associated layer thickness are enhanced for higher curvature parameter k. Variation of Deborah number β on velocity $f'(\zeta)$ is sketched in Fig. 8.3. Larger Deborah number β causes an increment in the velocity field $f'(\zeta)$ and corresponding layer thickness. Fig. 8.4 depicts the effect of ratio of relaxation to retardation times λ_1 on velocity distribution $f'(\zeta)$. An increment in λ_1 ultimately give rise in relaxation time that depicts that the material require much more time to come in equilibrium system from perturbed system and hence the fluid velocity. Variation of M on velocity $f'(\zeta)$ is displayed in Fig. 8.5. An increase in the magnitude of magnetic paramter generates a resistive force and ultimately velocity field reduces. Effects of curvature parameter k, magnetic parameter M, Prandtl number Pr, thermophoresis parameter N_t, Brownian motion parameter N_b and heat generation/absorption variable δ on dimensionless temperature profile $\theta(\zeta)$ are displayed in the Figs. $8.6-8.11$ respectively. Fig. 8.6 elucidates variation of dimensionless radius of curvature parameter k on $\theta(\zeta)$. Both temperature $\theta(\zeta)$ and associated layer thickness are enhanced for higher curvature parameter k. Impact of magnetic variable M on temperature profile $\theta(\zeta)$ is displayed in Fig. 8.7. Clearly both temperature and corresponding layer thickness are higher for bigger M. Fig. 8.8 shows variation of Prandtl number Pr on temperature $\theta(\zeta)$. Larger Prandtl number Pr shows a reduction in temperature field and related layer thickness. Influence of N_t on $\theta(\zeta)$ is sketched in Fig. 8.9. By increasing thermophoresis parameter N_t, both temperature distribution $\theta(\zeta)$ and related layer thickness are enhanced. Fig. 8.10 elucidates the impacts of N_b on $\theta(\zeta)$. Both temperature and associated layer thickness are greater for bigger Brownian motion variable N_b. Influence of heat generation/absorption variable δ on temperature profile $\theta(\zeta)$ is shown in Fig. 8.11. Here temperature and corresponding layer thickness are enhanced for higher $\delta\ (>0)$ whereas opposite trend is observed for larger $\delta\ (<0)$. Contributions of curvature parameter k, magnetic parameter M, thermophoresis parameter N_t, Brownian motion N_b and Schmidt parameter Sc on $\phi(\zeta)$ are presented in Figs. $8.12-8.16$ respectively. By enhancing curvature parameter k, magnetic parameter M and thermophoresis parameter N_t, the concentration distribution $\phi(\zeta)$ is increased while reverse behavior is seen for Brownian motion parameter N_b and Schmidt parameter Sc. Table 8.2 elucidates numerical

data for skin friction through k, β, λ_1 and M. It is examined that skin friction is enhanced for larger β and M while the reverse trend is noticed through k and λ_1. Table 8.3 is displayed to analyze the numerical data for local Nusselt number for distinct k, Pr, δ, N_b and N_t. Clearly local Nusselt number is lower for higher curvature parameter k, Prandtl number Pr, Brownian motion N_b and thermophoresis N_t paramters.

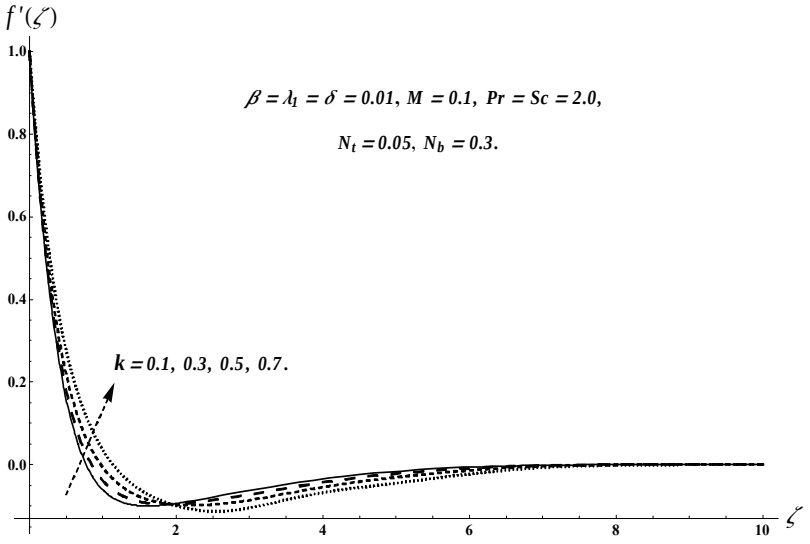

Fig. 8.2. Plots of $f'(\zeta)$ for k.

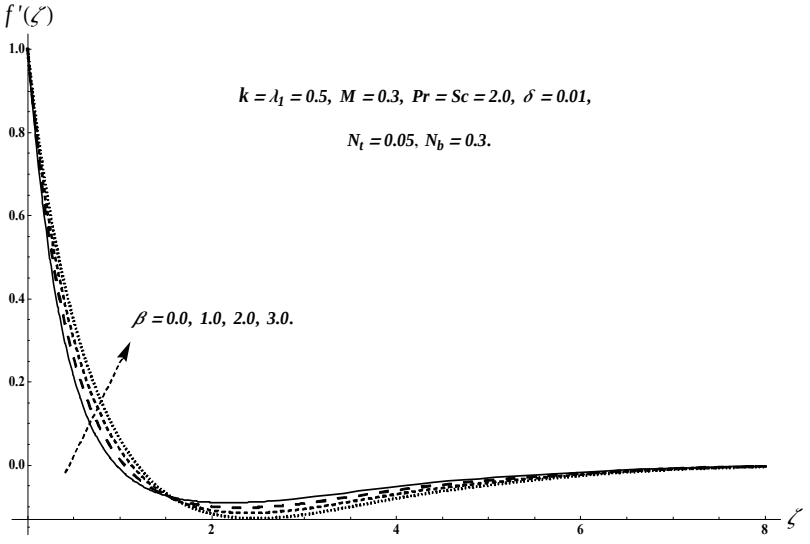

Fig. 8.3. Plots of $f'(\zeta)$ for β.

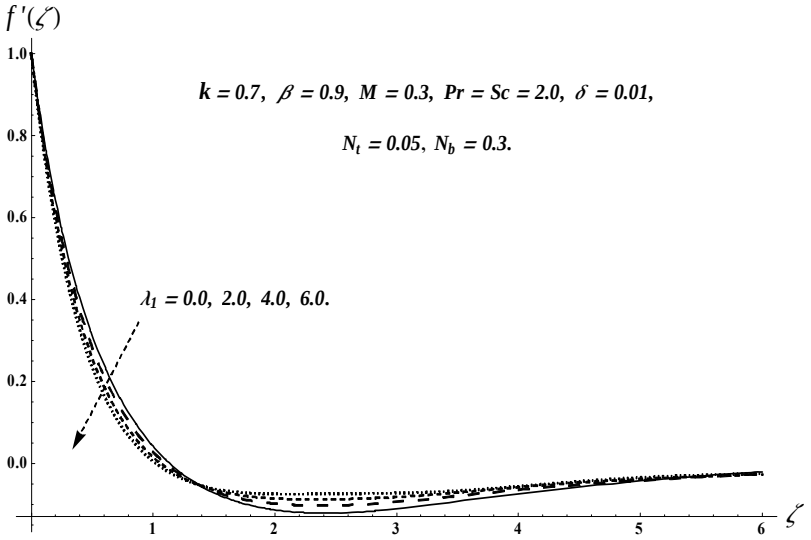

Fig. 8.4. Plots of $f'(\zeta)$ for λ_1.

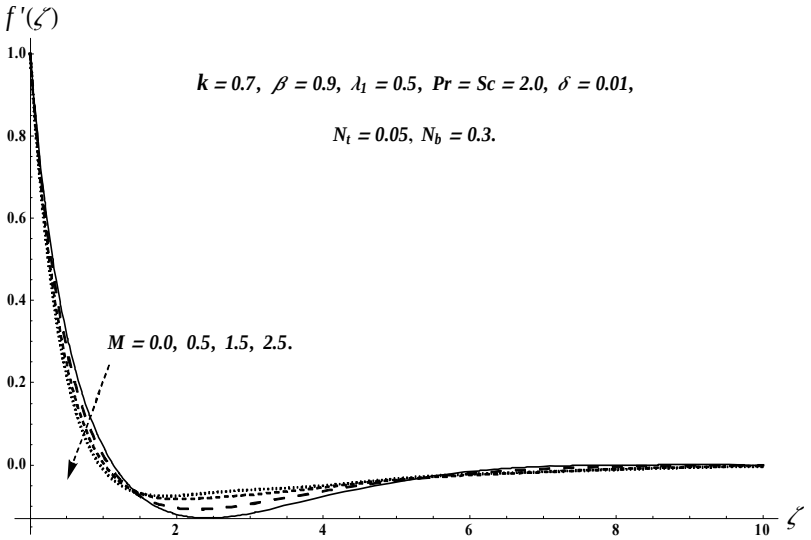

Fig. 8.5. Plots of $f'(\zeta)$ for M.

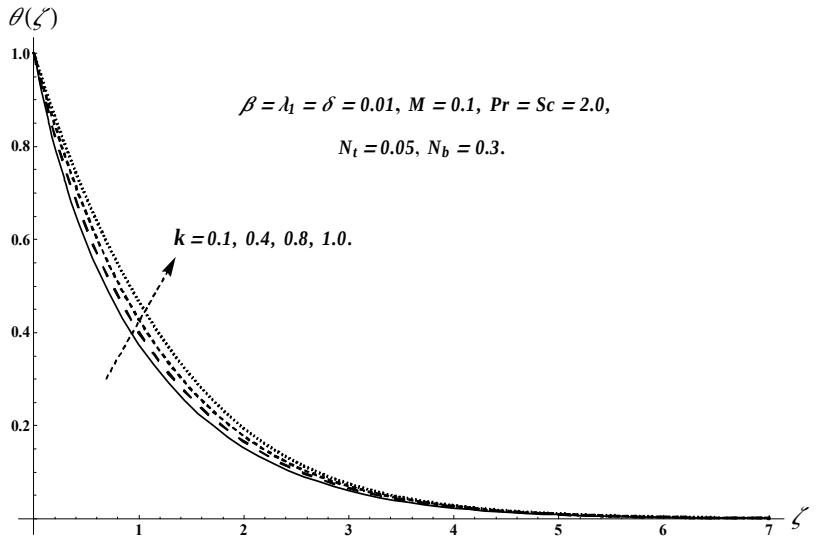

Fig. 8.6. Plots of $\theta(\zeta)$ for k.

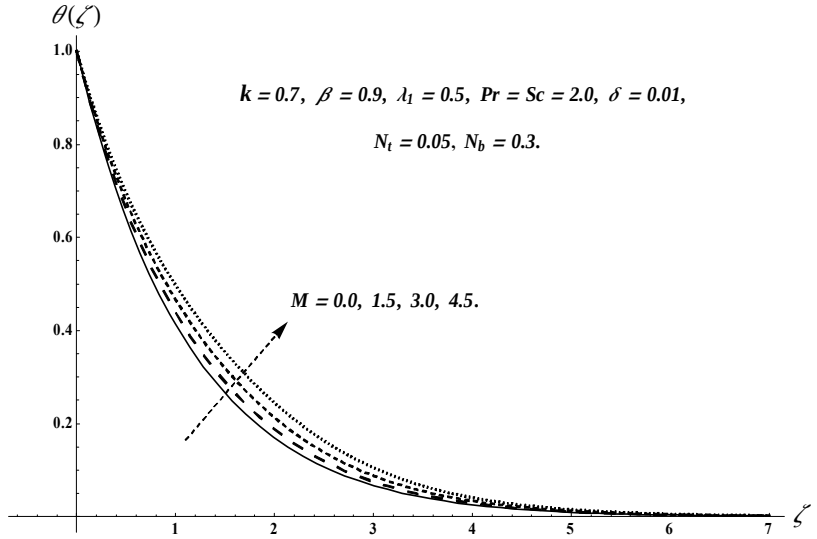

Fig. 8.7. Plots of $\theta(\zeta)$ for M.

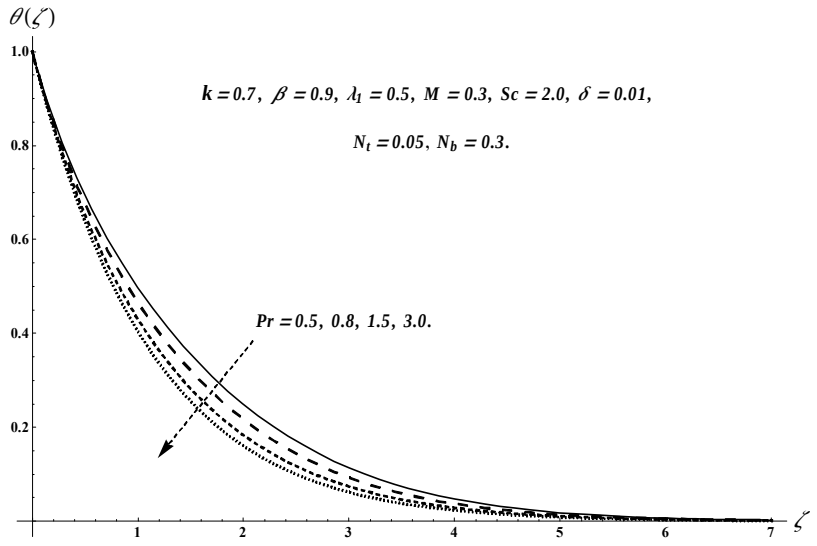

Fig. 8.8. Plots of $\theta(\zeta)$ for Pr.

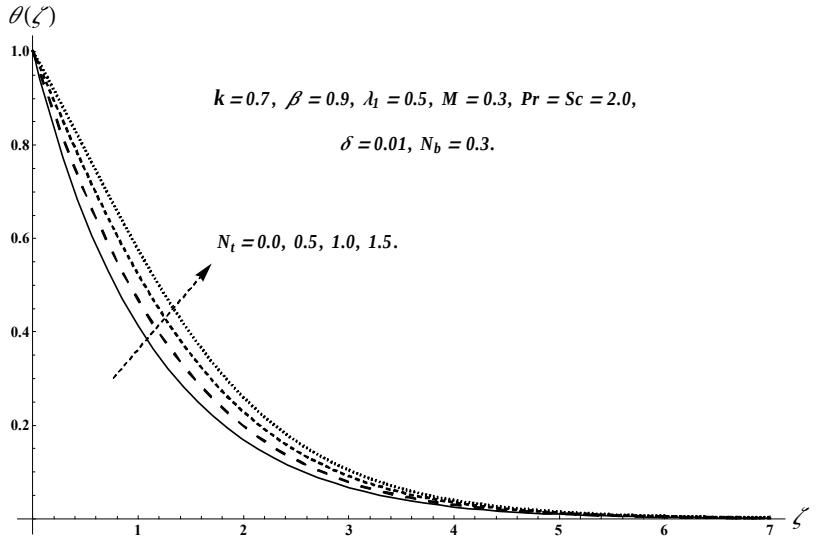

Fig. 8.9. Plots of $\theta(\zeta)$ for N_t.

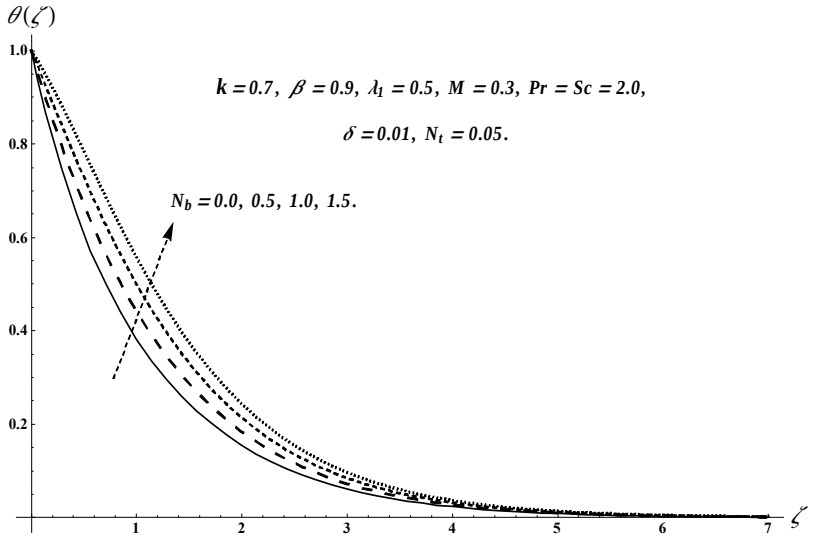

Fig. 8.10. Plots of $\theta(\zeta)$ for N_b.

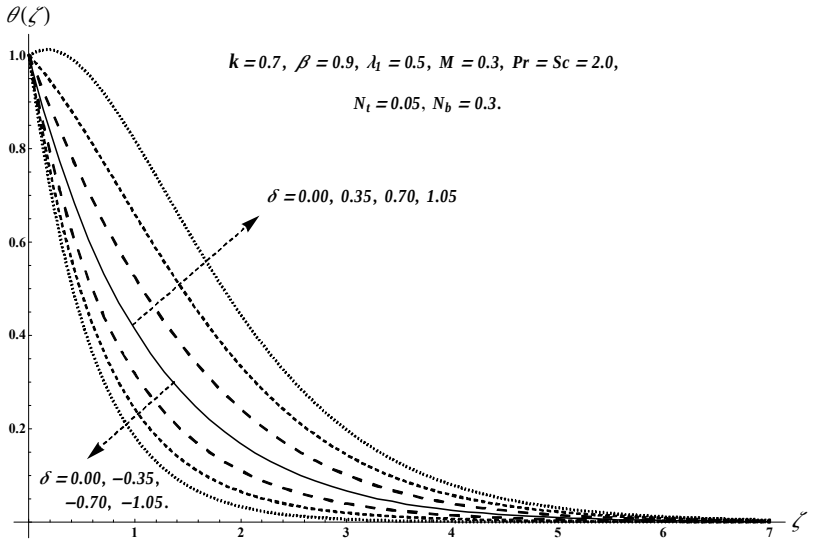

Fig. 8.11. Plots of $\theta(\zeta)$ for δ.

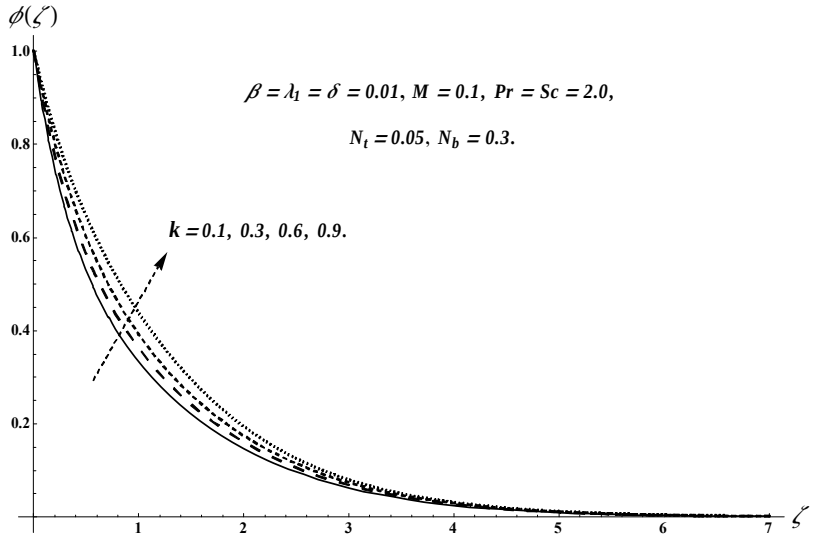

Fig. 8.12. Plots of $\phi(\zeta)$ for k.

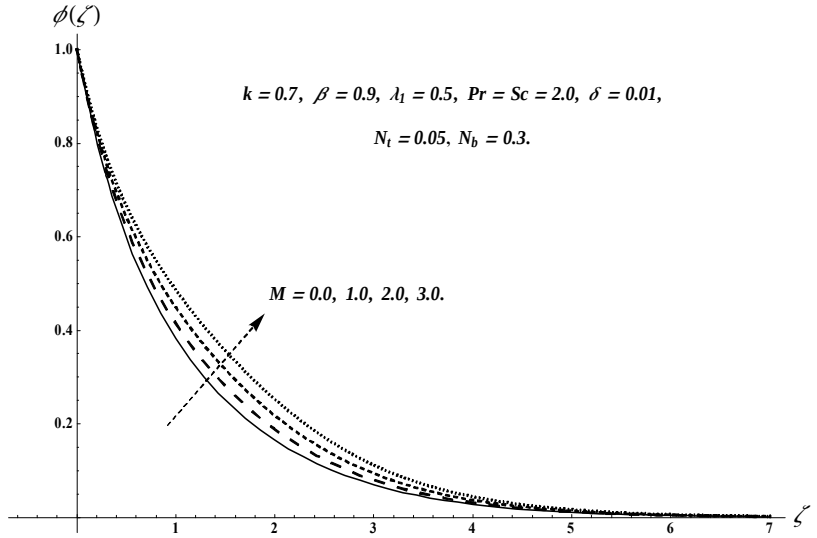

Fig. 8.13. Plots of $\phi(\zeta)$ for M.

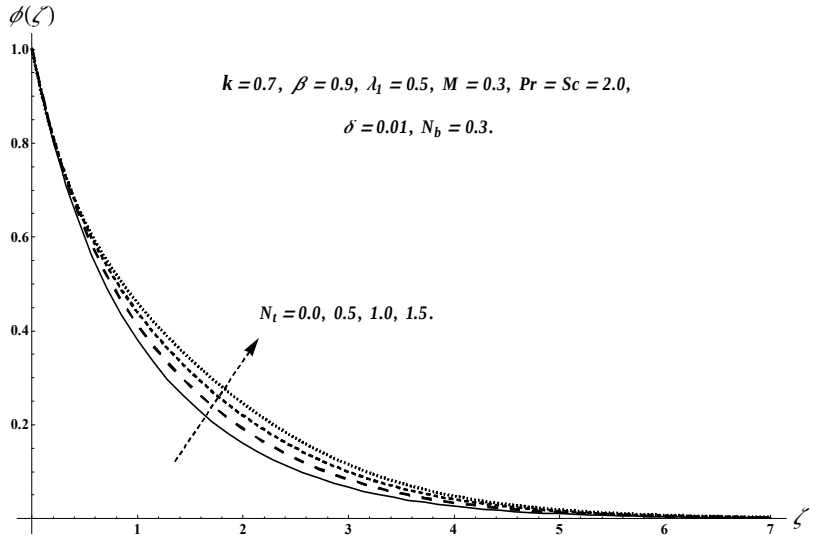

Fig. 8.14. Plots of $\phi(\zeta)$ for N_t.

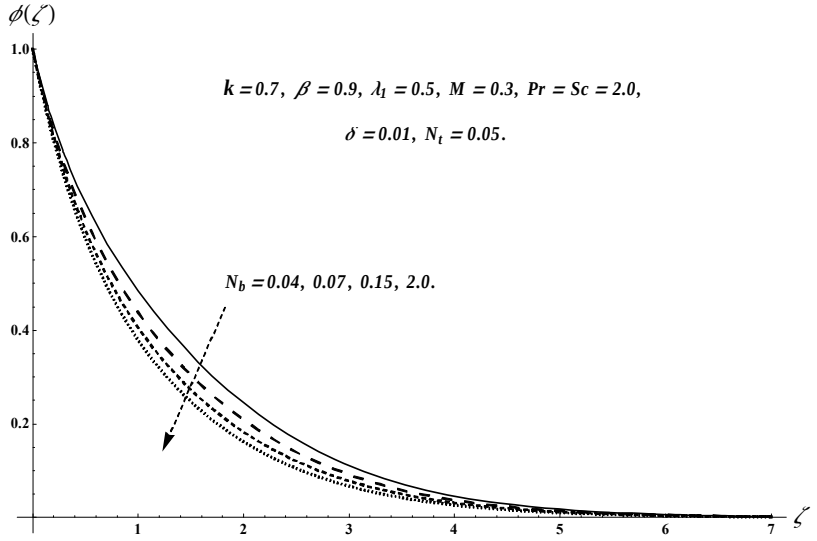

Fig. 8.15. Plots of $\phi(\zeta)$ for N_b.

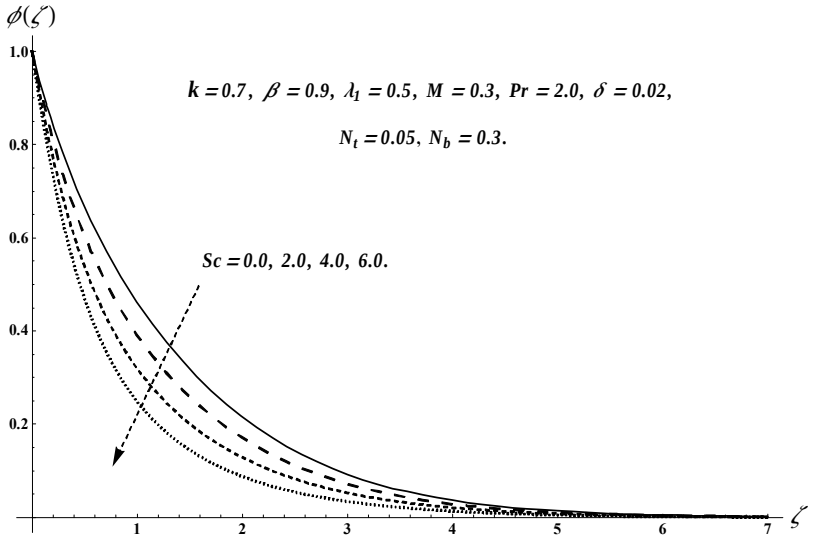

Fig. 8.16. Plots of $\phi(\zeta)$ for Sc.

Table 8.2. Numerical data of skin friction coefficient for distinct values of k, β, λ_1 and M.

k	β	λ_1	M	$-\frac{1}{2}C_{fs_3}\left(Re_{s_1}\right)^{1/2}$
0.1	0.1	0.1	0.1	12.0182
0.2				7.4196
0.3				5.8319
0.1	0.1	0.1	0.1	12.0182
	0.3			12.7076
	0.5			13.3944
0.1	0.1	0.1	0.1	12.0182
		0.2		11.0170
		0.3		10.1699
0.1	0.1	0.1	0.1	12.0182
			0.4	12.0267
			0.7	12.0351

Table 8.3. Numerical data of local Nusselt number for distinct values of k, N_t, Pr, N_b and δ when $\beta = \lambda_1 = M = 0.1$ and $Sc = 2.0$.

k	Pr	N_t	N_b	δ	$Nu_s Re_{s_1}^{-1/2}$
0.1	2.0	0.05	0.3	0.01	1.3762
0.2					1.2099
0.3					1.0807
0.1	1.0	0.05	0.3	0.01	1.7834
	2.0				1.3762
	3.0				1.2067
0.1	2.0	0.05	0.3	0.01	1.3762
		0.10			1.3476
		0.15			1.3196
0.1	2.0	0.05	0.3	0.01	1.3762
			0.7		1.1508
			1.1		0.9457
0.1	2.0	0.05	0.3	0.01	1.3762
				0.02	1.3561
				0.03	1.3357

8.4 Conclusions

Hydromagnetic flow of Jeffrey nanomaterial due to a curved stretchable surface with heat generation/absorption is investigated. Main observations of presented research are listed below.

- Velocity distribution $f'(\zeta)$ is enhanced for higher values of k and β whereas reverse trend is seen for λ_1 and M.
- Larger thermophoresis N_t and Brownian motion N_b parameters show higher temperature field $\theta(\zeta)$ while opposite behavior is seen for Prandtl number Pr.
- Concentration field $\phi(\zeta)$ is higher for larger curvature k, magnetic M and thermophoresis N_t parameters whereas opposite trend is observed for Brownian motion parameter N_b and

Schmidt number Sc.

- Skin friction is enhanced via β and M while the reverse trend is noticed through k and λ_1.
- Local Nusselt number is lowered for higher curvature parameter k, Prandtl number Pr, Brownian motion N_b and thermophoresis N_t paramters.

Chapter 9

Flow due to a convectively heated nonlinear curved stretchable surface having homogeneous-heterogeneous reactions

The objective of current chapter is to provide a treatment of viscous fluid flow induced by nonlinear curved stretchable surface. Concept of homogeneous and heterogeneous reactions has been utilized. Heat transfer process is explored through convective heating mechanism. Boundary layer approximation is employed in the mathematical development. The reduction of partial differential system to nonlinear ordinary differential system has been made by employing suitable variables. The obtained nonlinear system of equations has been solved and analyzed. The characteristics of various sundry parameters are examined and discussed graphically. Further the physical quantities like surface drag force and local Nusselt number are computed numerically.

9.1 Formulation

Ongoing formulation examine the two-dimensional (2D) flow of viscous fluid by a nonlinear curved stretchable sheet which is coiled in a circle having radius R. The curved surface is stretchable with non-linear velocity ($u_w(s) = a_1 s^n$) along the arc length direction. The distance R of the stretching curved surface from the origin determines the shape of curved surface i.e., for higher value of $R\,(\to \infty)$ the surface tends to flat. The surface of stretching curved sheet is warmed by convection from a heated fluid at temperature T_f which yields a convective heat transfer coefficient h_f. Further two chemical species A_1 and B_1 for homogeneous and heterogeneous reactions respectively are taken into account. For cubic autocatalysis, the homogeneous reaction is given by

$$A_1 + 2B_1 \to 3B_1, \qquad \text{rate} = k_c a b^2, \tag{9.1}$$

whereas the heterogeneous reaction on the catalyst surface is

$$A_1 \to B_1, \qquad \text{rate} = k_s a, \tag{9.2}$$

The boundary layer equations governing the current flow are

$$\frac{\partial}{\partial r}\left((r+R)\,v\right) + R\frac{\partial u}{\partial s} = 0, \tag{9.3}$$

$$\frac{1}{r+R}u^2 = \frac{1}{\rho_f}\frac{\partial p}{\partial r}, \tag{9.4}$$

$$\begin{aligned} v\frac{\partial u}{\partial r} + \frac{R}{r+R}u\frac{\partial u}{\partial s} + \frac{1}{r+R}uv &= -\frac{1}{\rho_f}\frac{R}{r+R}\frac{\partial p}{\partial s} \\ &\quad +\nu\left(\frac{\partial^2 u}{\partial r^2} + \frac{1}{r+R}\frac{\partial u}{\partial r} - \frac{1}{(r+R)^2}u\right), \end{aligned} \tag{9.5}$$

$$\rho_f c_p\left(v\frac{\partial T}{\partial r} + \frac{R}{r+R}u\frac{\partial T}{\partial s}\right) = k_f\left(\frac{1}{r+R}\frac{\partial T}{\partial r} + \frac{\partial^2 T}{\partial r^2}\right), \tag{9.6}$$

$$v\frac{\partial a}{\partial r} + \frac{R}{r+R}u\frac{\partial a}{\partial s} = D_{A_1}\left(\frac{1}{r+R}\frac{\partial a}{\partial r} + \frac{\partial^2 a}{\partial r^2}\right) - k_c a b^2, \tag{9.7}$$

$$v\frac{\partial b}{\partial r}+\frac{R}{r+R}u\frac{\partial b}{\partial s}=D_{B_1}\left(\frac{1}{r+R}\frac{\partial b}{\partial r}+\frac{\partial^2 b}{\partial r^2}\right)+k_c ab^2, \tag{9.8}$$

with the boundary conditions

$$\left.\begin{array}{c} u=u_w(s)=a_1 s^n,\ v=0,\ -k_f\frac{\partial T}{\partial r}=h_f\left(T_f-T\right), \\ D_A\frac{\partial a}{\partial r}=k_s a,\ D_B\frac{\partial b}{\partial r}=-k_s a \end{array}\right\} \text{ at } r=0, \tag{9.9}$$

$$u\to 0,\quad \frac{\partial u}{\partial r}\to 0,\quad T\to T_\infty,\quad a\to a_0,\quad b\to 0 \text{ as } \ r\to\infty. \tag{9.10}$$

Here n the power-law stretching index ($n=1$ corresponds to linear stretching, $n\neq 1$ correspond to non-linear stretching whereas $n=0$ gives linear stretching surface). Moreover for the case of curved surface pressure is no longer consistent within the boundary layer. Using the following transformations

$$\left.\begin{array}{c} u=a_1 s^n f'(\zeta),\quad v=-\frac{R}{r+R}\sqrt{a_1\upsilon s^{n-1}}\left(\frac{n+1}{2}f(\zeta)+\frac{n-1}{2}\zeta f'(\zeta)\right),\quad \zeta=\sqrt{\frac{a_1 s^{n-1}}{\upsilon}}r, \\ p=\rho_f a_1^2 s^{2n}P(\zeta),\quad k=\sqrt{\frac{a_1 s^{n-1}}{\upsilon}}R,\quad \theta(\zeta)=\frac{T-T_\infty}{T_f-T_\infty},\quad a=a_0\phi(\zeta),\quad b=a_0 h(\zeta). \end{array}\right\} \tag{9.11}$$

Eq. (9.3) is symmetrically verified and Eqs. (9.4) – (9.10) yield

$$\frac{\partial P}{\partial\zeta}=\frac{f'^2}{\zeta+k}, \tag{9.12}$$

$$\begin{aligned}\frac{2nk}{\zeta+k}P+\frac{(n-1)\zeta k}{2(\zeta+k)}\frac{\partial P}{\partial\zeta} &= f'''+\frac{f''}{\zeta+k}-\frac{f'}{(\zeta+k)^2}-\left(\frac{2nk+(n+1)\zeta}{2(\zeta+k)^2}\right)kf'^2 \\ &\quad +\frac{(n+1)k}{2(\zeta+k)}ff''+\frac{(n+1)k}{2(\zeta+k)^2}ff',\end{aligned} \tag{9.13}$$

$$\frac{1}{\mathrm{Pr}}\left(\theta''+\frac{\theta'}{\zeta+k}\right)+\frac{k}{\zeta+k}\left(\frac{n+1}{2}\right)f\theta'=0, \tag{9.14}$$

$$\frac{1}{Sc}\left(\phi''+\frac{\phi'}{\zeta+k}\right)+\frac{k}{\zeta+k}\left(\frac{n+1}{2}\right)f\phi'-k_1\phi h^2=0, \tag{9.15}$$

$$\frac{\delta_1}{Sc}\left(h''+\frac{h'}{\zeta+k}\right)+\frac{k}{\zeta+k}\left(\frac{n+1}{2}\right)fh'+k_1\phi h^2=0, \tag{9.16}$$

$$\left.\begin{array}{c} f=0, \quad f'=1, \quad \theta'=-\gamma_t\left(1-\theta\right), \quad \phi'=k_2\phi, \quad \delta_1 h'=-k_2\phi \quad \text{at} \quad \zeta=0, \\ f'\to 0, \quad f''\to 0, \quad \theta\to 0, \quad \phi\to 1, \quad h\to 0 \quad \text{as} \quad \zeta\to\infty, \end{array}\right\} \tag{9.17}$$

where k stands for dimensionless curvature parameter, k_1 for strength of homogeneous reaction, k_2 for strength of heterogeneous reaction and γ_t for Biot number and. These parameters can be expressed as follows:

$$k=R\sqrt{\frac{a_1 s^{n-1}}{\upsilon}},\ k_1=\frac{a_0^2 k_c}{a_1 s^{n-1}},\ k_2=\frac{k_s}{D_{A_1}}\sqrt{\frac{\upsilon}{a_1 s^{n-1}}},\ \gamma_t=\frac{h_f}{k_f}\sqrt{\frac{\upsilon}{a_1 s^{n-1}}}. \tag{9.18}$$

Now eliminating pressure P from equations (9.12) and (9.13), we get

$$f^{iv}+\frac{2f'''}{\zeta+k}-\frac{f''}{\left(\zeta+k\right)^2}+\frac{f'}{\left(\zeta+k\right)^3}+\frac{\left(n+1\right)k}{2\left(\zeta+k\right)}ff'''+\frac{\left(n+1\right)k}{2\left(\zeta+k\right)^2}ff''-\frac{\left(n+1\right)k}{2\left(\zeta+k\right)^3}ff'$$

$$-\frac{\left(3n-1\right)}{2\left(\zeta+k\right)^2}kf'^2-\frac{\left(3n-1\right)}{2\left(\zeta+k\right)}kf'f''=0. \tag{9.19}$$

Pressure P can be calculated from Eq. (9.13) as

$$P=\frac{\zeta+k}{2nk}\left(\begin{array}{c} f'''+\frac{f''}{\zeta+k}-\frac{f'}{\left(\zeta+k\right)^2}-\left(\frac{2nk+\left(n+1\right)\zeta}{2}+\left(\frac{n-1}{2}\right)\zeta\right)\frac{k}{\left(\zeta+k\right)^2}f'^2 \\ +\frac{\left(n+1\right)k}{2\left(\zeta+k\right)}ff''+\frac{\left(n+1\right)k}{2\left(\zeta+k\right)^2}ff' \end{array}\right). \tag{9.20}$$

When $D_{A_1}=D_{B_1}$ then $\delta_1=1$ and so

$$\phi\left(\zeta\right)+h\left(\zeta\right)=1. \tag{9.21}$$

Now Eqs. (9.15) and (9.16) yield

$$\frac{1}{Sc}\left(\phi''+\frac{\phi'}{\zeta+k}\right)+\frac{k}{\zeta+k}\left(\frac{n+1}{2}\right)f\phi'-k_1\phi\left(1-\phi\right)^2=0, \tag{9.22}$$

with the boundary conditions

$$\phi'\left(0\right)=k_2\phi\left(0\right), \quad \phi\left(\infty\right)\to 1. \tag{9.23}$$

The definitions of surface drag and heat transfer rate are

$$C_{f_{s_1}} = \frac{\tau_{rs_1}}{\rho_f u_w^2}, \qquad Nu_s = \frac{sq_{w_r}}{k_f\left(T_w - T_\infty\right)}, \tag{9.24}$$

with

$$\left.\begin{aligned} \tau_{rs_1} &= \mu\left(\frac{\partial u}{\partial r} - \frac{u}{r+R}\right)\Big|_{r=0}, \\ q_{w_r} &= -k_f\left(\frac{\partial T}{\partial r}\right)\Big|_{r=0}. \end{aligned}\right\} \tag{9.25}$$

Expressions of skin friction coefficient and local Nusselt number are

$$\left.\begin{aligned} C_{fs_1} Re_{s_2}^{1/2} &= f''(0) - \tfrac{1}{k} f'(0), \\ Nu_s Re_{s_2}^{-1/2} &= -\theta'(0), \end{aligned}\right\} \tag{9.26}$$

where $\mathrm{Re}_{s_2} = \frac{a_1 s^{n+1}}{\upsilon}$ stands for local Reynolds number.

9.2 Solutions

Initial approximations $\left(f_{0_3},\ \theta_{0_3},\ \phi_{0_3}\right)$ for homotopic solutions are defined by

$$\left.\begin{aligned} f_{0_3}(\zeta) &= \exp(-\zeta) - \exp(-2\zeta), \\ \theta_{0_3}(\zeta) &= \left(\tfrac{\gamma_t}{1+\gamma_t}\right)\exp(-\zeta), \\ \phi_{0_3}(\zeta) &= 1 - \tfrac{1}{2}\exp(-k_2\zeta), \end{aligned}\right\} \tag{9.27}$$

and auxiliary linear operators $\left(\mathcal{L}_{f_2},\ \mathcal{L}_{\theta_1},\ \mathcal{L}_{\phi_1}\right)$ are

$$\mathcal{L}_{f_2} = \frac{d^4 f}{d\zeta^4} - 5\frac{d^2 f}{d\zeta^2} + 4\frac{df}{d\zeta}, \quad \mathcal{L}_{\theta_1} = \frac{d^2\theta}{d\zeta^2} - \theta, \quad \mathcal{L}_{\phi_1} = \frac{d^2\phi}{d\zeta^2} - \phi. \tag{9.28}$$

The above operators satisfy the following relations:

$$\left.\begin{aligned} \mathcal{L}_{f_2}\left[C_{38}^* \exp(\zeta) + C_{39}^* \exp(-\zeta) + C_{40}^* \exp(2\zeta) + C_{41}^* \exp(-2\zeta)\right] &= 0, \\ \mathcal{L}_{\theta_1}\left[C_{42}^* \exp(\zeta) + C_{43}^* \exp(-\zeta)\right] &= 0, \\ \mathcal{L}_{\phi_1}\left[C_{44}^* \exp(\zeta) + C_{45}^* \exp(-\zeta)\right] &= 0, \end{aligned}\right\} \tag{9.29}$$

in which C_i^* $(i = 38 - 45)$ elucidate the arbitrary constants.

9.2.1 Deformation problems at zeroth-order

$$(1-\breve{p})\mathcal{L}_{f_2}\left[\hat{f}(\zeta,\ \breve{p})-f_{0_3}(\zeta)\right]=\breve{p}\hbar_f\mathcal{N}_{f_6}[\hat{f}(\zeta,\ \breve{p})], \tag{9.30}$$

$$(1-\breve{p})\mathcal{L}_{\theta_1}\left[\hat{\theta}(\zeta,\ \breve{p})-\theta_{0_3}(\zeta)\right]=\breve{p}\hbar_\theta\mathcal{N}_{\theta_6}[\hat{f}(\zeta,\ \breve{p}),\ \hat{\theta}(\zeta,\ \breve{p})], \tag{9.31}$$

$$(1-\breve{p})\mathcal{L}_{\phi_1}\left[\hat{\phi}(\zeta,\ \breve{p})-\phi_{0_3}(\zeta)\right]=\breve{p}\hbar_\phi\mathcal{N}_{\phi_5}[\hat{f}(\zeta,\ \breve{p}),\ \hat{\phi}(\zeta,\ \breve{p})], \tag{9.32}$$

$$\left.\begin{array}{c}\hat{f}(0,\ \breve{p})=0,\quad \hat{\theta}'(0,\ \breve{p})=-\gamma_t\left(1-\hat{\theta}(0,\ \breve{p})\right),\quad \hat{f}'(0,\ \breve{p})=1,\quad \hat{\phi}'(0,\ \breve{p})=k_2\hat{\phi}(0,\ \breve{p})\\ \hat{f}'(\infty,\ \breve{p})=0,\quad \hat{\theta}(\infty,\ \breve{p})=0,\quad \hat{f}''(\infty,\ \breve{p})=0,\quad \hat{\phi}(\infty,\ \breve{p})=1,\end{array}\right\} \tag{9.33}$$

$$\begin{aligned}\mathcal{N}_{f_6}\left[\hat{f}(\zeta,\ \breve{p})\right] &= \frac{\partial^4\hat{f}}{\partial\zeta^4}+\left(\frac{2}{\zeta+k}\right)\frac{\partial^3\hat{f}}{\partial\zeta^3}-\left(\frac{1}{\zeta+k}\right)^2\frac{\partial^2\hat{f}}{\partial\zeta^2}+\left(\frac{1}{\zeta+k}\right)^3\frac{\partial\hat{f}}{\partial\zeta}\\ &\quad+\frac{(n+1)\,k}{2\,(\zeta+k)}\hat{f}\frac{\partial^3\hat{f}}{\partial\zeta^3}+\frac{(n+1)\,k}{2\,(\zeta+k)^2}\hat{f}\frac{\partial^2\hat{f}}{\partial\zeta^2}-\frac{(n+1)\,k}{2\,(\zeta+k)^3}\hat{f}\frac{\partial\hat{f}}{\partial\zeta}\\ &\quad-\frac{(3n-1)}{2\,(\zeta+k)^2}k\frac{\partial\hat{f}}{\partial\zeta}\frac{\partial\hat{f}}{\partial\zeta}-\frac{(3n-1)}{2\,(\zeta+k)}k\frac{\partial\hat{f}}{\partial\zeta}\frac{\partial^2\hat{f}}{\partial\zeta^2},\end{aligned} \tag{9.34}$$

$$\mathcal{N}_{\theta_6}\left[\hat{f}(\zeta,\ \breve{p}),\ \hat{\theta}(\zeta,\ \breve{p})\right]=\frac{\partial^2\hat{\theta}}{\partial\zeta^2}+\frac{1}{\zeta+k}\frac{\partial\hat{\theta}}{\partial\zeta}+\mathrm{Pr}\,\frac{k}{\zeta+k}\left(\frac{n+1}{2}\right)\hat{f}\frac{\partial\hat{\theta}}{\partial\zeta}, \tag{9.35}$$

$$\begin{aligned}\mathcal{N}_{\phi_5}\left[\hat{f}(\zeta,\ \breve{p}),\ \hat{\phi}(\zeta,\ \breve{p})\right] &= \frac{\partial^2\hat{\phi}}{\partial\zeta^2}+\frac{1}{\zeta+k}\frac{\partial\hat{\phi}}{\partial\zeta}+Sc\frac{k}{\zeta+k}\left(\frac{n+1}{2}\right)\hat{f}\frac{\partial\hat{\phi}}{\partial\zeta}\\ &\quad-k_1Sc\hat{\phi}\left(1-\hat{\phi}\right)^2.\end{aligned} \tag{9.36}$$

Setting $\breve{p}=0$ and $\breve{p}=1$ one obtains

$$\hat{f}(\zeta,\ 0)=f_{0_3}(\zeta),\qquad \hat{f}(\zeta,\ 1)=f(\zeta), \tag{9.37}$$

$$\hat{\theta}(\zeta,\ 0)=\theta_{0_3}(\zeta),\qquad \hat{\theta}(\zeta,\ 1)=\theta(\zeta), \tag{9.38}$$

$$\hat{\phi}(\zeta,\ 0)=\phi_{0_3}(\zeta),\qquad \hat{\phi}(\zeta,\ 1)=\phi(\zeta). \tag{9.39}$$

When $\breve{p}$ varies from 0 to 1 then $\hat{f}(\zeta,\breve{p})$, $\hat{\theta}(\zeta,\breve{p})$ and $\hat{\phi}(\zeta,\breve{p})$ display alteration from primary approximations $f_{0_3}(\zeta)$, $\theta_{0_3}(\zeta)$ and $\phi_{0_3}(\zeta)$ to desired ultimate solutions $f(\zeta)$, $\theta(\zeta)$ and $\phi(\zeta)$.

9.2.2 Deformation problems at $\hat{m}$th-order

$$\mathcal{L}_{f_6}\left[f_{\hat{m}}(\zeta)-\chi_{\hat{m}}f_{\hat{m}-1}(\zeta)\right]=\hbar_f\tilde{\mathcal{R}}^{\hat{m}}_{f_6}(\zeta), \tag{9.40}$$

$$\mathcal{L}_{\theta_6}\left[\theta_{\hat{m}}(\zeta)-\chi_{\hat{m}}\theta_{\hat{m}-1}(\zeta)\right]=\hbar_\theta\tilde{\mathcal{R}}^{\hat{m}}_{\theta_6}(\zeta), \tag{9.41}$$

$$\mathcal{L}_{\phi_5}\left[\phi_{\hat{m}}(\zeta)-\chi_{\hat{m}}\phi_{\hat{m}-1}(\zeta)\right]=\hbar_\phi\tilde{\mathcal{R}}^{\hat{m}}_{\phi_5}(\zeta), \tag{9.42}$$

$$\left.\begin{array}{c}\theta'_{\hat{m}}(0)-\gamma_t\theta_{\hat{m}}(0)=0,\ f_{\hat{m}}(0)=f'_{\hat{m}}(0)=0,\ \phi'_{\hat{m}}(0)-k_2\phi_{\hat{m}}(0)=0,\\ f'_{\hat{m}}(\infty)=\theta_{\hat{m}}(\infty)=f''_{\hat{m}}(\infty)=\phi_{\hat{m}}(\infty)=0,\end{array}\right\} \tag{9.43}$$

$$\begin{aligned}\tilde{\mathcal{R}}^{\hat{m}}_{f_6}(\zeta) &= f''''_{\hat{m}-1}+\left(\frac{2}{\zeta+k}\right)f'''_{\hat{m}-1}-\left(\frac{1}{\zeta+k}\right)^2f''_{\hat{m}-1}\\ &+\left(\frac{1}{\zeta+k}\right)^3f'_{\hat{m}-1}+\frac{(n+1)\,k}{2\,(\zeta+k)}\left(\sum_{\hat{k}=0}^{\hat{m}-1}\left(f_{\hat{m}-1-\hat{k}}f'''_{\hat{k}}\right)\right)\\ &+\frac{(n+1)\,k}{2\,(\zeta+k)^2}\left(\sum_{\hat{k}=0}^{\hat{m}-1}\left(f_{\hat{m}-1-\hat{k}}f''_{\hat{k}}\right)\right)-\frac{(n+1)\,k}{2\,(\zeta+k)^3}\left(\sum_{\hat{k}=0}^{\hat{m}-1}\left(f_{\hat{m}-1-\hat{k}}f'_{\hat{k}}\right)\right)\\ &-\frac{(3n-1)}{2\,(\zeta+k)^2}k\left(\sum_{k=0}^{\hat{m}-1}\left(f'_{\hat{m}-1-k}f'_k\right)\right)-\frac{(3n-1)}{2\,(\zeta+k)}k\left(\sum_{k=0}^{\hat{m}-1}\left(f'_{\hat{m}-1-\hat{k}}f''_k\right)\right),\end{aligned} \tag{9.44}$$

$$\tilde{\mathcal{R}}^{\hat{m}}_{\theta_6}(\zeta)=\theta''_{\hat{m}-1}+\frac{1}{\zeta+k}\theta'_{\hat{m}-1}+\mathrm{Pr}\,\frac{k}{\zeta+k}\left(\frac{n+1}{2}\right)\left(\sum_{\hat{k}=0}^{\hat{m}-1}f_{\hat{m}-1-\hat{k}}\theta'_{\hat{k}}\right), \tag{9.45}$$

$$\begin{aligned}\tilde{\mathcal{R}}^{\hat{m}}_{\phi_5}(\zeta) &= \phi''_{\hat{m}-1}+\frac{1}{\zeta+k}\phi'_{\hat{m}-1}+Sc\frac{k}{\zeta+k}\left(\frac{n+1}{2}\right)\left(\sum_{\hat{k}=0}^{\hat{m}-1}f_{\hat{m}-1-\hat{k}}\phi'_{\hat{k}}\right)\\ &-k_1Sc\left(\sum_{\hat{k}=0}^{\hat{m}-l}\phi_{\hat{m}-1-\hat{k}}\sum_{l=0}^{\hat{k}}\left(1-\phi_{\hat{k}-l}\right)(1-\phi_l)\right),\end{aligned} \tag{9.46}$$

The following expressions are derived via Taylor's series expansion:

$$\hat{f}(\zeta,\ \breve{p})=f_{0_3}(\zeta)+\sum_{\hat{m}=1}^{\infty}f_{\hat{m}}(\zeta)\breve{p}^{\hat{m}},\ f_{\hat{m}}(\zeta)=\frac{1}{\hat{m}!}\frac{\partial^{\hat{m}}\hat{f}(\zeta,\ \breve{p})}{\partial\breve{p}^{\hat{m}}}\bigg|_{\breve{p}\,=\,0}, \tag{9.47}$$

$$\hat{\theta}(\zeta,\ \breve{p}) = \theta_{0_3}(\zeta) + \sum_{\hat{m}=1}^{\infty} \theta_{\hat{m}}(\zeta)\breve{p}^{\hat{m}},\ \theta_{\hat{m}}(\zeta) = \frac{1}{\hat{m}!}\frac{\partial^{\hat{m}}\hat{\theta}(\zeta,\ \breve{p})}{\partial \breve{p}^{\hat{m}}}\bigg|_{\breve{p}\,=\,0}, \tag{9.48}$$

$$\hat{\phi}(\zeta,\ \breve{p}) = \phi_{0_3}(\zeta) + \sum_{\hat{m}=1}^{\infty} \phi_{\hat{m}}(\zeta)\breve{p}^{\hat{m}},\ \phi_{\hat{m}}(\zeta) = \frac{1}{\hat{m}!}\frac{\partial^{\hat{m}}\hat{\phi}(\zeta,\ \breve{p})}{\partial \breve{p}^{\hat{m}}}\bigg|_{\breve{p}\,=\,0}. \tag{9.49}$$

The convergence regarding Eqs. $(9.47) - (9.49)$ is strongly based upon the suitable choices of $\hbar_f$, $\hbar_\theta$ and $\hbar_\phi$. Choosing adequate values of $\hbar_f$, $\hbar_\theta$ and $\hbar_\phi$ so that Eqs. $(9.47) - (9.49)$ converge at $\breve{p} = 1$ then

$$f(\zeta) = f_{0_3}(\zeta) + \sum_{\hat{m}=1}^{\infty} f_{\hat{m}}(\zeta), \tag{9.50}$$

$$\theta(\zeta) = \theta_{0_3}(\zeta) + \sum_{\hat{m}=1}^{\infty} \theta_{\hat{m}}(\zeta), \tag{9.51}$$

$$\phi(\zeta) = \phi_{0_3}(\zeta) + \sum_{\hat{m}=1}^{\infty} \phi_{\hat{m}}(\zeta). \tag{9.52}$$

In terms of special solutions $(f^*_{\hat{m}},\ \theta^*_{\hat{m}},\ \phi^*_{\hat{m}})$, the general solutions $(f_{\hat{m}},\ \theta_{\hat{m}},\ \phi_{\hat{m}})$ of the Eqs. $(9.40) - (9.42)$ are defined by the following expressions:

$$f_{\hat{m}}(\zeta) = f^*_{\hat{m}}(\zeta) + C^*_{38}\exp(\zeta) + C^*_{39}\exp(-\zeta) + C^*_{40}\exp(2\zeta) + C^*_{41}\exp(-2\zeta), \tag{9.53}$$

$$\theta_{\hat{m}}(\zeta) = \theta^*_{\hat{m}}(\zeta) + C^*_{42}\exp(\zeta) + C^*_{43}\exp(-\zeta), \tag{9.54}$$

$$\phi_{\hat{m}}(\zeta) = \phi^*_{\hat{m}}(\zeta) + C^*_{44}\exp(\zeta) + C^*_{45}\exp(-\zeta), \tag{9.55}$$

in which the constants C^*_i $(i = 38 - 45)$ through the boundary conditions (9.43) are given by

$$C^*_{38} = C^*_{40} = C^*_{42} = C^*_{44} = 0,\ C^*_{41} = \frac{\partial f^*_{\hat{m}}(\zeta)}{\partial \zeta}\bigg|_{\zeta\,=\,0} + f^*_{\hat{m}}(0),\ C^*_{39} = -C^*_{41} - f^*_{\hat{m}}(0), \tag{9.56}$$

$$C^*_{43} = \frac{1}{1+\gamma}\left(\frac{\partial \theta^*_{\hat{m}}(0)}{\partial \zeta}\bigg|_{\zeta\,=\,0} - \gamma\theta^*_{\hat{m}}(0)\right),\ C^*_{45} = \frac{1}{1+k_2}\left(\frac{\partial \phi^*_{\hat{m}}(\zeta)}{\partial \zeta}\bigg|_{\zeta\,=\,0} - k_2\phi^*_{\hat{m}}(0)\right). \tag{9.57}$$

9.2.3 Convergence analysis

The nonzero auxiliary parameters $\hbar_f$, $\hbar_\theta$ and $\hbar_\phi$ have significant role to define convergence region. For acceptable values of such parameters, we have mapped out $\hbar-$ curves at 20th

order of deformations. Fig. 9.1 indicates that the convergence zone lies inside the values $-1.5 \leq \hbar_f \leq -0.6$, $-1.7 \leq \hbar_\theta \leq -0.3$ and $-1.4 \leq \hbar_\phi \leq -0.5$. Table 9.1 indicates that 20th order of deformation is enough for convergent approximate solutions.

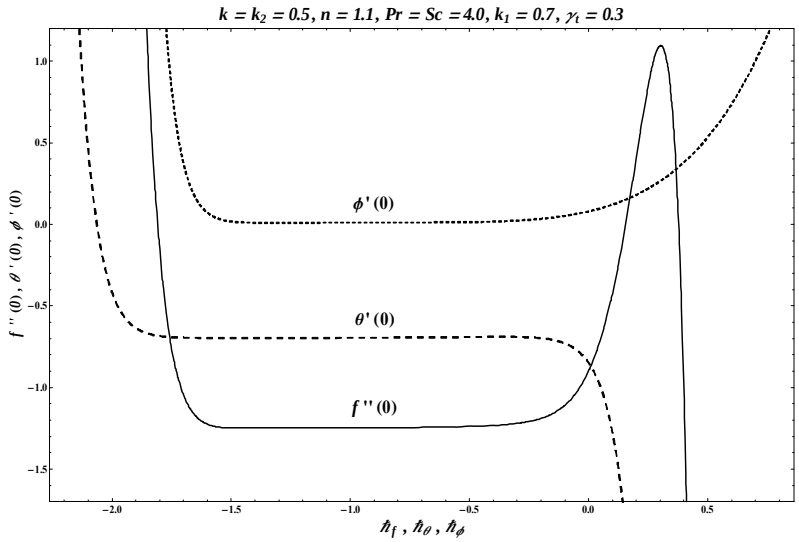

Fig. 9.1: $\hbar-$plots of $f(\zeta)$, $\theta(\zeta)$ and $\phi(\zeta)$.

Table 9.1. Convergence of series solutions when $k = k_2 = 0.5$, $n = 1.1$, $Pr = Sc = 4.0$, $k_1 = 0.7$ and $\gamma_t = 0.3$.

Order of approximations	$-f''(0)$	$-\theta'(0)$	$\phi'(0)$
1	1.1193	0.7433	0.0147
5	1.2341	0.7622	0.0134
10	1.2448	0.7721	0.0122
15	1.2469	0.7866	0.0118
20	1.2469	0.7910	0.0111
25	1.2469	0.7910	0.0111
30	1.2469	0.7910	0.0111

9.3 Discussion

This portion has been organized to explore the impact of several effective parameters including dimensionless radius of curvature parameter k, power law stretching index n, Prandtl num-

ber Pr, Biot number γ_t, magnitude of homogeneous reaction k_1, magnitude of heterogeneous reaction k_2 and Schmidt number Sc on dimensionless velocity $f'(\zeta)$, temperature $\theta(\zeta)$ and concentration $\phi(\zeta)$ profiles. Influences of k and n on $f'(\zeta)$ are presented in Figs. 9.2 and 9.3 respectively. Fig. 9.2 elucidates impact of dimensionless radius of curvature parameter k on velocity distribution $f'(\zeta)$. Both velocity field and momentum layer thickness are higher for larger curvature parameter k. Behavior of power law stretching index n on velocity $f'(\zeta)$ is displayed in Fig. 9.3. An enhancement is seen for larger stretching index n for both velocity and momentum layer thickness. It is vital here to mention that $n = 1$ relates to linear stretching, $n \neq 1$ for non-linear stretching whereas $n = 0$ is for non-stretching surface. Behaviors of curvature parameter k, power law stretching index n, Prandtl number Pr and Biot number γ_t on dimensionless temperature profile $\theta(\zeta)$ are presented in Figs. $9.4 - 9.7$ respectively. Fig. 9.4 elucidates the impact of curvature parameter k on $\theta(\zeta)$. Note that θ and corresponding layer thickness are enhanced for greater curvature parameter k. Behavior of power law stretching index n on temperature distribution $\theta(\zeta)$ is presented in Fig. 9.5. It is noticed that both temperature and associated layer thickness are reduced when n enhances. Fig. 9.6 displays Prandtl number Pr variation on temperature $\theta(\zeta)$. Larger Prandtl number Pr decrease temperature field and thermal layer thickness. Outcome of Biot number γ_t on temperature distribution $\theta(\zeta)$ is displayed in Fig. 9.7. Temperature $\theta(\zeta)$ and related layer thickness are larger when γ_t increases. Impacts of dimensionless curvature parameter k, strength of homogeneous reaction k_1, Schmidt number Sc and strength of heterogeneous reaction k_2 on dimensionless concentration profile $\phi(\zeta)$ are presented in Figs. $9.8 - 9.11$ respectively. By enhancing curvature parameter k, strength of homogeneous reaction k_1 and Schmidt number Sc, the concentration distribution $\phi(\zeta)$ reduces while reverse behavior is seen for strength of heterogeneous reaction k_2. It is noticed that, magnitude of homogeneous reaction k_1 and magnitude of heterogeneous reaction k_2 have opposite effects on concentration distribution $\phi(\zeta)$. Table 9.2 elucidates numerical data of skin friction coefficient via curvature parameter k and power-law index n. Skin friction coefficient reduces for larger curvature parameter k and power-law index n. Table 9.3 is organized to analyze the numerical data of local Nusselt number for curvature parameter k, Prandtl number Pr and Biot number γ_t. It is observed that local Nusselt number is higher for larger Prandtl

(Pr) and Biot (γ_t) numbers whereas reverse trend is seen for curvature paramter k.

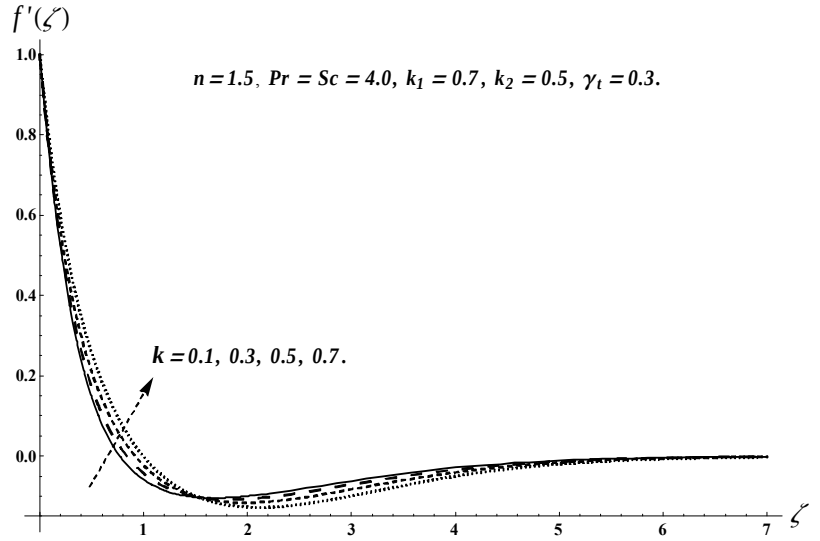

Fig. 9.2. Plots of $f'(\zeta)$ for k.

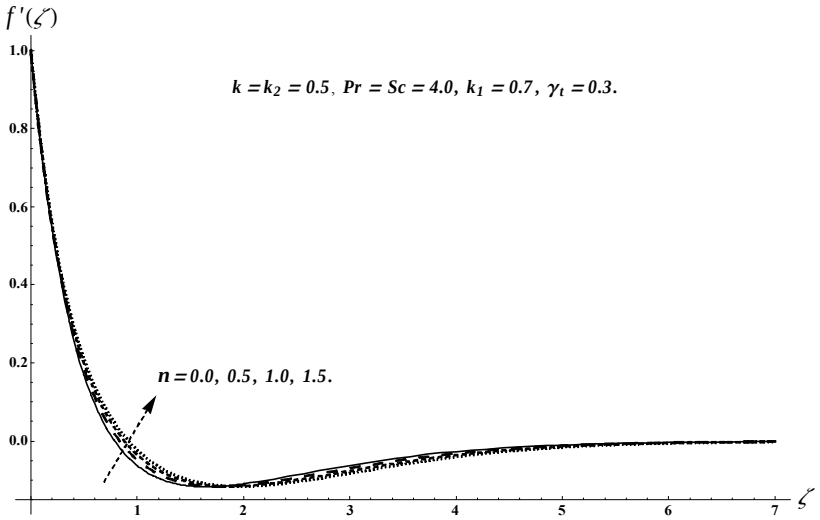

Fig. 9.3. Plots of $f'(\zeta)$ for n.

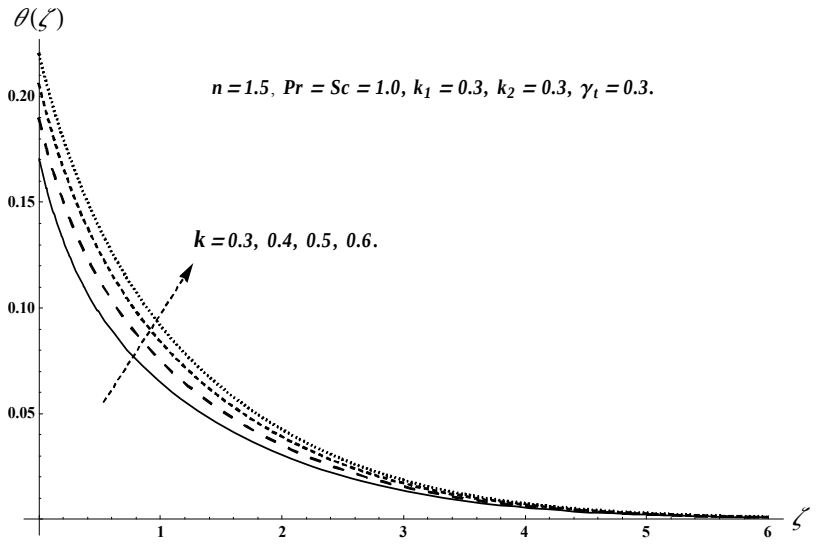

Fig. 9.4. Plots of $\theta(\zeta)$ for k.

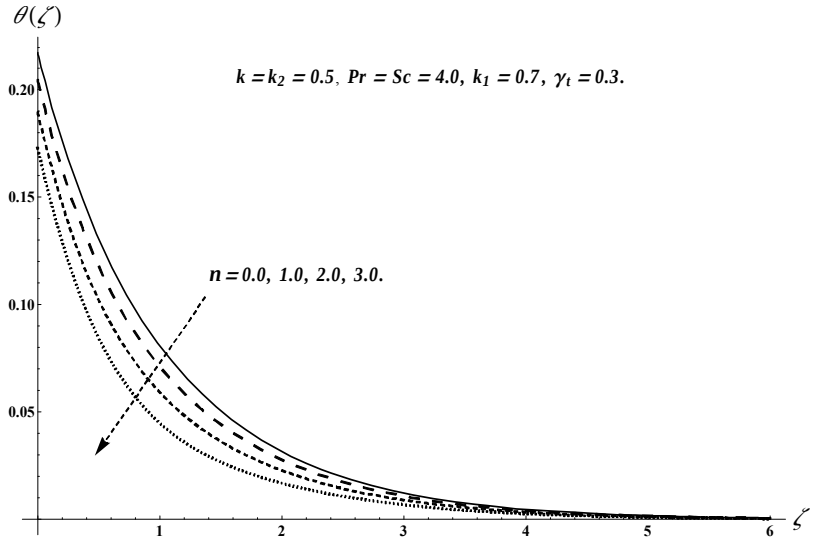

Fig. 9.5. Plots of $\theta(\zeta)$ for n.

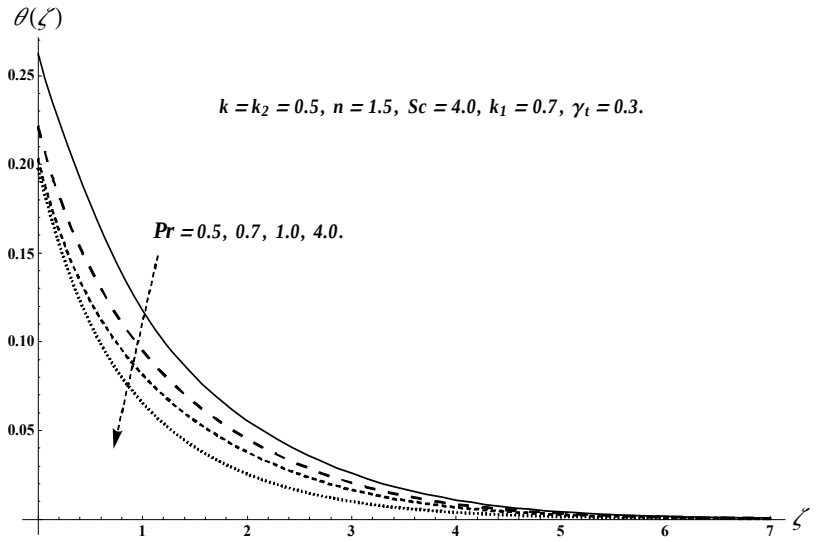

Fig. 9.6. Plots of $\theta(\zeta)$ for Pr.

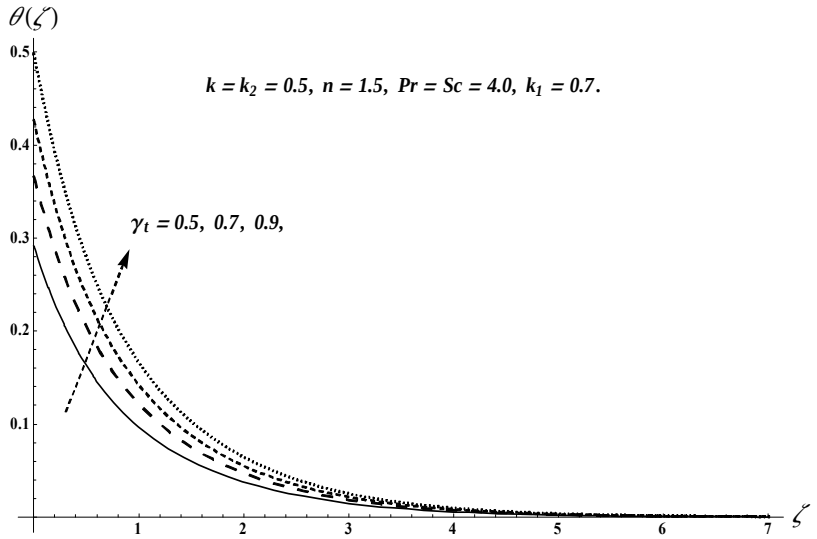

Fig. 9.7. Plots of $\theta(\zeta)$ for γ_t.

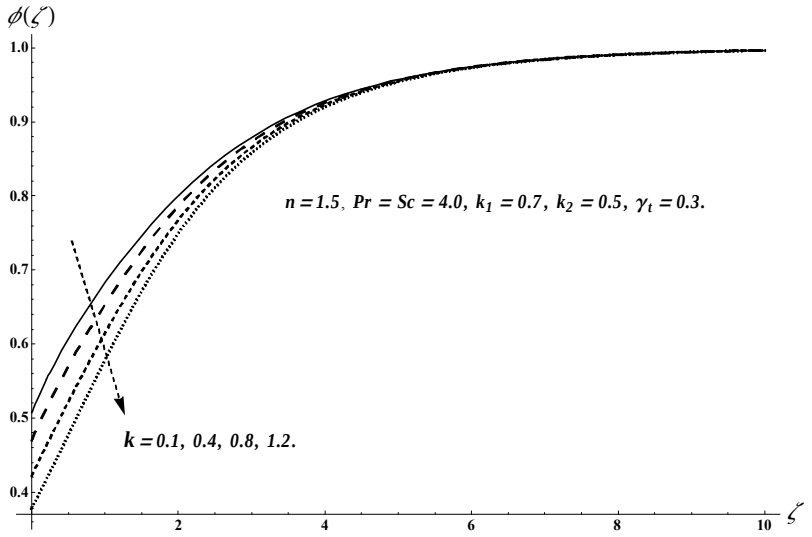

Fig. 9.8. Plots of $\phi(\zeta)$ for k.

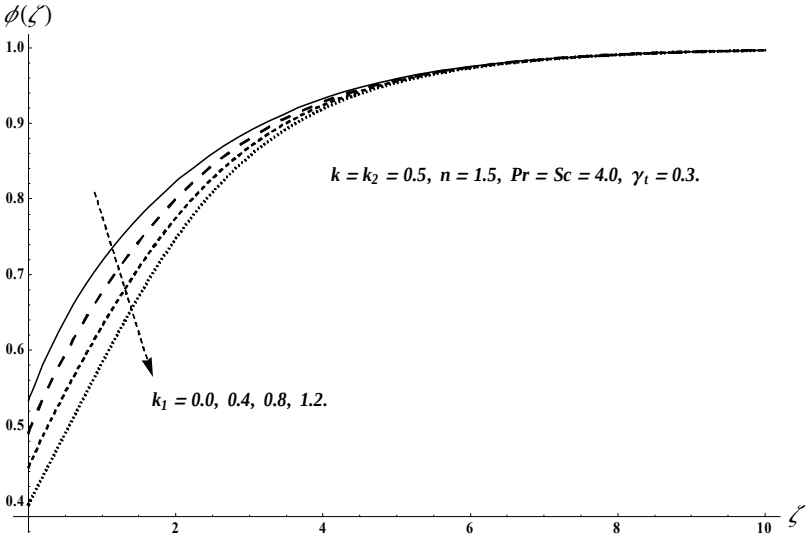

Fig. 9.9. Plots of $\phi(\zeta)$ for k_1.

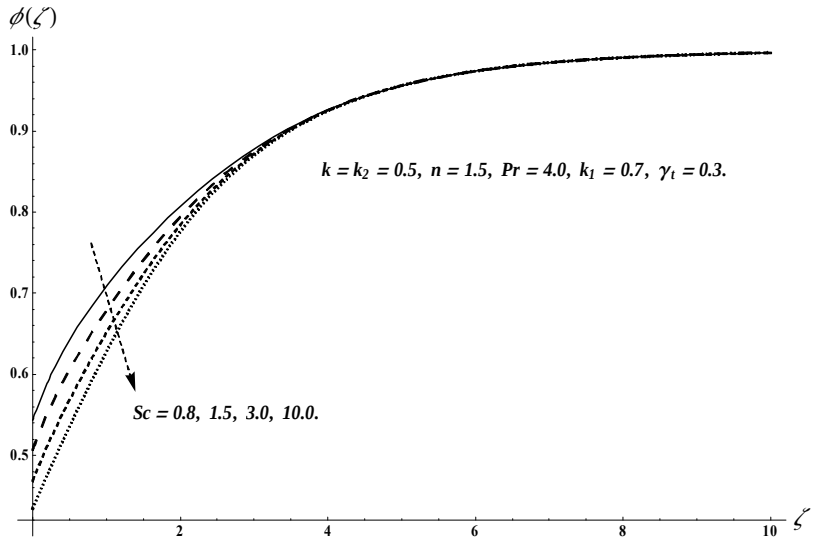

Fig. 9.10. Plots of $\phi(\zeta)$ for Sc.

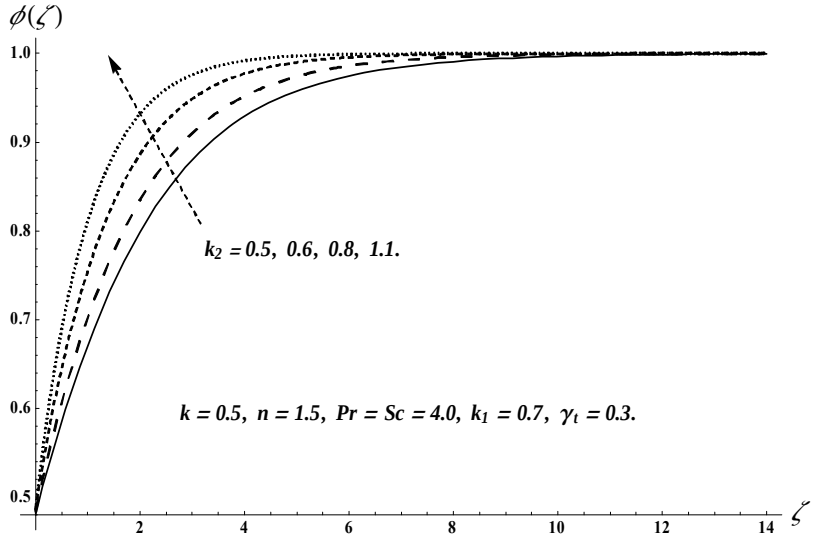

Fig. 9.11. Plots of $\phi(\zeta)$ for k_2.

Table 9.2. Variations of k and n on skin friction coefficient.

k	n	$-C_{fs_1}Re_{s_2}^{1/2}$
0.3	1.1	6.7480
0.4		5.4531
0.5		4.4423
0.5	0.9	4.7160
	1.0	4.7134
	1.1	4.7107

Table 9.3. Local Nusselt number for k, Pr and γ_t when $n = 1.1$, $k_1 = 0.7$, $k_2 = 0.5$ and $Sc = 4.0$.

k	Pr	γ	$Nu_s Re_{s_2}^{-1/2}$
0.3	4.0	0.3	0.2469
0.4			0.2454
0.5			0.2443
0.5	3.0	0.3	0.2432
	6.0		0.2452
	9.0		0.2455
0.5	4.0	0.2	0.1737
		0.3	0.2443
		0.4	0.3067

9.4 Conclusions

Flow for homogeneous-heterogeneous reactions and convective condition is investigated. Main observations of presented research are listed below.

- Velocity distribution $f'(\zeta)$ is enhanced for larger k and n.
- Larger curvature parameter k and Prandtl number Pr show decay in temperature field $\theta(\zeta)$ while opposite trend is noticed for Biot number γ_t.

- Influences of homogeneous k_1 and heterogeneous k_2 parameters on concentration field $\phi(\zeta)$ are quite reverse.
- Concentration field $\phi(\zeta)$ is reduced for higher curvature k and Schmidt number Sc.
- Skin friction coefficient is lowered for larger curvature parameter k and power-law index n.
- Local Nusselt number is enhanced for higher Prandtl Pr and Biot γ_t numbers.

Chapter 10

Numerical study for nonlinear curved stretching sheet flow subject to convective conditions

This chapter provides a numerical simulation for boundary-layer flow of viscous fluid bounded by nonlinear curved stretchable surface. Convective conditions of heat and mass transfer have been employed at the curved nonlinear stretchable surface. Moreover heat and mass transfer attributes have been explored through chemical reaction and heat absorption/generation. Boundary layer expressions are reduced to nonlinear ordinary differential system. Shooting algorithm is employed to construct the solutions for the resulting nonlinear system. The characteristics of various sundry parameters are studied. Moreover the skin friction coefficient and local Sherwood and Nusselt numbers are tabulated.

10.1 Formulation

We consider flow of viscous fluid by curved stretchable surface with nonlinear velocity. The curved stretchable surface is coiled in a circle having radius R. Heat and mass transfer characteristics are explored via chemical reaction and heat absorption/generation. Nonlinear stretchable sheet has convective heat and mass conditions. Surface is heated through hot fluid having temperature T_f and concentration C_f that give heat and mass transfer coefficents h_f and k_m

respectively. The boundary-layer expressions can be put into the forms:

$$\frac{\partial}{\partial r}\left(\left(r+R\right)v\right)+R\frac{\partial u}{\partial s}=0, \tag{10.1}$$

$$\frac{1}{r+R}u^2=\frac{1}{\rho_f}\frac{\partial p}{\partial r}, \tag{10.2}$$

$$\begin{aligned} v\frac{\partial u}{\partial r}+\frac{R}{r+R}u\frac{\partial u}{\partial s}+\frac{1}{r+R}uv &= -\frac{1}{\rho_f}\frac{R}{r+R}\frac{\partial p}{\partial s} \\ &\quad +\nu\left(\frac{\partial^2 u}{\partial r^2}+\frac{1}{r+R}\frac{\partial u}{\partial r}-\frac{1}{\left(r+R\right)^2}u\right), \end{aligned} \tag{10.3}$$

$$\rho_f c_p\left(v\frac{\partial T}{\partial r}+\frac{R}{r+R}u\frac{\partial T}{\partial s}\right)=k_f\left(\frac{\partial^2 T}{\partial r^2}+\frac{1}{r+R}\frac{\partial T}{\partial r}\right)+Q_0\left(T-T_\infty\right), \tag{10.4}$$

$$v\frac{\partial C}{\partial r}+\frac{R}{r+R}u\frac{\partial C}{\partial s}=D_m\left(\frac{\partial^2 C}{\partial r^2}+\frac{1}{r+R}\frac{\partial C}{\partial r}\right)-R_c\left(C-C_\infty\right), \tag{10.5}$$

with the boundary conditions

$$u=u_w\left(s\right)=a_1 s^n,\ v=0,\ -k_f\frac{\partial T}{\partial r}=h_f\left(T_f-T\right),\ -D_m\frac{\partial C}{\partial r}=k_m\left(C_f-C\right)\ \text{at}\ r=0, \tag{10.6}$$

$$u\to 0,\ \ \frac{\partial u}{\partial r}\to 0,\ \ T\to T_\infty,\ \ C\to C_\infty\ \ \text{as}\ \ r\to\infty. \tag{10.7}$$

Here R_c the rate of chemical reaction. Moreover for the case of curved surface pressure is no longer consistent within the boundary layer. Using the following transformations

$$\left.\begin{aligned} u=a_1 s^n f'\left(\zeta\right), \quad v=-\tfrac{R}{r+R}\sqrt{a_1 \upsilon s^{n-1}}\left(\tfrac{n+1}{2}f\left(\zeta\right)+\tfrac{n-1}{2}\zeta f'\left(\zeta\right)\right), \quad \zeta=\sqrt{\tfrac{a_1 s^{n-1}}{\upsilon}}r, \\ p=\rho_f a_1^2 s^{2n}P\left(\zeta\right), \quad k=\sqrt{\tfrac{a_1 s^{n-1}}{\upsilon}}R, \quad \theta\left(\zeta\right)=\tfrac{T-T_\infty}{T_f-T_\infty}, \quad \phi\left(\zeta\right)=\tfrac{C-C_\infty}{C_f-C_\infty}, \end{aligned}\right\} \tag{10.8}$$

Eq. (10.1) is identically verified and Eqs. (10.2) – (10.7) yield

$$\frac{\partial P}{\partial\zeta}=\frac{f'^2}{\zeta+k}, \tag{10.9}$$

$$\frac{2nk}{\zeta+k}P+\frac{(n-1)\,\zeta k}{2\,(\zeta+k)}\frac{\partial P}{\partial \zeta} = f'''+\frac{f''}{\zeta+k}-\frac{f'}{(\zeta+k)^2}-\left(\frac{2nk+(n+1)\,\zeta}{2\,(\zeta+k)^2}\right)kf'^2 + \frac{(n+1)\,k}{2\,(\zeta+k)}ff''+\frac{(n+1)\,k}{2\,(\zeta+k)^2}ff', \tag{10.10}$$

$$\frac{1}{\mathrm{Pr}}\left(\theta''+\frac{\theta'}{\zeta+k}\right)+\frac{k}{\zeta+k}\left(\frac{n+1}{2}\right)f\theta'+\delta\theta=0, \tag{10.11}$$

$$\frac{1}{Sc}\left(\phi''+\frac{\phi'}{\zeta+k}\right)+\frac{k}{\zeta+k}\left(\frac{n+1}{2}\right)f\phi'-R_c^*\phi=0, \tag{10.12}$$

$$\left.\begin{aligned} f=0,\quad f'=1,\quad \theta'=-\gamma_t\,(1-\theta)\,,\quad \phi'=-\gamma_c\,(1-\phi)\quad \text{at}\quad \zeta=0,\\ f'\to 0,\quad f''\to 0,\quad \theta\to 0,\quad \phi\to 0,\quad \text{as}\quad \zeta\to\infty, \end{aligned}\right\} \tag{10.13}$$

in which δ stands for heat generation/absorption parameter, R_c^* for chemical reaction parameter, Sc for Schmidt number, γ_t for thermal Biot number and γ_c for concentration Biot number. These parameters are

$$\left.\begin{aligned} \delta=\tfrac{Q_0}{a_1\rho_f c_p s^{n-1}},\ R_c^*=\tfrac{R_c}{a_1 s^{n-1}},\\ Sc=\tfrac{\upsilon}{D_m},\ \gamma_t=\tfrac{h_f}{k_f}\sqrt{\tfrac{\upsilon}{a_1 s^{n-1}}},\ \gamma_c=\tfrac{k_m}{D_m}\sqrt{\tfrac{\upsilon}{a_1 s^{n-1}}}. \end{aligned}\right\} \tag{10.14}$$

Elimination of pressure from Eqs. (10.9) and (10.10) gives

$$f^{iv}+\frac{2f'''}{\zeta+k}-\frac{f''}{(\zeta+k)^2}+\frac{f'}{(\zeta+k)^3}+\frac{(n+1)\,k}{2\,(\zeta+k)}ff'''+\frac{(n+1)\,k}{2\,(\zeta+k)^2}ff''-\frac{(n+1)\,k}{2\,(\zeta+k)^3}ff' -\frac{(3n-1)}{2\,(\zeta+k)^2}kf'^2-\frac{(3n-1)}{2\,(\zeta+k)}kf'f''=0. \tag{10.15}$$

Pressure P can be calculated from Eq. (10.10) as

$$P=\frac{\zeta+k}{2nk}\left(\begin{array}{c} f'''+\frac{f''}{\zeta+k}-\frac{f'}{(\zeta+k)^2}-\left(\frac{2nk+(n+1)\zeta}{2}+\left(\frac{n-1}{2}\right)\zeta\right)\frac{k}{(\zeta+k)^2}f'^2\\ +\frac{(n+1)k}{2(\zeta+k)}ff''+\frac{(n+1)k}{2(\zeta+k)^2}ff' \end{array}\right). \tag{10.16}$$

The relations for skin friction coefficient and local Nusselt and Sherwood numbers are

$$C_{f_{s_1}}=\frac{\tau_{rs_1}}{\rho_f u_w^2},\qquad Nu_s=\frac{sq_{w_r}}{k_f\,(T_w-T_\infty)},\qquad Sh_{s_2}=\frac{sj_{w_2}}{D_m\,(C_w-C_\infty)}. \tag{10.17}$$

Here τ_{rs_1} stands for wall shear stress, q_{w_r} for wall heat flux and j_{w_2} for wall mass flux which are expressed by

$$\left.\begin{aligned} \tau_{rs_1} &= \mu\left(\frac{\partial u}{\partial r}-\frac{u}{r+R}\right)\Big|_{r=0}, \\ q_{w_r} &= -k_f\left(\frac{\partial T}{\partial r}\right)\Big|_{r=0}, \\ j_{w_2} &= -D_m\left(\frac{\partial C}{\partial r}\right)\Big|_{r=0}. \end{aligned}\right\} \tag{10.18}$$

Dimensionless forms of skin friction coefficient and local Nusselt and Sherwood numbers are

$$\left.\begin{aligned} C_{fs_1}Re_{s_2}^{1/2} &= f''(0)-\tfrac{1}{k}f'(0), \\ Nu_sRe_{s_2}^{-1/2} &= -\theta'(0), \\ Sh_{s_2}Re_{s_2}^{-1/2} &= -\phi'(0), \end{aligned}\right\} \tag{10.19}$$

10.2 Analysis

The systems consisting of Eqs. (10.11), (10.12) , (10.13) and (1.15) are numerically computed by shooting technique. Main interest here is to examine the velocity $f'(\zeta)$, temperature $\theta(\zeta)$ and concentration $\phi(\zeta)$ profiles for several influential variables like dimensionless radius of curvature parameter k, power-law stretching index n, Prandtl number Pr, heat absorption/generation variable δ, Schmidt number Sc, chemical reaction parameter R_c^*, thermal Biot number γ_t and concentration Biot number γ_c. Effects of curvature parameter k and power-law stretching index n on velocity distribution $f'(\zeta)$ are presented in the Figs. 10.1 and 10.2 respectively. Fig. 10.1 elucidates the impact of dimensionless radius of curvature k on velocity distribution $f'(\zeta)$. Both velocity and momentum layer thickness are higher for larger curvature parameter k. Variation of power-law stretching index n on velocity $f'(\zeta)$ is displayed in Fig. 10.2. Larger power-law stretching index n show decay in velocity $f'(\zeta)$ and momentum layer thickness. Effects of curvature parameter k, power-law stretching index n, Prandtl number Pr, heat generation/absorption variable δ and thermal Biot number γ_t on dimensionless temperature profile $\theta(\zeta)$ are displayed in the Figs. $10.3-10.7$ respectively. Fig. 10.3 elucidates the variation of dimensionless radius of curvature parameter k on temperature profile $\theta(\zeta)$. Both temperature $\theta(\zeta)$ and thermal layer thickness are enhanced for higher curvature k. Impact of power-law stretching index n on temperature distribution $\theta(\zeta)$ is plotted in Fig. 10.4. Clearly both temperature and thermal layer thickness are lower for higher n. Fig. 10.5 shows variation of Prandtl number Pr on tem-

perature $\theta(\zeta)$. Larger Prandtl number Pr shows a decay in temperature field and related layer thickness. Impact of heat absorption/generation variable δ on temperature $\theta(\zeta)$ is displayed in Fig. 10.6. Here temperature $\theta(\zeta)$ and corresponding layer thickness are enhanced for higher δ (> 0) whereas opposite trend is observed for larger δ (< 0). Influence of thermal Biot number γ_t on temperature profile $\theta(\zeta)$ is sketched in Fig. 10.7. For higher thermal Biot number γ_t, both temperature $\theta(\zeta)$ and related layer thickness are enhanced. Contributions of curvature parameter k, power-law stretching index n, Schmidt number Sc, chemical reaction parameter R_c^* and concentration Biot number γ_c on dimensionless concentration profile $\phi(\zeta)$ are presented in the Figs. $10.8 - 10.12$ respectively. Fig. 10.8 elucidates the impact of dimensionless radius of curvature parameter k on concentration $\phi(\zeta)$. It is noted that concentration $\phi(\zeta)$ is enhanced for larger curvature parameter k. Variation of power-law stretching index n on concentration $\phi(\zeta)$ is displayed in Fig. 10.9. Larger power-law stretching index n causes a reduction in concentration $\phi(\zeta)$. Fig. 10.10 shows the impact of Schmidt number Sc on concentration $\phi(\zeta)$. Larger Schmidt number Sc show a decay in concentration $\phi(\zeta)$. Plots of $\phi(\zeta)$ via R_c^* are given in Fig. 10.11. Concentration $\phi(\zeta)$ is reduced for higher R_c^* (> 0) whereas opposite trend is observed for larger R_c^* (< 0). Impact of concentration Biot number γ_c on concentration $\phi(\zeta)$ is sketched in Fig. 10.12. For larger concentration Biot number γ_c, the concentration $\phi(\zeta)$ is enhanced. Table 10.1 elucidates the numerical data of skin friction coefficient for distinct values of curvature k and power-law stretching index n. It is examined that skin friction coefficient is enhanced for larger n while reverse trend is noticed for k. Table 10.2 is displayed to analyze the numerical data of local Nusselt number for distinct values of curvature parameter k, power-law stretching index n, Prandtl number Pr, heat generation/absorption variable δ and thermal Biot number γ_t. Here local Nusselt number is increased for higher curvature parameter k, power-law stretching index n, Prandtl number Pr and thermal Biot number γ_t whereas the opposite trend is seen via heat generation variable δ (> 0). Table 10.3 describes the numerical data of local Sherwood number for curvature k, power-law stretching index n, chemical reaction parameter R_c^*, Schmidt number Sc and concentration Biot number γ_c. Clearly local Sherwood number is increased for larger power-law stretching index n, Schmidt number Sc, chemical reaction parameter R_c^* (> 0) and concentration Biot number γ_c while reverse trend is noticed for curvature

parameter k.

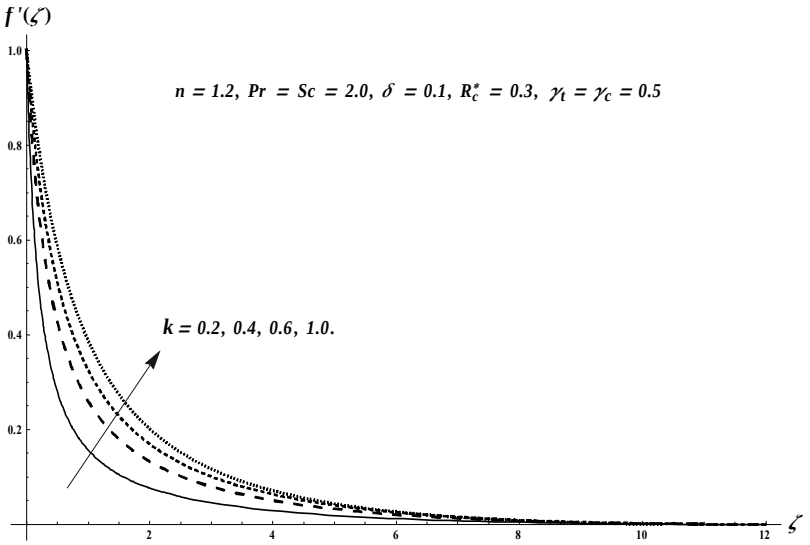

Fig. 10.1. Plots of $f'(\zeta)$ for k.

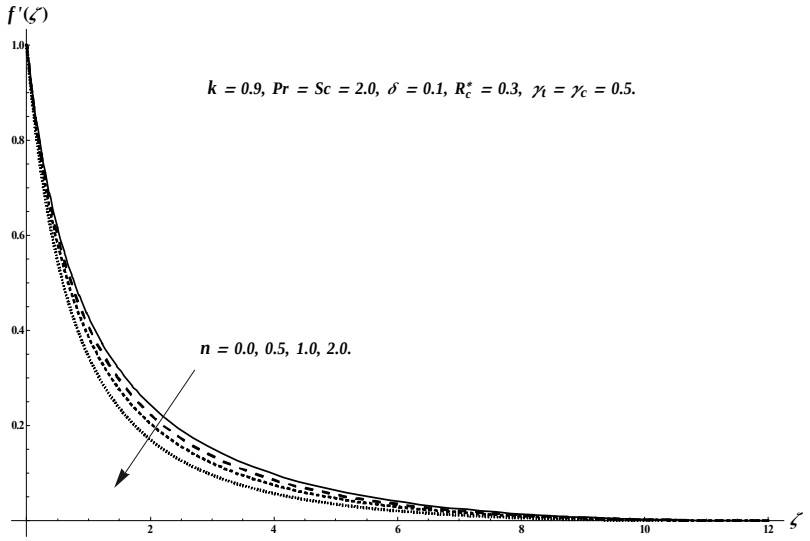

Fig. 10.2. Plots of $f'(\zeta)$ for n.

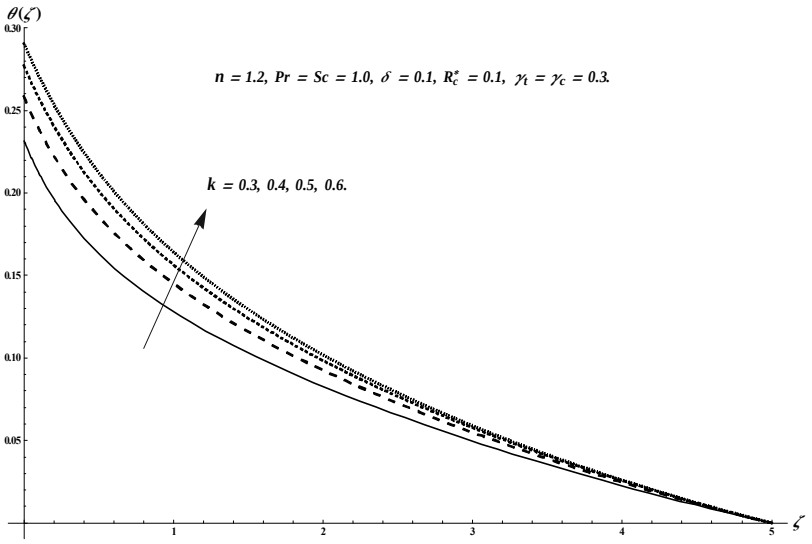

Fig. 10.3. Plots of $\theta(\zeta)$ for k.

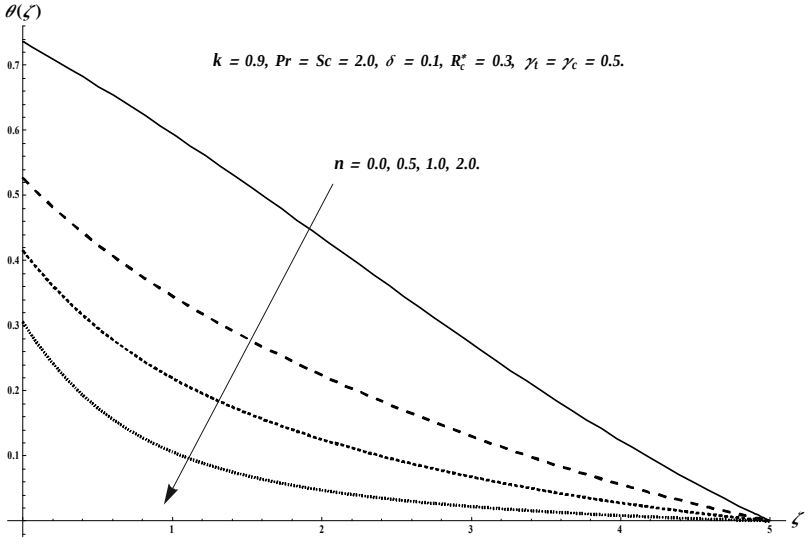

Fig. 10.4. Plots of $\theta(\zeta)$ for n.

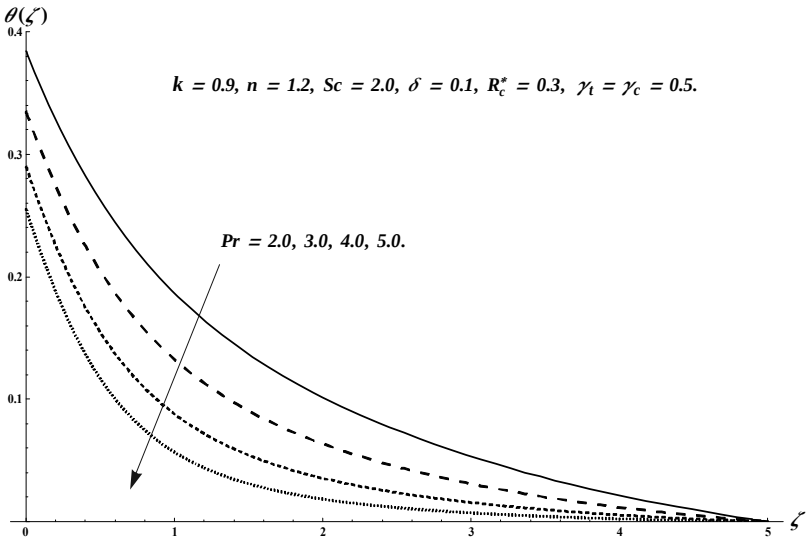

Fig. 10.5. Plots of $\theta(\zeta)$ for Pr.

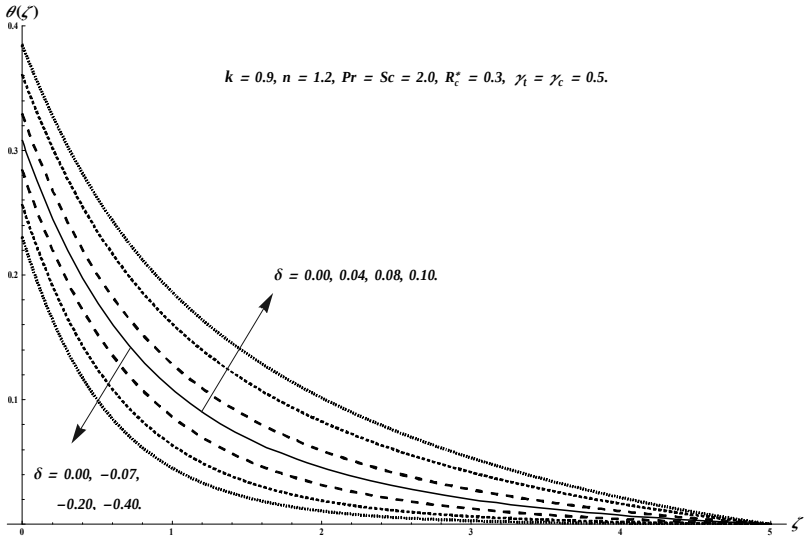

Fig. 10.6. Plots of $\theta(\zeta)$ for δ.

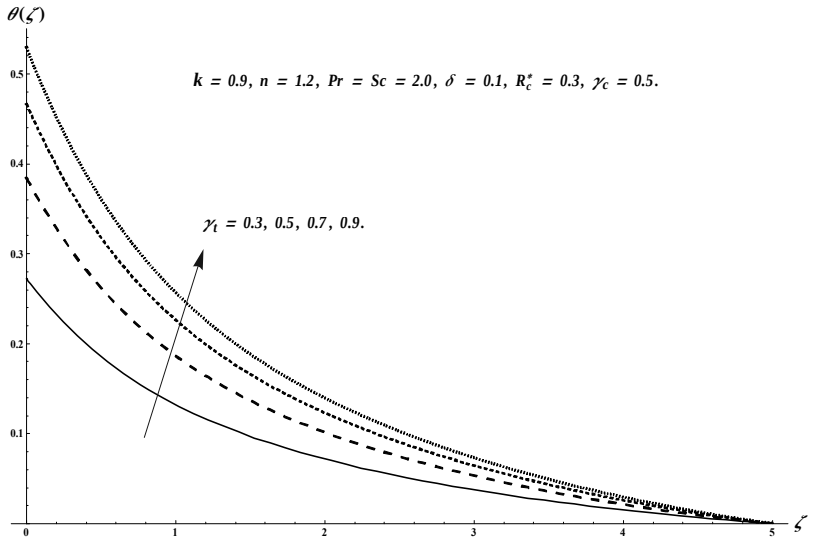

Fig. 10.7. Plots of $\theta(\zeta)$ for γ_t.

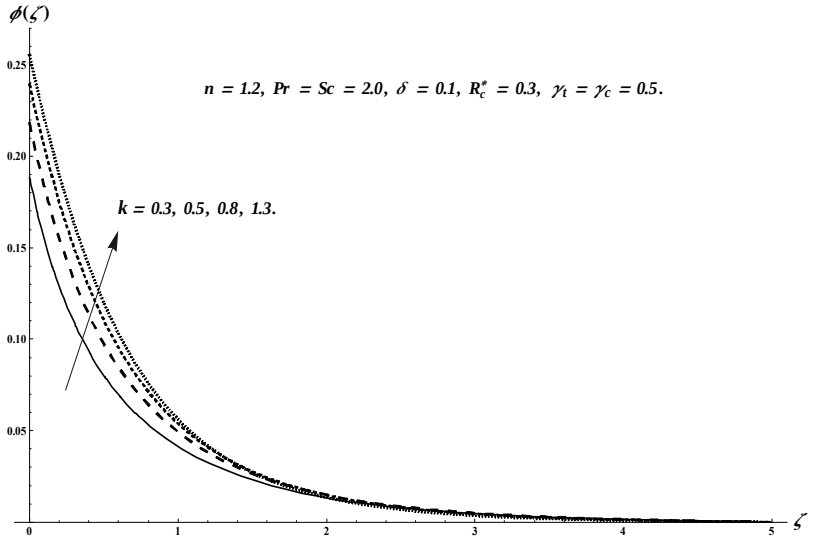

Fig. 10.8. Plots of $\phi(\zeta)$ for k.

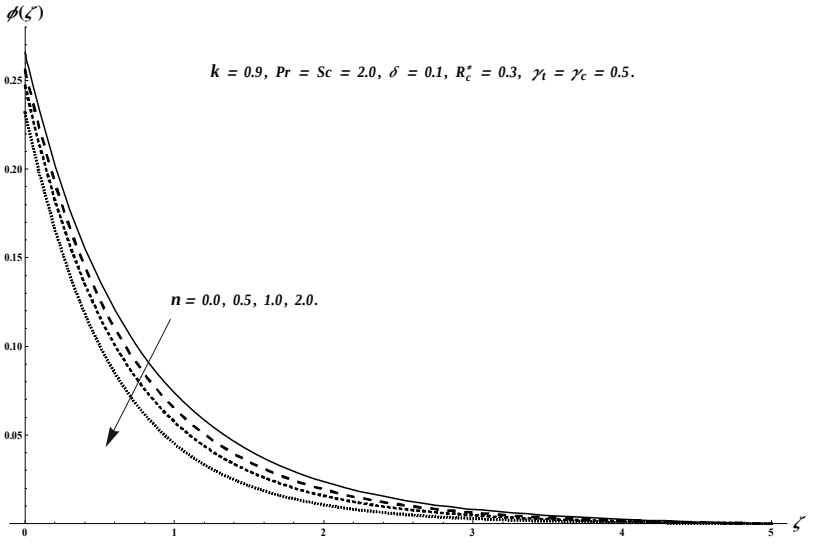

Fig. 10.9. Plots of $\phi(\zeta)$ for n.

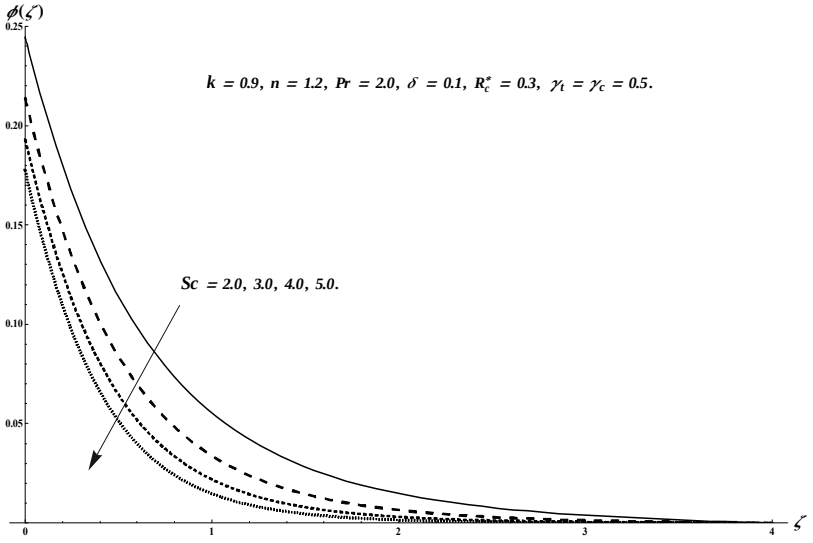

Fig. 10.10. Plots of $\phi(\zeta)$ for Sc.

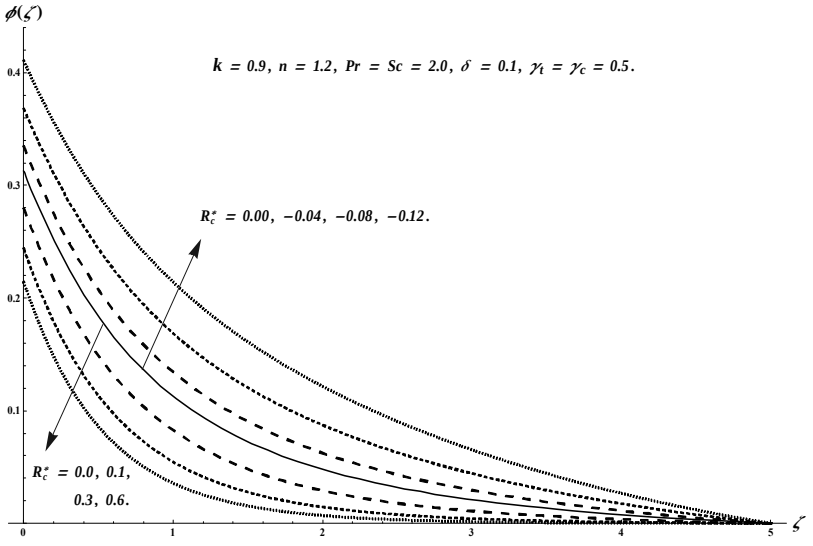

Fig. 10.11. Plots of $\phi(\zeta)$ for R_c^*.

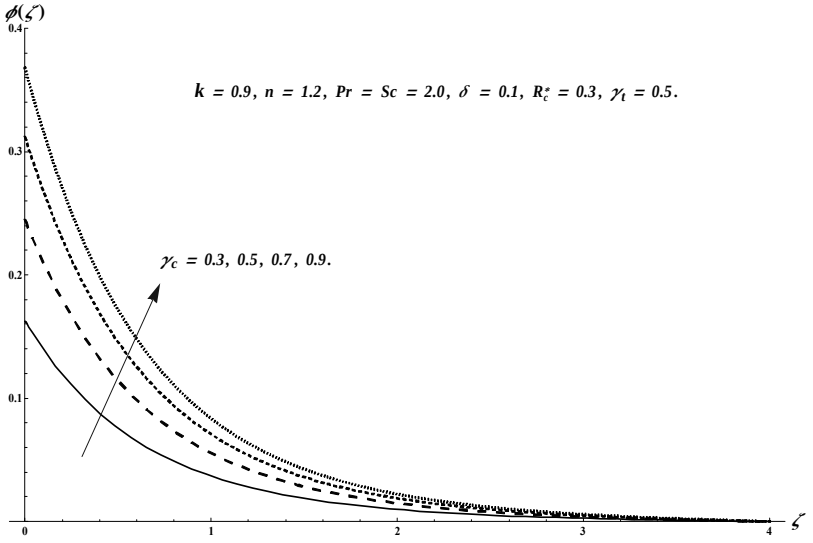

Fig. 10.12. Plots of $\phi(\zeta)$ for γ_c.

Table 10.1. Numerical data of skin friction coefficient for distinct values of k and n.

k	n	$-C_{fs_1}Re_{s_2}^{1/2}$
0.7	1.2	3.01252
0.8		2.68941
0.9		2.44795
0.9	0.5	2.35078
	1.0	2.41760
	1.5	2.57099

Table 10.2. Numerical data of local Nusselt number for distinct values of k, γ_t, n, δ and Pr when $Sc = 2.0$, $\gamma_c = 0.5$ and $R_c^* = 0.3$.

k	n	Pr	δ	γ_t	$-Nu_sRe_{s_2}^{-1/2}$
0.7	1.2	2.0	0.10	0.5	0.320250
1.0					0.326890
1.3					0.329249
0.9	0.5	2.0	0.10	0.5	0.259056
	1.0				0.312047
	2.0				0.358824
0.9	1.2	2.0	0.10	0.5	0.325390
		4.0			0.363273
		6.0			0.390522
0.9	1.2	2.0	0.00	0.5	0.348027
			0.01		0.345153
			0.02		0.341351
0.9	1.2	2.0	0.10	0.4	0.279858
				0.5	0.325390
				0.6	0.364750

Table 10.3. Local Sherwood number for distinct values of k, γ_c, n, R_c^* and Sc when $Pr = 2.0$, $\delta = 0.1$ and $\gamma_t = 0.5$.

k	n	Sc	R_c^*	γ_c	$-Sh_{s_2}Re_{s_2}^{-1/2}$
0.7	1.2	2.0	0.3	0.5	0.383966
1.0					0.377471
1.3					0.373538
0.9	0.5	2.0	0.3	0.5	0.372970
	1.0				0.377548
	2.0				0.385298
0.9	1.2	2.0	0.3	0.5	0.379238
		4.0			0.404760
		6.0			0.418212
0.9	1.2	2.0	0.0	0.5	0.345022
			0.2		0.372093
			0.4		0.384874
0.9	1.2	2.0	0.3	0.4	0.318789
				0.5	0.379238
				0.6	0.434103

10.3 Conclusions

Viscous fluid flow due to a nonlinear curved stretchable surface with convective heat and mass conditions is addressed. Chemical reaction and heat absorption/generation effects are also considered. Main observations of presented research are listed below.

- Velocity distribution $f'(\zeta)$ is enhanced for higher values of k whereas reverse trend is noticed for n.

- Larger power-law stretching index n, Prandtl number Pr and heat variable δ (< 0) show lower temperature field $\theta(\zeta)$ while opposite trend is seen for curvature parameter k, thermal Biot number γ_t and heat variable δ (> 0).

- Concentration field $\phi(\zeta)$ is higher for larger curvature parameter k, chemical reaction

parameter R_c^* (< 0) and concentration Biot number γ_c. However opposite behavior of $\phi(\zeta)$ is found for power-law stretching index n, chemical reaction parameter R_c^* (> 0) and Schmidt number Sc.

- Skin friction coefficient for k and n has opposite impact.
- Local Nusselt number is enhanced for larger curvature parameter k, power-law stretching index n, Prandtl number Pr and thermal Biot number γ_t. The parameter δ (> 0) on local Nusselt number has opposite influence when compared with k.
- Local Sherwood number is increasing function of power-law stretching index n, Schmidt number Sc,chemical reaction parameter R_c^* (> 0) and concentration Biot number γ_c. Further effects of k and n on local Sherwood number are quite reverse.

References

Bibliography

[1] B. C. Sakiadis, Boundary-layer behavior on continuous solid surfaces: I. Boundary-layer equations for two-dimensional and axisymmetric flow, AICHE J., 7 (1961) 26-28.

[2] L. J. Crane, Flow past a stretching plate, J. Appl. Math. Phys. (ZAMP), 21 (1970) 645-647.

[3] P. S. Gupta and A. S. Gupta, Heat and mass transfer on a stretching sheet with suction or blowing, Can. J. Chem. Eng., 55 (1977) 744-746.

[4] K. Vajravelu, Viscous flow over a nonlinearly stretching sheet, Appl. Math. Comput., 124 (2001) 281-288.

[5] R. Cortell, Viscous flow and heat transfer over a nonlinear stretching sheet, Appl. Math. Comput., 184 (2007) 864-873.

[6] K. V. Prasad, K. Vajravelu and P. S. Dattri, Mixed convection heat transfer over a non-linear stretching surface with variable fluid properties, Int. J. Non-linear Mech., 45 (2010) 320-330.

[7] M. H. Yazdi, S. Abdullah, I. Hashim and K. Sopian, Slip MHD liquid flow and heat transfer over non-linear permeable stretching surface with chemical reaction, Int. J. Heat Mass Transfer, 54 (2011) 3214-3225.

[8] M. Mustafa, J. A. Khan, T. Hayat and A. Alsaedi, Analytical and numerical solutions for axisymmetric flow of nanofluid due to non-linearly stretching sheet, Int. J. Non-Linear Mech., 71 (2015) 22-29.

[9] T. Hayat, A. Aziz, T. Muhammad and B. Ahmad, On magnetohydrodynamic flow of second grade nanofluid over a nonlinear stretching sheet, J. Magn. Magn. Mater., 408 (2016) 99-106.

[10] M. Sajid, N. Ali, T. Javed and Z. Abbas, Stretching a curved surface in a viscous fluid, Chin. Phys. Lett., 27 (2010) 024703.

[11] N. C. Rosca and I. Pop, Unsteady boundary layer flow over a permeable curved stretching/shrinking surface, Eur. J. Mech. B. Fluids, 51 (2015) 61-67.

[12] M. Naveed, Z. Abbas and M. Sajid, MHD flow of a microploar fluid due to curved stretching surface with thermal radiation, J. Appl. Fluid Mech., 9 (2016) 131-138.

[13] Z. Abbas, M. Naveed and M. Sajid, Hydromagnetic slip flow of nanofluid over a curved stretching surface with heat generation and thermal radiation, J. Mol. Liq., 215 (2016) 756-762.

[14] T. Hayat, M. Rashid, M. Imtiaz and A. Alsaedi, MHD convective flow due to a curved surface with thermal radiation and chemical reaction, J. Mol. Liq., 225 (2017) 482-489.

[15] M. Imtiaz, T. Hayat and A. Alsaedi, Convective flow of ferrofluid due to a curved stretching surface with homogeneous-heterogeneous reactions, Powder Tech., 310 (2017) 154-162.

[16] K. M. Sanni, S. Asghar, M. Jalil and N. F. Okechi, Flow of viscous fluid along a nonlinearly stretching curved surface, Results Phys., 7 (2017) 1-4.

[17] T. Fang, J. Zhang and Y. Zhong, Boundary layer flow over a stretching sheet with variable thickness, Appl. Math. Comput., 218 (2012) 7241-7252.

[18] M. M. Khader and A. M. Megahed, Numerical solution for boundary layer flow due to a nonlinearly stretching sheet with variable thickness and slip velocity, Eur. Phys. J. Plus, 128 (2013) 100.

[19] S. V. Subhashini, R. Sumathi and I. Pop, Dual solutions in a thermal diffusive flow over a stretching sheet with variable thickness, Int. Commun. Heat and Mass Transfer, 48 (2013) 61-66.

[20] M. S. Abdel-Wahed, E. M. A. Elbashbeshy and T. G. Emam, Flow and heat transfer over a moving surface with non-linear velocity and variable thickness in a nanofluids in the presence of Brownian motion, Appl. Maths. Comput., 254 (2015) 49-62.

[21] T. Hayat, Z. Hussain, T. Muhammad and A. Alsaedi, Effects of homogeneous and heterogeneous reactions in flow of nanofluids over a nonlinear stretching surface with variable surface thickness, J. Mol. Liq., 221 (2016) 1121-1127.

[22] T. Hayat, T. Abbas, M. Ayub, M. Farooq and A. Alsaedi, Flow of nanofluid due to convectively heated Riga plate with variable thickness, J. Mol. Liq., 222 (2016) 854-862.

[23] M. Farooq, A. Anjum, T. Hayat and A. Alsaedi , Melting heat transfer in the flow over a variable thicked Riga plate with homogeneous-heterogeneous reactions, J. Mol. Liq., 224 (2016) 1341-1347.

[24] T. Hayat, Ikram Ullah, A. Alsaedi and M. Farooq, MHD flow of Powell-Eyring nanofluid over a non-linear stretching sheet with variable thickness, Results Phys., 7 (2017) 189-196.

[25] A. C. Eringen, Simple microfluids, Int. J. Eng. Sci., 2 (1964) 205-207.

[26] A. C. Eringen, Theory of micropolar fluids, J. Math. Mech., 16 (1966) 1-18.

[27] G. Lukaszewicz, Micropolar Fluids: Theory and Applications, Birkhauser, Boston (1999).

[28] A. C. Eringen, Microcontinuum Field Theories II: Fluent Media, Springer, New York (2000).

[29] R. Nazar, N. Amin, T. Groşan and I. Pop, Free convection boundary layer on a sphere with constant surface heat flux in a micropolar fluid, Int. Commun. Heat Mass Transfer, 29 (2002) 1129-1138.

[30] D. Srinivasacharya and C. R. Reddy, Heat and mass transfer by natural convection in a doubly stratified non-Darcy micropolar fluid, Int. Commun. Heat Mass Transfer, 37 (2010) 873-880.

[31] T. Hayat and M. Qasim, Effects of thermal radiation on unsteady magnetohydrodynamic flow of a micropolar fluid with heat and mass transfer, Z. Naturforsch. A, 65a (2010) 950-960.

[32] M. M. Rashidi, S. A. Mohimanian and S. Abbasbandy, Analytic approximation solutions for heat transfer of a micropolar fluid through a porous medium with radiation, Commun. Nonlinear Sci. Numer. Simul., 16 (2011) 1874-1879.

[33] L. Cao, X. Si and L. Zheng, The flow of a micropolar fluid through a porous expanding channel: A Lie group analysis, Appl. Math. Comput., 270 (2015) 242-250.

[34] M. Waqas, M. Farooq, M. I. Khan, A. Alsaedi, T. Hayat and T. Yasmeen, Magnetohydrodynamic (MHD) mixed convection flow of micropolar liquid due to nonlinear stretched sheet with convective condition, Int. J. Heat Mass Transfer, 102 (2016) 766-772.

[35] M. Turkyilmazoglu, Mixed convection flow of magnetohydrodynamic micropolar fluid due to a porous heated/cooled deformable plate: Exact solutions, Int. J. Heat Mass Transfer, 106 (2017) 127-134.

[36] R. E. Powell and H. Eyring, Mechanism for relaxation theory of viscosity, Nature, 154 (1944) 427-428.

[37] T. Hayat, Z. Iqbal, M. Qasim and S. Obaidat, Steady flow of an Eyring Powell fluid over a moving surface with convective boundary conditions, Int. J. Heat Mass Transfer, 55 (2012) 1817-1822.

[38] A. V. Rosca and I. Pop, Flow and heat transfer of Powell-Eyring fluid over a shrinking surface in a parallel free stream, Int. J. Heat Mass Transfer, 71 (2014) 321-327.

[39] T. Hayat, M. Imtiaz and A. Alsaedi, Effects of homogeneous-heterogeneous reactions in flow of Powell-Eyring fluid, J. Cent. South Univ., 22 (2015) 3211-3216.

[40] R. Ellahi, E. Shivanian, S. Abbasbandy and T. Hayat, Numerical study of magnetohydrodynamics generalized Couette flow of Eyring-Powell fluid with heat transfer and slip condition, Int. J. Numer. Methods Heat Fluid Flow, 26 (2016) 1433-1445.

[41] T. Hayat, I. Ullah, T. Muhammad, A. Alsaedi and S. A. Shehzad, Three-dimensional flow of Powell-Eyring nanofluid with heat and mass flux boundary conditions, Chinese Phys. B, 25 (2016) 074701.

[42] T. Hayat, R. Sajjad and S. Asghar, Series solution for MHD channel flow of a Jeffery fluid, Int. J. Heat Mass Transfer, 15 (2010) 2400-2406.

[43] N. Dalir, Numerical study of entropy generation for forced convection flow and heat transfer of a Jeffrey fluid over a stretching sheet, Alexandria Eng. J., 53 (2014) 769-778.

[44] R. Ellahi and F. Hussain, Simultaneous effects of MHD and partial slip on peristaltic flow of Jeffery fluid in a rectangular duct, J. Magn. Magn. Mater., 393 (2015) 284-292.

[45] T. Hayat, T. Muhammad, S. A. Shehzad and A. Alsaedi, A mathematical study for three-dimensional boundary layer flow of Jeffrey nanofluid, Z. Naturforsch. A, 70a (2015) 225-233.

[46] H. P. Azikri de Deus, C. O. R. Negrao and A. T. Franco, The modified Jeffreys model approach for elasto-viscoplastic thixotropic substances, Phys. Lett. A, 380 (2016) 585-595.

[47] W. C. Tan, T. Masuoka, Stokes first problem for second grade fluid in a porous half space, Int. J. Non-Linear Mech., 40 (2005) 515–522.

[48] M. Jamil, A. Rauf, C. Fetecau and N. A. Khan, Helical flows of second grade fluid due to constantly accelerated shear stresses, Commun. Nonlinear Sci. Numer. Simul., 16 (2011) 1959-1969.

[49] A. Ahmad and S. Asghar, Flow of a second grade fluid over a sheet stretching with arbitrary velocities subject to a transverse magnetic field, Appl. Math. Lett., 24 (2011) 1905–1909.

[50] M. Ramzan and M. Bilal, Time dependent MHD nano-second grade fluid flow induced by permeable vertical sheet with mixed convection and thermal radiation, PloS one, 10 (2015) e0124929.

[51] T. Hayat, I. Ullah, T. Muhammad and A. Alsaedi, Magnetohydrodynamic (MHD) three-dimensional flow of second grade nanofluid by a convectively heated exponentially stretching surface, J. Mol. Liq., 220 (2016) 1004-1012.

[52] S. U. S. Choi, Enhancing thermal conductivity of fluids with nanoparticles, ASME, FED 231/MD 66 (1995) 99-105.

[53] J. Buongiorno, Convective transport in nanofluids, ASME J. Heat Transfer, 128 (2006) 240-250.

[54] M. Turkyilmazoglu, Exact analytical solutions for heat and mass transfer of MHD slip flow in nanofluids, Chem. Eng. Sci., 84 (2012) 182-187.

[55] M. Goodarzi, M. R. Safaei, K. Vafai, G. Ahmadi, M. Dahari, S. N. Kazi and N. Jomhari, Investigation of nanofluid mixed convection in a shallow cavity using a two-phase mixture model, Int. J. Thermal Sci., 75 (2014) 204-220.

[56] M. Sheikholeslami, M. G. Bandpy, R. Ellahi and A. Zeeshan, Simulation of MHD CuO–water nanofluid flow and convective heat transfer considering Lorentz forces, J. Magn. Magn. Mater., 369 (2014) 69-80.

[57] A. Malvandi and D. D. Ganji, Brownian motion and thermophoresis effects on slip flow of alumina/water nanofluid inside a circular microchannel in the presence of a magnetic field, Int. J. Thermal Sci., 84 (2014) 196-206.

[58] H. Togun, M. R. Safaei, R. Sadri, S. N. Kazi, A. Badarudin, K. Hooman and E. Sadeghinezhad, Numerical simulation of laminar to turbulent nanofluid flow and heat transfer over a backward-facing step, Appl. Math. Comput., 239 (2014) 153-170.

[59] A. V. Kuznetsov and D. A. Nield, Natural convective boundary-layer flow of a nanofluid past a vertical plate: A revised model, Int. J. Thermal Sci., 77 (2014) 126-129.

[60] A. Malvandi, M. R. Safaei, M. H. Kaffash and D. D. Ganji, MHD mixed convection in a vertical annulus filled with Al_2O_3-water nanofluid considering nanoparticle migration, J. Magn. Magn. Mater., 382 (2015) 296-306.

[61] T. Hayat, T. Muhammad, A. Alsaedi and M. S. Alhuthali, Magnetohydrodynamic three-dimensional flow of viscoelastic nanofluid in the presence of nonlinear thermal radiation, J. Magn. Magn. Mater., 385 (2015) 222-229.

[62] B. J. Gireesha, R. S. R. Gorla and B. Mahanthesh, Effect of suspended nanoparticles on three-dimensional MHD flow, heat and mass transfer of radiating Eyring-Powell fluid over a stretching sheet, J. Nanofluids, 4 (2015) 474-484.

[63] T. Hayat, A. Aziz, T. Muhammad and B. Ahmad, Influence of magnetic field in three-dimensional flow of couple stress nanofluid over a nonlinearly stretching surface with convective condition, Plos One, 10 (2015) e0145332.

[64] C. Zhang, L. Zheng, X. Zhang and G. Chen, MHD flow and radiation heat transfer of nanofluids in porous media with variable surface heat flux and chemical reaction, Appl. Math. Model., 39 (2015) 165-181.

[65] A. Chamkha, S. Abbasbandy and A. M. Rashad, Non-Darcy natural convection flow for non-Newtonian nanofluid over cone saturated in porous medium with uniform heat and volume fraction fluxes, Int. J. Numer. Methods Heat Fluid Flow, 25 (2015) 422-437.

[66] H. Togun, G. Ahmadi, T. Abdulrazzaq, A. J. Shkarah, S. N. Kazi, A. Badarudin and M. R. Safaei, Thermal performance of nanofluid in ducts with double forward-facing steps, J. Taiwan Inst. Chem. Eng., 47 (2015) 28-42.

[67] Z. Nikkhah, A. Karimipour, M. R. Safaei, P. F. Tehrani, M. Goodarzi, M. Dahari and S. Wongwises, Forced convective heat transfer of water/functionalized multi-walled carbon nanotube nanofluids in a microchannel with oscillating heat flux and slip boundary condition, Int. Commun. Heat Mass Transfer, 68 (2015) 69-77.

[68] O. A. Akbari, D. Toghraie, A. Karimipour, M. R. Safaei, M. Goodarzi, H. Alipour and M. Dahari, Investigation of rib's height effect on heat transfer and flow parameters of laminar water-Al_2O_3 nanofluid in a rib-microchannel, Appl. Math. Comp., 290 (2016) 135-153.

[69] H. R. Goshayeshi, M. Goodarzi, M. R. Safaei and M. Dahari, Experimental study on the effect of inclination angle on heat transfer enhancement of a ferrofluid in a closed loop

oscillating heat pipe under magnetic field, Experimental Thermal Fluid Sci., 74 (2016) 265-270.

[70] H. R. Goshayeshi, M. R. Safaei, M. Goodarzi and M. Dahari, Particle size and type effects on heat transfer enhancement of Ferro-nanofluids in a pulsating heat pipe, Powder Tech., 301 (2016) 1218-1226.

[71] A. Malvandi, Film boiling of magnetic nanofluids (MNFs) over a vertical plate in presence of a uniform variable-directional magnetic field, J. Magn. Magn. Mater., 406 (2016) 95-102.

[72] A. Malvandi, A. Ghasemi and D. D. Ganji, Thermal performance analysis of hydromagnetic Al_2O_3-water nanofluid flows inside a concentric microannulus considering nanoparticle migration and asymmetric heating, Int. J. Thermal Sci., 109 (2016) 10-22.

[73] T. Hayat, M. I. Khan, M. Waqas, T. Yasmeen and A. Alsaedi, Viscous dissipation effect in flow of magnetonanofluid with variable properties, J. Mol. Liq., 222 (2016) 47-54.

[74] T. Hayat, T. Muhammad, S. A. Shehzad and A. Alsaedi, On three-dimensional boundary layer flow of Sisko nanofluid with magnetic field effects, Adv. Powder Tech., 27 (2016) 504-512.

[75] K. L. Hsiao, Stagnation electrical MHD nanofluid mixed convection with slip boundary on a stretching sheet, Appl. Thermal Eng., 98 (2016) 850-861.

[76] M. Ramzan, M. Bilal, U. Farooq and J. D. Chung, Mixed convective radiative flow of second grade nanofluid with convective boundary conditions: An optimal solution, Results Phys., 6 (2016) 796-804.

[77] T. Hayat, T. Muhammad, S. A. Shehzad and A. Alsaedi, An analytical solution for magnetohydrodynamic Oldroyd-B nanofluid flow induced by a stretching sheet with heat generation/absorption, Int. J. Thermal Sci., 111 (2017) 274-288.

[78] T. Hayat, T. Muhammad, S. A. Shehzad and A. Alsaedi, On magnetohydrodynamic flow of nanofluid due to a rotating disk with slip effect: A numerical study, Comp. Methods Appl. Mech. Eng., 315 (2017) 467-477.

[79] S. Choi and S. J. Kim, Effect of initial cooling on heat and mass transfer at the cryogenic surface under natural convective condition, Int. J. Heat Mass Transfer, 112 (2017) 850–861.

[80] J. Zueco, S. Ahmed and L. M. Lopez-Gonzalez, 2-D unsteady free convective heat and mass transfer Newtonian Hartmann flow with thermal diffusion and Soret effects: Network model and finite differences, Int. J. Heat Mass Transfer, 110 (2017) 467–475.

[81] K. M. Shirvan, M. Mamourian, S. Mirzakhanlari, R. Ellahi and K. Vafai, Numerical investigation and sensitivity analysis of effective parameters on combined heat transfer performance in a porous solar cavity receiver by response surface methodology, Int. J. Heat Mass Transfer, 105 (2017) 811–825.

[82] M. Sheikholeslami, T. Hayat, A. Alsaedi and S. Abelman, Numerical analysis of EHD nanofluid force convective heat transfer considering electric field dependent viscosity, Int. J. Heat Mass Transfer, 105 (2017) 2558–2565.

[83] T. Hayat, A. Aziz, T. Muhammad and A. Alsaedi, On magnetohydrodynamic three-dimensional flow of nanofluid over a convectively heated nonlinear stretching surface, Int. J. Heat Mass Transfer, 100 (2016) 566-572.

[84] G. V. Ramanaiah, M. S. Babu and M. Lavanya, Convective heat and mass transfer flow of Siskonanofluid past a nonlinear stretching sheet with thermal radiation, Int. Ref. J. Eng. Sci. (IRJES), 5 (2016) 17-37.

[85] K. Das, R. P. Sharma and A. Sarkar, Heat and mass transfer of a second grade magneto-hydrodynamic fluid over a convectively heated stretching sheet, J. Comput. Design Eng., 3 (2016) 330–336.

[86] J. B. J. Fourier, Theorie analytique De La chaleur, Paris, (1822).

[87] C. Cattaneo, Sulla conduzione del calore, Atti Semin. Mat Fis Uni Modena Reggio Emilia, 3 (1948) 83–101.

[88] C. I. Christov, On frame indifferent formulation of the Maxwell-Cattaneo model of finite-speed heat conduction, Mech. Res. Commun., 36 (2009) 481–486.

[89] M. Ciarletta and B. Straughan, Uniqueness and structural stability for the Cattaneo-Christov equations, Mech. Res. Commun., 37 (2010) 445–447.

[90] V. Tibullo and V. Zampoli, A uniqueness result for the Cattaneo-Christov heat conduction model applied to incompressible fluids, Mech. Res. Commun., 38 (2011) 77–79.

[91] S. Han, L. Zheng, C. Li, and X. Zhang, Coupled flow and heat transfer in viscoelastic fluid with Cattaneo-Christov heat flux model, Appl. Math. Lett., 38 (2014) 87–93.

[92] T. Hayat, M. I. Khan, M. Farooq, A. Alsaedi, M. Waqas and T. Yasmeen, Impact of Cattaneo-Christov heat flux model in flow of variable thermal conductivity fluid over a variable thicked surface, Int. J. Heat Mass Transfer, 99 (2016) 702–710.

[93] L. Liu, L. Zheng, F. Liu and X. Zhang, Anomalous convection diffusion and wave coupling transport of cells on comb frame with fractional Cattaneo-Christov flux, Commun. Nonlinear Sci. Numer. Simul., 38 (2016) 45–58.

[94] T. Hayat, T. Muhammad, M. Mustafa and A. Alsaedi, Three-dimensional flow of Jeffrey fluid with Cattaneo–Christov heat flux: An application to non-Fourier heat flux theory, Chinese J. Phy., 55 (2017) 1067–1077.

[95] E. Magyari and A. J. Chamkha, Combined effect of heat generation or absorption and first-order chemical reaction on micropolar fluid flows over a uniformly stretched permeable surface: The full analytical solution, Int. J. Thermal Sci. 49 (2010) 1821-1828.

[96] A. M. Salem and M. A. El-Aziz, Effect of Hall current and chemical reaction on hydromagnetic flow of a stretching vertical surface with internal heat generation/absorption, Appl. Math. Modell. 32 (2008) 1236-1254.

[97] C. H. Chen, On the analytic solution of MHD flow and heat transfer for two types of viscoelastic fluid over a stretching sheet with energy dissipation, internal heat source and thermal radiation, Int. J. Heat Mass Transfer 53 (2010) 4264-4273.

[98] C. H. Chen, Magneto-hydrodynamic mixed convection of a power-law fluid past a stretching surface in the presence of thermal radiation and internal heat generation/absorption, Int. J. Non-Linear Mech. 44 (2009) 596-603.

[99] S. Siddiqa, S. Asghar and M. A. Hossain, Natural convection flow over an inclined flat plate with internal heat generation and variable viscosity, Math. Comput. Modell. 52 (2010) 1739-1751.

[100] R. A. Van Gorder and K. Vajravelu, Convective heat transfer in a conducting fluid over a permeable stretching surface with suction and internal heat generation/absorption, Appl. Math. Comput. 217 (2011) 5810-5821.

[101] P. Rana and R. Bhargava, Numerical study of heat transfer enhancement in mixed convection flow along a vertical plate with heat source/sink utilizing nanofluids, Commun. Nonlinear Sci. Numer. Simulat. 16 (2011) 4318-4334.

[102] A. Alsaedi, M. Awais and T. Hayat, Effects of heat generation/absorption on stagnation point flow of nanofluid over a surface with convective boundary conditions, Commun. Nonlinear Sci. Numer. Simulat. 17 (2012) 4210-4223.

[103] N. F. M. Noor, S. Abbasbandy and I. Hashim, Heat and mass transfer of thermophoretic MHD flow over an inclined radiate isothermal permeable surface in the presence of heat source/sink, Int. J. Heat Mass Transfer 55 (2012) 2122-2128.

[104] M. Turkyilmazoglu and I. Pop, Soret and heat source effects on the unsteady radiative MHD free convection flow from an impulsively started infinite vertical plate, Int. J. Heat Mass Transfer 55 (2012) 7635-7644.

[105] W. T. Cheng and C. H. Lin, Melting effect on mixed convective heat transfer with aiding and opposing external flows from the vertical plate in a liquid-saturated porous medium, Int. J. Heat Mass Transfer, 50 (2007) 3026-3034.

[106] C. Tien and Y. C. Yen, The effect of melting on forced convection heat transfer, J. Appl. Meteorol., 4 (1965) 523-527.

[107] M. Epstein and D. H. Cho, Melting heat transfer in steady laminar flow over a flat plate, ASME J. Heat Transfer, 98 (1976) 531-533.

[108] W. T. Cheng and C. H. Lin, Transient mixed convective heat transfer with melting effect from the vertical plate in a liquid saturated porous medium, Int. J. Eng. Sci., 44 (2006) 1023-1036.

[109] N. A. Yacob, A. Ishak and I. Pop, Melting heat transfer in boundary layer stagnation-point flow towards a stretching/shrinking sheet in a micropolar fluid, Comput. Fluids, 47 (2011) 16-21.

[110] M. Mustafa, T. Hayat and A. A. Hendi, Influence of melting heat transfer in the stagnation-point flow of a Jeffrey fluid in the presence of viscous dissipation, J. Appl. Mech., 79 (2012) 024501.

[111] T. Hayat, M. Hussain, M. Awais and S. Obaidat, Melting heat transfer in a boundary layer flow of a second grade fluid under Soret and Dufour effects, Int. J. Numer. Methods Heat Fluid Flow, 23 (2013) 1155-1168.

[112] A. Rasekh, D. D. Ganji, S. Tavakoli and S. Naeejee, Melting effect on steady laminar flow of a micropolar fluid over a stagnation point on a vertical surface, J. Eng. Phys. Thermophys., 86 (2013) 1210-1216.

[113] K. Das and L. Zheng, Melting effects on the stagnation point flow of a Jeffrey fluid in the presence of magnetic field, Heat Transfer Res., 44 (2013) 493-506.

[114] M. Awais, T. Hayat and A. Alsaedi, Investigation of heat transfer in flow of Burgers' fluid during a melting process, J. Egyptian Math. Soc., 23 (2015) 410-415.

[115] J. H. Merkin, A model for isothermal homogeneous-heterogeneous reactions in boundary-layer flow, Math. Comp. Modell., 24 (1996) 125-136.

[116] M. A. Chaudhary and J. H. Merkin, A simple isothermal model for homogeneous-heterogeneous reactions in boundary-layer flow. II Different diffusivities for reactant and autocatalyst, Fluid Dyn. Res., 16 (1995) 335-359.

[117] N. Bachok, A. Ishak and I. Pop, On the stagnation-point flow towards a stretching sheet with homogeneous-heterogeneous reactions effects, Commun. Nonlinear Sci. Numer. Simul., 16 (2011) 4296-4302.

[118] P. K. Kameswaran, S. Shaw, P. Sibanda and P. V. S. N. Murthy, Homogeneous-heterogeneous reactions in a nanofluid flow due to porous stretching sheet, Int. J. Heat Mass Transfer, 57 (2013) 465-472.

[119] T. Hayat, Z. Hussain, A. Alsaedi and B. Ahmad, Heterogeneous-homogeneous reactions and melting heat transfer effects in flow with carbon nanotubes, J. Mol. Liq., 220 (2016) 200-207.

[120] T. Hayat, Z. Hussain, T. Muhammad and A. Alsaedi, Effects of homogeneous and heterogeneous reactions in flow of nanofluids over a nonlinear stretching surface with variable surface thickness, J. Mol. Liq., 221 (2016) 1121-1127.

[121] Z. Abbas and M. Sheikh, Numerical study of homogeneous-heterogeneous reactions on stagnation point flow of ferrofluid with non-linear slip condition, Chinese J. Chem. Eng., 25 (2017) 11-17.

[122] T. Hayat, Z. Hussain, A. Alsaedi and M. Mustafa, Nanofluid flow through a porous space with convective conditions and heterogeneous-homogeneous reactions, J. Taiwan Inst. Chem. Eng., 70 (2017) 119-126.

[123] M. Sajid, S. A. Iqbal, M. Naveed and Z. Abbas, Effect of homogeneous-heterogeneous reactions and magnetohydrodynamics on Fe3O4 nanofluid for the Blasius flow with thermal radiations, J. Mol. Liq., 233 (2017) 115-121.

[124] T. Hayat, F. Haider, T. Muhammad and A. Alsaedi, Darcy-Forchheimer flow with Cattaneo-Christov heat flux and homogeneous-heterogeneous reactions, Plos One, 12 (2017) e0174938.

[125] P. Forchheimer, Wasserbewegung durch boden, Z. Ver. Dtsch. Ing., 45 (1901) 1782–1788.

[126] M. Muskat, The Flow of Homogeneous Fluids Through Porous Media, Edwards, MI. (1946).

[127] V. D. Federico, S. Longo, L. Chiapponi, R. Archetti and V. Ciriello, Radial gravity currents in vertically graded porous media: theory and experiments for Newtonian and power-law fluids, Adv. Water Resour. 70 (2014) 65–76.

[128] S. Rashidi, M. Dehghan, R. Ellahi, M. Riaz and M. T. Jamal-Abad, Study of stream wise transverse magnetic fluid flow with heat transfer around an obstacle embedded in a porous medium, J. Magnetism Magnetic Materials, 378 (2015) 128-137.

[129] T. Hayat, T. Muhammad, S. Al-Mezal and S. J. Liao, Darcy-Forchheimer flow with variable thermal conductivity and Cattaneo-Christov heat flux, Int. J. Numer. Methods Heat Fluid Flow, 26 (2016) 2355–2369.

[130] T. Hayat, F. Haider, T. Muhammad and A. Alsaedi, On Darcy-Forchheimer flow of viscoelastic nanofluids: A comparative study, J. Mol. Liq., 233 (2017) 278–287.

[131] Z. Kang, D. Zhao and H. Rui, Block-centered finite difference methods for general Darcy–Forchheimer problems, Appl. Maths. Comput., 307 (2017) 124–140.

[132] S. J. Liao, On the homotopy analysis method for nonlinear problems, Appl. Math. Comput., 147 (2004) 499-513.

[133] P. R. Sharma and G. Singh, Effects of variable thermal conductivity and heat source/sink on MHD flow near a stagnation point on a linearly stretching sheet, J. Appl. Fluid Mech., 2 (2009) 13-21.

[134] T. Hayat, R. Sajjad, Z. Abbas, M. Sajid and Awatif A. Hendi, Radiation effects on MHD flow of Maxwell fluid in a channel with porous medium, Int. J. Heat Mass Transf., 54 (2011) 854–862.